1988

Investigations of the electrical characteristics of a vacuum arc centrifuge

Julian Whichello
University of Wollongong

INVESTIGATIONS OF THE ELECTRICAL CHARACTERISTICS OF A VACUUM ARC CENTRIFUGE

A thesis submitted in fulfilment of the requirements for the award of the degree of

MASTER OF ENGINEERING (HONOURS)

from

THE UNIVERSITY OF WOLLONGONG

by

JULIAN WHICHELLO B.E.

DEPARTMENT OF ELECTRICAL AND COMPUTER ENGINEERING

1988

ABSTRACT

Australian interest in the development of a vacuum arc centrifuge (VAC) was initiated by a concern for the continued availability of certain stable metal isotopes. The long term objective was the establishment of a commercial enrichment facility using a range of separation techniques to produce industrial and medical isotopes. The VAC was seen to be ideal for the production of limited quantities of moderately enriched metal isotopes.

Isotope separation takes place in a vacuum vessel where a highly ionised column of plasma is initiated by a vacuum arc. An external magnetic field is applied axially to the cathode and arc. Azimuthal rigid body rotation of the plasma is achieved by the induced E_r X B_z Lorentz force. Plasma confinement is maintained by the J_θ X B_z force, due to the azimuthal current, balancing the outward plasma pressure gradient force.

Rigid body plasma rotation of approximately 1.5×10^5 rad/S for an axial magnetic field of 0.1 T was achieved in the 1.5 metre long ANSTO VAC. Typical arc impedances of 15 and 33 mΩ were respectively measured with and without axial magnetic field. Cathode erosion experiments yielded an erosion rate of 48 µg/C. An axial velocity of 1.5×10^4 m/S was measured. From these results, plasma ion densities of 3×10^{19} m^{-3} were estimated. Approximately 15 % zinc separation was measured for a copper-zinc plasma at B_z = 0.125 T. A 1 % enrichment of ^{65}Cu was measured for a copper plasma.

This thesis presents an over-view of isotope separation techniques, particularly using rotating plasmas and outlines recent developments in VAC technology. The theoretical basis, design and construction of the ANSTO VAC is described. An explanation of the experimental apparatus and data acquisition system follows. The vacuum arc discharge characteristics and plasma measurements are presented. The degree of measured separation is analysed against theoretical predictions which indicate that greater separation performance is achievable.

CONTENTS

1. INTRODUCTION 1

1.1 Isotope Separation Techniques. 4

1.2 A Review of Isotope Separation using Plasmas. 6

1.3 Developments in Vacuum Arc Centrifuge Technology 18

1.4 Vacuum Arc Centrifuge Development at the Australian Nuclear Science and Technology Organisation (ANSTO). 19

2. A THEORETICAL DESCRIPTION OF THE VAC PROCESS 22

2.1 The Vacuum Arc. 22

2.2 Plasma Rotation. 28

2.3 Plasma Confinement. 31

2.4 Plasma Density. 33

2.5 Separation Processes. 35

3. ENERGY STORAGE AND DISCHARGE SYSTEMS 39

3.1 A High Voltage Series RLC Discharge Circuit. 41

3.2 A Low Voltage Pulse Forming Network. 49

4. DESCRIPTION OF EXPERIMENTAL APPARATUS 54

4.1 Vacuum Chamber. 54

4.2 Vacuum System. 56

4.3 Electrode Configurations and Trigger Systems. 57

4.3.1 The Laser Triggered Electrode. 57

4.3.2 The High Voltage Triggered Electrode. 59

4.4 The Solenoid Magnet. 64

4.5 Plasma Deposition Collectors 70

4.5.1 Rotation and Axial Drift Velocity Collector. 70

4.5.2 Isotope Analysis Collector. 72

4.6 Measurement Apparatus. 73

4.6.1 Magnetic Probes. 73

4.6.2 Langmuir Probes. 75

4.6.3 High Voltage Probes. 76

4.6.4 Current Monitor. 76

4.6.5 Isotope Separation. 77

4.7 Data Acquisition System. 79

5. ARC MEASUREMENTS 80

5.1 Arc Current and Voltage. 81

5.2 Arc Characteristics. 85

6. PLASMA MEASUREMENTS 91

6.1 Direction of Plasma Rotation. 93

6.2 Speed of Rotation. 97

6.3 Axial Drift Velocity. 104

6.4 Confinement. 107

6.5 Density. 111

7. SEPARATION MEASUREMENTS 119

7.1 Rate of Erosion. 119

7.2 Analysis of Plasma Deposits. 123

7.3 Discussion. 128

8. CONCLUSIONS 141

9. ACKNOWLEDGMENTS 146

BIBLIOGRAPHY 147

APPENDICES

A1 The VAC Laboratory and Equipment. 163

A2 A Derivation of Design Equations for a PFN. 167

A3 VAC Ancillary Equipment Electrical Circuits. 169

A4 A Mathematical Model and Computer Program for the Opimisation of the Solenoid Magnet Spacings. 175

A5 VAC Data Acquisition, Recording and Analysis. 183

1. INTRODUCTION

For each element, there exists a variety of possible atomic structures defined by the number of neutrons in the nucleus. These are termed "isotopes". Whilst the atomic weights of isotopes of the same element differ, chemically, they are usually indistinguishable in reaction.

All the known elements have more than one isotope. Some occur naturally and are termed to be "stable". Others may only occur for a certain length of time and are regarded as "unstable". This latter group are also radioactive due to the emission of alpha, beta and gamma particles as the nucleus disintegrates. Figure 1.0.1 shows the division of elements to four sub-groups according to stability and classification.

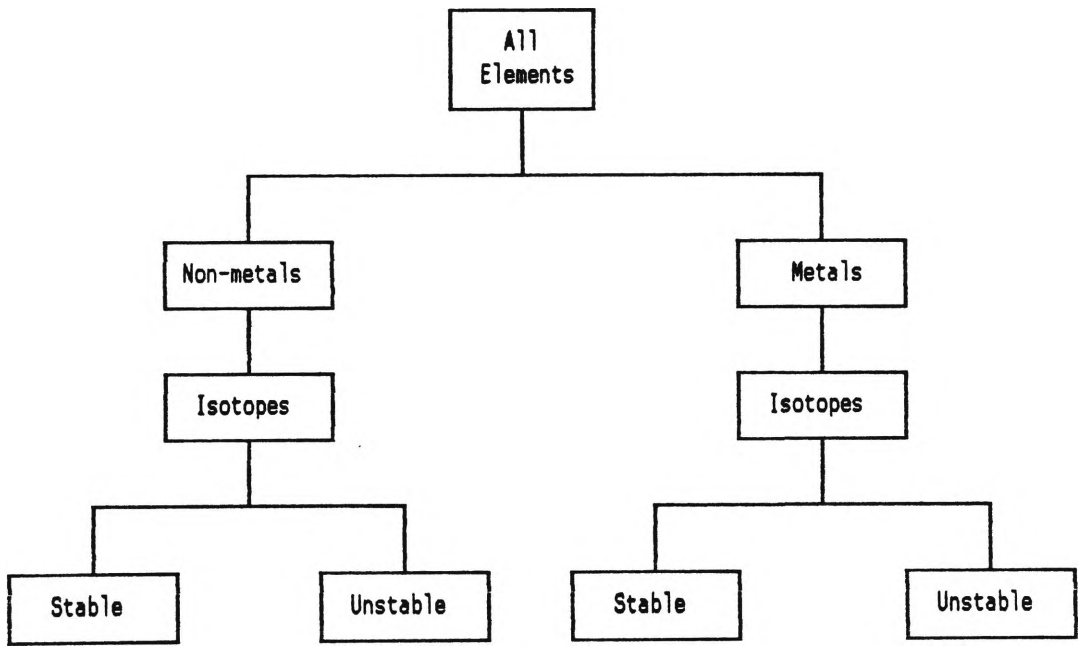

Fig 1.0.1 The classification of elements

Today, instruments have been developed which can resolve to one atomic mass unit (a.m.u.) the difference in the atomic weights of isotopes. Sensitive devices also exist which can detect the decay of a single nuclei. The unique properties of isotopes have brought about significant advances in medicine, industry, agriculture and scientific research.

A number of authors have produced extensive reviews of isotope applications [1-4]. Table 1.1 provides examples of a range of isotopes and particular applications. Stable metal isotopes and the stable isotopes of carbon may be separated without special radiological protection.

TABLE 1.0.1

Particular Isotopes Applications

Element	Classification	Isotope	Stability	Application
	M - Metal NM - Non-metal		St - Stable U - Unstable	A - Agricultural I - Industrial M - Medical N - Nuclear S - Scientific research
Americium	M	^{241}Am	U	I Smoke detectors
Cadmium	M	^{115m}Cd	U	S Water and soil pollution studies
Calcium	M	^{45}Ca	U	A Radioactive tracer
		^{46}Ca	St	M Metabolism studies
		^{48}Ca	St	M Metabolism studies
Carbon	NM	^{12}C	St	S Water and soil pollution studies S Pesticide research
		^{13}C	St	S Water and soil pollution studies S Pesticide research M Organic compound labeling M Nuclear magnetic resonance studies
		^{14}C	U	S Water and soil pollution studies A Soil movement and weed control

TABLE 1.0.1 (continued)

Particular Isotopes Applications

Element	Classification	Isotope	Stability	Application
	M - Metal NM - Non-metal		St - Stable U - Unstable	A - Agricultural I - Industrial M - Medical N - Nuclear S - Scientific research
Chromium	M	^{50}Cr	St	M Haemotology
Copper	M	^{64}Cu	St	S Pesticide research
		^{65}Cu	St	S Water and soil pollution studies
Iron	M	^{58}Fe	St	M Haemotology
Molybdenum	M	^{98}Mo	St	M Radiopharmaceutical production
Nickel	M	^{64}Ni	St	M Source material for ^{67}Cu production
Thallium	M	^{203}Tl	St	M Diagnostic radiology
Zinc	M	^{68}Zn	St	M Source material for ^{67}Ga production
Zirconium	M	^{90}Zr	St	N Zircaloy cladding of nuclear fuel
		^{91}Zr	St	N Zircaloy cladding of nuclear fuel

It has been suggested [5,6] that critical parts in fission and fusion reactors could be replaced with components fabricated from isotopically tailored materials. This would result in less hazardous waste for disposal.

1.1 A Review of Isotope Separation Techniques

Over the past four decades, various processes have been developed to separate stable isotopes on a commercial scale. Electromagnetic methods [7] have mainly been used since 1947. The major producers, U.S.A. and U.S.S.R., have supplied most of the world's supply of over 200 isotopes. Both countries have large facilities that were originally built for the production of enriched uranium. For example, the Oak Ridge National Laboratory (ORNL) in the U.S.A. separates isotopes by the calutron process [8]. In this process, an ion beam of the element to be separated is directed into a magnetic field. Separation is achieved by the different trajectories taken by the isotopes as they pass through the field. The rate of separation is limited by the large space charge forces that exist within the beam.

Whilst calutrons were used successfully to separate fissile material for early nuclear weapons programs, the high energy cost for relatively low throughput could not compete with the diffusion process for the separation of uranium on a commercial scale. ORNL had over 1000 calutron units. However, only a fraction of the total number remain operational [8,9]. These are devoted to the separation of small quantities of highly enriched isotopes. Increased costs of operation recently precipitated a rationalisation of the ORNL facility and production has ceased for many isotopes which are now seen to be uneconomic by the calutron method. Yet, the demand for affordable, specialised isotopes has continued to grow. The

situation has prompted researchers in a number of overseas institutions to investigate stable isotope production by alternative processes.

For the diffusion process [10], a gaseous compound containing a mixture of isotopic species is made to pass through a porous barrier into an evacuated space. The average speed of an isotope molecule is dependent on atomic mass weight. Isotopes with different average speeds separate because the lighter species can pass more easily through the barrier.

In the gas centrifuge process [10], a gaseous compound of the element is rotated at very high speed in a long cylinder. The different centrifugal forces on the various isotopic species cause the gas to take up a distribution within the cylinder with respect to isotopic mass variation. The separation factor for this process increases with the peripheral velocity to forth power. Rotational velocities approaching 500 m/s are possible. The speed of the gas is ultimately limited by the availability of materials for rotor fabrication.

Separation factors for individual diffusion and centrifuge separation units are comparatively low for a single pass of feed stock. Therefore, stages of separation are configured into a cascade to improve the product enrichment. Both processes are ideal for production of large quantities of moderately enriched isotopes. However, they are not suitable for the production of small quantities of highly enriched isotopes.

The atomic vapor laser process (AVLIS) [10] is still under development in a number of countries. The laser process uses a vapor of the element to be separated. The isotopic mass difference results in resonant specific isotopic characteristics. A tunable dye laser is used to selectively resonate and ionise the desired isotope leaving the remainder of the vapor neutral. Electrostatic precipitation is used to collect the ions from the vapor.

The Nozzle process [10] and the Ion Exchange chemical process [10] are alternative methods for the separation of uranium isotopes. Both are still under development but are not seen as likely successors to the diffusion and gas centrifuge methods.

Separation of isotopes by the rotation of a plasma has been considered for some time [11]. Unlike the gas centrifuge process, only the plasma is rotated and not limited by the mechanical strength of the containing vessel.

1.2 A Review of Isotope Separation Using Plasma Processes

In the early 1940s, Slepian [11] is believed to have first suggested the separation of isotopes using a rotating plasma. His idea for an "Ionic Centrifuge" came after the observation of high rotational speeds in early plasma research experiments. The development of such a device was slow with the fledgling nuclear industry's initial commitment to the calutron process. As the demand for enriched uranium increased, the calutrons were eventually displaced by the

diffusion process as the major method for the separation of uranium isotopes. In 1957, after consistently disappointing results with the ionic centrifuge, Slepian proposed a Magneto-Ionic Expander for the separation of uranium isotopes [12].

During this period, a theory for the formation of the solar system was put forward by Alfvén [13]. He postulated that the neutral gases present around the sun were accelerated toward it by gravitational attraction. Once the gas reached a certain velocity, it became ionised and then was trapped by the sun's magnetic field. The velocity for a particular gas molecule was given by

$$\tfrac{1}{2}mv_c^2 = eV_{ion} \qquad (1.2.1)$$

where eV_{ion} = ionisation energy

m = mass of an atom of the accelerating gas

v_c = Alfvén critical velocity

Although originally unconnected with isotope separation, Alfvén's theory has significant implications for the maximum speed obtainable with plasmas in partially ionised plasma centrifuges. Here the presence of the neutral particles limit the ion rotation velocity. When the kinetic energy of the ions equals the ionisation potential of the neutrals, energy is removed from the ions to ionise the neutrals. The mechanism of this transference of energy has still to be explained, but the Alfvén critical velocity has been observed by plasma centrifuge researchers [14].

After the initial work of Slepian, a number of research workers explored the possibility of plasma centrifuges. Bonnevier suggested the use of a fully ionised plasma in 1966 [15]. Later, he suggested the use of a plasma centrifuge which comprised a fully ionised plasma surrounded by a mixture of partially ionised plasma and neutral gas [16]. In the presence of an axial magnetic field, the fast moving inner plasma would cause the outer mixture to rotate about the machine's axis.

A comprehensive review of theoretical and experimental investigations of rotating plasmas was presented by Lehnert in 1971 [14]. It provided a systematic overview of contemporary developments in rotating plasma research. Since that time investigations have continued with some notable achievements in the separation of isotopes. Table 1.2.1 is a summary of isotope separation using rotating plasma devices since Lehnert's paper.

TABLE 1.2.1

A Summary of Isotope Separation Studies using Rotating Plasma Devices since 1970

AUTHOR YEAR [REF.]	DEVICE	ELEMENTS OR ISOTOPES STUDIED	PARTICLE DENSITY n_e (m^{-3}) n_i (m^{-3})	ROTATIONAL SPEED v_θ (m/s) ω (rad/s)	B_o (T)	MAXIMUM MEASURED SEPARATION*	SPECIAL FEATURES AND COMMENTS
Bonnevier 1971 [16]	PC	H_2-D_2 Ne-H H_2-Ar	$n_i \sim 10^{21}$		0.6		Partially ionised plasma. $\Omega = \frac{E}{B_r}$
Nathrath 1973 [17]	Discussion Paper	Ar	$n_e = 10^{20}$	$v_\theta = 1.5 \times 10^4$	1.0		Model assumes a pin cathode and and ring anode.
James & Simpson 1974 [18]	SUPPER III	Ne				8 % ^{22}Ne-^{20}Ne	Discharge between a 5 cm dia. short electrode and an outer ring.
Boeschoten 1975 [19]	PC	Ar Ar + H	$n_i \sim 10^{19}$-10^{20}	$\omega = 10^5$	0.34	25 %	Hollow cathode discharge. Hydrogen carrier gas improved separation.
Nathrath et al. 1975 [20]	Discussion Paper	U					Comparison of separation using partially and fully ionised plasma centrifuges.

* Separation is defined by the following expression:

$$\text{Separation (Enrichment)} = \left[\frac{(n_1/n_2)_p}{(n_1/n_2)_n} - 1 \right] \times 100\ \%$$

where: n_1 ~ rel. abundance of fraction 1
n_2 ~ rel. abundance of fraction 2
p,n ~ denote, respectively, product and natural

TABLE 1.2.1 (Continued)

AUTHOR YEAR [REF.]	DEVICE	ELEMENTS OR ISOTOPES STUDIED	PARTICLE DENSITY	ROTATIONAL SPEED	B_o	MAXIMUM MEASURED SEPARATION*	SPECIAL FEATURES AND COMMENTS
Cairns 1975 [21]	Vortex II	Ne	$n_e=10^{20}$	$v_\theta=1.3\times10^4$	0.2	16 % ^{22}Ne-^{20}Ne	Device based on solar wind experimental apparatus. Not an optimum plasma centrifuge design.
James et al. 1975 [22]	SUPPER III	Ne	$n_e\sim10^{21}$		1.5	10 %	Experimental results compared with elementary equilibrium theory.
James & Simpson 1976 [23]	SUPPER III	Ne	$n_e=10^{21}$	$v_\theta=7\times10^3$	0.5 1.0 1.5	10 % ^{22}Ne-^{20}Ne	Partially ionised plasma. Electron density ~ 10^{21} Addition of H_2 improved sep. performance.
Himmel et al. 1976 [24]	PC	He	$n_e=10^{20}$	$v_\theta=3.5\times10^4$	0.6		Alfvén critical velocity and the occurrence of plasma spoke structure are discussed.
Hirshfield 1976 [25]	Discussion Paper	H^+-D^+ C Fe	$n_i=10^{23}$				A vacuum arc ion source is proposed for an ion resonance separator.
Himmel 1976 [26]	PC	He		$v_\theta=3\times10^4$			Further investigation of crit. vel. phenomena.
McClure & Nathrath 1977 [27]	Discussion Paper	U					Includes an investigation of background element effects.

TABLE 1.2.1 (Continued)

AUTHOR YEAR [REF.]	DEVICE	ELEMENTS OR ISOTOPES STUDIED	PARTICLE DENSITY	ROTATIONAL SPEED	B_o	MAXIMUM MEASURED SEPARATION *	SPECIAL FEATURES AND COMMENTS
Mück & Simon 1977 [28]	PC	He Ne Kr		$v_\theta=9\times10^2$	0.6	6 % ^{82}Kr-^{86}Kr	Device used a pin cathode and ring anode.
Nathrath 1977 [29]	PC	U	10^{20}	$v_\theta=2.5\times10^3$	0.8	10 % ^{235}U-^{238}U	Fully ionised a background of helium gas Rotational velocities > v_c
Kaneko et al. 1978 [30]	PC	He-Ar		$v_\theta=2\times10^2$	0.75	55 % He-Ar	Partially ionised plasma.
James & Simpson 1978 [31]		Ne		$v_\theta=4\times10^3$	0.5 1.0 1.5		Primarily a theoretical study.
Walsh et al. 1978 [32]	SUPPER V	Ar Plasma + Cu & Ni				35 % Cu-Ni	Cu - Ni introduced after into already rotating argon plasma
Wijnakker et al. 1979 [33]		Ar-Xe Diffuse Contracted	8×10^{18} 5×10^{19}	$v_\theta=7.5\times10^2$ $v_\theta=1.9\times10^3$	0.13 0.26	150 % Ar-He	Two hollow cathodes at both ends of a cylinder with 24 electrically insulated rings. Two are biased as ring anodes.

TABLE 1.2.1 (Continued)

AUTHOR YEAR [REF.]	DEVICE	ELEMENTS OR ISOTOPES STUDIED	PARTICLE DENSITY	ROTATIONAL SPEED	B_o	MAXIMUM MEASURED SEPARATION*	SPECIAL FEATURES AND COMMENTS
Belorusov et al. 1979 [34]	PC	Xe-He Xe-Ne Xe	$n_e \sim 2 \times 10^{20}$	$v_\theta \sim 10^3$	0.16	20% Xe-He 20% Xe-Ne 6% ^{136}Xe-^{129}Xe	Discusses plasma inhomogeneity in the axial direction and plasma temperature reduction for increased PC efficiency.
Wijnakker & Granneman 1980 [35]		Ar-Xe Diffuse		Ar $v_\theta = 1.4 \times 10^3$ Xe $v_\theta = 8.3 \times 10^2$	0.17	150 % Ar-He	Device is similar to ref [33]. Diffuse mode is favoured for separation.
Krishnan & Hirshfield 1980 [36]	VAC	Cu C				18 % $^{63}Cu^{2+}$-$^{65}Cu^{2+}$ 17 % $^{13}C^+$-$^{12}C^+$	Paper mainly discusses a new ion energy and momentum spectrometer.
Krishnan et al. 1981 [37]	VAC	Cu-Ni Cu		$w = 10^5$ $v_\theta = 7.4 \times 10^3$	0.2	60 % Cu-Ni 100 % ^{65}Cu	ESCA technique used to measure separation of Cu-Ni. Energy momentum spec. used for Cu.
Simpson 1981 [38]	Discussion Paper	H He N Ar					Theoretical study and comparison with Angerth and Fahleson.
Korobtsev et al. 1981 [39]	PC	H Ne	$n_e \sim 10^{19}$	$v_\theta \sim 1.5 \times 10^2$ $v_\theta \sim 10^2$ $v_\theta = 3.5 \times 10^3$	0.05 0.15		Rotational velocities > 10^4 were measured for hydrogen at low pressure.

TABLE 1.2.1 (Continued)

AUTHOR YEAR [REF.]	DEVICE	ELEMENTS OR ISOTOPES STUDIED	PARTICLE DENSITY	ROTATIONAL SPEED	B_0	MAXIMUM MEASURED SEPARATION*	SPECIAL FEATURES AND COMMENTS
Hora & Hoyle 1981 [40]	Discussion Paper	U					Discussion and review of work by previous researchers. Paper includes a possible design of a PC to enrich uranium.
Simpson 1981 [41]	Discussion Paper						Development of a three fluid model. Paper concludes that a partially ionised PC is less effective than gas centrifuge for a.m.u. > 200
Belorusov 1981 [42]		He Ne Ne-He	He He+H	$v_\theta=3\times10^3$ $v_\theta=8\times10^3$	0.23	^{3}He-^{4}He 44%	Hydrogen added to reduce viscosity and achieve higher rot. velocities.
Geva et al. 1981 [43]	VAC	Al-Ti Cu-Ni Cu		$v_\theta=1.1\times10^4$ $v_\theta=7.4\times10^3$ $w=10^5$	0.2	60 % Cu	v_θ in excess of the Alfvén crit. velocity for Cu. Multiple charge states observed.
Tomimura & Nicoli 1982 [44]	Discussion Paper	U					Typical data applied to a model developed from the general momentum eqn.
Krishnan 1983 [45]	VAC	Zr	$n_i=3\times10^{19}$	$w=2.5\times10^5$	0.17	$^{91}Zr^{2+}$ 47% $^{92}Zr^{2+}$ 280% $^{94}Zr^{2+}$ 330% $^{96}Zr^{2+}$ 1700%	Fully ionised plasma. Rel. abundance normalised to $^{90}Zr^{2+}$ isotope.

TABLE 1.2.1 (Continued)

AUTHOR YEAR [REF.]	DEVICE	ELEMENTS OR ISOTOPES STUDIED	PARTICLE DENSITY	ROTATIONAL SPEED	B_0	MAXIMUM MEASURED SEPARATION *	SPECIAL FEATURES AND COMMENTS
Del Bosco et al. 1984 [46]	VAC				1.33 pulsed		Unpublished note describing the design and construction of a VAC at INPE. Laser triggered.
Geva et al. 1984 [47,48]	VAC	C Al-Ti Cu-Ni Cu Cd-Sn	$n_i=10^{19}$	$w=10^5$	0.13	100 % $^{65}Cu^+ - ^{63}Cu^+$	A mean charge state of $\langle Z\rangle=3$ measured. Plasma temp. assumed to be 1 eV. Erosion rate of 65 µg/C measured for copper.
Boldyrev et al. 1985 [49]	PC	Ar Kr Xe	$n_e=5\times10^{21}$	$v_\theta\sim3\times10^4$ $v_\theta\sim2\times10^4$ $v_\theta\sim1\times10^4$	0.7		Highly ionised plasma. Separation proportional to exp(ϕ), where $\phi=\frac{mv_\theta^2}{2T}$
Prasad & Krishnan 1985 [50]	VAC	C Mg Al Cu		$w=10^5$	0.1		PFN used. Ion temp. for CII line at 6578Å measured. $T_i\sim3$eV
Seebacher et al. 1985 [51]	PC	H_2 Ar Kr					Conference paper discussing the early results from a continuously driven partially ionised plasma centrifuge
Bittencourt & Ludwig 1986 [52]	VAC	Cu-Ni					Theoretical study based on experimental results of the Yale group.

TABLE 1.2.1 (Continued)

AUTHOR YEAR [REF.]	DEVICE	ELEMENTS OR ISOTOPES STUDIED	PARTICLE DENSITY	ROTATIONAL SPEED	B_o	MAXIMUM MEASURED SEPARATION*	SPECIAL FEATURES AND COMMENTS
Prasad et al. 1986 [53]	VAC	C	$n_e \sim 10^{21}$	$w \sim 10^5$	0.2		Erosion rates studied. Typical cost for for carbon ionisation=350eV/ion
Ludwig 1986 [54]	Discussion Paper						An analytical model is developed which gives plasma electric potential and current distributions in the rotating plasma.
Bittencourt 1986 [55]	VAC	Cu-Ni					Theoretical study. Multiple species fluid model is presented.
Del Bosco et al. 1987 [56]	VAC	C		$w \sim 10^5$	0.12	^{13}C 390%	Enrichment is measured at r = 6 cm.
		Cu			0.09		
		Mg		$v_\theta = 8.4 \times 10^3$	0.1		
Simpson et al. 1987 [57]	PC (CPC I)	Ar			<0.2		Optical cross-correlation technique is used to study plasma non-uniformities.
Prasad & Krishnan 1987 [58-60]	VAC	Ca	$n_e \sim 10^{20}$	$w \sim 10^5$	0.14	^{25}Mg-^{24}Mg 20%	$T_i \sim 2$ eV Cost of separation calculated ~70 keV/sepd atom
		Tl					
		Mg				^{26}Mg-^{24}Mg 30%	

TABLE 1.2.1 (Continued)

AUTHOR YEAR [REF.]	DEVICE	ELEMENTS OR ISOTOPES STUDIED	PARTICLE DENSITY	ROTATIONAL SPEED	B_o	MAXIMUM MEASURED SEPARATION *	SPECIAL FEATURES AND COMMENTS
Geva et al.	VAC	Cu	$n_e \sim 10^{19}$	$w \sim 10^5$			Results from VAC experiments at Isomed Ltd. in Israel.
		Cu-Ni					
1987 [61]		Cu-Zn			0.13	300% Zn-Cu	T_i assumed to be 1 eV.
		Co					$v_z \sim 10^4$ m/S
		Cu-Co					
		Co-Fe					

NOTES:
PC — Plasma Centrifuge.
SUPPER III & SUPPER V — Experimental facilities at the Wills Plasma Physics Department of the University of Sydney.
VAC — Vacuum Arc Centrifuge.

Basically, plasma centrifuges may be categorised by the degree of plasma ionisation. Partially ionised plasma centrifuges have been studied in Sweden [14,15], the German Federal Republic [17,20,24], Australia [18,22,23,31,32,38,40, 41,51,57], The Netherlands [19,33,35], the United Kingdom [21], Japan [30], and the U.S.S.R. [34,39,42,49]. Fully ionised plasma centrifuges, a category which encompass the Vacuum Arc Centrifuge (VAC), have been built in the U.S.A. [36,37,43,45,47,48,53,58-60], Brazil [44,46,52,54-56], Israel [61] and, recently, Australia [62,63]. The principle differences in construction between a vacuum arc centrifuge and a plasma centrifuge may be seen in figures 1.2.1 and 1.2.2.

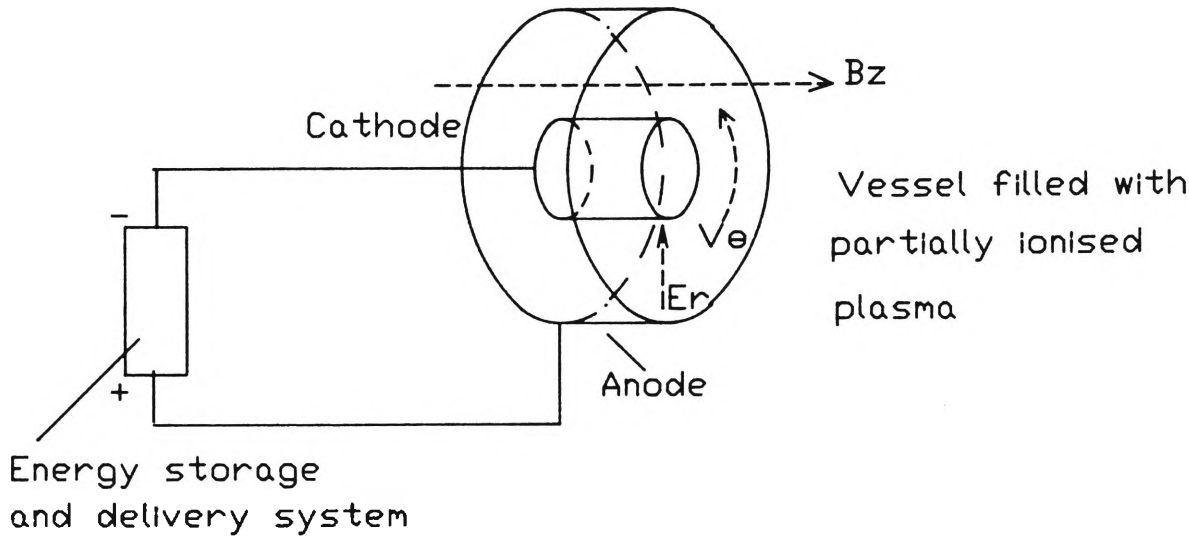

Fig. 1.2.1 Diagram of a plasma centrifuge (PC)

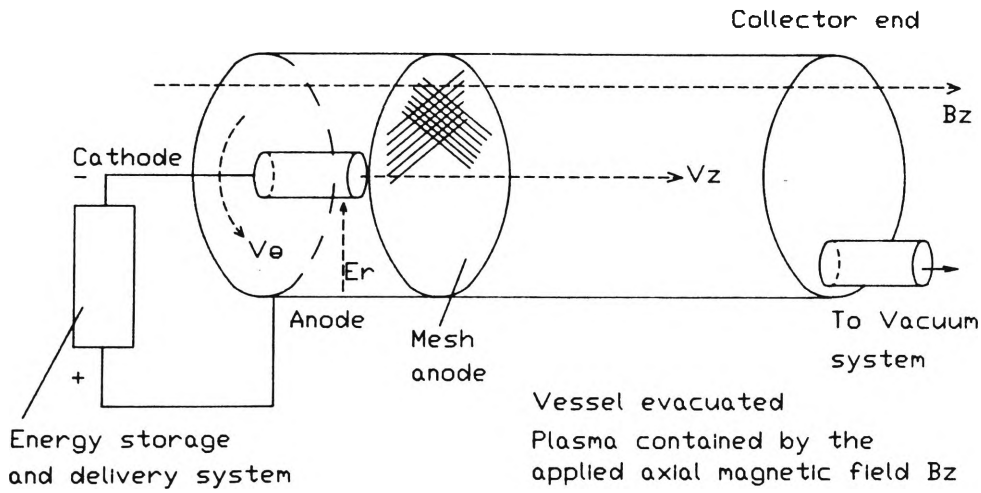

fig. 1.2.2 Diagram of a vacuum arc centrifuge (VAC)

Initial plasma centrifuge research was aimed at the separation of uranium isotopes. This was based on the premise that the plasma process could achieve rotational speeds, orders of magnitude higher than those obtainable by the gas centrifuge. The ^{235}U isotope, required in large quantities for the fabrication of nuclear fuel, was identified as a most profitable isotope to pursue. However, it was shown that, given the limitation of the Alfvén critical velocity, there is little benefit in using plasma centrifuges to separate isotopes over an atomic mass number of ~200 [41].

Recent plasma centrifuge research has concentrated on the separation of the light gas elements where it appears to have a competitive advantage over other methods.

1.3 Developments in Vacuum Arc Centrifuge Technology

The production of a fully ionised plasma in a vacuum enabled researchers at Yale University to produce rotational velocities of 7.4×10^3 m/s for a copper plasma [43]. This was higher than the calculated Alfvén critical velocity of 4.48×10^3 m/s for copper. Following the publication of the results, Atomic Energy of Canada Ltd. (AECL) contracted Yale University to investigate the production of zirconium depleted to less than 3% in ^{91}Zr for the CANDU nuclear reactors [64]. Zirconium metal, used as cladding for the nuclear fuel, possesses a number of naturally occurring isotopes. The ^{91}Zr isotope has a large neutron absorption cross section. Its removal from the zirconium cladding was calculated to give a

30% saving in fuel over the lifetime of the reactor.

Separation of zirconium isotopes by a VAC process was demonstrated by Krishnan and co-workers in 1983 [45]. Using a 1.5 m long vacuum vessel, evacuated to a pressure of less than 10^{-6} Torr, they achieved rigid body rotation frequencies of between 6 X 10^4 and 2.5 X 10^5 rad/S. Erosion of the zirconium target was measured to be ~30 µg/C.

Although AECL decided against the use of isotope depleted zirconium, they recognised the potential of the VAC as a viable means for the production of limited quantities (kg/year) of moderately enriched (90-98%) isotopes [64].

Further experimentation by research groups in the U.S.A., Brazil, and Israel have demonstrated the versatility of the VAC. Isotopes of a range of metals and carbon have now been successfully separated.

1.4 Vacuum Arc Centrifuge Development at Lucas Heights Research Laboratories

Australian interest in VAC technology was initiated by a plan to establish a facility for the production of a broad range of stable isotopes. Based on the initial findings of the Yale group, the VAC was identified as a suitable method for isotope separation where small, moderately enriched quantities were required. Other technologies (gas centrifuge, laser and electromagnetic) would also be employed depending on the material and required quantity.

The proposal to develop a VAC at ANSTO was first suggested by Evans [65] in 1984. Following its acceptance, work began on the construction of a VAC facility complemented by a theoretical analysis of the VAC process [62]. A schematic of the ANSTO VAC is shown in figure 1.4.1. Appendix 1 provides details of the VAC laboratory and associated equipment.

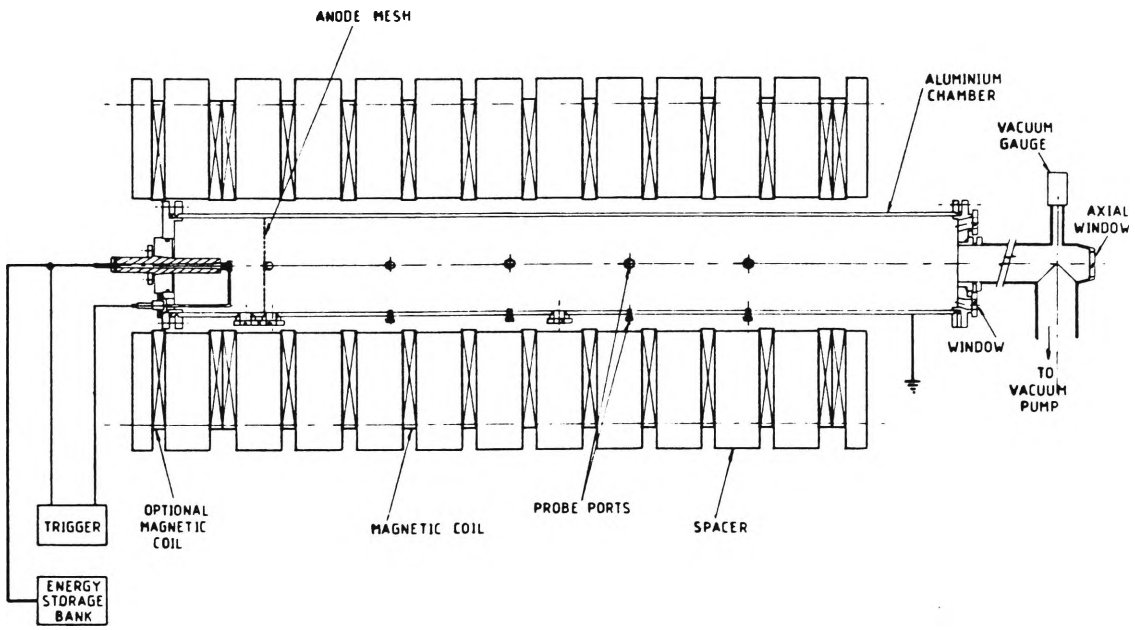

Fig. 1.4.1 Schematic of the ANSTO VAC (shown with the high voltage, vacuum arc trigger)

In a previous study, undertaken by ANSTO's Isotope Division, a potential demand was anticipated for highly enriched ^{99}Mo [66]. This particular molybdenum isotope decays with a half-life of 66 hours to the technetium metastable isotope ^{99m}Tc: an important short lived radiopharmaceutical isotope used for diagnosis in hospitals.

Stable ^{98}Mo is transmutable to the radionuclide ^{99}Mo, by neutron irradiation. It was proposed to separate ^{98}Mo from natural molybdenum metal in the VAC to provide source material

for irradiation. Production of ^{99}Mo isotope would be completed in the ANSTO's HIFAR nuclear reactor.

Although the eventual aim of the VAC work was to separate a range of metal isotopes which included molybdenum, it was decided to demonstrate and test the ANSTO VAC using copper and copper alloys as the main experimental ion sources. Copper is a machinable, cheap and more readily available metal. It also has much lower melting and boiling points when compared to molybdenum. For the purposes of gauging the performance of the VAC, results could also be compared to published overseas reports.

2. A THEORETICAL DESCRIPTION OF THE VAC PROCESS

2.1 The Vacuum Arc

The plasma source for the VAC is an electric arc initiated in a vacuum vessel evacuated to a pressure of approximately 10^{-6} torr. Considerable research has been conducted into vacuum arcs since the 1930s, principally for the distribution and switching of extremely high voltages and currents used in the power generation industry [67,68]. However, many associated arc phenomena remain unexplained by theory [69,70]. One important characteristic is the formation and behaviour of "cathode spots". This term refers to the very hot, discrete cells which have been observed moving rapidly and randomly over the surface of the cathode during an arc discharge. Cathode spots are the plasma emitters in the VAC.

Under certain conditions, "anode spots" have also been observed by researchers studying arcs. The formation of an anode spot is partly dependent on high current densities, anode material and surface temperatures [71-73]. However, the geometry of the VAC, with the large surface area anode some distance from the cathode, precludes a number of the major mechanisms required for the formation of anode spots.

The following is a summary of cathode spot characteristics compiled from various publications covering arc phenomena:

i) The number of spots observed on the cathode surface is proportional to the arc current and dependent on the cathode

material. For copper electrodes the maximum current per cathode spot is estimated to be ~100 amps with a cathode fall of ~18 volts [68,74]. When the arc current is increased beyond a critical level, the cathode spot divides and forms multiple spots [75].

ii) The lifetime of a cathode spot has been observed to be variable but finite during the arc discharge [76].

iii) Current densities of 10^8 to 10^{12} A/m² [76-79] have been estimated through a single cathode spot. A recent paper by Prock [75] concludes that it is more likely to be closer to 10^{12} A/m².

iv) Examination of arc traces left on the cathode surfaces have shown that they consist of small craters ($\approx 10^{-6}$ m diameter) [80] indicating that the cathode spot is an extremely high, localised time-limited heatload [69].

v) In the presence of a magnetic field which is parallel to the cathode surface, the cathode spots move in a retrograde direction [81,82]. The Lorentz force predicts otherwise. Retrograde velocity has been found to depend on arc current, electrode spacing, cathode material, cathode surface condition and cathode temperature [70].

vi) In the presence of a magnetic field which is perpendicular to the electrode surface (axial to the direction of the arc), the vacuum arc spreads uniformly over the surface of the electrode and burns in the interelectrode region [83-91]. This implies that the cathode spot motion is statistically uniform over the electrode surface.

A minimum arc current occurs for a particular value of axial magnetic field [88,90,91]. The arc becomes unstable and concentrates locally for applied magnetic fields below the arc minimum current. In some cases electrode over heating and melting has been observed.

In low current (< 10 kA) vacuum arc experiments and VAC research, the cathode voltage has been observed to rise with increasing axial magnetic field [48,53].

vii) The erosion rate measured for copper arcs below 10 kA is approximately 10^{-4} g/C [92-94]. Erosion rates are also believed to be dependent on cathode temperature [95].

viii) The maximum ion current is a fixed percentage of the total arc current over a large range of arc currents. For a wide range of materials, the percentage is in the range of 8% to 12%. The value for copper has been measured and found to be 10% [73]. For each material tested, the maximum spot current is found to relate to the thermal parameter:

$$I_{spot} \approx T_B k^{\frac{1}{2}} \qquad (2.1.1)$$

where T_B is the normal boiling point temperature and k is the low temperature thermal conductivity of the cathode material.

ix) Ions are emitted from the cathode spots with typical measured ion velocities of ~10^4 m/S. The angular distribution function is largest in the direction normal to the cathode surface [74,96].

x) The emitted plasma consists of multiply charged ions and free electrons [74,97]. The ion flux is proportional to the discharge current.

In the VAC, the arc is initiated by one of two methods: the ablated copper plasma caused when a high power (> 1 J/pulse) laser is focused on the cathode surface [98,99] or the production of a small amount of plasma by triggering an arc between the cathode and a separate trigger electrode. Current begins to conduct rapidly between the cathode and grid anode when sufficient plasma has been produced to fill the inter-electrode region. As more current is drawn from the main energy storage bank (either high voltage capacitor or pulse forming network), cathode spots begin to appear on the cathode surface. If a maximum current of 100 amps/spot is assumed, then, at a peak current of 4000 amps, one would expect to observe the presence of approximately 40 cathode spots.

The hemispherical crater model of a cathode spot suggested by Schrade [69] is shown in figure 2.1.1. The spot is divided into five distinct zones.

ZONE I - A current carrying plasma channel.

ZONE II - A hemispherical crater.

ZONE III - A molten metal layer.

ZONE IV - Solid metal cathode.

ZONE V - Ambient vapour jet.

The plasma channel (ZONE I) is a mixture of macroparticles, metal ions and, in negligible quantities, neutral vapour [77,94,100].

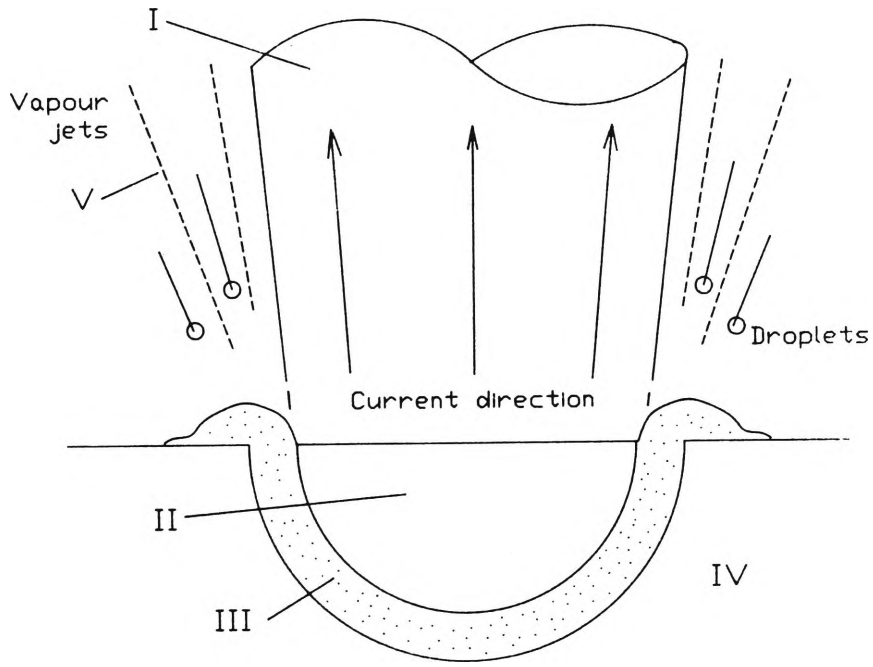

Fig. 2.1.1 Schrade's hemispherical model of a non-stationary cathode spot

In the presence of the axial magnetic field, the cathode spot movement covers the surface of the cathode producing a plasma column. The radial distribution of the plasma is thought to be non-uniform, with a peak at the middle of the arc discharge due to the pinch force by the arc's self-magnetic field [101].

Most of the arc voltage drop occurs across a space charge sheath at the cathode. The cathode fall voltage has been determined [78] for a wide variety of electrode materials. For copper vacuum arcs the cathode fall of ~18 to 20 volts has been measured.

To obtain the total arc voltage, several individual voltage drops must be added [75]:

$$V_{arc} = V_{cath} + V_{anode} + V_{cf} + V_{af} + V_s \qquad (2.1.2)$$

where:

V_{cath} = voltage drop in the cathode material.

V_{anode} = voltage drop in the anode material ≈ 0 because of the diffuse current at the anode.

V_{cf} = cathode fall voltage ≈ 18 to 20 volts for copper electrodes.

V_{af} = anode fall voltage

V_s = additional column voltage drop ≈ 0 also because of the diffuse current at the anode.

therefore:

$$V_{arc} = V_{cath} + V_{cf} + V_{af} \qquad (2.1.3)$$

The arc voltage is the sum of a constant term V_{TO} and a current dependent components $V_T(I)$ which can be identified with the anode fall. This new relationship may therefore be expressed as:

$$V_{arc} = V_T(I) + V_{TO} \qquad (2.1.4)$$

If it is assumed that the voltage drop in the cathode metal rises with increasing current, a point will be reached where the current in the cathode becomes greater than the maximum spot current. In this case the spot will split.

Ions leaving the cathode region are multiply charged and have mean energies of about ~20 to 40 eV [74]. The axial magnetic field reduces the electron mobility more than the ion mobility, in the radial direction. This effect establishes a radial electric field [102,55].

2.2 Plasma Rotation

The behaviour of a plasma in a magnetic field can be modelled by the equations describing particle motion in conjunction with Maxwell's Equations.

$$\nabla \cdot \mathbf{E} = \frac{\rho_c}{\epsilon_o} \qquad (2.2.1)$$

$$\nabla \cdot \mathbf{B} = 0 \qquad (2.2.2)$$

$$\nabla \times \mathbf{B} = -\frac{\delta \mathbf{B}}{\delta t} \qquad (2.2.3)$$

$$\frac{1}{\mu_o} \nabla \times \mathbf{B} = \mathbf{J} + \epsilon_o \frac{\delta \mathbf{E}}{\delta t} \qquad (2.2.4)$$

Assumptions can be applied to reduce this set of equations to a readily usable form.

i) If it is assumed that the plasma is electrically neutral, then equation (2.2.1) no longer applies.

ii) If it is assumed that the plasma system is in an essentially steady state, then:

$$\frac{\delta}{\delta t} = 0$$

Equation (2.2.4) becomes:

$$\frac{1}{\mu_o} \nabla \times \mathbf{B} = \mathbf{J} \qquad (2.2.5)$$

The general momentum equation for a fluid j, mixed with fluid k, with an additional component representing the effects of the magnetic field on the fluid, can be used to describe the plasma:

$$m_j n_j \frac{\delta \mathbf{v}_j}{\delta t} + m_j n_j (\mathbf{v}_j \cdot \nabla)\, \mathbf{v}_j = -\nabla P_j - \nabla \cdot \pi_j + n_j q_j (\mathbf{E} + \mathbf{v}_j \times \mathbf{B}) + \sum_k m_{jk} n_j f_{jk} (\mathbf{v}_k - \mathbf{v}_j) \qquad (2.2.6)$$

Simplification is possible by the application of the following assumptions:

i) The viscous stress tensor π_j is negligible.

ii) The plasma is fully ionised.

iii) Electron - ion collisions will be ignored.

The bulk motion of a plasma can now be described by a simplified, general momentum equation:

$$n_j m_j \frac{\delta \mathbf{v}_j}{\delta t} + n_j m_j (\mathbf{v}_j \cdot \nabla)\mathbf{v}_j = -\nabla P_j + n_j q_j (\mathbf{E} + \mathbf{v}_j \times \mathbf{B}) \qquad (2.2.7)$$

By considering the momentum equation in the radial direction and the relationship:

$$w = \frac{v_\theta}{r} \approx \frac{1}{B} \left[\frac{1}{r} \frac{d\theta}{dr} \right] \qquad (2.2.8)$$

Equations for electrons and ions may be written:

$$-n_e m_e w_e^2 r = n_e e\left[E_r + w_e r B \right] - \frac{dP_e}{dr} \qquad \text{electrons} \qquad (2.2.9)$$

$$-n_i m_i w_i^2 r = n_i Z_i e\left[E_r + w_i r B \right] - \frac{dP_i}{dr} \qquad \text{ions in a plasma with a charge state } Z_i$$

$$(2.2.10)$$

For an isothermal plasma:

$$P = nkT \qquad (2.2.11)$$

$$\text{therefore,} \quad \frac{dP_i}{dr} = kT_i \frac{dn_i}{dr} \qquad (2.2.12)$$

For an azimuthally symmetric plasma:

$$E = - \nabla \Phi \qquad (2.2.13)$$

$$\text{therefore,} \quad E_r = - \frac{d\Phi}{dr} \qquad (2.2.14)$$

The substitution of these two relationships and division by $-n_i m_i r$ yields the following equation in terms of the rotational frequency w_i:

$$w_i^2 + \frac{Z_i e B}{m_i} w_i - \frac{Z_i e}{m_i} \frac{1}{r} \frac{d\Phi}{dr} - \frac{kT_i}{m_i} \frac{1}{r} \frac{1}{n_i} \frac{dn_i}{dr} = 0 \qquad (2.2.15)$$

$$\text{since} \quad \frac{1}{n_i} \frac{dn_i}{dr} = \frac{d}{dr} (\ln(n_i)) \qquad (2.2.16)$$

From the general equation for ion cyclotron resonance:

$$\Omega_i = \frac{Z_i e B}{m_i} \qquad (2.2.17)$$

Substitution into equation (2.2.8) results in the following equation in quadratic form:

$$w_i^2 + \Omega_i w_i - \frac{\Omega_i}{B_z}\left[\frac{1}{r}\frac{d\Phi}{dr} + \frac{kT_i}{Z_i e}\frac{1}{r}\frac{dn_i}{dr}\right] \qquad (2.2.18)$$

Theoretically, two solutions exist for w_i:

$$w_i = \Omega_i\left[-\tfrac{1}{2} \pm \tfrac{1}{2}\sqrt{1 + \frac{4}{\Omega_i B_z}\left[\frac{1}{r}\frac{d\Phi}{dr} + \frac{kT_i}{Z_i e r}\frac{d\ \ln(n_i)}{dr}\right]}\right] \qquad (2.2.19)$$

Solutions for w_i have been used by Prasad [58,59] to compare measured and predicted values for rotational frequency at various levels of applied axial magnetic field B_z. Close agreement has been reported for the lower rotational frequency. Experimental evidence of the higher rotational frequency has still to be found. If the predicted higher values can be used, an even greater separation performance appears possible.

2.3 Plasma Confinement

Confinement of the plasma in the VAC takes place after the formation of the plasma column. To simplify the treatment of the plasma dynamics, a number of assumptions must be made:

(i) The plasma column is regarded as being infinitely long.

(ii) The plasma is uniform in both radial and azimuthal directions.

(iii) An electron gradient exists in the r direction and the density is a maximum at r=0.

(iv) The plasma is fully ionised and moves as a whole radially outward across the magnetic field.

(v) The magnetic fields due to currents within the plasma are much less than the externally applied magnetic field B_z.

According to Ohm's Law, the radial motion of the plasma will set up a current in the azimuthal direction, J_θ, given by:

$$J_\theta = \sigma\left[E_\theta - v_r B_z \right] \qquad (2.3.1)$$

Since the externally applied magnetic field is assumed to be greater than the magnetic field associated with the plasma currents, then the following additional assumption may be made:

$$\nabla \times B = 0 \qquad (2.3.2)$$

From symmetry, $E_\theta = 0$

Therefore $$J_\theta = -\sigma v_r B_z \qquad (2.3.3)$$

The azimuthal current will exert a force on the plasma proportional to the radial velocity. Applying equation (2.3.3) to the momentum equation (2.2.7) for the radial direction gives the following relationship:

$$m_j n_j \frac{\delta v_r}{\delta t} + m_j n_j \frac{\delta v_r}{\delta r} v_r = - \frac{\delta P}{\delta r} - J_\theta B_z \qquad (2.3.4)$$

Equation (2.3.4) shows how the plasma will move under the influence of the pressure gradient. Because the radius of the plasma column is assumed to be constant along the axis, the convection term can be neglected. Essentially, the plasma will accelerate until the two terms on the right hand side of the equation balance. That is, the acceleration component will be zero when the radial outward force due to the pressure gradient is equal to the radial inward confining force due to the current J_θ.

2.4 Plasma Density

The plasma density can be found by considering the general momentum equation (2.2.7) in terms of a single ionic species.

$$n_i m_i v_{ri} \frac{\delta v_{ri}}{\delta r} - n_i m_i \frac{v_{\theta i}^2}{r} = - \frac{\delta P_i}{\delta r} + n_i Z_i e \, (E_r + v_{\theta i} B) \qquad (2.4.1)$$

The first term of (2.4.1) can be neglected if it is assumed that no diffusion occurs. A simpler form may now be written:

$$\frac{\delta P_i}{\delta r} = n_i Z_i e \, (E_r + v_{\theta i} B) + n_i m_i \frac{v_{\theta i}^2}{r} \qquad (2.4.2)$$

For an isothermal plasma:

$$P_i = n_i kT \qquad (2.4.3)$$

$$\frac{dP_i}{dr} = \frac{dn_i}{dr} kT \qquad (2.4.4)$$

Equation (2.4.2) can now be written in terms of ion density:

$$\frac{dn_i}{dr} = \frac{n_i Z_i e}{kT}(E_r + v_{\theta i}B) + \frac{n_i m_i}{kT}\frac{v_{\theta i}^2}{r} \qquad (2.4.5)$$

Since the field is symmetric, then equation (2.2.14) will apply and (2.4.5) becomes:

$$\frac{dn_i}{dr} = \frac{n_i Z_i e}{kT}\left[-\frac{d\Phi}{dr} + v_{\theta i}B\right] + \frac{n_i m_i}{kT}\frac{v_{\theta i}^2}{r} \qquad (2.4.5)$$

$$v_\theta = wr \qquad (2.4.6)$$

$$\int \frac{1}{n_i}\, dn_i = \int -\frac{Z_i e}{kT}\frac{d\Phi}{dr}\, dr + \int \frac{Z_i e w_i r B}{kT}\, dr + \int \frac{m_i w_i^2 r}{kT}\, dr \qquad (2.4.7)$$

The solution of (2.4.7) yields an equation for plasma density in natural logarithmic form:

$$\ln(n_i) + C_1 = -\frac{Z_i e\Phi}{kT} + \frac{Z_i e w_i r^2 B}{2kT} + \frac{m_i w_i^2 r^2}{2kT} + C_2 \qquad (2.4.8)$$

The plasma density n_i can be expressed as a function of the radial distance r.

$$n_i = n_i(0)\exp\left[\frac{e}{kT}\left[-Z_i\Phi + \frac{Z_i w_i r^2 B}{2} + \frac{m_i w_i^2 r^2}{2e}\right]\right] \qquad (2.4.9)$$

Equation (2.4.9) shows that the distribution of the plasma column is an exponential function in the radial direction. For the distribution to be Gaussian, the following condition must apply at large radii:

$$\Phi > \frac{w_i r^2 B}{2} + \frac{m_i w_i^2 r^2}{2 Z_i e} \qquad (2.4.10)$$

Equation 2.4.10 implies a quadratic relationship between plasma potential and radius. Furthermore, it follows from equation 2.2.14 that the potential E_r will be proportional to the radius.

2.5 Separation Processes

Centrifugal mass separation takes place in the rotating, confined plasma, by ion-ion collision processes [45]. Heavier ion species preferentially move to the outer regions of the plasma column. When the plasma reaches the collector surface, the expected deposition profile will be dependent on the various species mass to charge ratios. For a singularly charged, two species plasma, the concentration of the heavier species will increase radially with respect to the lighter fraction. From the kinetic theory of gases, the average

$$\text{kinetic energy per particle} = \frac{3}{2} kT.$$

Let C be the speed of a particle. $\bar{C}$ is defined as the average speed over all particles. Therefore,

$$\text{kinetic energy} = \frac{1}{2} m \bar{C}^2$$

$$C_{rms} = \sqrt{\bar{C}^2} = \sqrt{\frac{3kT}{m}} \qquad (2.5.1)$$

The collision cross section σ is:

$$\sigma = 4\pi R^2 \qquad (2.5.2)$$

where R is the collision radius of the molecule.

The collision frequency $f = n_i C_{rms} \sigma$ (2.5.3)

By taking some typical measured values, an estimate of the collision frequency can be made. Ion density in a VAC has been estimated to be 10^{19} m^{-3} [45]. Geva has estimated the ion temperature for a copper plasma to be 1 eV ($\approx 8 \times 10^3$ °K) and the ion-ion collision mean free path ($= 1/n\sigma$) $\approx 10^{-3}$ to 10^{-2} m [48]. Therefore $f \approx 10^5$ to 10^6 collisions / second.

If the plasma column length is 1 m and the plasma axial velocity is assumed to be 10^4 m/S (see section 2.1) then the expected average number of collisions experienced by each ion can be estimated.

$$\text{Av. no. of ion-ion collisions} = \frac{f}{v_z} \approx 10 \text{ to } 100$$

Plasma density with respect to the radial distance r was found to be a exponential function with a Gaussian shape in equation (2.4.9). Suppose the plasma is made up of ions of two species with masses m_1 and m_2 (m_2 not equal to m_1). If it is assumed that both species move in solid body rotation and both have equal charge components, then the following equation can be written from the radial density distribution for the ratios of the two species:

$$\ln\left[\frac{n_2}{n_1}\frac{n_1(0)}{n_2(0)}\right] = \frac{w^2 r^2}{2ZkT}\left[m_2 - m_1\right] \qquad (2.5.4)$$

where $w_i = w_1 = w_2 = w$

and $Z_i = Z_1 = Z_2 = Z$

Re-writing (2.5.4) in the Gaussian form:

$$\frac{n_2}{n_1}\frac{n_1(0)}{n_2(0)} = \exp\left[\frac{w^2r^2}{2ZkT}\left[m_2 - m_1\right]\right] = \alpha \text{ (abundance ratio)} \qquad (2.5.5)$$

It is useful to express separation or enrichment as a percentage. Thus, an additional definition is adopted.

$$\%\ \text{Separation (\% Enrichment)} = (\alpha - 1) \times 100\ \% \qquad (2.5.6)$$

For this thesis, "% Separation" is adopted for elements and "% Enrichment" is adopted for isotopes.

As an illustrative example, figure 2.5.1 shows the density distribution for a copper-zinc (60% Cu: 40% Zn), plasma which has a mean charge <Z> = 3. The copper and zinc fraction mean weights respectively are 63.55 and 65.38 a.m.u.. Other parameters are assumed based on nominal values taken from the literature (r_{max} = 0.1 m, $w_i = 10^5$ rad/S, $T_i = 10^4$ °K and B_z = 0.1 T). In accordance with equation (2.4.10), $\Phi > \Gamma r^2$ where:

$$\Gamma = \frac{w_iB}{2} + \frac{m_iw_i^2}{2Z_ie} \approx 6 \times 10^3 \text{ T/S} \qquad (2.5.7)$$

Percentage enrichment of the copper fraction with respect to the zinc fraction is also shown. The calculated enrichment at r = 0.05m (half chamber diameter) is 32 %.

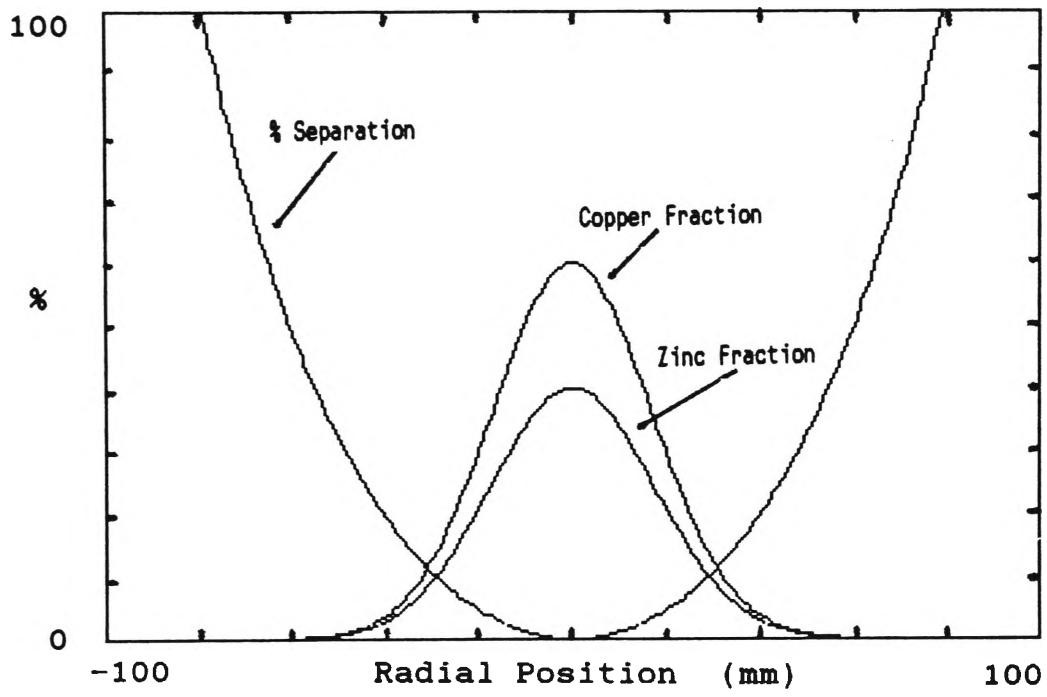

Fig 2.5.1 Radial density and percentage enrichment profiles for a copper-zinc plasma

The general separation equation for isotopic ions with various charge states is defined by the following:

$$\text{\% Separation} = \text{(\% Enrichment)} \left[\left[\frac{\frac{\Sigma\, n_{i,z}(r)}{\Sigma\, n_{j,z}(r)}}{\frac{\Sigma\, n_{i,z}(o)}{\Sigma\, n_{j,z}(o)}} \right] - 1 \right] \times 100\ \% \qquad (2.5.8)$$

where n_i, n_j respectively refer to the relative abundance of fractions i, j and z refers to the charge state.

3. ENERGY STORAGE AND DISCHARGE SYSTEMS

The production rate of ions in a vacuum arc is directly proportional to the arc current [78,103]. To produce an arc with sufficient ion emission for the VAC requires an electrical source capable of delivering kilojoules of energy [53]. When the arc is formed the cathode erodes as ions stream from its surface.

Some previous measurements of the erosion rates for copper electrodes are given in Table 3.0.1. The wide variation in results indicates that erosion is dependent on the flow of current through the arc. Electrode geometry, electrode material, surface temperature and the application of external magnetic fields affect the current flow (see section 2). The last measurement in the table [104] was made under conditions where anode spots were formed.

Geva [48] measured a 65 μg/C erosion rate for Cu - Ni alloy cathode. Krishnan [45] measured an erosion rate of 30 μg/C for a zirconium cathode.

The present experimental VAC required a large input of electrical energy for a relatively short time. A.C. mains supplies were unsuitable because the direct conversion and delivery of hundreds of volts at thousands of amps from the mains would have incurred considerable capital investment, even for millisecond durations. The problem was solved by the incorporation of electrical energy storage systems which could accumulate large amounts of energy over a relatively long period then deliver it in a short, high current, pulse. Both a

high voltage (5 kV) capacitor system and a lower voltage (400 V) pulse forming network were used with the ANSTO VAC.

TABLE 3.0.1

Measured Values of Erosion Rates for Copper Electrodes

Reference	Cathode Diameter mm	Erosion Rate µg/C	Axial Mag. Field T	Discharge Current kA
[78]	Anode 25 Cathode 25	115	0	~ 0.1
[92]	-	130	0	~ 0.1
[94]	Anode (tapered) 14 -> 4 Cathode (cylinder) 14	140	0	1.0
[99]	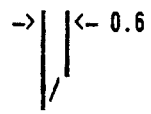	62	0	0.1 to 10
[102]	Anode 12.7 Cathode(1) 25.4 Cathode(2) 50.8	104	0 to 0.1	0.165
[104]	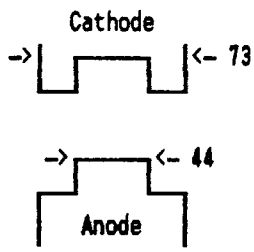	8000	0	10 to 40

3.1 A High Voltage, Series RLC, Discharge Circuit

The energy stored in a capacitor is calculated by the relationship:

$$E_{stored} = \frac{1}{2} CV_c^2 \qquad (3.1.1)$$

For the series of experiments described here, the VAC used a 1000 μF storage bank consisting of four 150 μF and four 100 μF capacitors in parallel. The maximum rated voltage of the bank was limited to 5 kV. For this arrangement, the maximum stored energy per pulse was 12.5 kJ.

A series inductor was used to limit the risetime of the pulse. A value of 3 μH was chosen in order to match overseas systems [45]. A series resistance was necessary to protect the capacitors against reverse voltage by heavily damping unwanted oscillations in the discharge circuit. However, the value of the resistor affected the overall circuit efficiency due to the energy it dissipated during the discharge. This was calculated by the following equation:

$$E_{diss} = R_{tot} \int_0^t i_{arc}(t)^2 \, dt \qquad (3.1.2)$$

where $R_{tot} = R_{series} + R_{arc}$

Experiments were conducted using the series resistor-inductor-capacitor (RLC) arrangement shown in figure 3.1.1. The circuit parameters were chosen to approximate those used by the Yale VAC group [43] in order to compare separation performance with published results.

The basic design was two separate circuits:

i) the capacitor charging side: comprised of the voltage source, current limiting resistor R_1 and the capacitor bank C. Switch S_1 closes at some time before t=0 to charge the capacitor bank and is opened at t=0.

ii) the capacitor discharging side: comprised of the inductor L, aqueous $CuSO_4$ resistor R_2 and the arc impedance R_{arc}. A switch S_2 represents the closure of the circuit by the formation of the arc at time t=0.

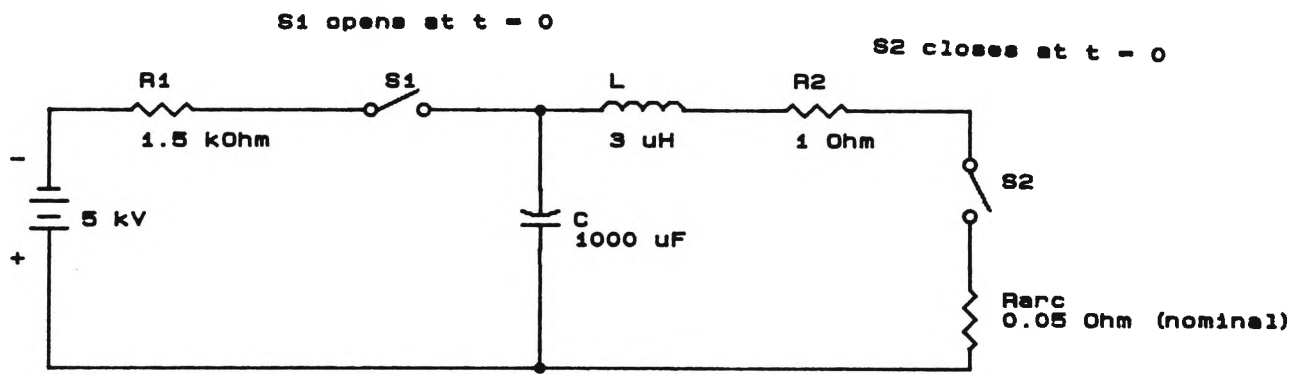

Fig. 3.1.1 A simplified circuit of the RLC high voltage discharge system

Applying Kirchoff's rules to the circuit in figure 3.1.1, gave the following set of equations: At $t = 0^+$

$$i_2R_1 + V_c(0^+) + \frac{1}{C}\int_0^t (i_2 - i_1)\,dt = V \qquad (3.1.3)$$

$$-V_c(0^+) - \frac{1}{C}\int_0^t (i_2 - i_1)\,dt + i_2R_2 + L\frac{di_2}{dt} = 0 \qquad (3.1.4)$$

For the case where $R_1 >> R_2$ then $i_2 >> i_1$. Thus the charging system may be neglected after the formation of the arc at t=0. Equation (3.1.8) was simplified to the following:

$$\frac{d^2i}{dt^2} + \frac{R_2}{L}\frac{di_2}{dt} + \frac{1}{LC}i_2 = 0 \qquad (3.1.5)$$

Equation (3.1.5) was a typical result for a second order, RLC, series circuit. Solution was further simplified by taking the Laplace transform and solving for s in the following:

$$s = -\frac{R_2}{2L} \pm \frac{1}{2}\sqrt{\left[\frac{R_2}{L}\right]^2 - \frac{4}{LC}} \qquad (3.1.6)$$

For the circuit to be heavily damped, the roots of the polynomial (3.1.5) must be real and unequal. Therefore,

$$\left[\frac{R_2}{2L}\right]^2 >> \frac{1}{\sqrt{LC}} \qquad (3.1.7)$$

The value of R_2 is specified at a nominal value of 1 Ω to give the desired pulse duration. Substitution of the real values of the circuit showed that the requirement of (3.1.7) was satisfied. i.e.:

$$\left[\frac{R_2}{2L}\right]^2 = 2.7 \times 10^{10} \gg \frac{1}{\sqrt{LC}} = 1.8 \times 10^4$$

A conversion from the Laplace form in terms of capacitance gave the following equation in the time domain:

$$i_2(t) = V_c(0)\, C \left[\frac{s_1 s_2}{s_1 - s_2}\right]\left[e^{s_2 t} - e^{s_1 t}\right] \qquad (3.1.8)$$

Substitution of the chosen values for the VAC circuit gave a numerical equation for the discharge pulse:

$$i_{arc}(t) = i_2(t) = 5030\left[e^{-1003\,t} - e^{-332330\,t}\right] \qquad (3.1.9)$$

Equation (3.1.2) was also used to estimate the circuit efficiency. An arc impedance of 50 mΩ was assumed. Energy from the capacitor bank was dissipated in the ratios shown in Table 3.1.1.

TABLE 3.1.1

Distribution of Energy for the High Voltage Capacitor Discharge Circuit

Circuit Load	Energy Dissipated kJ
R_{series}	11.9
R_{arc}	0.6
R_{tot}	12.5

Neglecting all other circuit losses, the energy available to the arc is only 4.8% of the total stored in the capacitors. Although the electrical inefficiencies of the circuit were recognised at the outset of the experimental program, it was decided to pursue this system of energy storage and delivery so that a comparison could be made with published results. The circuit is shown in detail in Appendix 2.

The charging stage for the capacitor bank was designed to match the maximum discharge rate of one pulse per second provided by the CO_2 laser. Three power transformers were used with primary windings connected in parallel to the incoming 240 volt mains. The three 1620 volt secondary windings, each rated to 12.5 kVA, were series connected to provide 4860 VAC for rectification. The bridge rectifier, comprised 32, 10 amp, silicon diodes.

The capacitor bank comprised four 100 μF, 10kV Maxwell capacitors in parallel with four 150 μF, 5kV English Electric capacitors. The total capacitance, C, was 1 mF with an energy storage capacity of 12.5 kJ at 5kV. A configuration to provide

a higher energy storage (up to 20 kJ @ 10 kV) would have been possible if only the Maxwell capacitors had been employed. The limitation imposed by the availability of suitable transformers made this option unattractive.

The charging current was limited by a 1.5 kΩ resistor bank consisting of 24, 1 kW, domestic radiator bars. After one second, the capacitor charge was approximately 4500 volts. An identical resistor bank was constructed for use as a safety dump in the event that the trigger failed to establish the vacuum arc.

Once the vacuum arc was formed, the energy stored in the capacitor bank was dissipated in the resistive elements of the discharge circuit (i.e. the damping resistor R and the arc resistance R_{arc}).

The inductor, L, limited the risetime of the current pulse in the initial stages of the discharge to 3 μS. In combination with the other circuit elements, the current pulse was effectively shaped. For a total series resistance of 1 Ω, the inductance, L, was 3 μH. The design of the inductor was based on Nagaoka's formula and the methods used by Grover [105].

$$\text{i.e.} \qquad L = 0.002\,\pi^2 a\left[\frac{2a}{b}\right]N^2K \quad \mu H \qquad (3.1.10)$$

where N = winding density

K = end effect factor

a = coil radius

b = coil length

$$a\left[\frac{2a}{b}\right]N^2K = 151.98$$

let $a = 15$ cm

$b = 20$ cm

therefore $\frac{2a}{b} = 1.5$ (i.e. a "short" coil)

From the tables given by Grover

$K = 0.59624$

solving for N

$$N = \sqrt{\frac{151.98}{15*1.5*0.596}} = 3.37 \text{ turns}$$

The 3 µH coil was wound from 20 mm o.d. copper pipe and secured inside a length of 310 mm i.d. plastic agricultural pipe.

A nominal value of 1 Ω was chosen for the damping resistor. The design is based on the liquid resistor described by Geva [47]. The resistor was constructed from a 50 litre plastic carboy with the top removed and filled with 41 litres of aqueous copper sulphate. Connection was made to the liquid by two copper plates which were immersed in the solution. An adjustable perspex plate which could be lowered into the solution was used to vary the terminal resistance by reducing the liquid conduction area. Construction of the resistor can be seen in figure 3.1.2. The relationship between plate depth and the measured terminal resistance is plotted in figure 3.1.3.

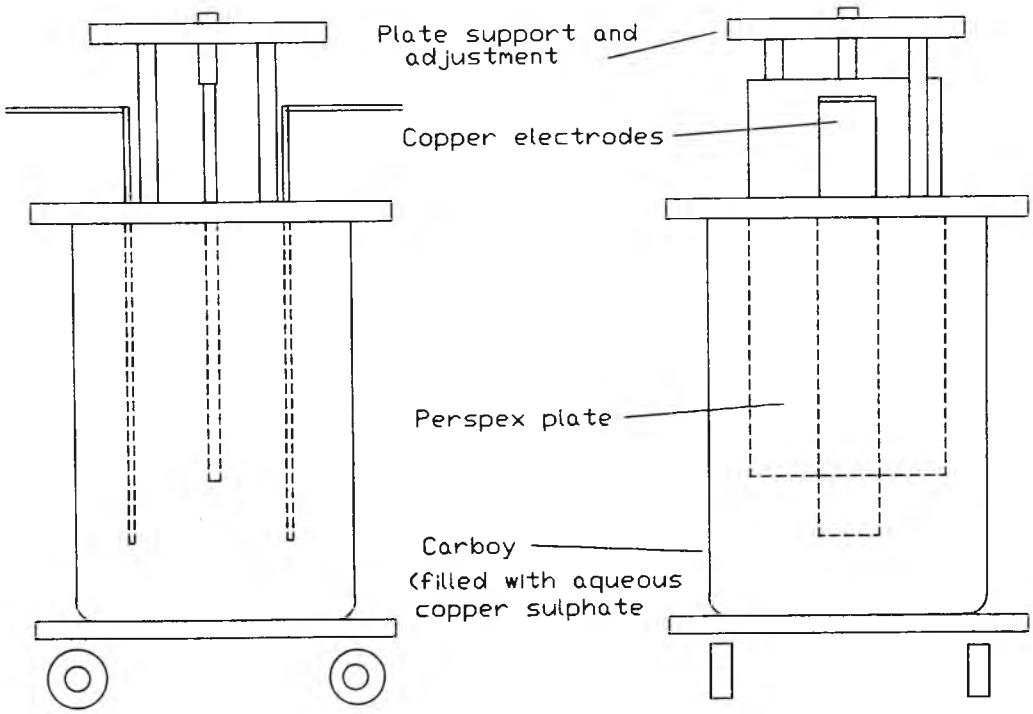

Fig. 3.1.2 Construction of the liquid resistor

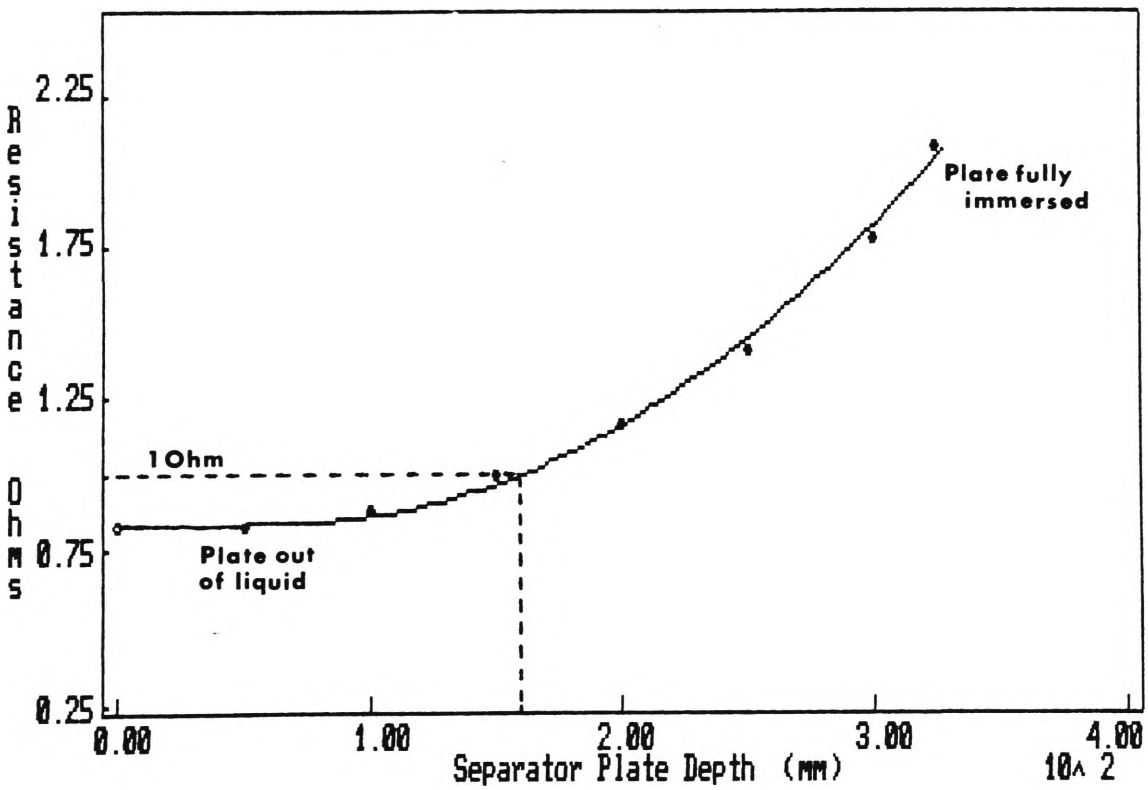

Fig. 3.1.3 Resistance vs. plate depth for the liquid resistor

3.2 A Low Voltage Pulse Forming Network

Elementary electrical theory states that maximum energy transfer will be achieved when the source impedance is equal to the load impedance; in this case the VAC electrode terminal impedance.

i.e. $Z_o = Z_{arc}$ (3.2.1)

To overcome the inherent inefficiencies of the high voltage capacitance discharge circuit, an efficient, low impedance pulse forming network (PFN) [106] was designed and built. There has been considerable interest in, and development of, PFNs for high energy physics and pulsed radar systems for some time. Synthesis methods have been developed to design PFN lines to give both simple (i.e. square) and complex pulse shapes [107].

The design of the PFN was initially specified to give a constant current pulse of approximately 3 mS duration. Unlike the capacitor discharge system, where the arc current was not constant, the PFN established steady state conditions during the arc discharge. This greatly facilitated the arc and plasma measurements.

A long, PFN line behaves similarly to a transmission line which consists of lumped circuit elements. A reasonable first stage model of the PFN was developed based on that similarity. The full treatment is included in Appendix 3.

The impedance of a lossless PFN is given by the following expression:

$$Z_o = \sqrt{\frac{L}{C}} \qquad (3.2.2)$$

If the arc impedance is considered to be fully resistive, then current flows from the PFN through the arc impedance according to the following function:

$$i(0,t) = i_{arc}(t) = \frac{V_o}{2Z_o}\left[\, H(t) - H(t-2N\sqrt{(LC)}) \,\right] \qquad (3.2.3)$$

Figure 3.2.3 is a plot of equation (3.2.3). Note that the duration of the pulse is given by the following expression:

$$T = 2N\sqrt{LC} \qquad (3.2.4)$$

where N is the number of sections in the line (always an integer) and L and C are, respectively, the inductance and capacitance of each section.

Both equation (3.2.2) and (3.2.4) were successfully used to select the initial working values for the pulse forming network. From discharge experiments carried out in a smaller vacuum chamber and using the high voltage discharge system, the average arc impedance was calculated to be between 30 mΩ to 80 mΩ. A prototype PFN was designed, based on a nominal value of 50 mΩ.

$$Z_{arc} = Z_o = \sqrt{\frac{L}{C}} = 50\ m\Omega$$

Five electrolytic capacitors (Sprague, 5100 μF, 350 VWDC) [108] were used. For C = 5100 μF, the inductance was 12.75 μH/section and the maximum pulse length was 2.55 mS. Once again, the design of the inductive element is based on the procedures from Grover [105]. i.e. for b > 2a

$$\frac{2a}{b} = 0.08$$

From Grover (table 37): k = 0.96685

Using Nagaoka's formula: N = 72.24 ≈ 70 Turns

Figure 3.2.1 shows the construction of the five section PFN. Individual sections are made at the junction of the continuously wound solenoid coil and the electrolytic capacitors.

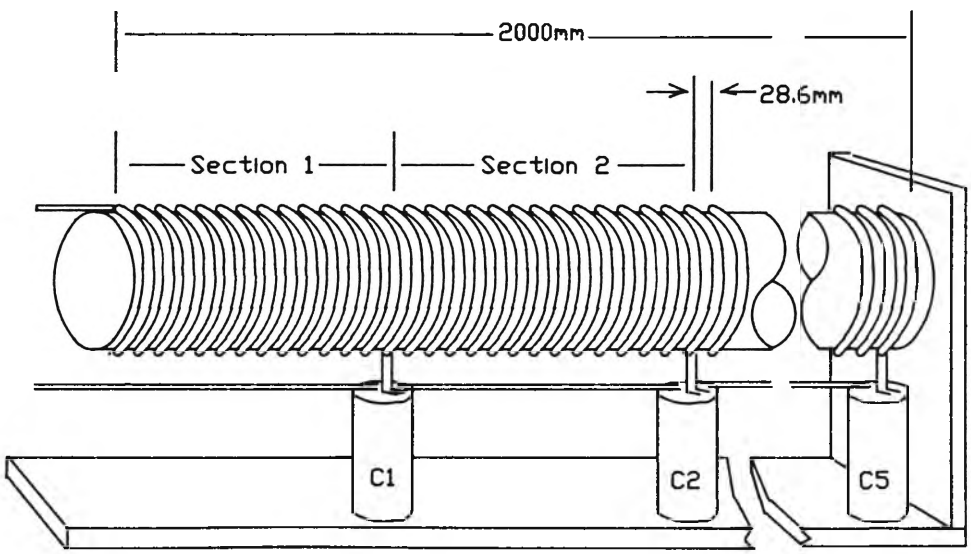

Fig. 3.2.1 Construction of the 5 section PFN

A numerical modeling technique was necessary to study the behaviour of the PFN when it was connected to the VAC electrodes. Figure 3.2.2 shows an accurate equivalent circuit of a 5 section PFN. The parasitic elements are included for the section inductance, L, and capacitance, C. The values assigned to the capacitor parasitic elements were based on information supplied by the manufacturer [109]. Analysis was greatly facilitated by the use of a SPICE computer program. Commercial software was used for this purpose [110]. Figure 3.2.3 shows the PFN ideal response compared to the computed response based on the circuit shown in figure 3.2.2.

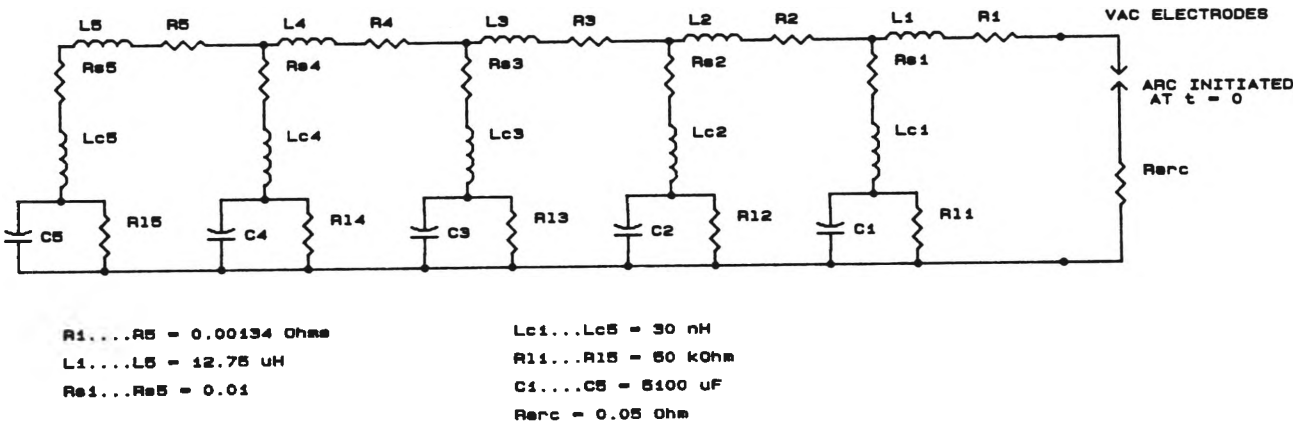

Fig 3.2.2 Equivalent circuit of the 5 section PFN

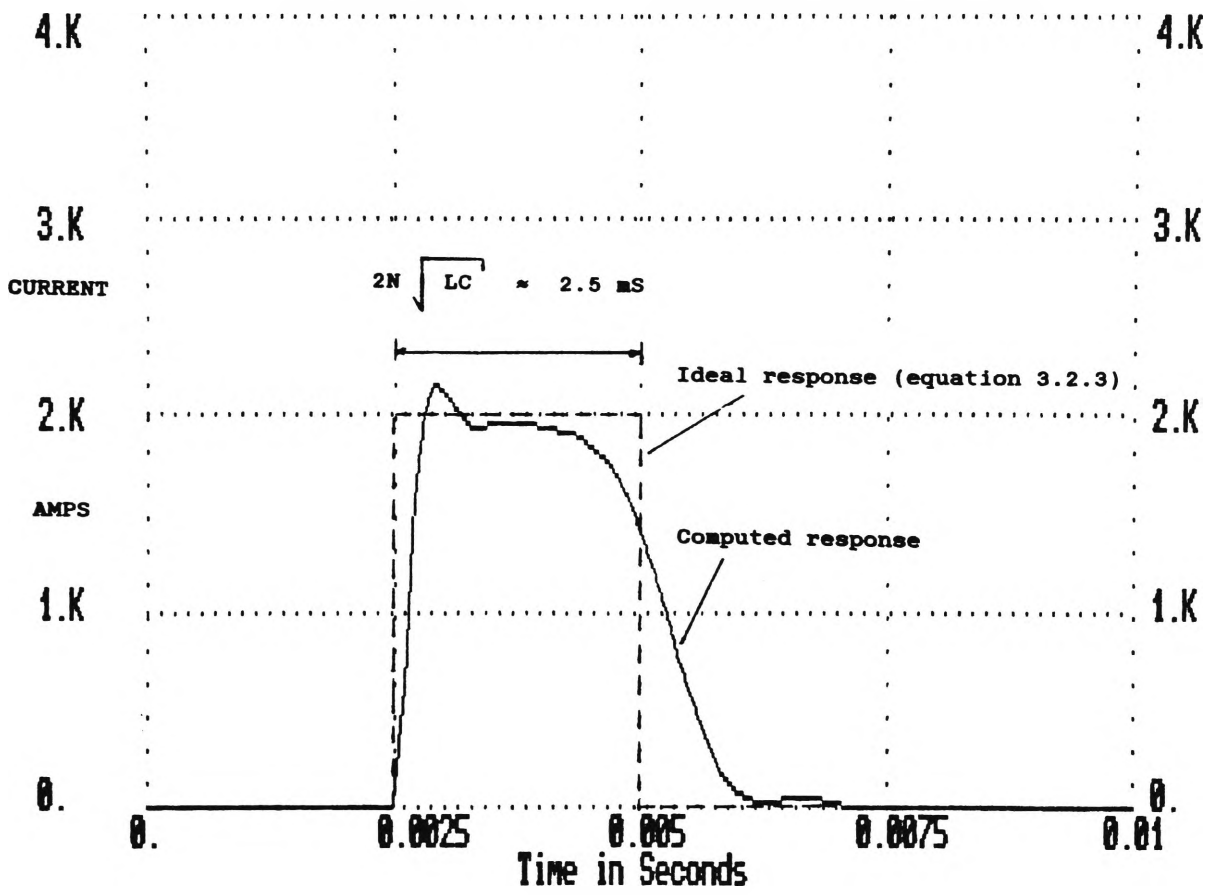

Fig. 3.2.3 The ideal (equation (3.2.2)) and the SPICE response for the 5 section PFN with and initial charge V_C = 200 V

The constructed PFN line, delivered a constant current pulse for approximately 2.5 mS. The energy available from the PFN was approximately 1000 J/pulse. The PFN was charged from a substantially smaller A.C. to D.C. power supply than was employed for the high voltage charging circuit. Charging voltage was variable up to 400 Volts by the inclusion of an autotransformer in the mains supply circuit. The circuit is shown in detail in Appendix 2.

4. DESCRIPTION OF THE EXPERIMENTAL APPARATUS

A diagram of the ANSTO VAC laboratory showing the placement of the major equipment items is given in Appendix 3. Six photographs of of the VAC equipment and data acquisition system are included.

4.1 The Vacuum Chamber

Two vacuum chambers of the same diameter were constructed. The short chamber, initially used for testing the triggering and discharge circuits, is shown in figure 4.1.1. The VAC chamber, used for all plasma and separation experiments, is shown in figure 4.1.2.

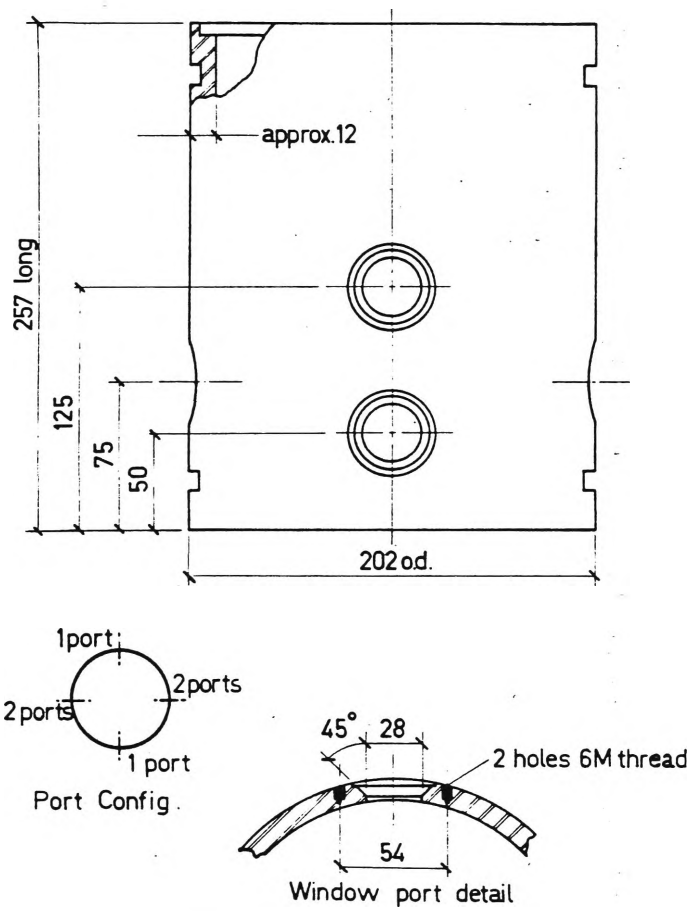

Fig. 4.1.1 The short aluminium vacuum chamber

The short chamber was made of 178 mm i.d. aluminium tubing. Its dimensions were sufficient to allow for the mounting and testing of the various electrode systems. A number of windows were machined into the chamber wall to facilitate observation of the vacuum arc discharge. Due to its low volume, evacuation of the chamber, between discharges, was considerably faster than with the longer VAC vessel.

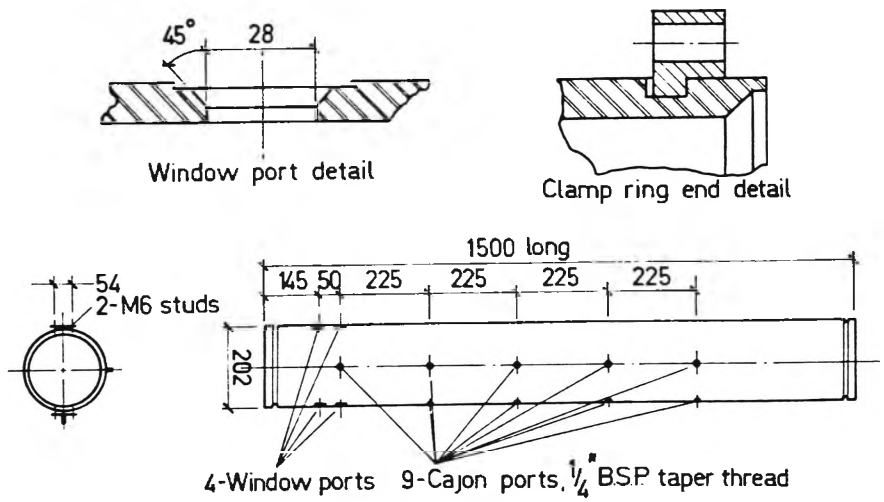

Fig. 4.1.2 The VAC aluminium chamber

The VAC chamber was fabricated from the same 178 mm i.d. aluminium tube stock. The overall length of the VAC was 1500 mm with a wall thickness of 12 mm. The chamber was used for plasma rotation and isotope separation experiments. The plasma axial drift length was approximately one metre. The expected number of ion-ion collisions was between 10 and 100 per shot.

Observation ports were machined into the chamber wall for the placement of optical, laser and spectroscopic instruments. Additionally, a series of screw tapped holes were added for the insertion of electrostatic and magnetic probes, through re-entrant ports, into the plasma region.

Removable aluminium mounts were fitted to each of the observation ports. Optical glass disks, cemented to the mounts with an epoxy glue, were used for the ordinary observation ports. Sapphire windows were attached to the port mounts located at the electrode end of the chamber. These were to be used for the spectroscopic measurements of the plasma column around the discharge region. A zinc selenide optical disk was used for the laser light entry port.

The end flanges were machined from aluminium plate and are interchangeable between the short chamber and the VAC. Vacuum "O" ring seals were used between the chamber and the end plates. Observation windows were also added to the electrode and collection end flanges.

The chamber and magnet for the larger system were supported on a strong metal frame. The whole system was mounted on wheels for optimum placement in the limited space of the laboratory.

4.2 The Vacuum System

The chamber was connected to a semi-automatic pumping system by a stainless steel bellows. A rotary pump was used initially to evacuate the chamber when it was at atmospheric pressures. When the chamber pressure was sufficiently low, a eight inch oil diffusion pump with a liquid nitrogen cooled baffle was brought on line. Background chamber pressures of 10^{-6} torr were achievable with this system.

The chamber pressure was electronically monitored by a Penning vacuum gauge. The evacuation sequence was controlled manually by opening, or closing, the various vacuum line valves. The pumping system was protected from a sudden increase in pressure by additional solenoid valves in the vacuum lines controlled by the output of an Ulvac gauge. The manually operated plate valve above the diffusion pump was fitted with a solenoid controlled gravity mechanism which closed in the event of an excessively high chamber pressure.

4.3 Electrode Configurations and Trigger Systems

Two methods were tested to trigger the VAC. Each system had its own relative merits.

4.3.1 The Laser Triggered Electrode

A review of the literature indicated that laser triggering was the preferred method for initiating the vacuum arc discharge in a VAC. By this method, the output of a high power, pulsed CO_2 laser was focused onto the electrode surface. The energy absorbed by the metal surface caused the production of a small expanding metal plasma. When sufficient plasma was produced, a path was created for breakdown of the vacuum gap between the target cathode and the vacuum chamber anode. A vacuum arc discharge resulted and current flowed from the energy storage system into the vacuum arc.

A pulsed TEA CO_2 laser (Lumonics model K103-2) with a rated output of 15 J/pulse and a maximum repetition rate of 1 pulse per second was made available to the VAC research group.

A cathode constructed for use with laser triggering is shown in figure 4.3.1.1. It is similar to the electrode described by Geva [47]. Figure 4.3.1.2. shows the optical arrangement used for focusing the laser beam onto the cathode surface.

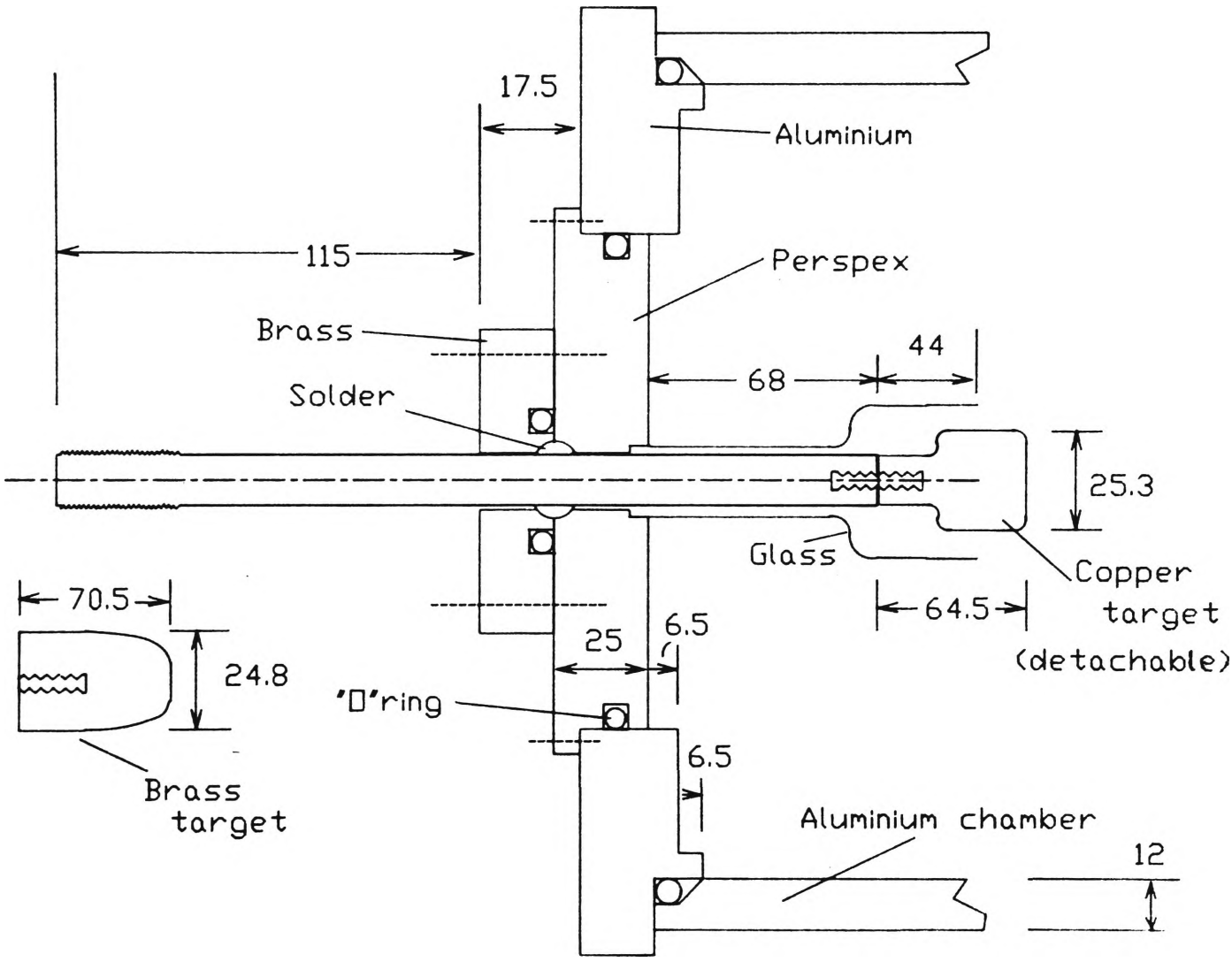

Fig. 4.3.1.1 Sectional view of the electrode and end flange used for laser triggering

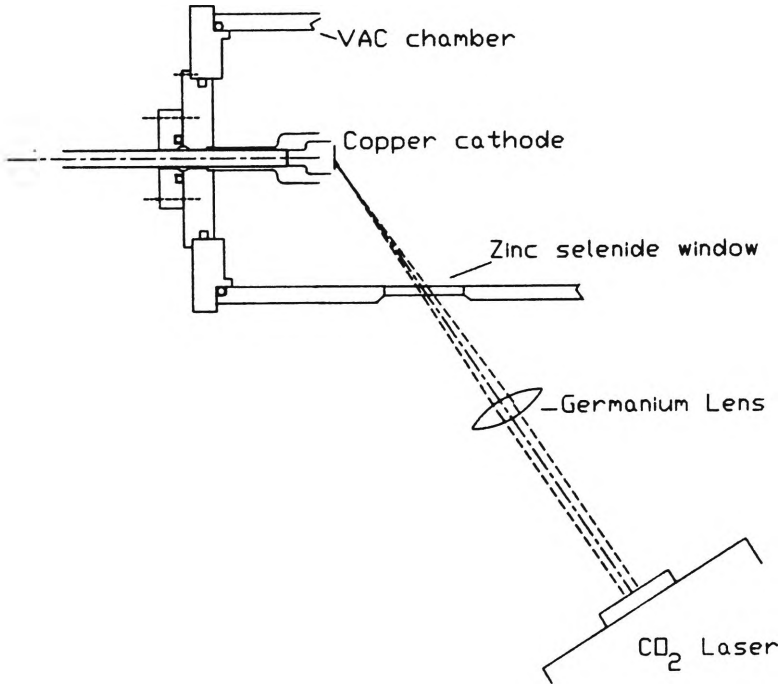

Fig. 4.3.1.2 Optics for laser triggering

4.3.2 The High Voltage Triggered Electrode

Laser triggering proved to be reliable for most of the experimental program. However, an alternative method was pursued for the following reasons:

i) the laser was electrically inefficient
ii) special precautions were required during its operation to protect personnel against eye damage
iii) the size of the laser was physically inconvenient in the limited space of the laboratory.
iv) some difficulties were experienced with the beam focus

A high voltage trigger (HVT) was designed and constructed to replace the laser as the vacuum arc trigger. To initiate the vacuum arc, a coaxial ring electrode was included at the

end of the main discharge cathode. The ring was insulated from the main electrode by an alumina ceramic cylinder. This feature is shown in figure 4.3.2.1.

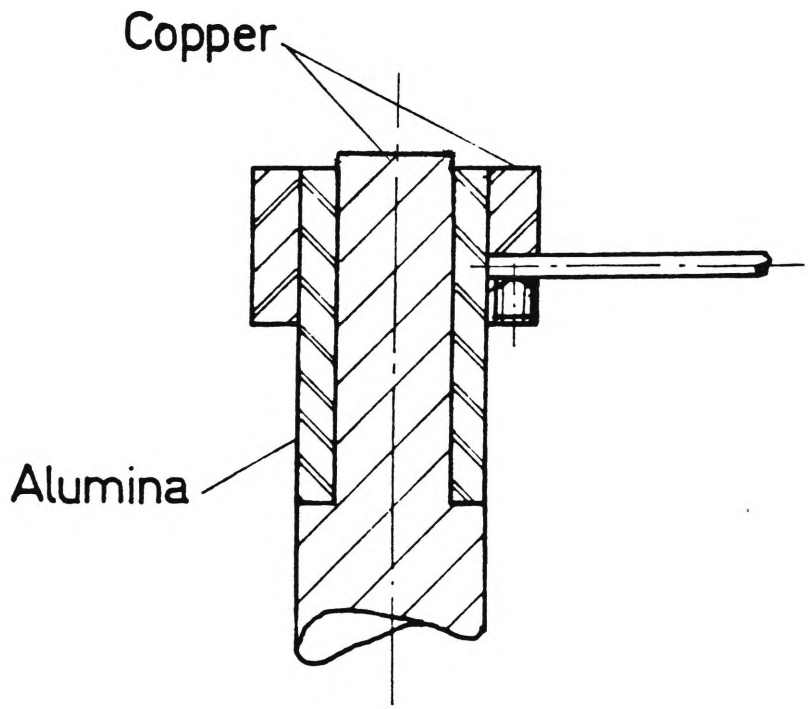

Fig. 4.3.2.1 Cathode with trigger electrode

Figure 4.3.2.2 is a simplified diagram showing the high voltage triggered electrode and feed-through arrangement. Photographs of the end flange, and the HVT electrodes, are given in figure 4.3.2.3.

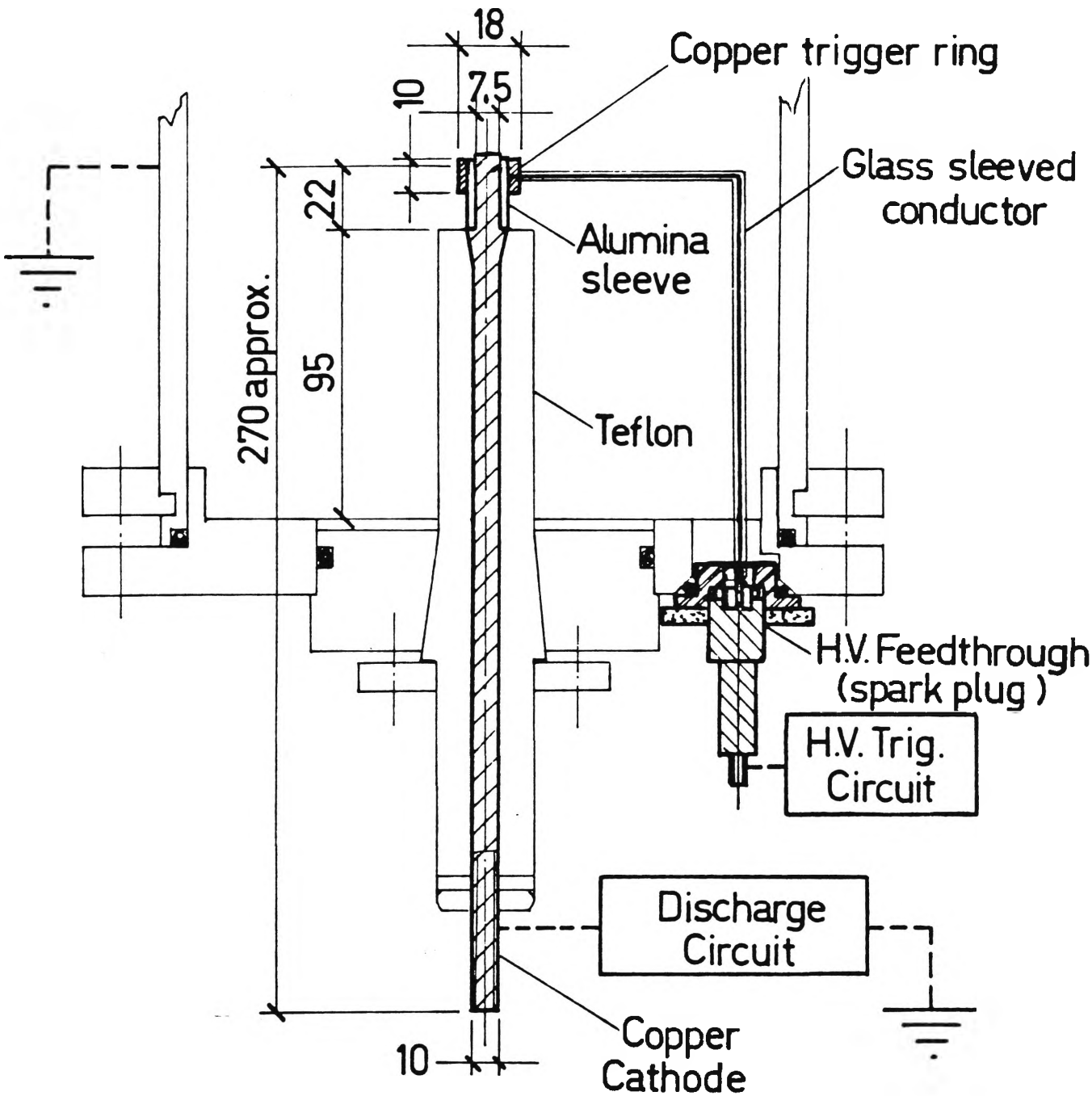

Fig. 4.3.2.2 The high voltage triggered electrode

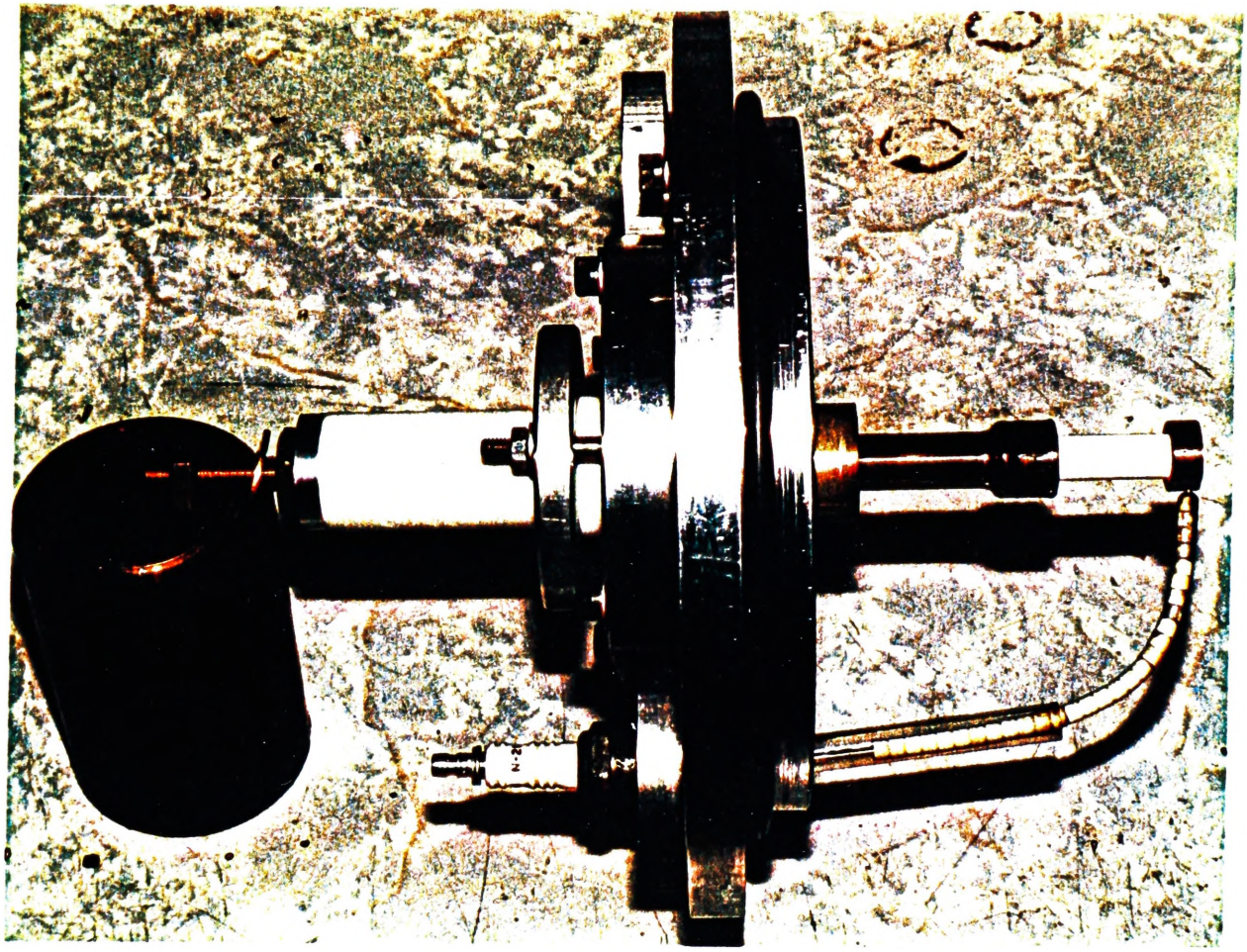

Fig. 4.3.2.3 (a) Photograph of the end flange and trigger components

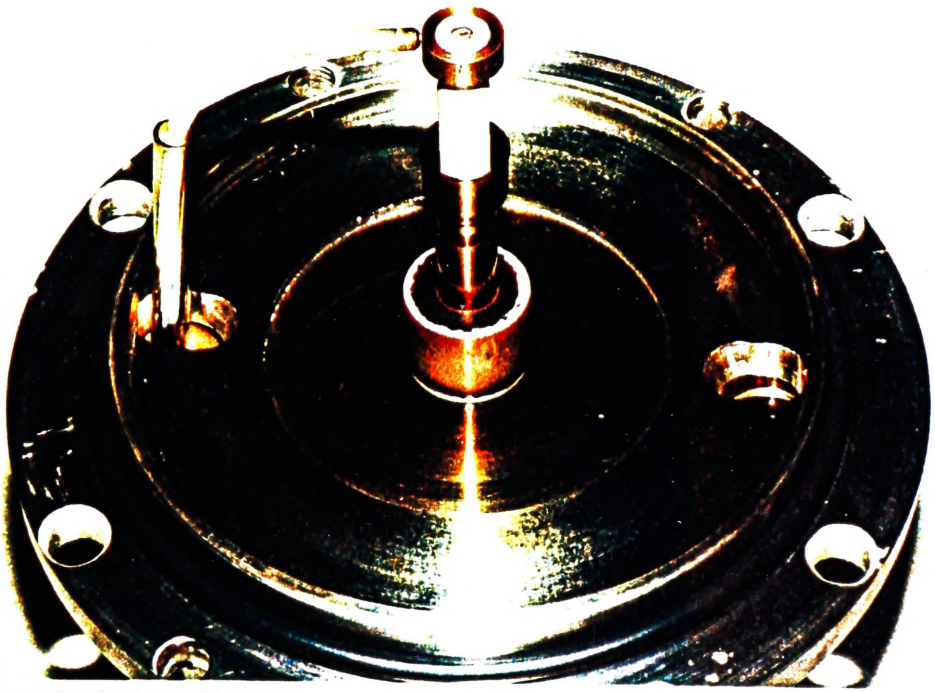

Fig. 4.3.2.3 (b) An alternative view of the electrode arrangement

Figure 4.3.2.4 is a simplified block diagram of the electrical circuit developed to trigger the vacuum gap. Details of the circuit are given in Appendix 2.

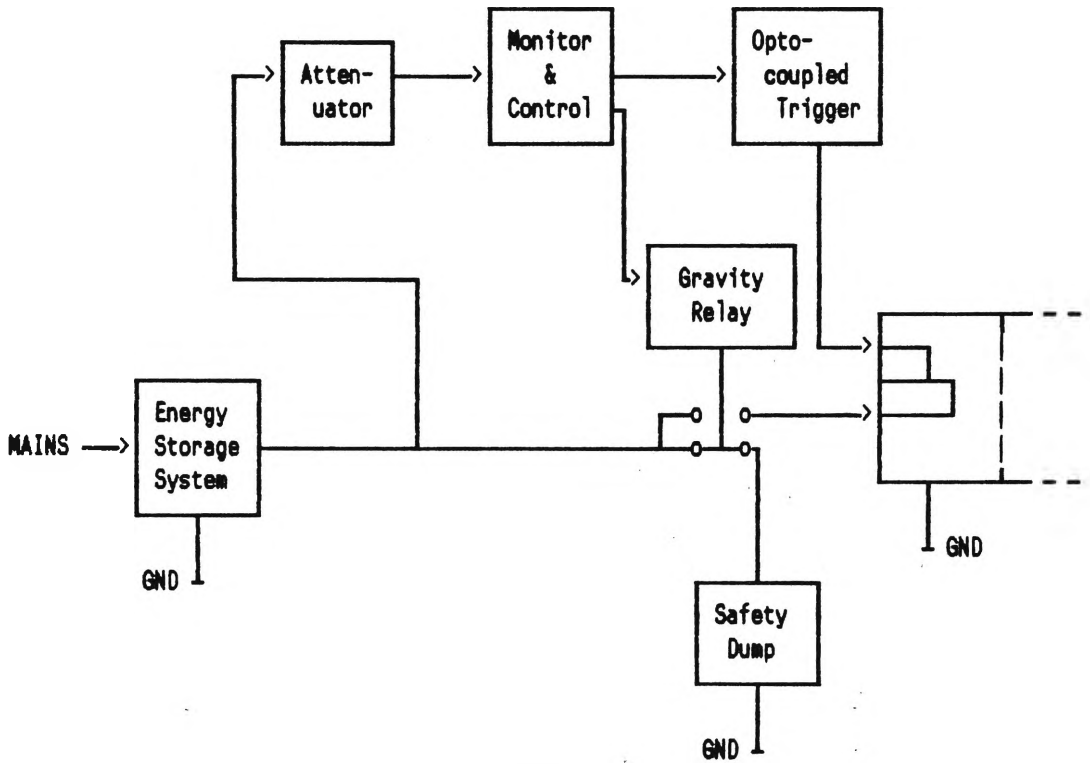

Fig. 4.3.2.4 Simplified block diagram of the VAC high voltage trigger (HVT) system

Capacitor charging voltage was monitored through an attenuator and compared to a pre-selected reference voltage. When the capacitor voltage equalled the reference, a trigger pulse was generated and this, in turn, triggered the HVT. The high voltage pulse, applied between the trigger electrode and the cathode, caused breakdown across the surface of the alumina insulator. The production of an electric arc discharge in the vacuum was facilitated by the presence of the alumina insulator which assisted breakdown by the following mechanisms:

i) distortion of the electric field across the insulator surface by the collection of electric charge

ii) production of free electrons from gas molecules absorbed in the porous insulator material [111]

The plasma produced by the trigger expanded away from the electrodes and filled the inter electrode region with free electrons and ions. A conductive path was thus provided between the cathode and the chamber anode and the main discharge arc was formed.

The HVT method provided reliable triggering for experiments conducted with low applied axial magnetic fields. Difficulties were experienced with triggering of the main arc at higher magnetic fields. The trigger plasma, which had a low relative density, was confined by the higher field and was unable to provide the necessary breakdown path required by the cathode discharge circuit.

4.4 The Solenoid Magnet

The magnetic field performed a twofold function in the VAC:

(i) it provided a magnetic component B_z at the electrode end of the chamber which caused the plasma to rotate

(ii) it provided a uniform axial magnetic field B_z which confined the plasma as it streamed down the length of the separation region of the chamber.

The project was greatly assisted by the loan of a set of solenoid "pancake" electromagnets from the Wills Plasma Physics Laboratory (Sydney University). Each pancake consisted of two spiral wound, hollow square section, 16 turn, copper coils. The conductors were encased in epoxy. Figure 4.4.1 is a diagram of an individual magnet coil.

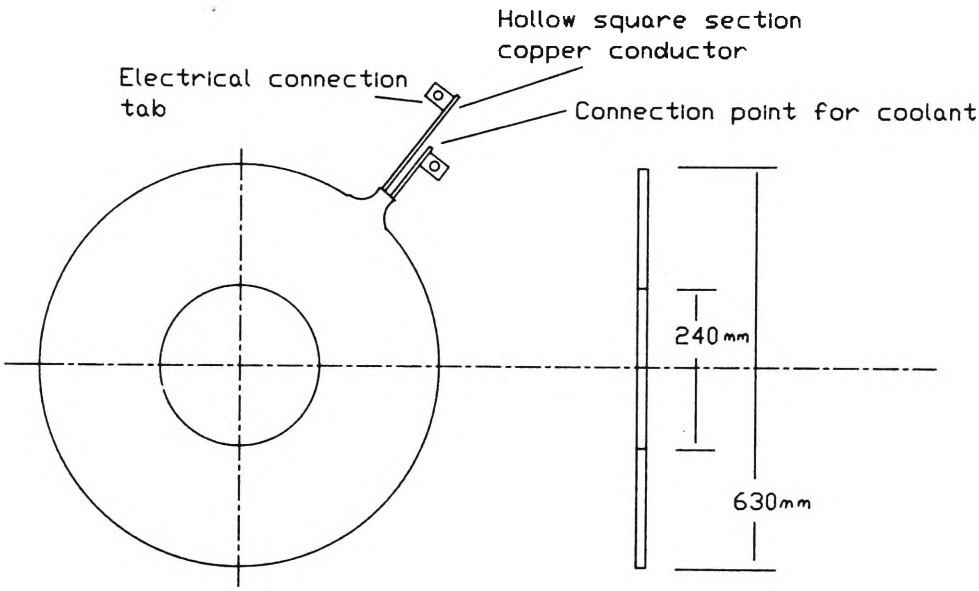

Fig. 4.4.1 Details of a single electromagnet (pancake) of the VAC electromagnet solenoid

A high current D.C. supply was modified to power the electromagnet. The electrical circuit of the supply is given in Appendix 2 and the output ratings are summarised in table 4.4.1. The maximum field produced by the solenoid was limited by the thermal limits of the electromagnets and the maximum ratings of the power supply. Tap water was the only available coolant to the laboratory. (A chilled water system has since been connected and will be used for future experimental work).

TABLE 4.4.1

Maximum Ratings for the Electromagnet Power Supply

Max. output power	50 kVA
Max. output current	500 Amps
Output Voltage	Remotely controlled and variable 0 to 100 volts

A test was performed using tap water as a coolant at a flow rate of 1 litre/minute through a single magnet pancake. At a maximum power supply current of 500 amps, the steady state temperature of the coil was measured to be approximately 41°C. Figure 4.4.2 is a plot of the rate of temperature rise of the water outflow. A constant temperature was achieved after approximately 30 minutes operation.

The magnetic field at the centre of the coil was measured with a calibrated Bell Hall Effect Fluxmeter to be 0.049 T for a current of 500 amps. This compared favourably with the value calculated in Appendix 4, Table A4.1, for the magnetic field $B_{Z(0,0,0)} = 0.0497$ T.

The solenoid magnet was arranged as a set of evenly spaced pancake coils which were coaxial to the chamber. The distance between individual pancakes was determined to allow the maximum instrumentation access for a maximum of magnetic field uniformity. The design of the magnet support structure and spacers was preceded by the design of the optimum magnet configuration. This was achieved by a BASIC computer program "VACMAG" which modeled specific designs given the line current

available and the desired spacing. Details of the program are given in Appendix 4.

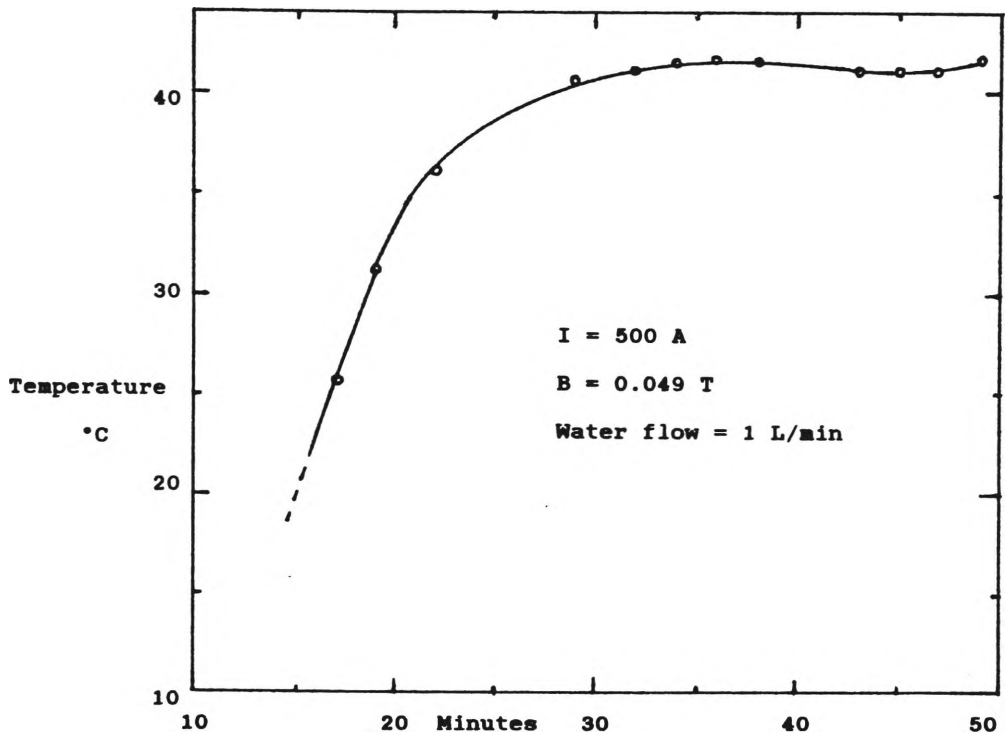

Fig 4.4.2 Plot of the rate of rise of coolant temperature for a single pancake operated at 500 amps

The most practical arrangement was found to be 11 pancakes spaced 112 mm between centres. Correction of end effects was achieved by an additional end pancake. This had the effect of increasing the current density at the end coils. The total number of coils used was 13. Plots of the calculated axial field profile for both cases are shown in figure 4.4.3.

An additional pancake was added to the cathode end of the solenoid for possible future experiments using non-linear magnetic fields around the arc. This additional coil was not used for this thesis.

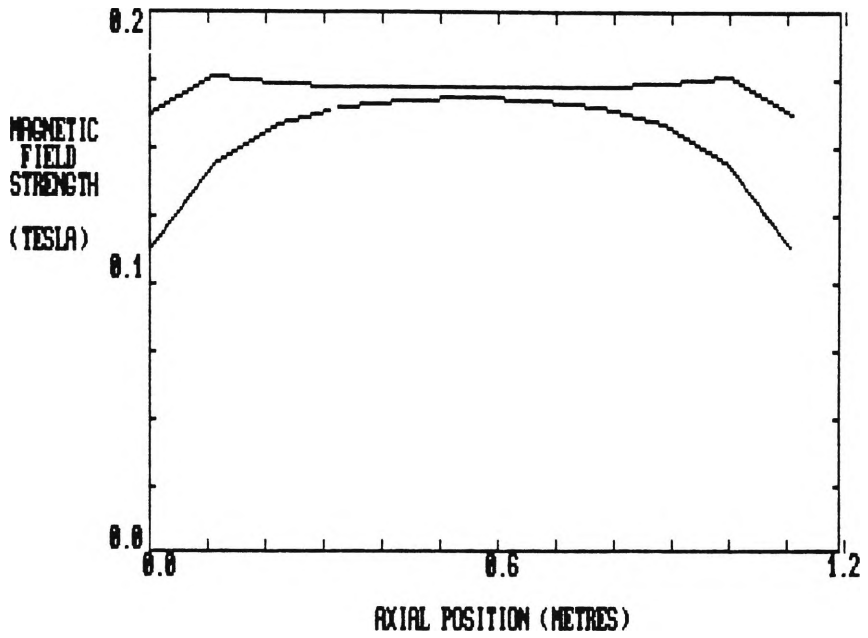

Fig. 4.4.3 Calculated magnetic field strength vs. axial position

Lower trace: result for 11 equally spaced coils
Upper trace: result for end effect correction

All fourteen pancakes were mounted on the chamber support structure with wooden spacers to separate individual pancakes. A plan of the solenoid including spacers is given in figure 4.4.4. Each pancake was electrically connected in series to the power supply and operated up to the maximum continuous line current of 500 amps. A plot of the calculated and measured axial magnetic field is given in figure 4.4.5.

The experimental work described here uses a maximum magnetic field of 0.17 T. This was considered sufficient as Krishnan had reported separation using much lower values of B_z [45].

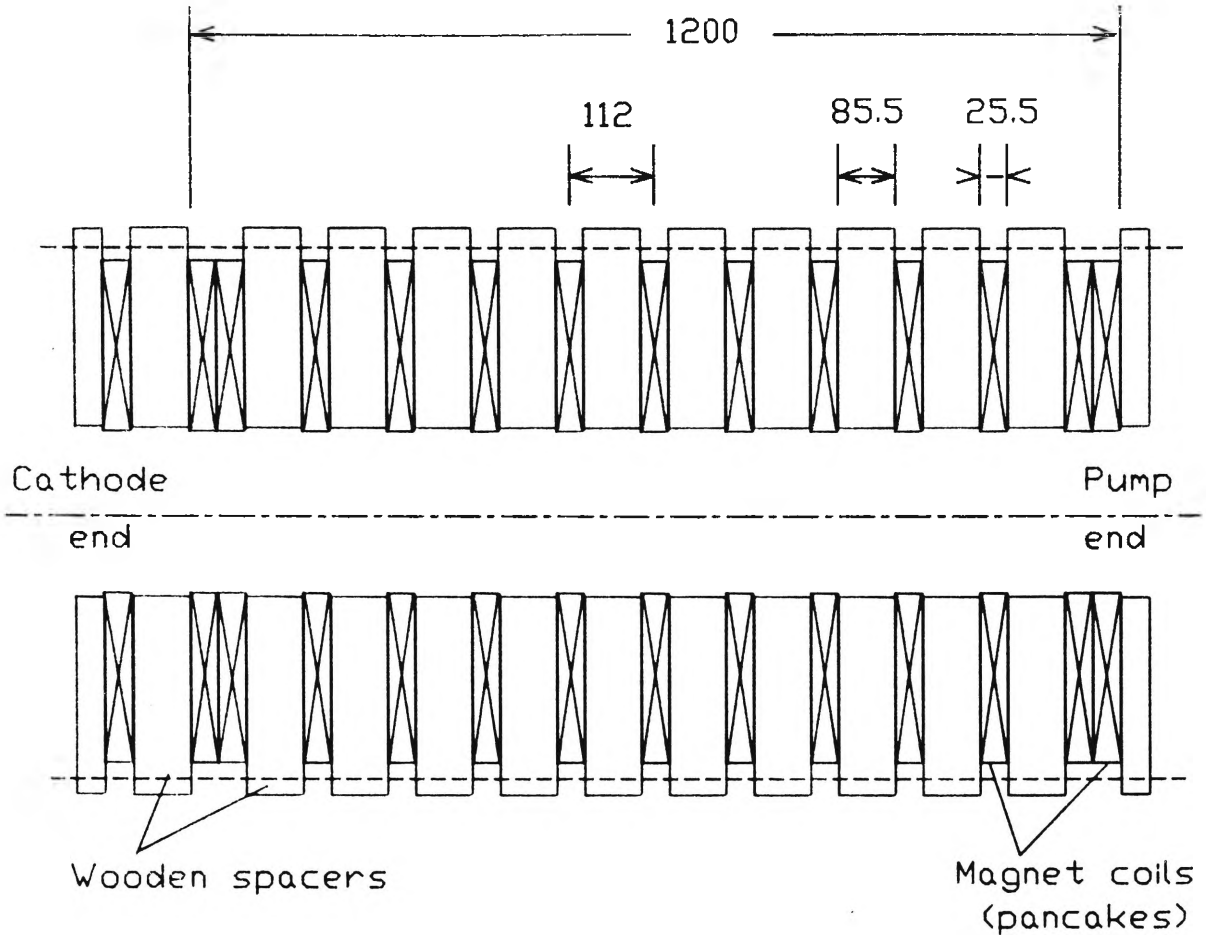

Fig. 4.4.4 Plan of the solenoid magnet

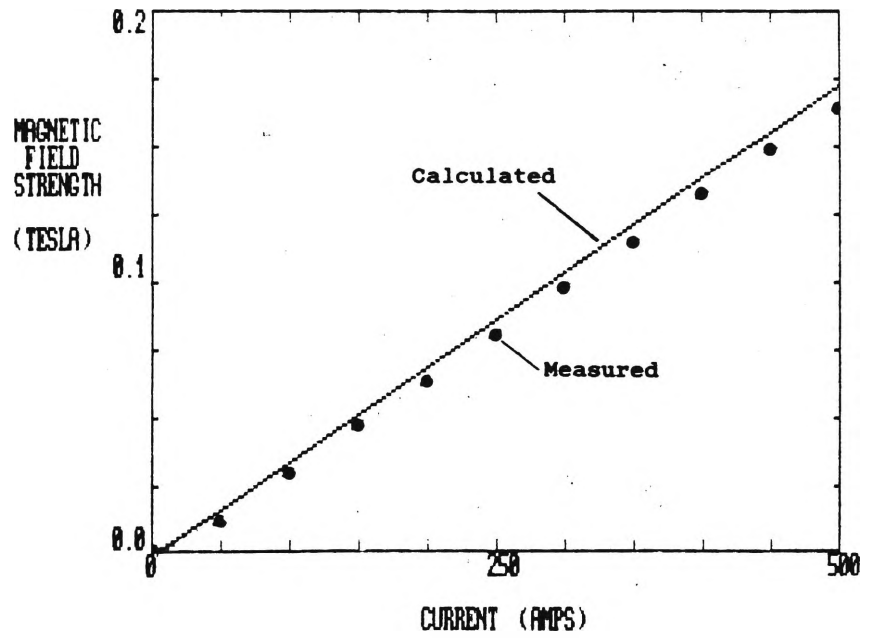

Fig 4.4.5 The calculated (upper trace) and measured (lower trace) magnetic field strength vs. solenoid current for a probe located at (0,0,0.56) metres

4.5 Plasma Deposition Collectors

4.5.1 Rotation and Axial Drift Velocity Collector

The construction of the collector arrangement used for rotation and time of flight experiments is shown in figure 4.5.1.1. A perspex disk with two narrow slits milled partly across the diameter was mounted 40 mm from a second perspex disk (collector). The whole arrangement was mounted on a perspex support.

Following the initiation of the arc, plasma streamed down the VAC chamber and was mostly deposited on the first disk. Some continued on through the slit to deposit on the collector.

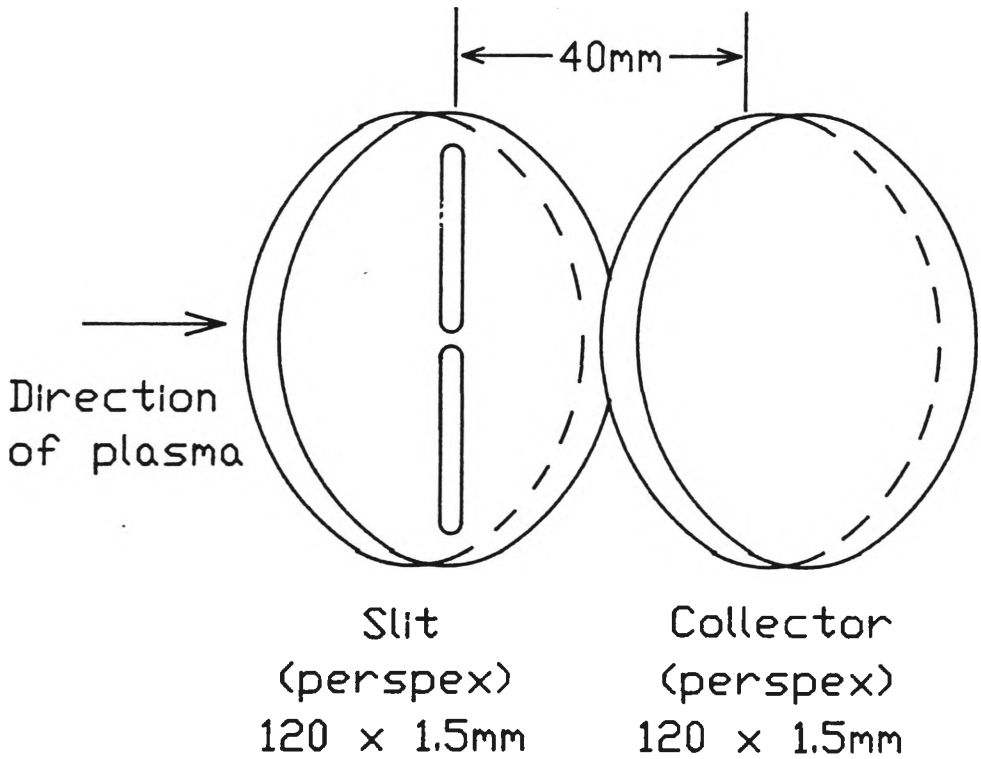

Fig. 4.5.1.1 Diagram of the end plate construction for plasma axial drift and rotation experiments

Consider an infinitesimally small element of plasma entering the region between the slit and the collector plates. A simplified diagram is given in figure 4.5.1.2.

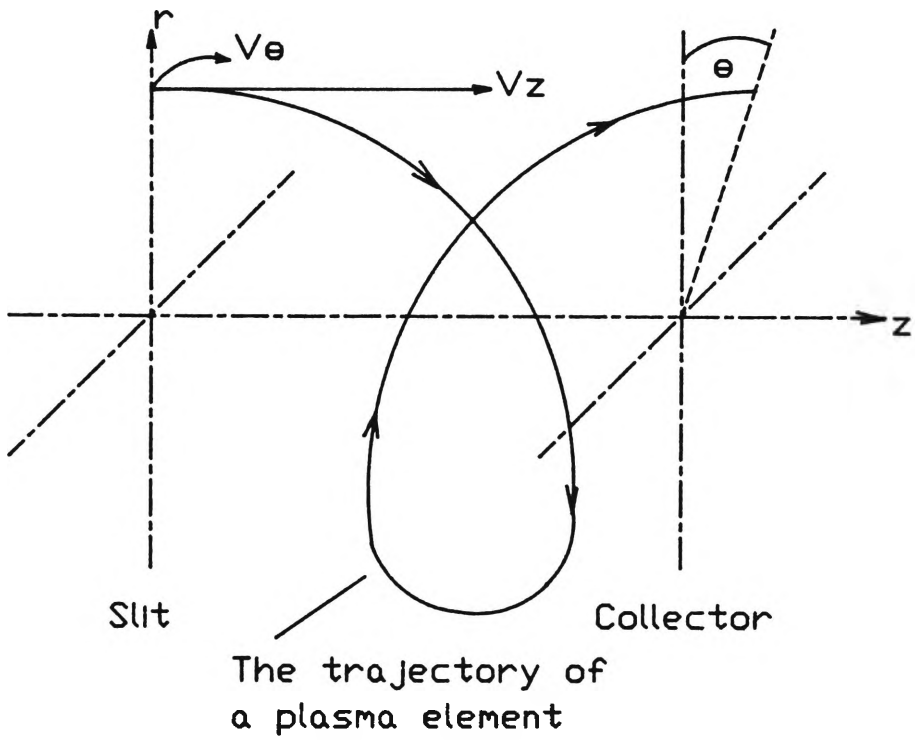

Fig. 4.5.1.2 Simplified diagram for the calculation of the axial drift velocity and plasma rotation

The particle has both axial velocity, v_z and rotational velocity, v_θ. If the element leaves the slit and completes one full revolution about the axis before it strikes the end collector, then the following equation describing its motion can be written:

$$\frac{v_\theta}{r} = w = 2\pi f = \frac{2\pi}{T} = \frac{\theta}{T} \qquad (4.5.1)$$

In the same time, T, the element has moved axially the distance, z, between the slit and the collector.

Therefore:

$$v_z = \frac{z}{T} \qquad (4.5.2)$$

By combining equations (4.5.1) and (4.5.2), the following relationship can be written:

$$v_z = \frac{zw}{\theta} \qquad (4.5.3)$$

Let $\emptyset$ = angular displacement from reference in degrees. If the element of plasma completes less than a full revolution, then (4.5.3) can be modified to the following:

$$v_z = \frac{fz\ 360°}{\emptyset} \qquad (4.5.4)$$

Where: $\theta = \frac{2\pi\emptyset}{360°}$

The value of $\emptyset$ was approximated by investigation of the deposition spread from a known reference after multiple discharges under constant current and axial field conditions.

4.5.2 Isotope Analysis Collector

The sample collector for element and isotope separation experiments is shown in figure 4.5.2.1. The collector was mounted on the same support mentioned in section 4.5.1. A strip of aluminium foil was attached to the side of the collector facing the ion stream. The foil was removed after the discharge series and cut into sections. Care was necessary

so that the thin layer of deposited metal was not disturbed. The samples were sent to other laboratories for element and isotope analysis.

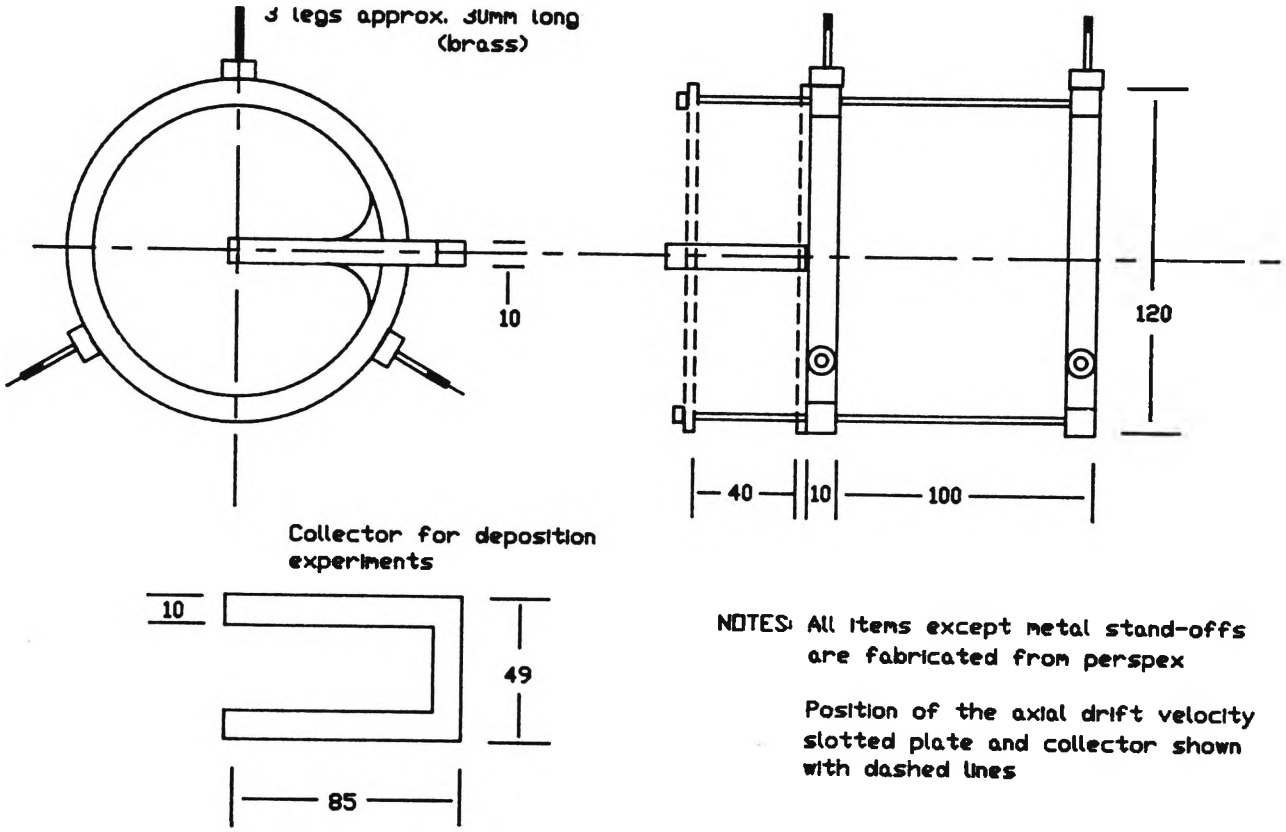

Fig. 4.5.2.1 Collector arrangement used for plasma separation experiments

4.6 Measurement Apparatus

4.6.1 Magnetic Probes

Magnetic probes [112] were constructed to measure the plasma current densities J_θ and J_z. The large electrical interference generated by the discharge system necessitated the use of a differentially connected coils to cancel extraneously induced noise voltage.

Coaxial cable type RG-58 was used for all signal connections. The length of the cable between the VAC rig and the data acquisition equipment was ~ 7 m, which provided the probe coils with a considerable capacitive load. To overcome undesirable overshoot and ringing in the probe circuit, a resistor was connected across the termination ends of each cable. The resistor value was calculated to provide critical damping of the natural resonance of the equivalent magnetic probe circuit. A circuit of the magnetic probe giving construction details is given in figure 4.6.1.1.

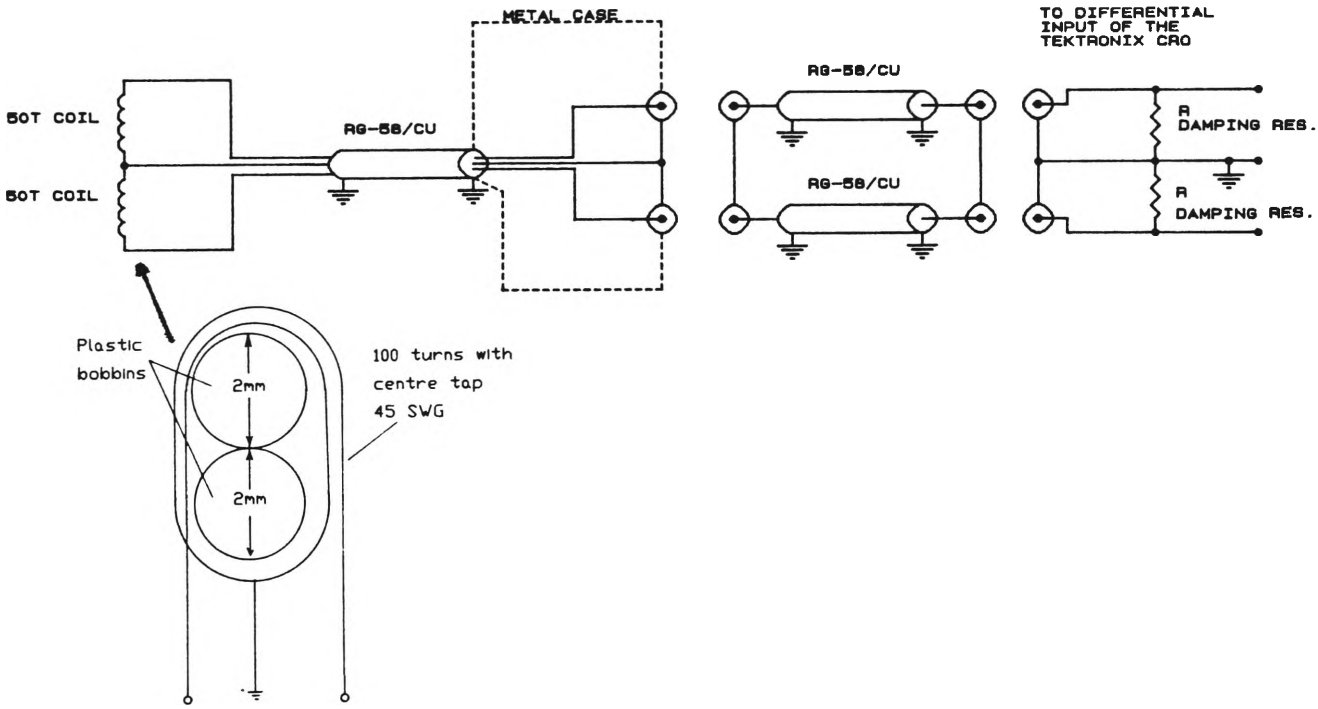

Fig. 4.6.1.1 Construction and equivalent circuit of the magnetic probes

4.6.2 Langmuir Probes

Plasma potential was measured by the insertion of an unbiased Langmuir probe [112] into the plasma region. The probes were constructed using an outer glass tube into which a length of RG-58 co-axial cable was inserted. A short length of Advance (copper-nickel alloy) wire was soldered to the inner conductor of the co-axial cable. The whole probe was made vacuum tight by sealing the ends of the glass tube with a high vacuum epoxy. Figure 4.6.2.1 is a diagram of the probe.

To measure the plasma density, the same probes were used with a potential bias of approximately -145 volts provided by the circuit shown in figure 4.6.2.2. The bias voltage was provided by a bank of series connected 9 volt batteries.

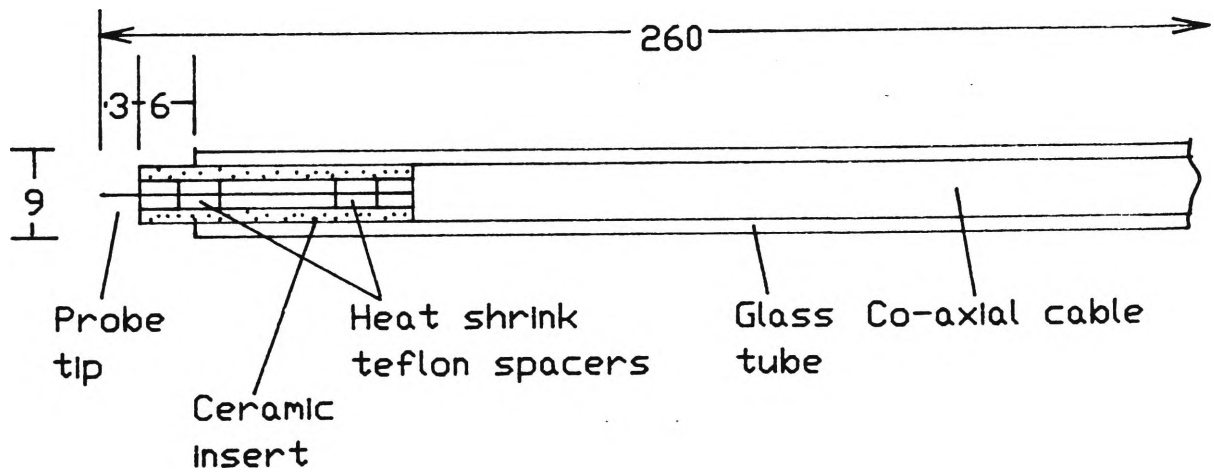

Fig. 4.6.2.1 Construction of the Langmuir probe

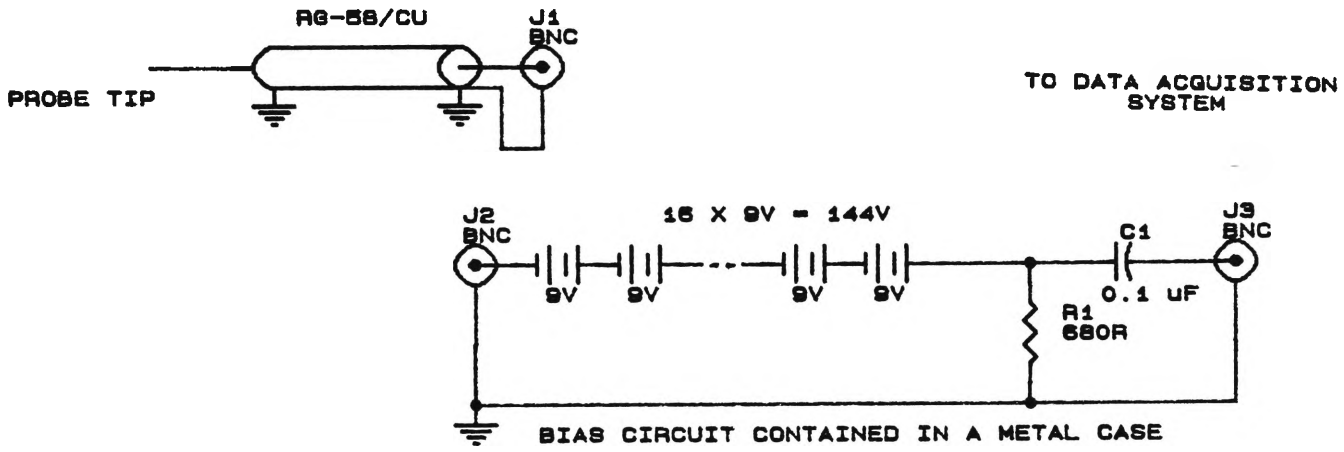

Fig. 4.6.2.2 Circuit of the biased Langmuir probe

4.6.3 High Voltage Probe

A Tektronix model P6015 high voltage probe was used to measure the discharge voltage waveform. It had a 1000:1 voltage reduction, wide frequency bandwidth and 40 kV maximum voltage rating.

4.6.4 Current Monitor

A Pearson model 301X high frequency current monitor was used to measure the discharge current waveform. It was essentially a current transformer which used the heavy metal conductor between the energy storage system and the vacuum arc electrode as the primary loop. The output was measured across the internally loaded secondary. The relationship between the

input current and the output voltage is given from the specifications as 0.01 V/A. This particular model was chosen for its excellent frequency bandwidth and its ability to withstand peak current overloads.

4.6.5 Isotope Separation

Measurement of the VAC separation performance was an important part of the experimental program. The analysis of VAC element and isotope samples relied on the availability of analytical equipment in other research laboratories. Measurements of copper-zinc separation were made by the ANSTO Applied Physics Division. Copper isotopes were analysed by the Commonwealth Scientific and Industrial Research Organisation (CSIRO) Division of Energy Chemistry.

Separation performance for the copper/zinc experiments was measured by proton induced x-ray emission (PIXE) [113,114]. PIXE is a non-destructive technique. Therefore it was possible to also measure the radial deposition densities of the copper samples prior to isotopic analysis. PIXE is based on the analysis of the characteristic x-rays produced when a thin film of material is bombarded by a beam of high energy protons. Energy from the protons stimulates the emission of x-rays as they decelerate within the deposited film. Each element emits x-rays of known, unique energy.

Protons with energies up to 3 MeV are produced by a Van de Graaff accelerator. The proton beam is steered into an evacuated target chamber containing one or more samples.

Measurement is made by a solid state Si(Li) detector connected to a multichannel analyser. The output is a series of peak values across the energy spectrum which identifies the element. Integration of the peaks provides a measure of the element concentration in the sample. The ratios of copper to zinc in the deposit were made to determine the separation performance. The total deposit density was calculated for copper/zinc by a simple summation of the individual element densities.

An inductively coupled plasma mass spectrometer (ICP-MS) [115] was used to measure the relative copper isotope concentrations. The ICP-MS is a two stage instrument comprising a radio frequency (RF) induction coil plasma source and a quadrupole mass spectrometer. Samples are introduced as solutions into the plasma region with an argon driven nebuliser. The ICP heats the sample to many thousands of degrees causing vapourisation and ionisation. Whilst the plasma operates at approximately 1 torr, the analytical stage requires a background pressure of approximately 10^{-5} torr. Ions leave the ICP region and enter the MS region of the instrument via a very small diameter orifice. The ions from the sample are then analysed by a quadrupole mass spectrometer which consists of four parallel rods. The rods are fed with D.C. and RF current (ca. 1 MHz) which is phase orientated to produce an alternating field. For a particular combination of DC and RF, ions of one mass are transmitted to a collector whilst the others spiral outward and are not collected.

4.7 Data Acquisition System

A Philips model PM 3302 two channel, digitising cathode ray oscilloscope (CRO) was used to record the probe, arc current and voltage waveforms. Each channel provided 1024 individual 8 bit resolution data points. The CRO data output and instrument control was provided through an IEEE 488 port. Data transfer and storage was controlled by a PC/XT compatible computer fitted with an IEEE 488 interface. A commercial program or a specially written BASIC program (see Appendix 5) were used to configure both instruments and to transfer data directly to floppy disk during experiments.

A number of programs were written using compiled BASIC to analyse, frequency transform, display and print the waveform data. A MOUSE [116] was incorporated into the programs to allow for easier manipulation and review of the data in the graphic form. Details of the instrumentation interconnection and computer software are given in Appendix 5.

5. ARC MEASUREMENTS

The vacuum arc and related plasma characteristics were studied through measurements of electrode terminal voltage and arc current for various levels of applied magnetic field. The efficiency of the VAC compared to other isotope separation processes was gauged by a comparison of the electrical cost per separated gram.

Initial investigation of the arc discharge utilised the high voltage discharge system and concentrated on the measurement of the arc impedance (Z_{arc}). Results were subsequently used for the five stage PFN design specification.

In section 2.1, a model of the arc was considered which assumed a functional relationship between arc voltage and current plus a constant running voltage related to the cathode material, geometry and thermal properties. Prasad [53] assumed a linear relationship between the vacuum arc voltage and electrode current. This relationship is restated in the following simplified expression for the terminal arc voltage:

$$V_{arc}(t) = Z_{arc}I_{arc}(t) + V_{const} \qquad (5.0.1)$$

An electrical equivalent circuit of the arc is shown in figure 5.0.1. To facilitate analysis of the model, Prasad assumed Z_{arc} to be a resistor. V_{const} was assumed to be a simple ideal diode with a voltage drop given by the cathode fall voltage (≈ 20 volts for 13 mm copper electrodes in the absence of an applied magnetic field) [68,74].

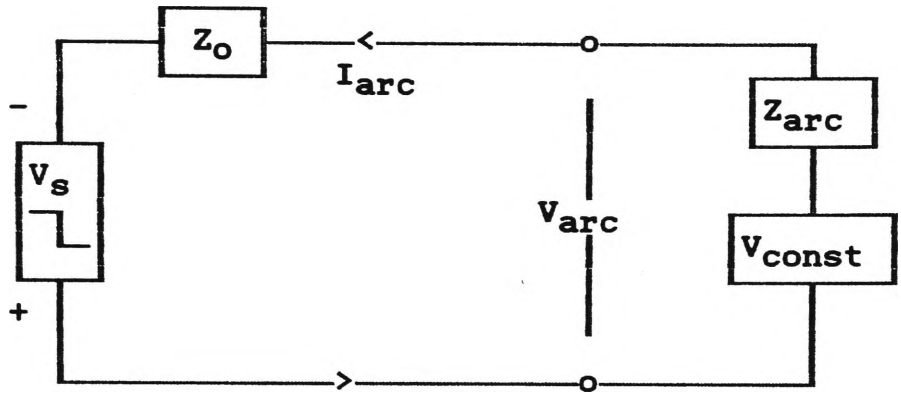

Fig. 5.0.1 Prasad's equivalent circuit of the arc connected to a voltage source with impedance Z_o

By inspection, an equation can be written for the value of Z_o.

$$Z_o(t) = \frac{V_s - V_{arc}(t)}{I_{arc}(t)} \qquad (5.0.2)$$

5.1 Arc Current and Voltage

Typical current and voltage discharges for the high voltage RLC system are shown in figure 5.1.1. Discharge voltages and currents for the PFN are shown in figure 5.1.2 for B_z = 0.1 T and V_c = 300 V. Figure 5.1.3 shows the current and voltage discharge waveforms predicted by the SPICE computer simulation (see section 3.2) for the initial conditions B_z = 0 and V_c = 300 V.

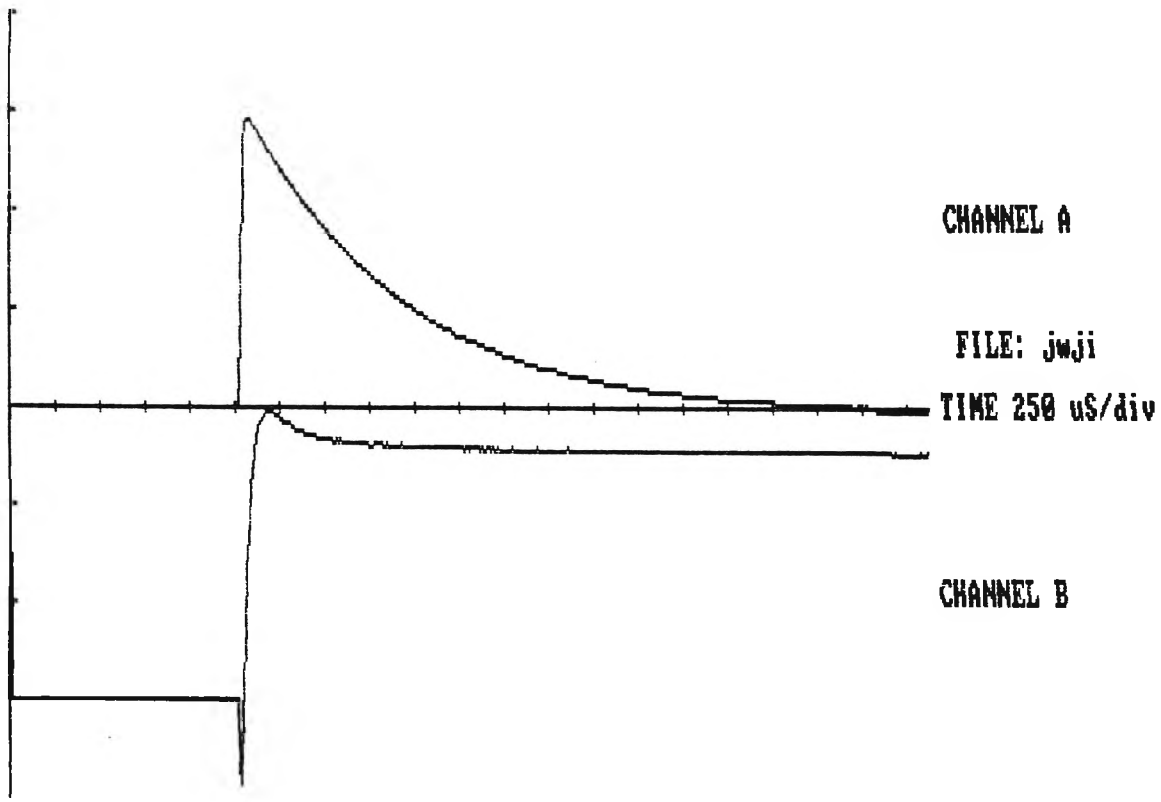

Fig. 5.1.1 High voltage RLC discharge current and voltage for V_C = -3 kV and B_Z = 0.1 T
Ch. A = 1 kA/div Ch. B = 1 kV/div

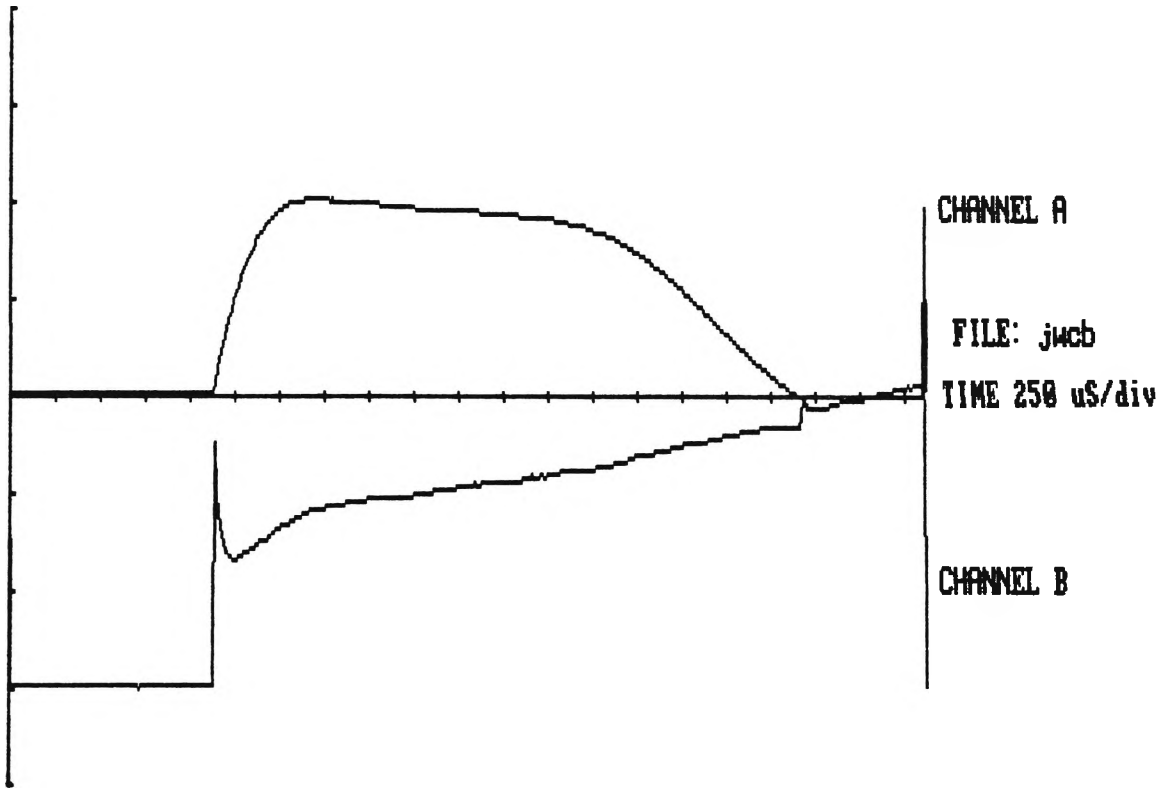

Fig. 5.1.2 Discharge current and voltage for V_C = -300 V and B_Z = 0.1 T
Ch. A = 2 kA/div Ch. B = 100 V/div

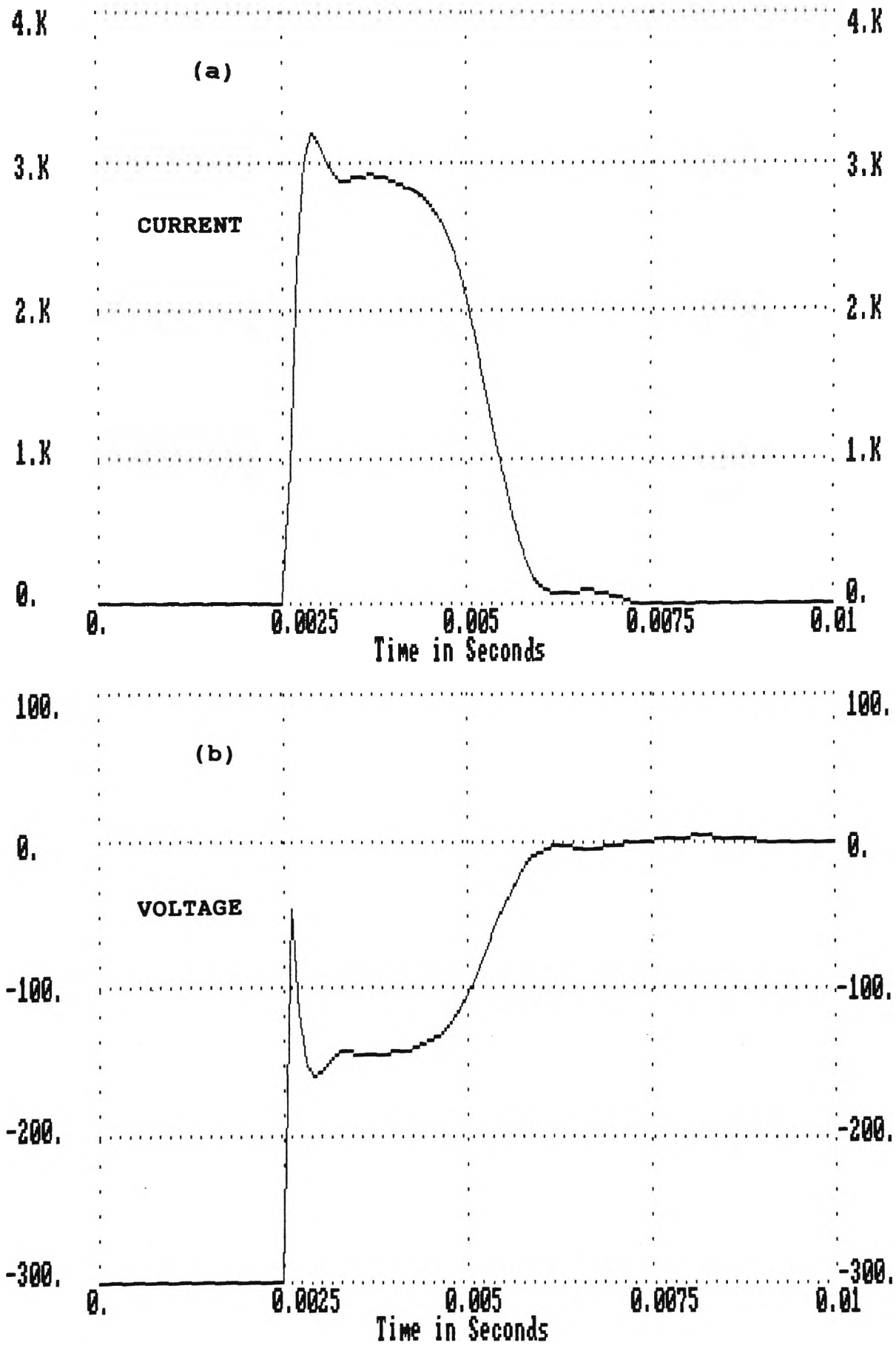

Fig. 5.1.3 Comparison between the SPICE model current (a) and voltage (b) and the experimental result (c) (over page) for V_C = 300 V and B_Z = 0 T

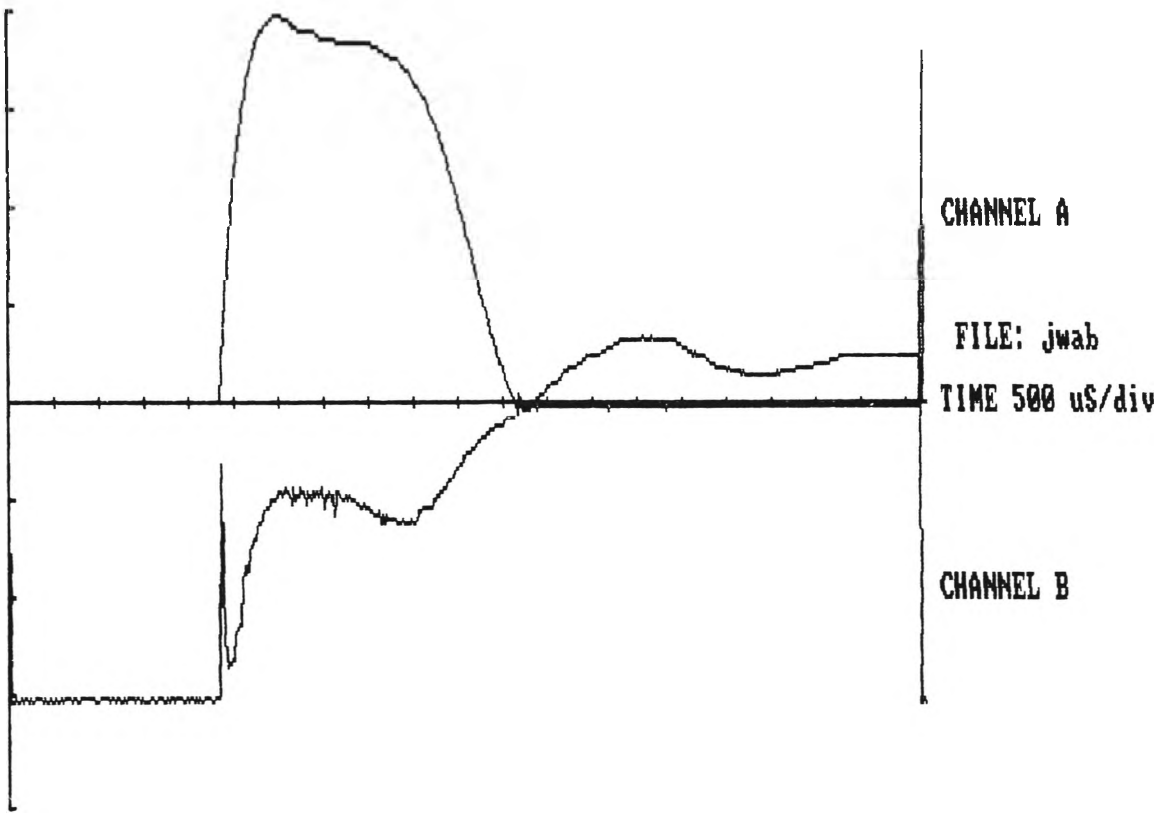

Fig. 5.1.3 (c) Experimental result for V_C = 300 V
and B_Z = 0 T
Ch. A = 1 kA/div Ch. B = 100 V/div

The voltage overshoot in figure 5.1.3 (c) was caused when the arc was extinguished and the PFN load suddenly went to an open circuit. Losses through the PFN parasitic elements then became the only appreciable circuit load. The PFN thus behaved like a "lossy" resonant LC circuit.

Differences between the measured values of current and voltage and those predicted by the computer simulation were due to the high estimation of the arc impedance (50 mΩ) in the circuit model shown in figure 3.2.2. More accurate measurements of the arc characteristics found that the actual arc impedance for B_Z = 0 T was less than the original design estimate. Details are given in the next section.

5.2 Arc Characteristics

The PFN provides near steady current conditions for most of the arc duration. Measurements of current and voltage were made 1.0 mS after the initiation of the arc. The computer program MPLOT.EXE (see Appendix 5) was used to locate the start of the arc on the current and voltage plots with the MOUSE. A typical current and voltage plot is shown in figure 5.2.1. The arrow is the MOUSE cursor.

The arc sustaining voltage (V_{arc}) was measured for a series of initial discharge voltages (V_c) at fixed axial magnetic fields (B_z). Measured values are plotted in figure 5.2.2 with a least squares fit to the data for each level of B_z. For the range of B_z tested, arc voltage rises linearly with the initial PFN charging voltage.

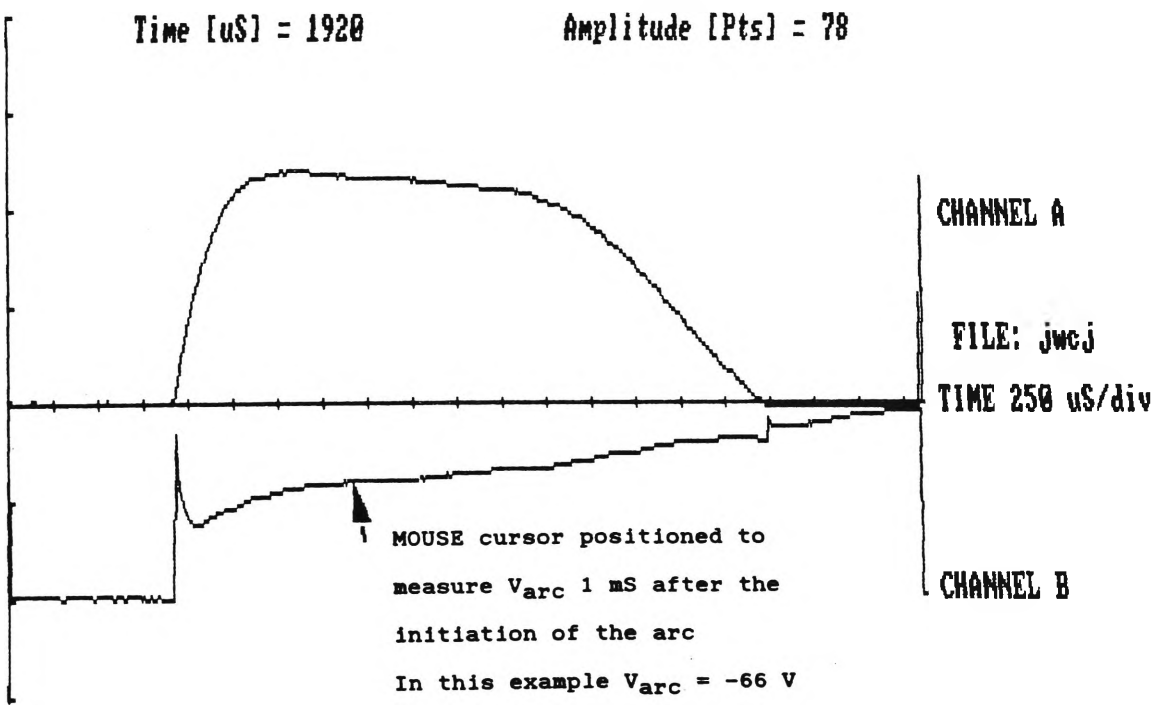

Fig. 5.2.1 Arc current and terminal voltage for V_c = 200 V and B_z = 0.15 T
Ch. A = 1 kA/div Ch. B = 100 V/div

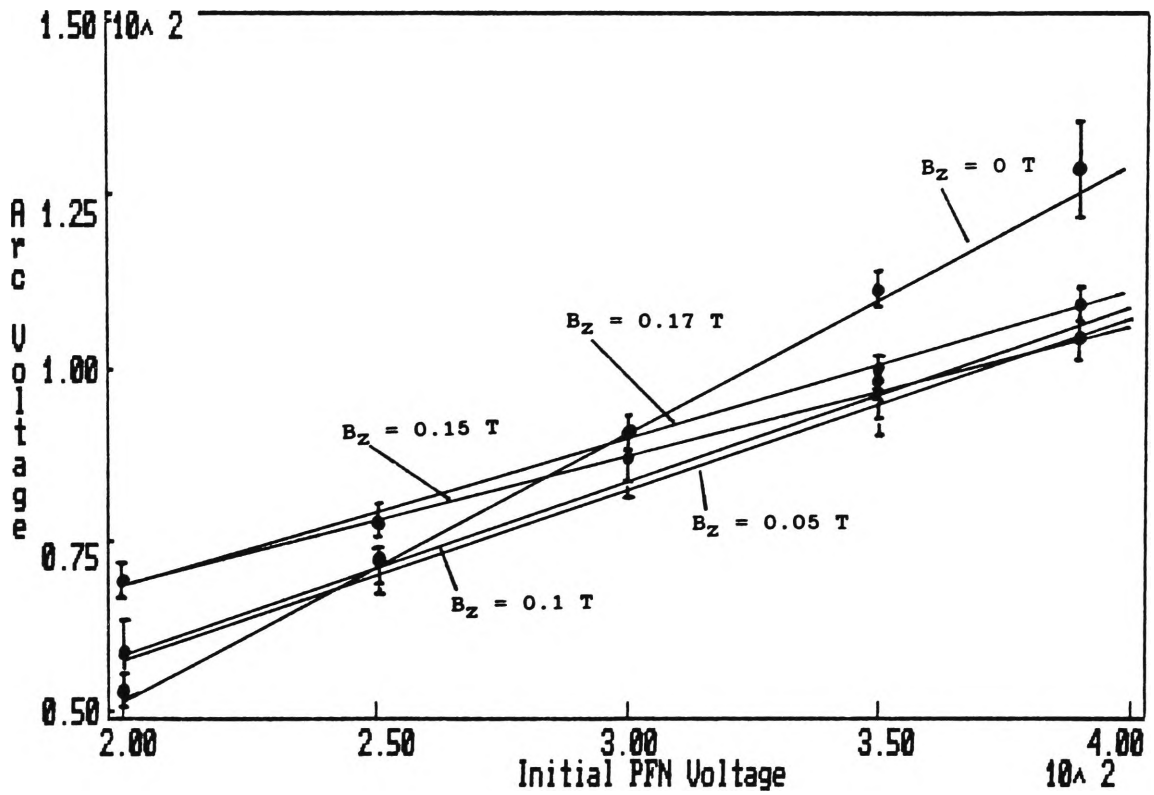

Fig. 5.2.2 Arc voltage vs. initial PFN discharge current for B_z = 0, 0.05, 0.1, 0.15 and 0.17 T

The case B_z = 0 exhibits a steeper slope over the range of V_c than all other cases where B_z > 0. The result indicates that the arc properties were altered by the presence of the axial magnetic field.

Investigation of the voltage waveforms for B_z = 0 revealed significant arc noise for all levels of V_c. Noise was also measured for V_c = 390 V at B_z= 0.05 T. A comparison of current and voltage, for B_z = 0 can be seen in figure 5.2.3(a) - (d).

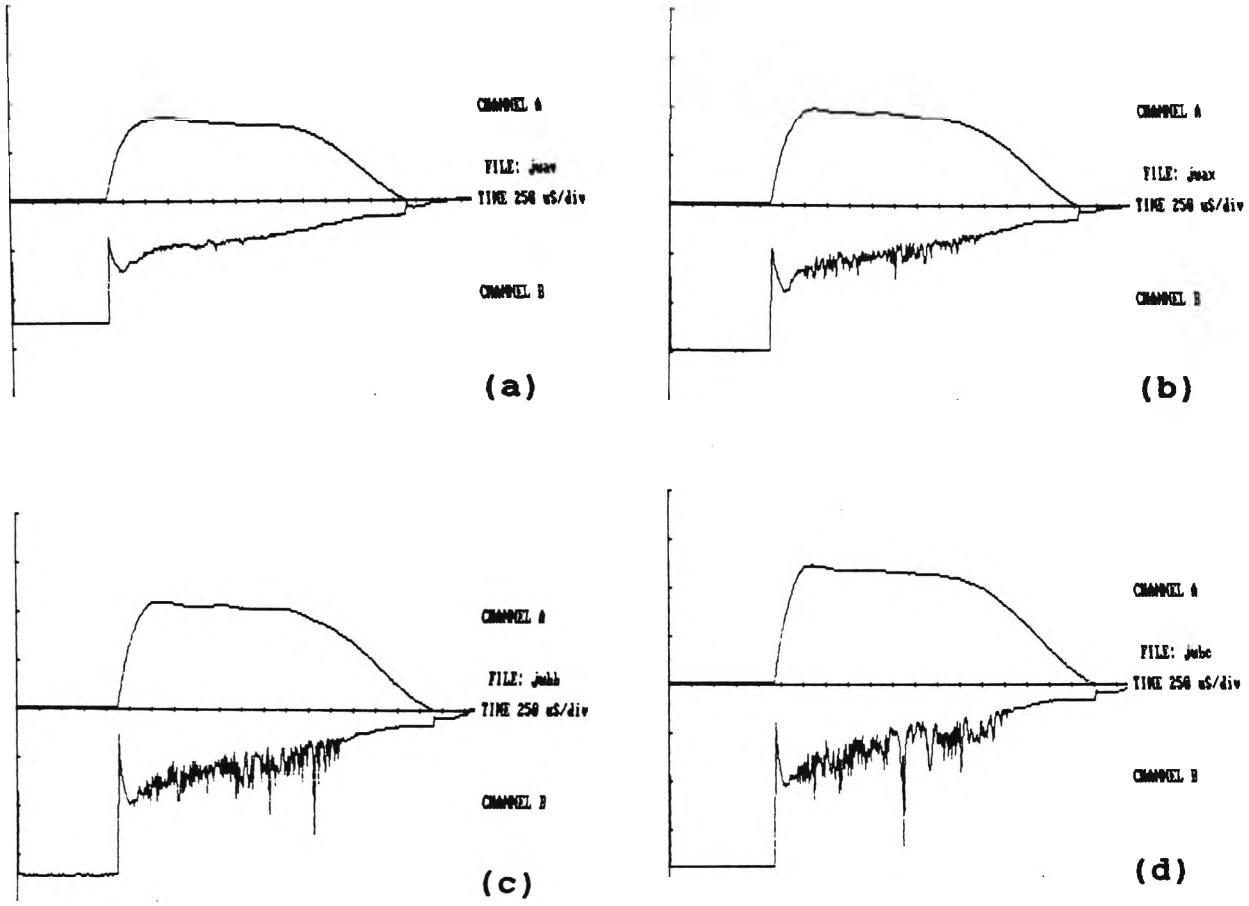

Fig. 5.2.3 Electrode current and voltage for B_z = 0 T at V_c = (a) 250 V, (b) 300 V, (c) 350 V and (d) 390 V

Yanabu and co-workers [88-91] have observed similar results in studies related to vacuum circuit breakers. For an applied magnetic field which produced less than the minimum arc voltage, the arc was extremely unstable and caused localised surface heating, emission of macroparticles and electrode melting. Operation at a minimum arc voltage produced a uniformly dispersed arc with minimum electrode erosion. Whilst this is favourable for prolonging the electrode life in circuit breakers, it is not a desirable condition for the VAC where electrode erosion and the production of plasma ions are essential mechanisms. Therefore, the VAC should be operated at magnetic field and voltage levels in the stable region below the arc voltage minimum for optimum, uniform erosion.

The relationships between V_{arc} and B_z for various levels of discharge voltage are plotted in figure 5.2.4. The curves are quadratic least squares fits to the data. The presence of the axial magnetic field causes a decrease in the arc voltage. This can be observed by the dip in the curves. After reaching a minimum value, the arc voltage rises for further increases in B_z.

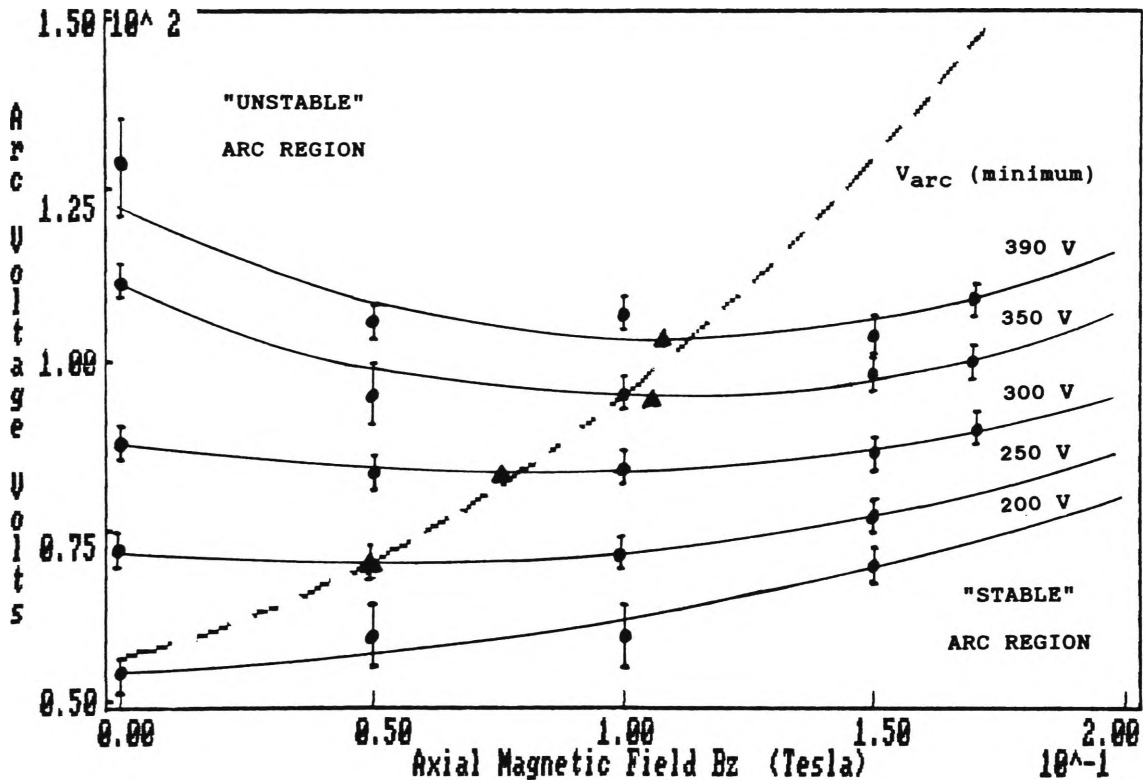

Fig. 5.2.4 Arc voltage vs. axial magnetic field
V_c = 200, 250, 300, 350 and 390 V
V_{arc} minimum shown as a dashed curve

An increase of 50 volts in the discharge voltage resulted in an increase of 10 to 20 volts in the measured arc voltage. Minimum values for each curve were calculated and also plotted in figure 5.2.4. The minimum stable arc voltage as a function of

B_z was found to have the following relationship:

$$V_{arc}\ (\text{minimum}) = 2115\ B_z^2 + 117\ B_z + 56 \quad (\text{volts})$$

Optimum stable arc operation of the VAC with high erosion rates using the present cathode geometry was found to be in the region below the V_{arc} minimum curve.

Arc voltage and current characteristics for various levels of B_z are plotted in figure 5.2.5. A quadratic least squares fit to the data has been used to extrapolate from the measured values to find the intercept arc voltage V_{const}. The result is in concordance with similar studies by Kimblin and co-workers [83,87] and demonstrates that the arc impedance over a large range of B_z is not linear.

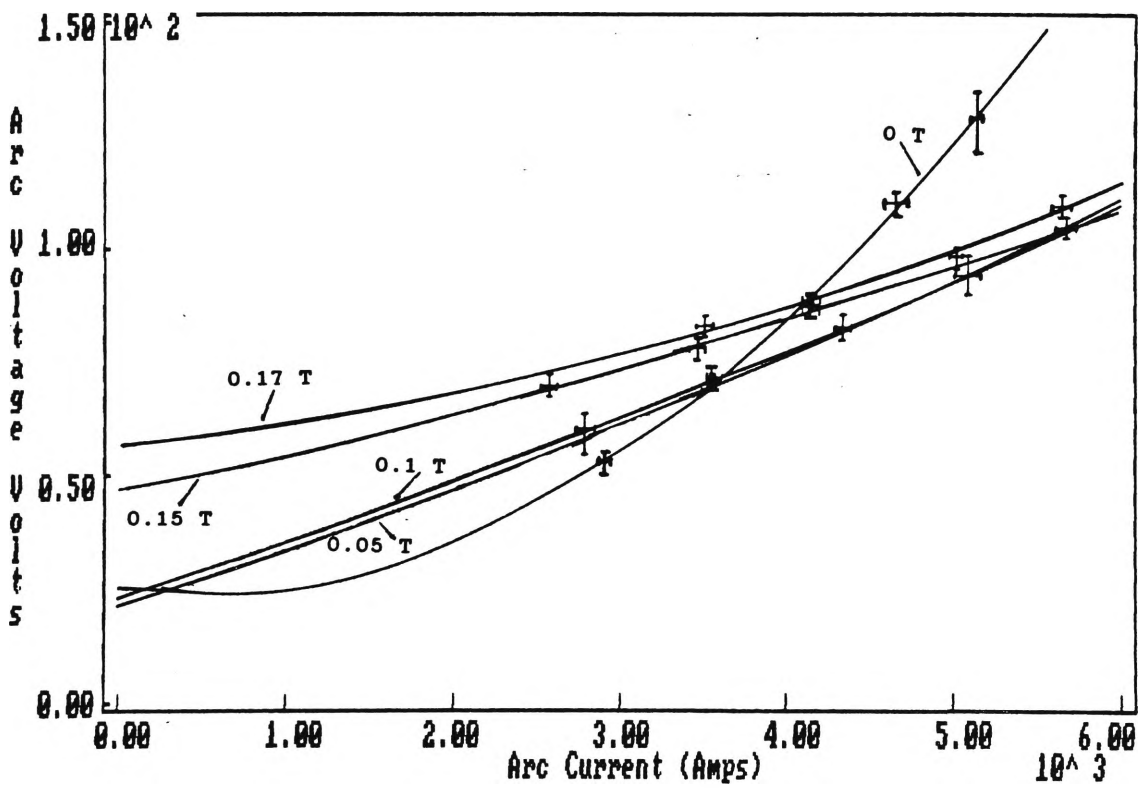

Fig. 5.2.5 Arc current and voltage characteristics for B_z = 0, 0.05, 0.1, 0.15 and 0.17 T

The arc impedance Z_{arc} and the voltage intercept V_{const} for the range B_z are given in Table 5.1. Z_{arc} was calculated at the mid-data point for each curve (~4 kA).

TABLE 5.1

Relationship between Arc Impedance and Axial Magnetic Field for V_c = 300 V

B_z (T)	Z_{arc} (mΩ)	V_{const} (V)
0	35.4	26.2
0.05	16.2	21.1
0.1	15.7	21.9
0.15	11.5	46.4
0.17	12.2	56.6

Arc impedance was reduced by more than 50% for an applied axial magnetic field of 0.05 T further demonstrating the interaction between the arc and the field.

The nominal impedance value for the PFN was chosen to be 50 mΩ. The PFN impedance was recalculated using equations 5.0.1 and 5.0.2 for the measured values of Z_{arc}, V_{const} and I_{arc} at an initial charge voltage V_c = 300 V. For B_z = 0 to 0.17 T, Z_o changed from 43 mΩ to 72 mΩ. The PFN design impedance appears to be a reasonable match for the electrode configuration. However, to achieve maximum electrical efficiency in a commercial VAC, Z_o should be more closely specified for the operation ranges of B_z and V_c that will give the desired separation performance.

6. PLASMA MEASUREMENTS

The plasma model, developed in section 3, assumed a singly ionised, axially symmetric, rotating cylinder of plasma. In practice, plasma consists of multiply charged ion species [48] and the density of the plasma column can vary both radially and azimuthally due to the irregular production of plasma by the arc discharge. The production of ions varies directly with the current drawn by the arc [78].

Density variations in the plasma column were detected by the introduction of Langmuir probes or magnetic probes into the plasma region [112]. The probe's measured voltage potential varied as the plasma moved past the probe tip. Figure 6.0.1 shows the typical recorded output from a floating Langmuir probe in the VAC chamber with no externally applied axial magnetic field. Plasma potential was seen to vary with the arc current. Figure 6.0.2 shows a plot for the same experimental conditions with the addition of a 0.05 T axial magnetic field. A superimposed periodic component was observed in the waveform due to the azimuthal movement of plasma microstructure past the probe. This particular characteristic was used to investigate the rotational direction and speed of the plasma column for various configurations of magnet and magnetic field strength.

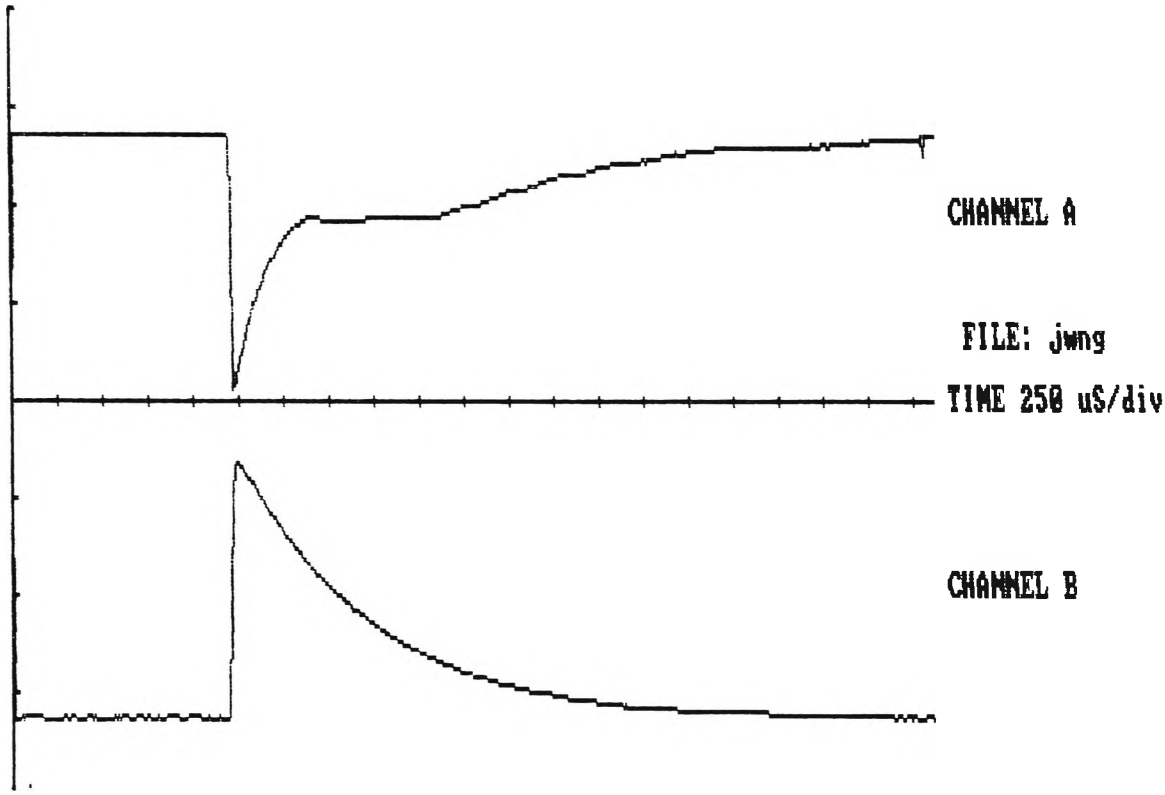

Fig. 6.0.1 Upper trace: floating Langmuir probe output for B_z = 0 T and V_c = 4 kV
Lower Trace: Arc Current ≈ 2 kA/div

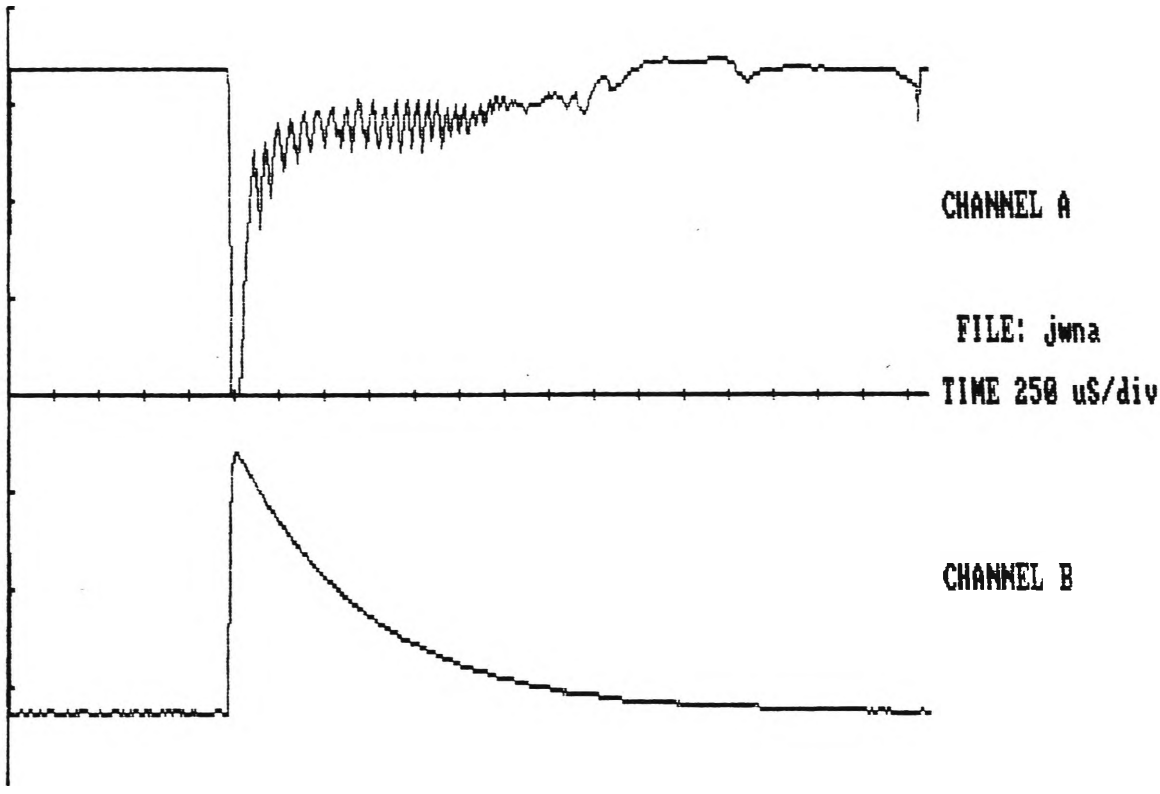

Fig. 6.0.2 Upper trace: floating Langmuir probe output for B_z = 0.05 T and V_c = 4 kV
Lower Trace: Arc Current ≈ 2 kA/div

6.1 Direction of Plasma Rotation

Two experiments were conducted to establish the relationship between the polarity of the magnetic field and the direction of plasma rotation.

The slotted plate and collector described in section 4.5.1 was used in the first experiment. The power supply connections were orientated so the magnetic field B_z direction was towards the VAC pump end (positive lead attached to the pump end of the solenoid, negative lead attached to the cathode end). The VAC was discharged using the PFN system. An initial capacitor charge of 380 V was used with an axial magnetic field of 0.15 T for each shot. After 180 shots the collector was removed and photographed. The resulting plasma deposit can be seen in figure 6.1.1. as a dark patch crossing the centre of the plate. A vertical line in the perspex disk (not seen in the photograph) was used for reference.

A second collector was assembled in the VAC and the electrical connections to the solenoid were reversed. A further 173 shots were discharged under the same experimental conditions with a reversed magnetic field. A photograph of the plasma deposition for this case is shown in figure 6.1.2. The radial displacement in both cases is sufficient to conclude that the direction of rotation was changed by the reversal of the axial magnetic field.

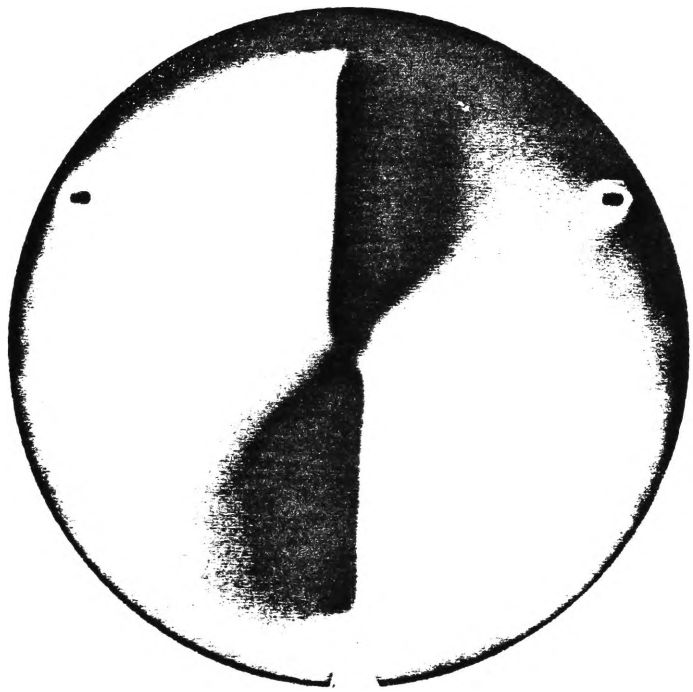

Fig. 6.1.1 Plasma deposits for the slotted plate and collector experiment. B_z = 0.15 T and V_c = 380 V. (reduced 70% full size)

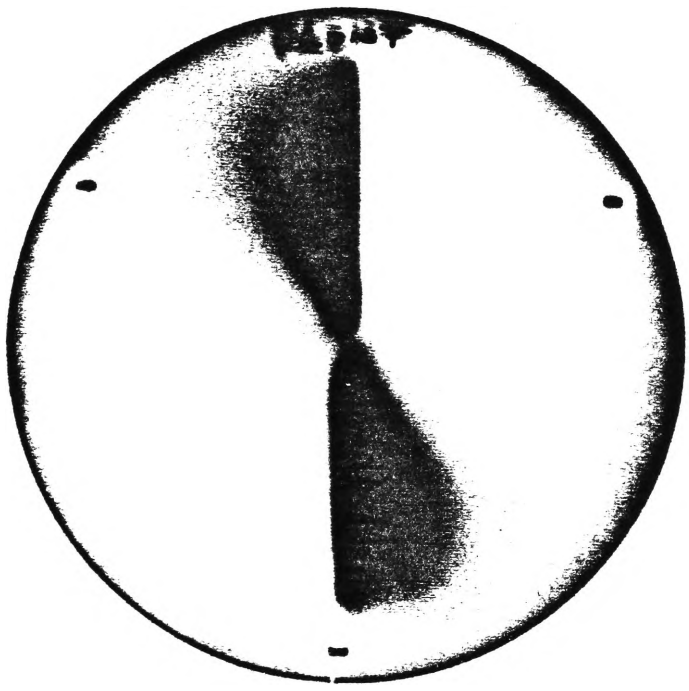

Fig. 6.1.2 Plasma deposits for the slotted plate and collector experiment. Reversed axial magnetic field. B_z = 0.15 T and V_c = 380 V. (reduced 70% full size)

In the second experiment, two biased Langmuir probes were inserted at chamber positions 3A and 3B (i.e. $z_{3A} = z_{3B} \approx 720$ mm from the cathode and $\theta_{3A} - \theta_{3B} = 90°$). The arrangement is shown in figure 6.1.3. The orientation of the field was set to point towards the VAC pump end. The signal outputs from both probes are shown in figure 6.1.4. Probe 3B (light trace) is used for reference. The recorded waveform for probe 3B leads 3A (dark trace) by 90° indicating clockwise rotation when viewed from the cathode end of the VAC.

In figure 6.1.5, the magnetic field was reversed for the same experimental conditions. The phase of the 3B (light trace) was seen to lag 3A (dark trace) and rotation was, therefore, in the counter-clockwise direction when viewed from the cathode end.

A summary of both the slotted collector and the Langmuir probe experiments is given in Table 6.1.1. The results are in agreement. Plasma rotation was determined to be in the same azimuthal direction as the electron cyclotron rotation.

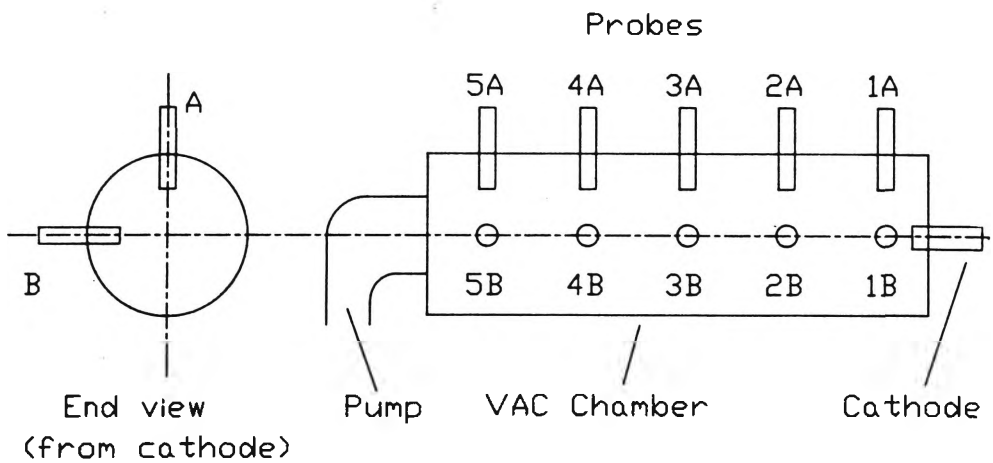

Fig. 6.1.3 Langmuir probe placement for the determination of the plasma rotation direction

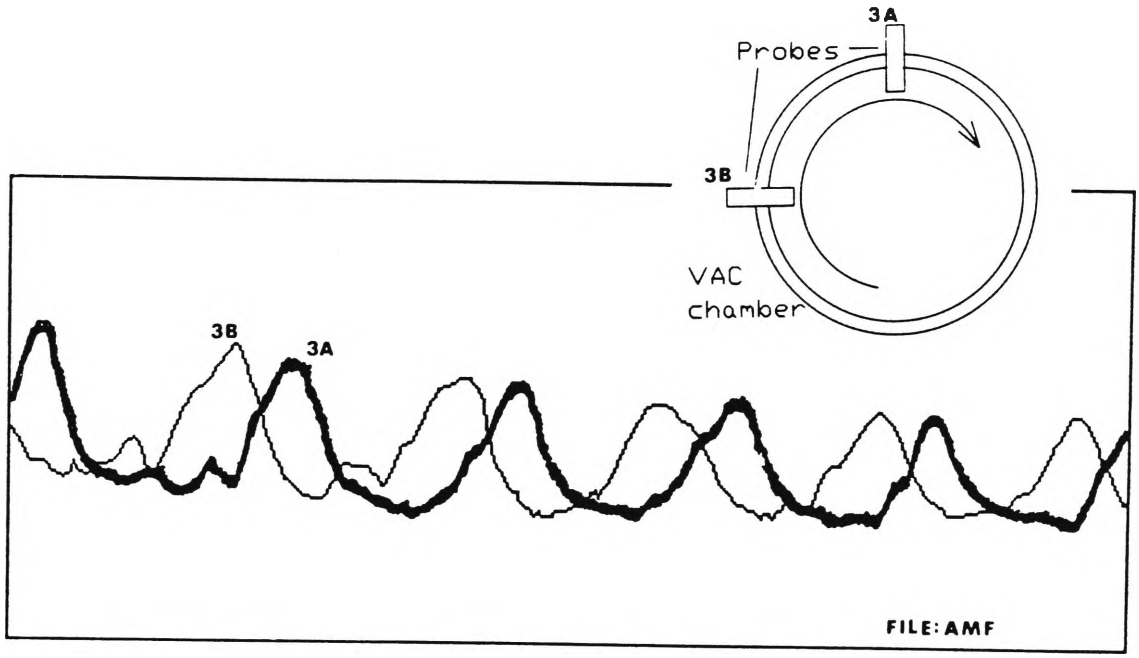

Fig. 6.1.4 Langmuir probe output for the determination of plasma rotation direction B_z = 0.05 T

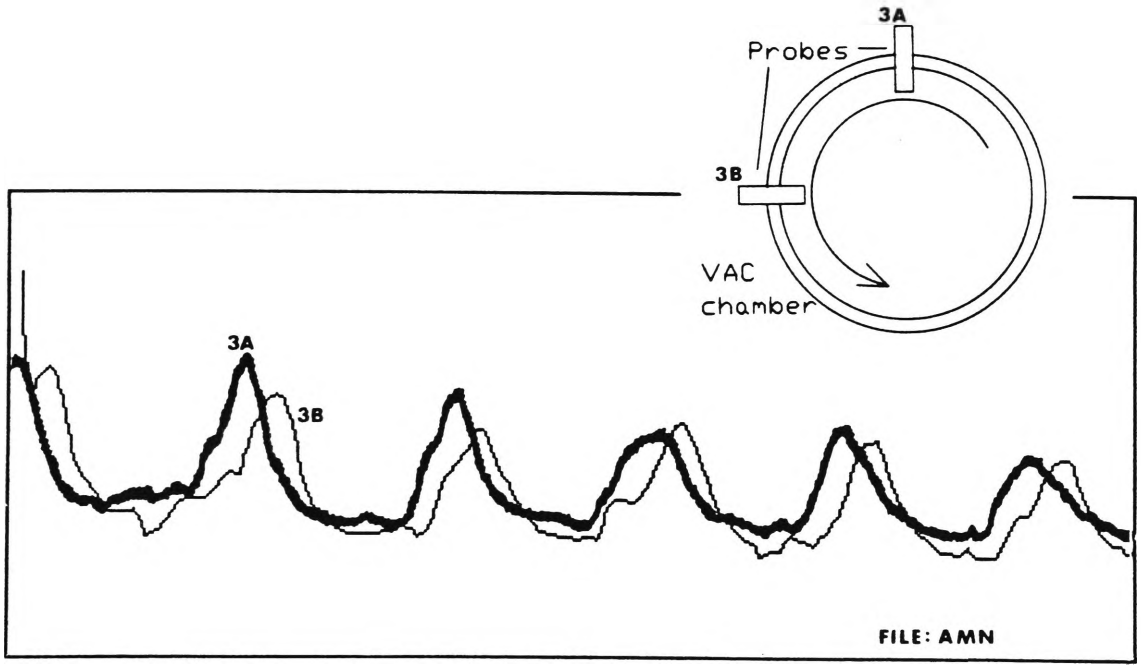

Fig. 6.1.5 Langmuir probe output for the determination of plasma rotation direction with reversed axial magnetic field B_z = 0.05 T

TABLE 6.1.1

Comparison of Results for Direction of Rotation Experiments

EXPERIMENT	SOLENOID ELECTRICAL CONNECTION	MAGNETIC FIELD Bz ORIENTATION	PROBE MEASUREMENTS	PLASMA DEPOSIT	DIRECTION OF ROTATION (Viewed from the Cathode End)
Slit & plate collector	+ lead at pump end	Pump end $\xrightarrow{B_z}$ Cath. end	-	see Fig. 6.1.1	Clockwise
Slit & plate collector	- lead at pump end	Pump end $\xleftarrow{B_z}$ Cath. end	-	see Fig. 6.1.2	Counter-clockwise
Langmuir probes	+ lead at pump end	Pump end $\xrightarrow{B_z}$ Cath. end	3B leads 3A see Fig. 6.1.4	-	Clockwise
Langmuir probes	- lead at pump end	Pump end $\xleftarrow{B_z}$ Cath. end	3A leads 3B see Fig. 6.1.5	-	Counter-clockwise

6.2 Speed of Rotation

Equation (2.2.19) predicted the plasma rotational speed for axial magnetic field B_z. For low values of B_z, the bulk plasma rotation frequency was estimated by inspection of the resultant Langmuir probe signal. At high magnetic field strengths the plasma microstructure tended to produce complex waveforms. For these conditions, a Fourier analysis technique was adopted to calculate the dominant frequency peaks in the Langmuir waveform (see Appendix 5).

To measure rotational speed in the VAC, probes were positioned at 4A or 4B. Frequency measurements were made with the probe tip at a nominal radius of 30 mm from the VAC axis.

Copper plasmas were measured with floating and biased Langmuir probes. Similar periodic fluctuations were observed from both probe types.

Figure 6.2.1 shows a typical series of data plots from biased Langmuir probes for different levels of axial magnetic field. Bias voltage was fixed at -145 volts. It can be seen that the frequency component increases for higher levels of magnetic field in accordance with equation (2.2.19).

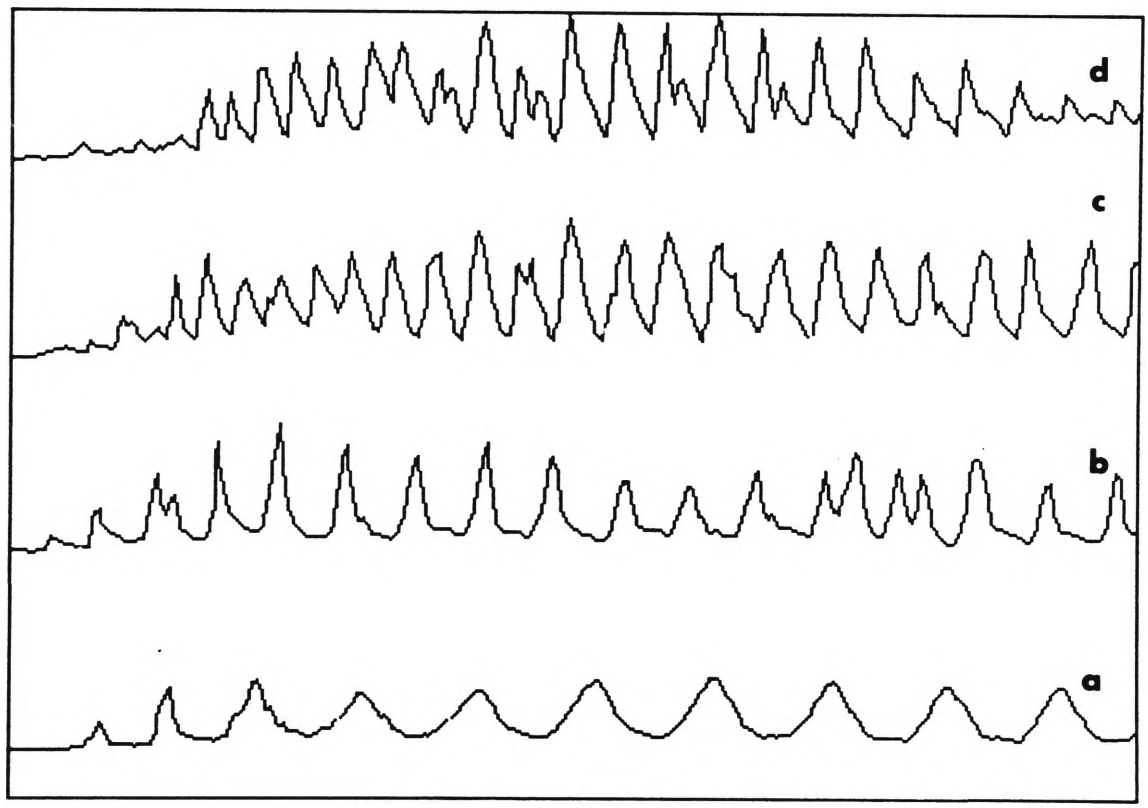

Fig. 6.2.1 Typical biased langmuir probe output for various values of B_z = (a) 0.025 T, (b) 0.05 T, (c) 0.083 T and (d) 0.1 T

The measured relationships between rotational velocity and applied axial magnetic field for various levels of initial discharge voltage are plotted in figure 6.2.2.

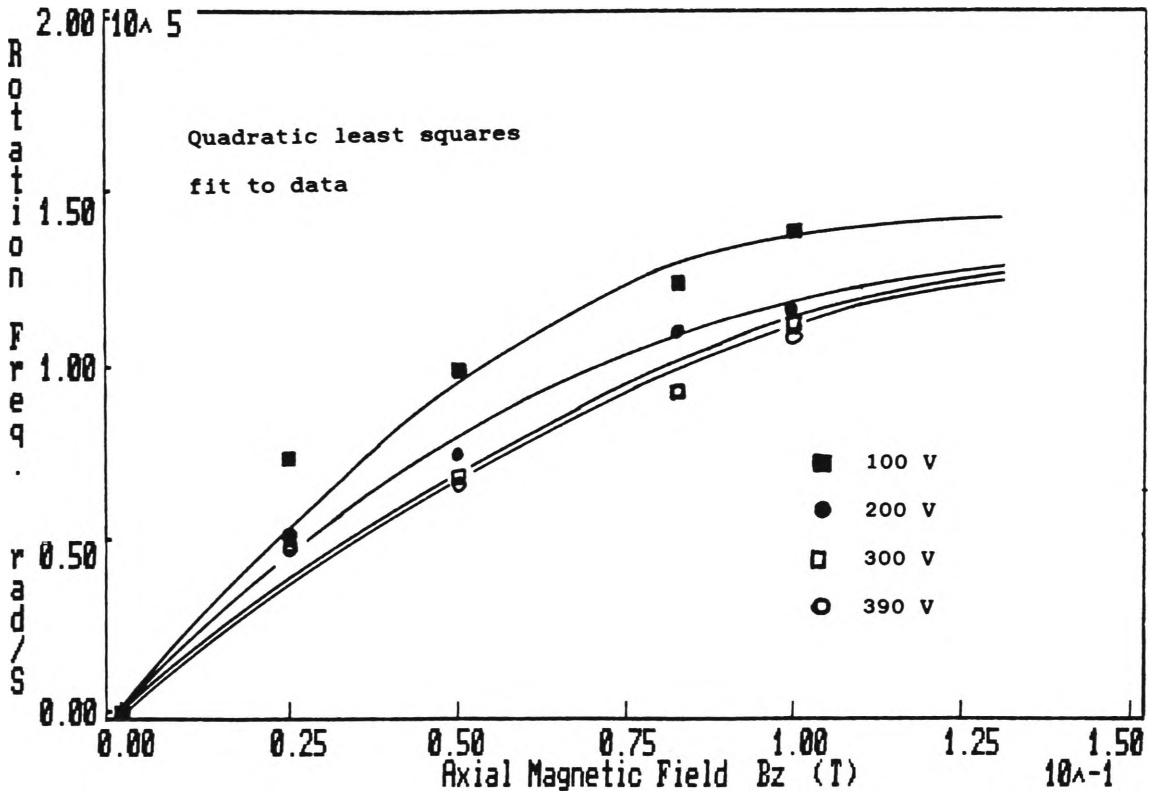

Fig. 6.2.2 Measured values of rotational frequency vs. magnetic field strength for V_c = 100, 200, 300 and 390 V

The effect of the initial discharge voltage on the rotational velocity can be seen in figure 6.2.3. Rotational frequency is plotted against the PFN initial discharge voltage for different levels of applied magnetic field. A straight line fit to the data has been calculated. The slope of the line is negative, over the range of discharge voltage tested. Plasma rotation frequency decreases for increasing discharge voltage.

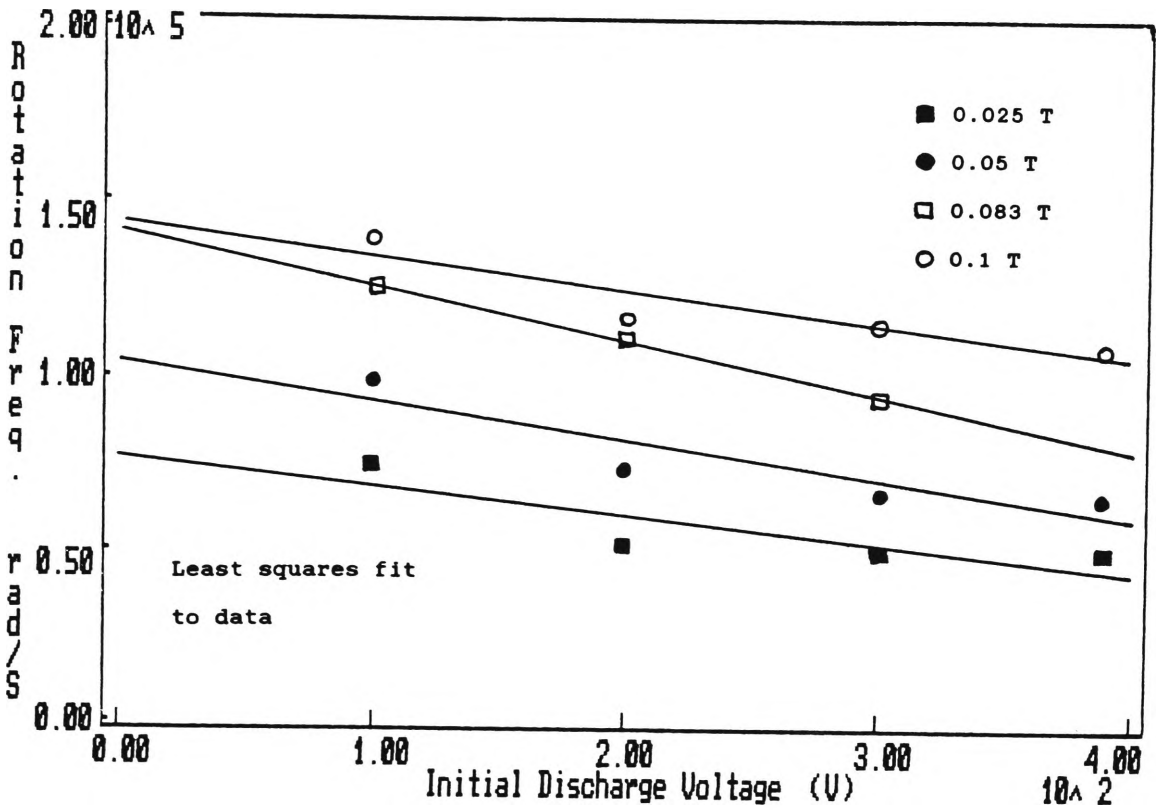

Fig. 6.2.3 Measured values of rotational velocity vs. initial discharge voltage for B_z = 0.025, 0.05, 0.083, 0.1 T

Rotation frequency measurements were also made for plasmas generated by the H.V. discharge system. Estimations in measurements were necessary since the rate of change in the arc current produced variations in the plasma rotation frequency. Figure 6.2.4 is a plot of the estimated plasma rotation frequencies for increasing magnetic field at an initial capacitor charge of 4 kV. A straight line fit to the data has also been included. For an increase in the applied magnetic field, the rotation frequency is observed to increase.

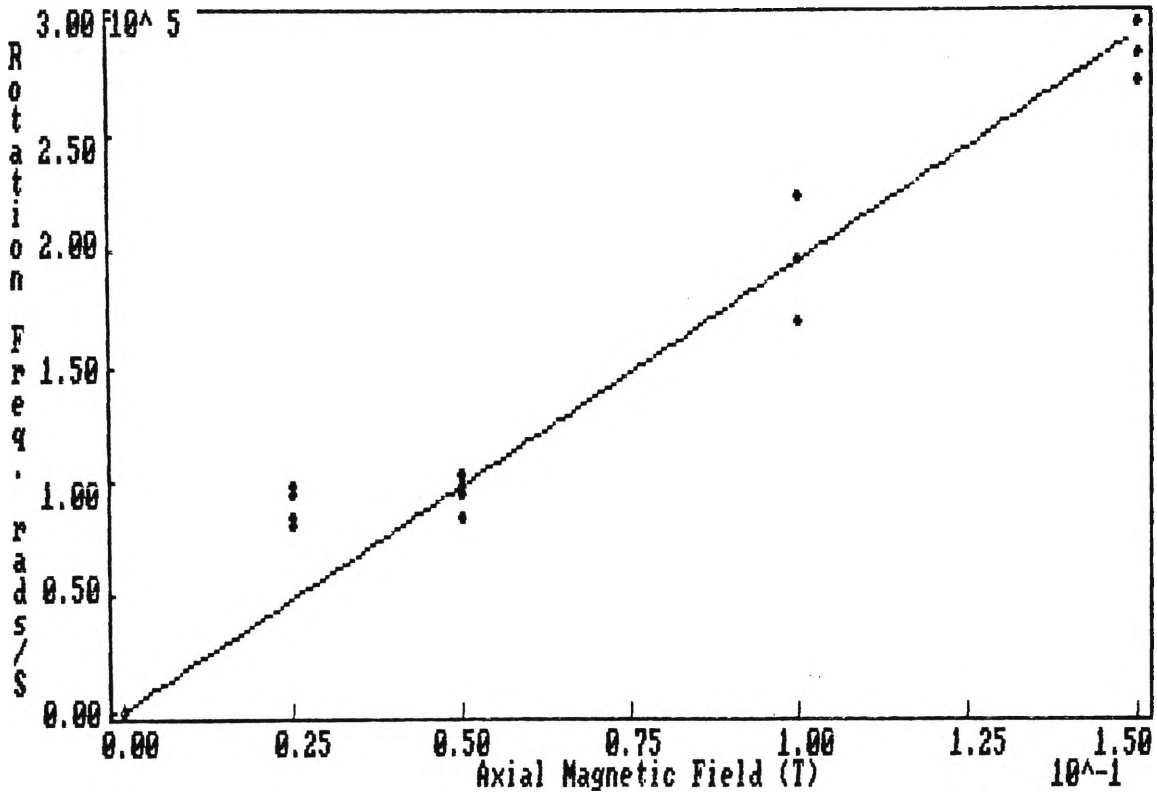

Fig. 6.2.4 Rotation frequency for the H.V. system V_C = 4 kV

Rigid rotor behaviour of the plasma column was investigated by making probe measurements radially from the axis to the chamber wall. Two probes located at positions 4A and 4B were used. Probe 4A was fixed at a radius of 30 mm. Probe 4B was varied at 10 mm intervals over the radius -20 mm (i.e. 20 mm on the opposite side of the VAC axis) to 80 mm (near the chamber wall). The frequency output of probe 4B was compared to the reference probe 4A for each radial position. In all cases, except r = 0, the rotation frequency component was the same in both traces. The result demonstrated that the plasma column moves about the axis as a solid body. Probe output plots for B_z = 0.05 T and V_C = 100 V are given in

figures 6.2.5 (a) - (f). At r = 0, only a small component of the rotation frequency signal was measured. A lower frequency component was also detected which was probably due to slight movements of the plasma column axis.

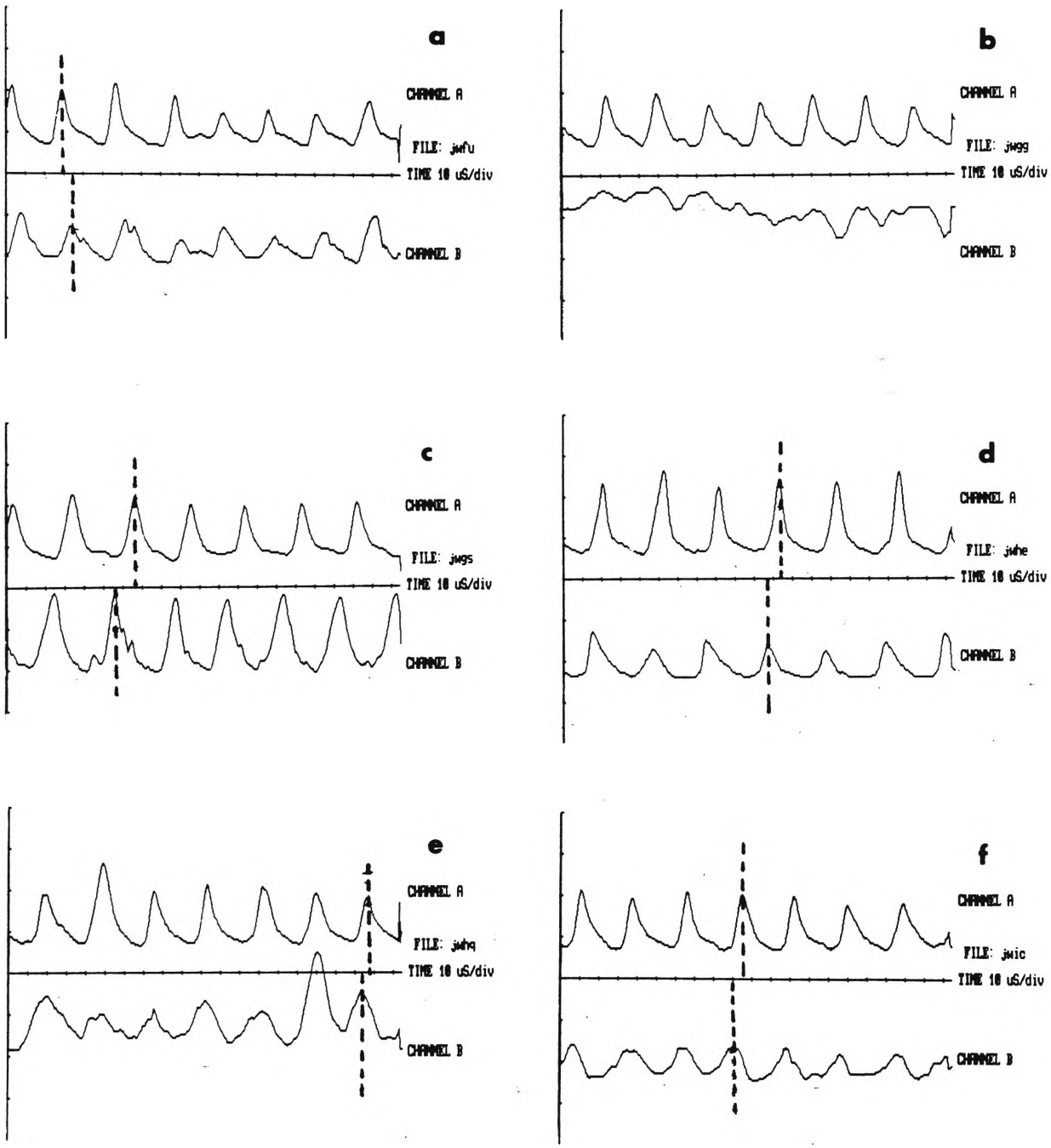

Fig. 6.2.5 Plots of biased Langmuir probe outputs for probe 4A at r = 30 mm and probe 4B at (a) r = -20, (b) r = 0, (c) r = 20, (d) r = 40, (e) r = 60 and (f) r = 80 mm

In figure 6.2.5 (a), the retractable probe 4B output at r = -20 mm lagged the output of the reference probe 4A. In figure 6.2.5 (c) the phase difference between both probes was reversed and probe 4B output led probe 4A. The result was further evidence that the plasma column was moving as a rigid body and that the periodic waveforms detected by the Langmuir probes were related to the plasma rotation. The rotation frequency amplitudes across the plasma radius were also measured using the computer program FFTP (see Appendix 5). Figure 6.2.6 is a plot showing the amplitude variation of the rotation component for various radii. Detected density variations were negligible near the axis and rose to a maximum at 20 mm < r < 60 mm. For r > 60 mm, there was a steady decline to the final measurement near the chamber wall.

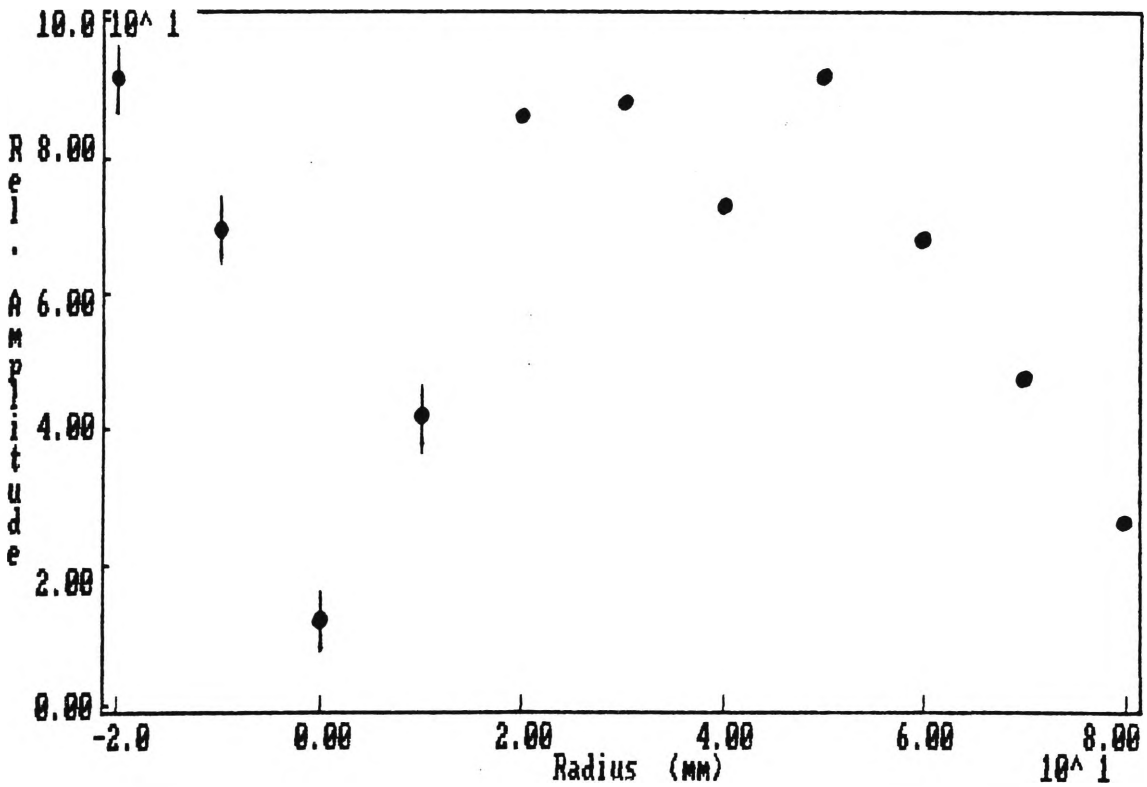

Fig. 6.2.6 Relative amplitude of the rotational frequency component vs. radius

6.3 Axial Drift Velocity

Two methods were adopted to estimate the plasma axial drift velocity:

i) Measurement of the angular displacement of deposited material on a collector plate after the plasma has passed through a narrow slot.

ii) Measurement of the time taken for the plasma front to pass two axially separated Langmuir probes.

The first experiment used the same slotted end plate and collector already described in section 6.1. Multiple discharges from the PFN, under constant experimental conditions, were initiated in order to deposit sufficient material on the collector for subsequent inspection. The distance between the slotted plate and the collector was set at z = 40 mm. An average plasma column rotation frequency of 1.5×10^5 rad/S (24 kHz) was estimated from figure 6.2.2 for B_z = 0.15 T and a capacitor charge voltage V_c = 380 V. A photocopy of the collector plate deposit after 180 discharges is shown in figure 6.3.1.

Inspection of the collector showed a deposit which diminished in thickness from the vertical axis to a maximum angle of $\phi \approx 52°$. An average value of 26° was used to calculate the axial drift velocity from equation 4.5.4. This gave an average axial drift velocity $v_z = 1.3 \times 10^4$ m/s. The spread in the deposit from ϕ = 0 to 52° indicates that the plasma axial velocity was not singular. Geva [48] found that

the rotation period varied in inverse proportion to the instantaneous arc current. Some of the spread in the results presented here may be due to the comparatively slow rise and decay times of the PFN current pulse.

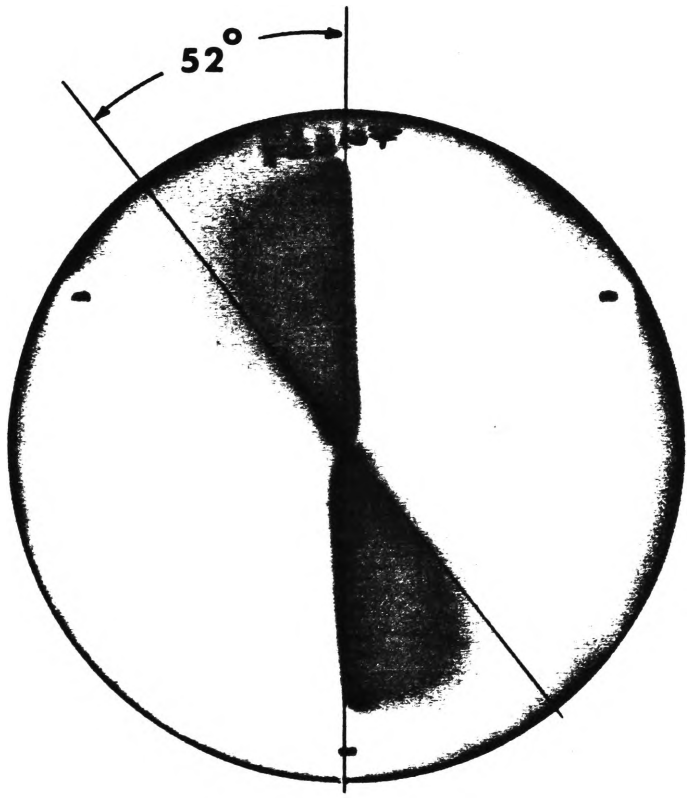

Fig. 6.3.1 Photocopy of the slotted plate collector deposit (reduced 70% full size)

In the second experiment, floating Langmuir probes were inserted at positions at 2B and 4A. Axial separation distance was 450 mm and both probes were inserted to a radius of r = 20 mm. Accurate measurements of the time taken for the plasma column front to pass two biased probes necessitated the use of the H.V. discharge system. The fast (3 μS) current risetime produced a plasma with a well defined plasma front. Data acquisition was triggered by the rise in arc current and the system was set to capture events preceding the trigger by 50 μS. Figure 6.3.2 shows the unfiltered outputs of both probes.

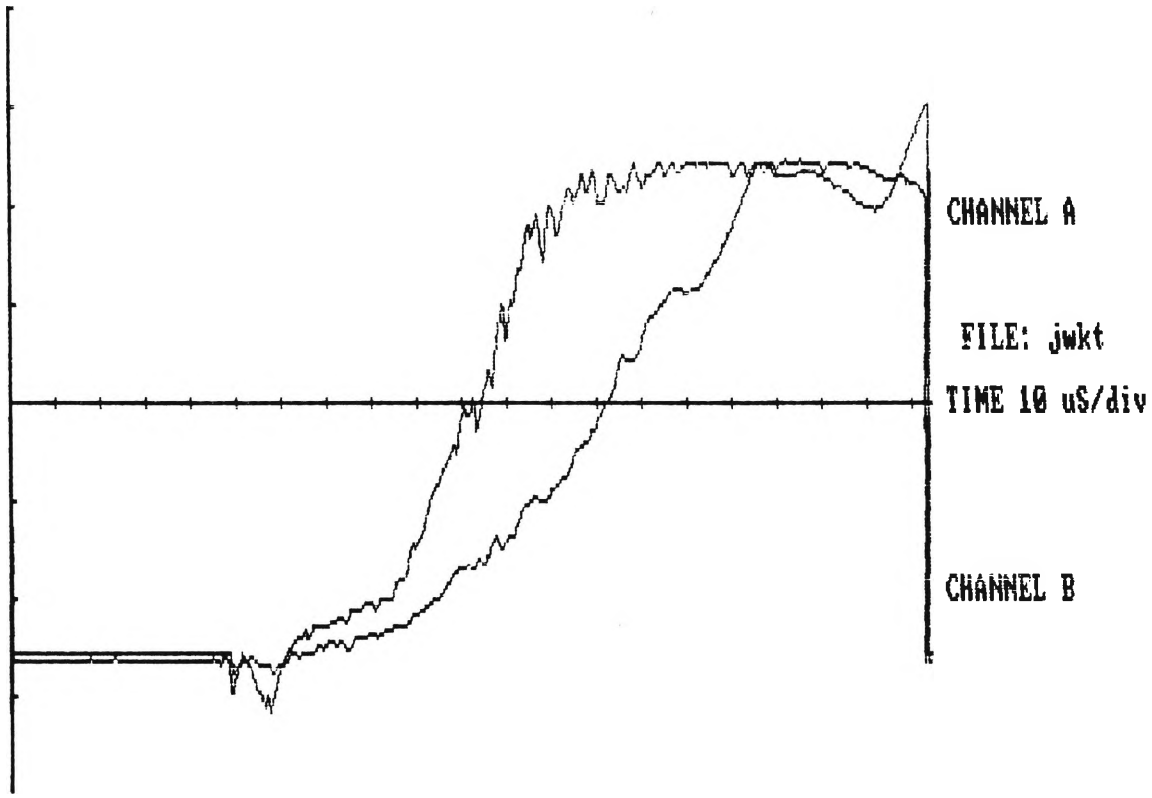

Fig 6.3.2 Output plots of probes at 2B and 4A for V_C = 3 kV and B_Z = 0.05 T

The axial drift velocity, v_z was calculated by measurement of the time difference between the the arrival of plasma at 2B and 4A using the computer program MPLOT.

$$v_z = \frac{\text{probe separation distance}}{\text{time difference}} \approx \frac{0.45 \text{ m}}{24.9 \text{ } \mu\text{S}} = 1.8 \times 10^4 \text{ m/S}$$

The effect of the applied magnetic field on the axial velocity was investigated. Figure 6.3.3 shows the relationship between B_Z and v_z for different initial discharge voltages. For B_Z = 0 T, the measured axial velocity in all cases approached 1.5×10^4 m/S. This is close to values reported by other workers [48,74,92,96].

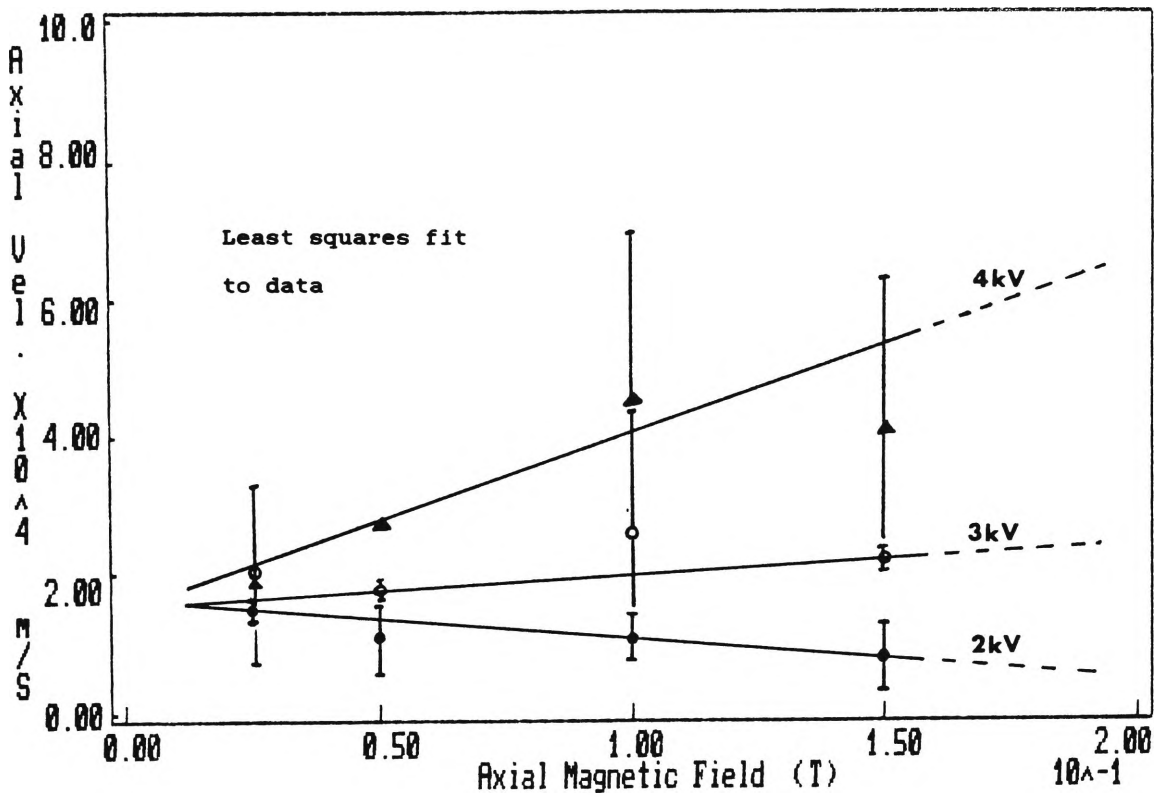

Fig. 6.3.3 Axial drift velocity vs. axial magnetic field for V_c = 2, 3 and 4 kV

6.4 Confinement

If the plasma current density is assumed to be axially symmetric, then equation (2.2.5) can be applied to find the plasma current density in cylindrical coordinates r,θ,z. For cylindric symmetry, d/dθ = d/dz = 0 and equation (2.2.5) can be reduced to the following set of equations:

$$J_r = 0 \qquad (6.4.1)$$

$$J_\theta = - \frac{1}{\mu_o} \frac{dB_z}{dr} \qquad (6.4.2)$$

$$J_z = \frac{1}{\mu_o r} \frac{d}{dr} \left[r\, B_\theta \right] \qquad (6.4.3)$$

The relative magnitude of the plasma current density was measured using magnetic probes of the type described in section 4.6.1. Radial measurements of B_θ, due to the plasma, were made for applied axial magnetic fields (B_z) of 0.025, 0.05 and 0.1 T.

Because the magnetic probe sensing coil delivered a voltage proportional to $dB_\theta(t)/dt$, the output required integration to give $B_\theta(t)$. Figure 6.4.1 shows the typical integrated probe output. Calibration of the probe and integrator was considered unnecessary because only relative values of plasma confinement and density were required.

Peak values of $B_\theta(t)$ were measured for each discharge. The relationship established by equation (6.4.3) was used to calculate the plasma current density. Figure 6.4.2 is a plot of radial current density $J_z(r)$ for a range of B_z.

Distortion of the plasma column, caused by the introduction of the magnetic probe, was neglected because the experiment was principally concerned with the measurement of a relative value of current density.

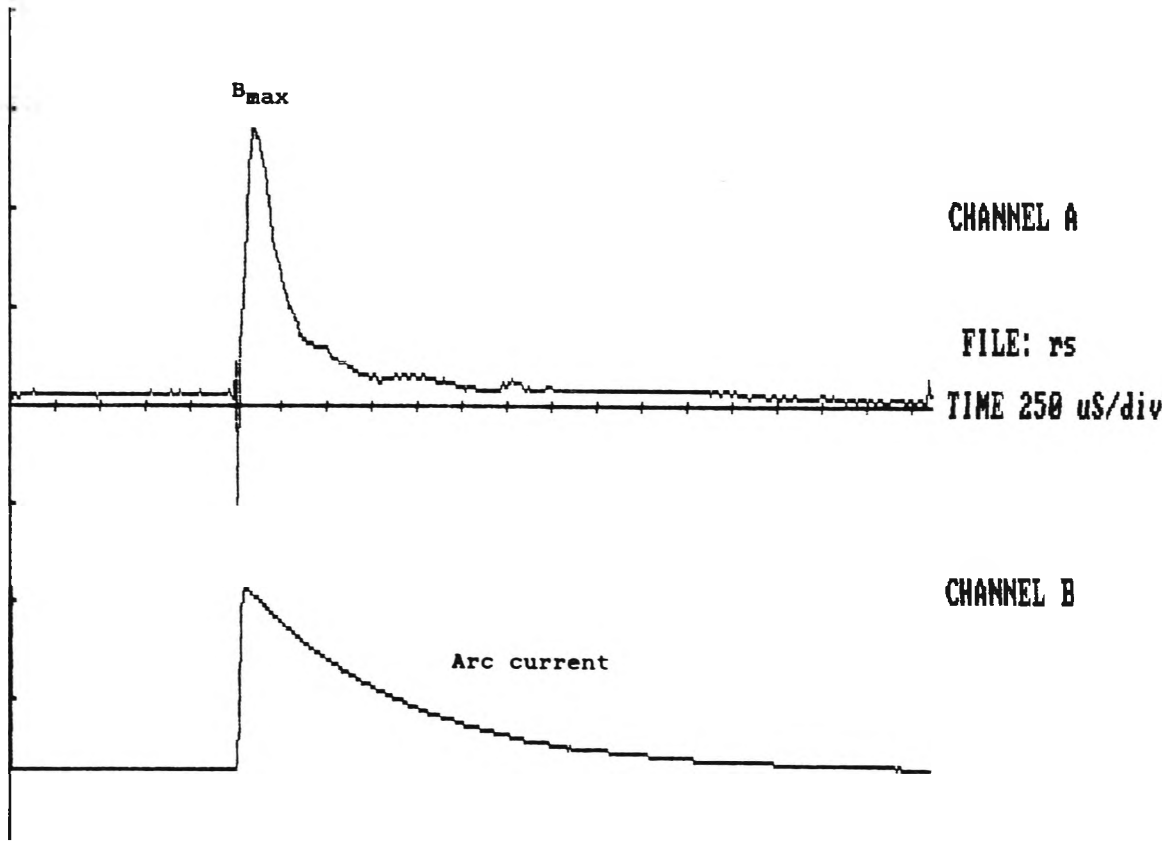

Fig. 6.4.1 Upper trace: integrated magnetic probe output
Lower trace: arc current

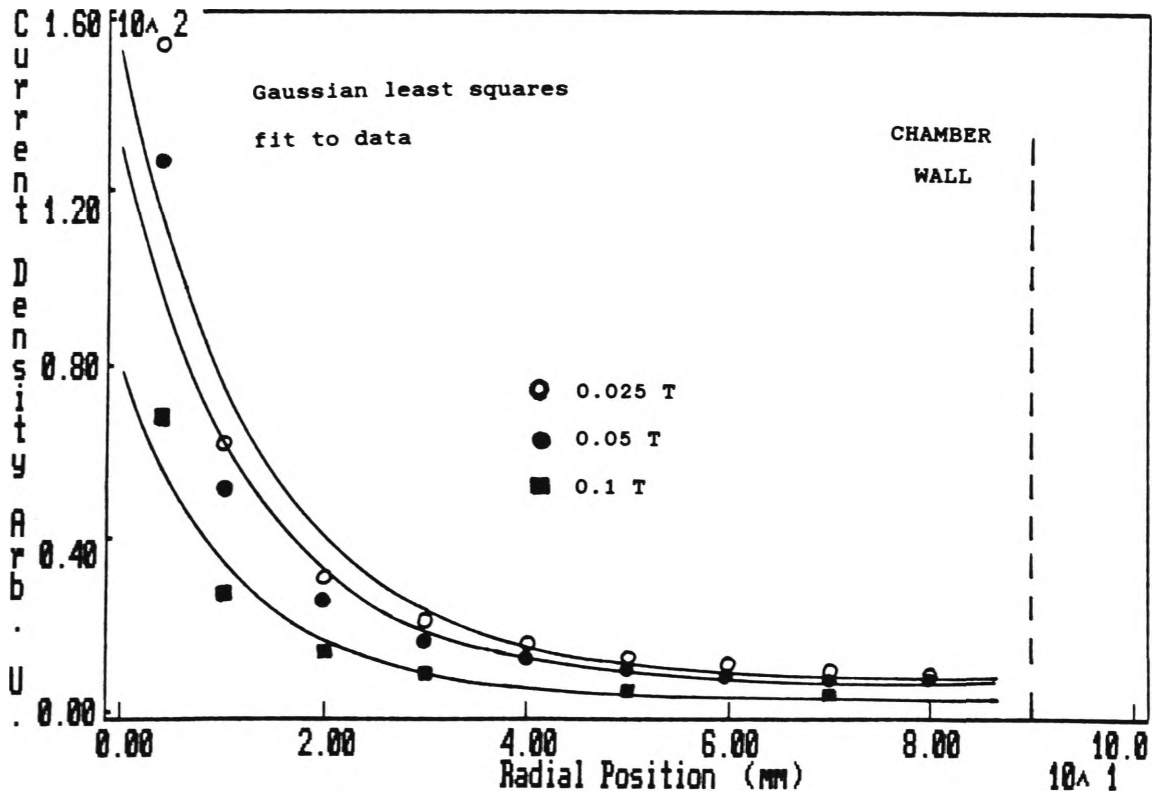

Fig. 6.4.2 Plot of current density J_r for B_z = 0.025, 0.05 and 0.1 T

The effect of the applied magnetic field on the plasma current density can be observed in the above figure. The radius of the axial current path decreased for an increase of the applied magnetic field. The data also implied that the axial current decreased for an increase in B_z. The current density for each curve plotted followed the same functional form. In figure 6.4.3, the relative amplitude of each curve was normalised to the plot for B_z = 0.025 T. Plasma current density was found to decrease for increasing B_z over the range of B_z investigated.

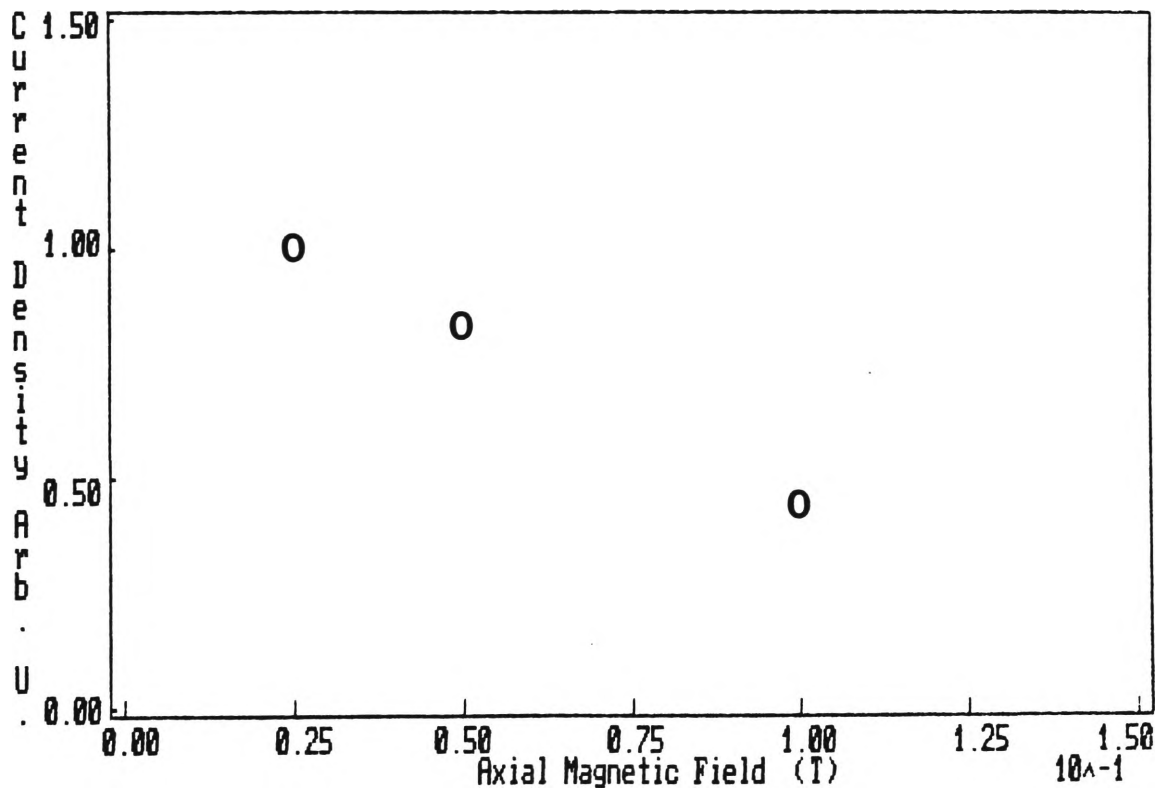

Fig. 6.4.3 Relationship between current density and the applied axial magnetic field.

6.5 Density

Plasma particle density is related to the current density by the following general expression:

$$J = \sum_k n_k q_k v_k \qquad (6.5.1)$$

For simplicity, the plasma is assumed to have a single charge state $< Z > = 3$ [43]. If the plasma column is assumed to be quasineutral, then $n_e = 3n_i$. Equation 6.5.1 may be simplified:

$$J = n_e q v_e \qquad (v_e >> v_i) \qquad (6.5.2)$$

From equation 6.5.2, it is possible to infer the plasma particle density from the plots of radial current density shown in figure 6.4.2.

Biased Langmuir probes were also used to measure the radial ion density profile. Figure 6.5.1 is a plot from the biased probe output at 30 mm. The initial discharge voltage was 300 V and the applied axial field was set at 0.05 T.

For this series of experiments, probe measurements were made from -20 mm to 80 mm at 10 mm intervals for V_c = 100, 200 and 300 V. The probe output was recorded for each discharge and the root mean square (RMS) level was calculated. Figure 6.5.2 is a plot showing the relative radial ion density profile for different levels of initial discharge voltage. A Gaussian least squares fit to the data has been used to test the theoretical distribution predicted by equation 2.4.9. Ion density increases for increased discharge voltage (arc current).

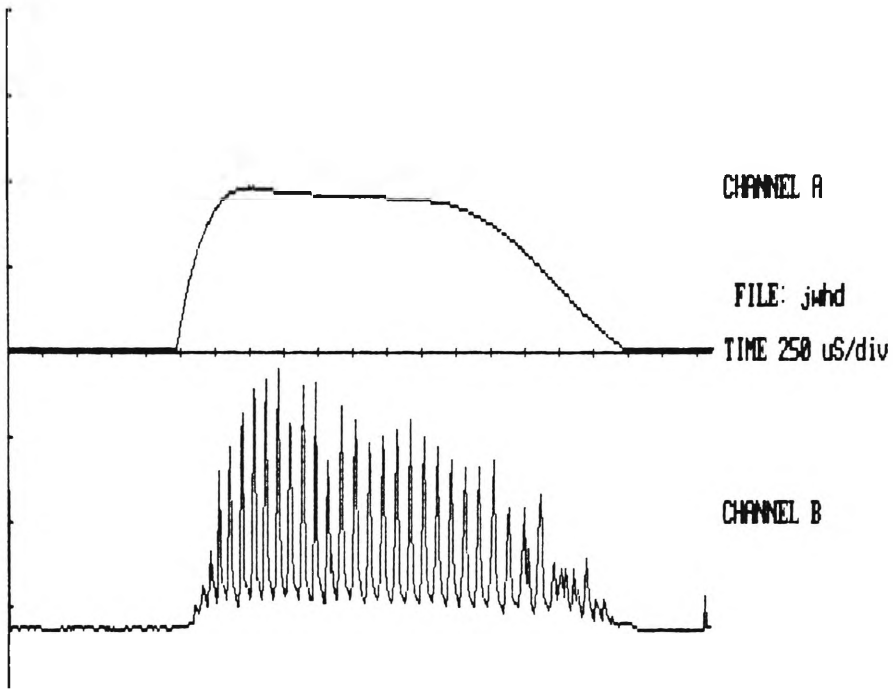

Fig. 6.5.1 Biased Langmuir probe output at r = 30 mm, V_C = 300 V and B_Z = 0.05 T
Upper trace: 2 kA/div
Lower trace: arbitrary units

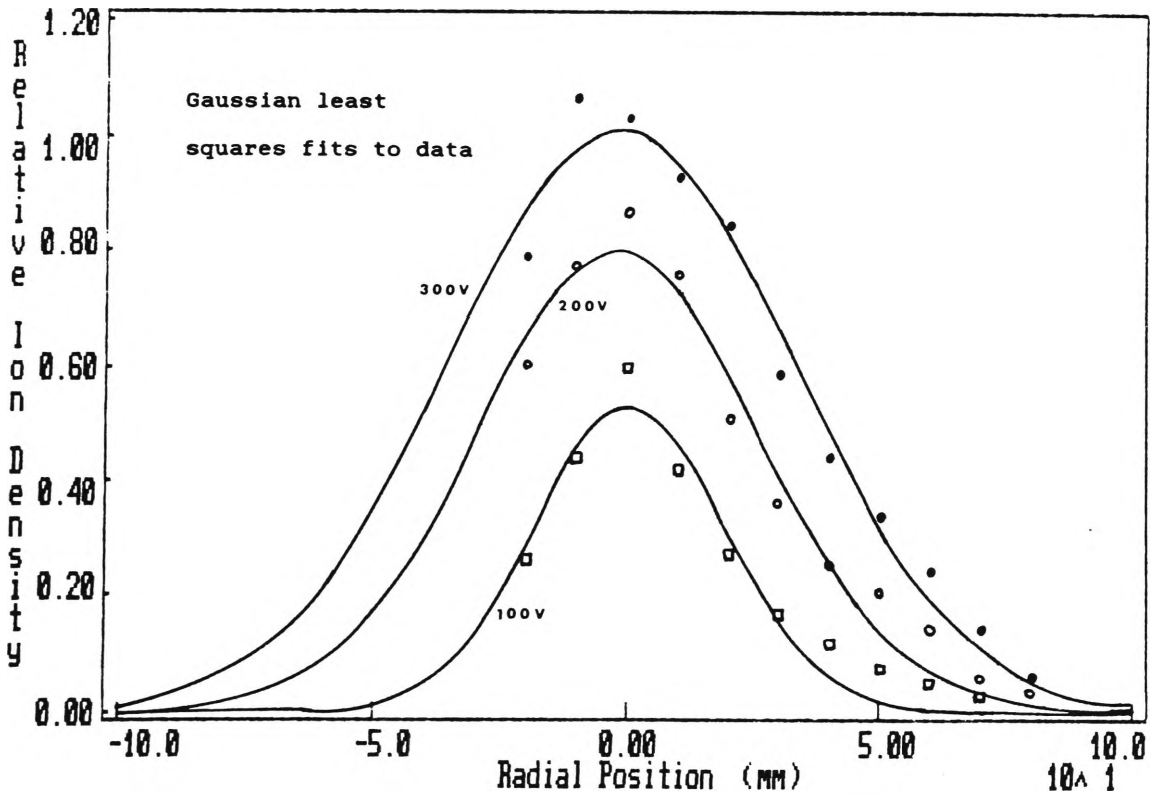

Fig. 6.5.2 Relative ion density profile for V_C = 100, 200 and 300 V

Relative plasma density as a function of the applied axial field for V_c = 100, 200, 300 and 390 V is presented in figure 6.5.3. The plots show that plasma density increases with initial discharge voltage due to the increase in arc current. Additionally, the applied magnetic field also increases the density via confinement effects.

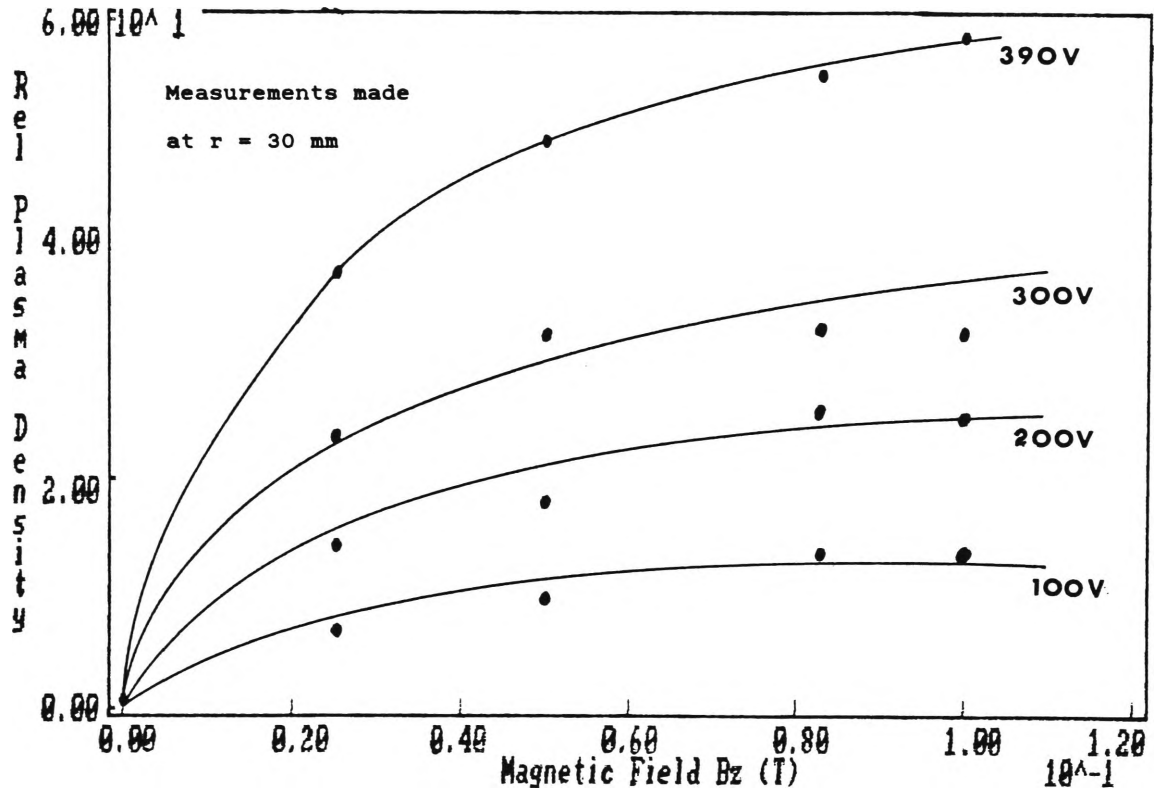

Fig. 6.5.3 Relative plasma density as a function of applied magnetic field for V_c = 100, 200, 300 and 390 V

Unbiased (floating) Langmuir probes were used to measure the radial plasma potential. The typical output of a floating probe is plotted in figure 6.5.3 for the same experimental conditions as figure 6.5.1. A plot of the radial plasma potential for V_c = 100, 200 and 300 V is shown in figure 6.5.5. The plot includes a quadratic least squares fit to the data for the plasma region 40 mm either side of the axis.

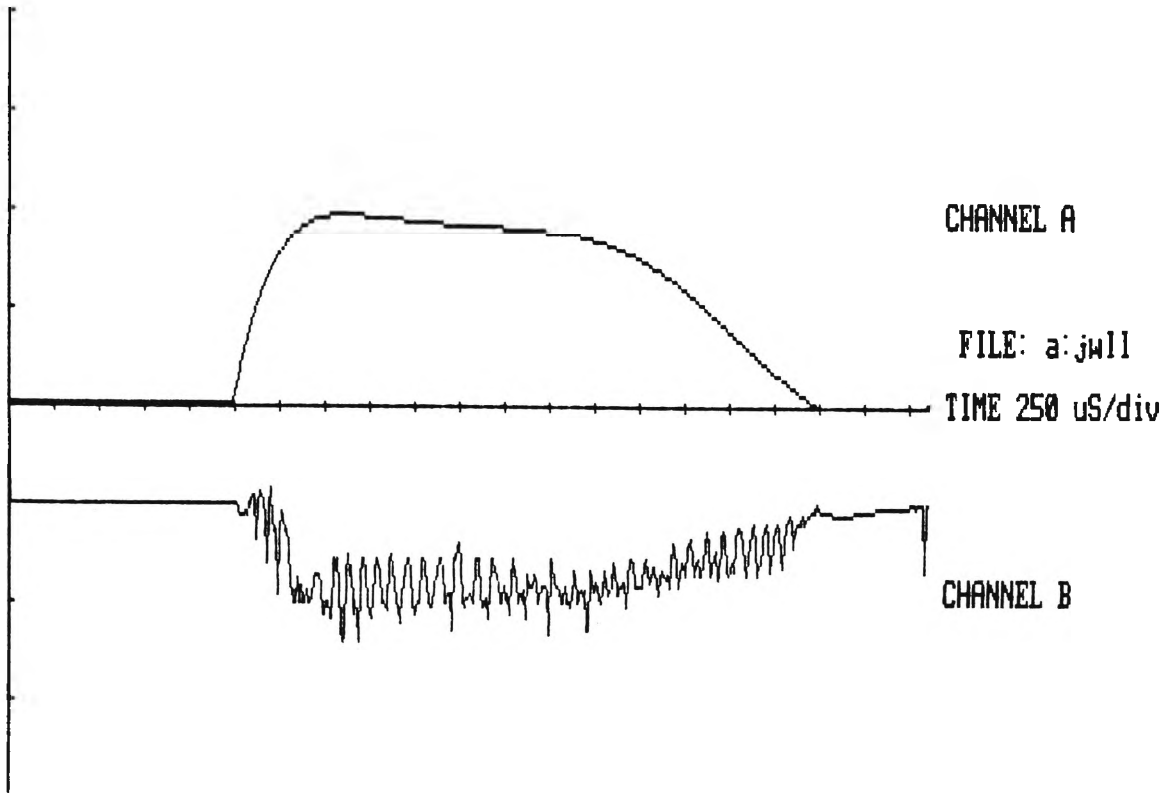

Fig. 6.5.4 Floating Langmuir probe output at r = 30 mm, V_C = 300 V and B_Z = 0.05 T.
Upper trace: 2 kA/div
Lower trace: 2.5 V/div

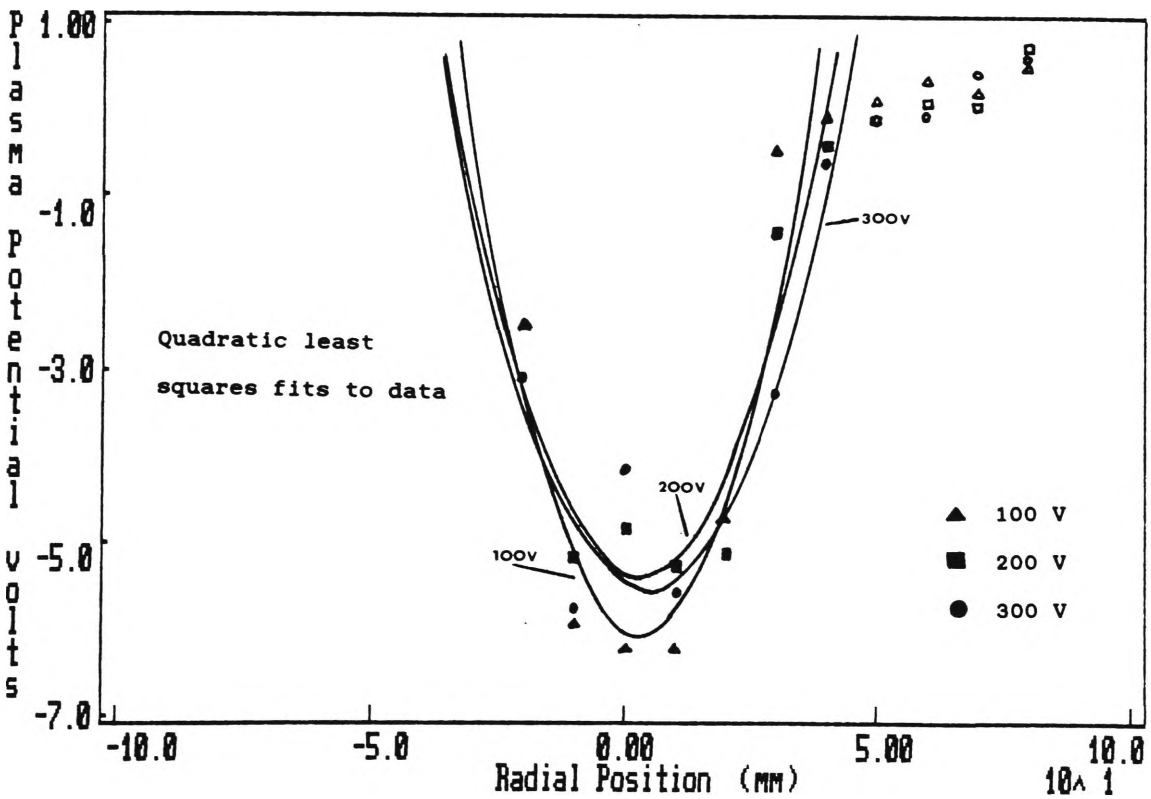

Fig. 6.5.5 Measured plasma potential for V_C = 100, 200 and 300 V at B_Z = 0.05 T

For r > 40 mm, the plasma potential appeared to rise at a much slower rate. Prasad [58] attributed this effect to the ion rich sheath, which surrounds the plasma column, distorting the potential.

Measured values of rotational frequency were compared to those predicted by equation 2.2.19. Values were calculated for $\frac{1}{r}\frac{d\Phi}{dr}$ and $\frac{1}{r}\frac{d(\ln(n_i))}{dr}$ from the least squares approximations shown in figures 6.5.2 and 6.5.5. Calculation was made by taking the gradient at a radius on the plasma potential curve which represented the half maximum (minus) peak voltage. The same radius was used for calculation of the ion density distribution gradient. Table 6.5.1 compares the predicted and measured values of rotation frequency for initial discharge voltages (100, 200 and 300 V) and plasma charge state (<Z>=3) at an applied axial magnetic field of 0.05 T. A plasma column ion temperature T_i of 1 eV was assumed, for a copper plasma away from the arc region, from other vacuum arc [72,101] and VAC experiments [45,48,55,61]. Reported electron and ion temperatures made in the arc region are usually higher [74,77,86,92].

The lower and upper rotation frequencies, respectively w_1 and w_2, are the solutions to equation (2.2.19). The predicted and measured values for rotation frequency were found to be of the same order. Although the measured values are slightly lower than predictions, they are in reasonable agreement with similar results by Geva [48,61] for copper plasmas in a VAC.

TABLE 6.5.1

Comparison Between Calculated and Measured Rotational Frequency for V_c = 100, 200 and 300 V

V_c	B_z	$\langle Z_i \rangle$	$\frac{1}{r}\frac{d\Phi}{dr}$	$\frac{1}{r}\frac{d(\ln(n_i))}{dr}$	Rotation Frequency			
					w_1	w_2	Ω_{ci}	$w_{measured}$
V	T		V/m²	/m²	rad/S	rad/S	rad/S	rad/S
			x10⁴	x10³	x10⁵	x10⁵	x10⁵	x10⁵
100	0.05	3	1.26	-2.90	1.55	-3.97	2.42	0.99 ± 0.11
200	0.05	3	0.91	-1.20	1.22	-3.64	2.42	0.75 ± 0.12
300	0.05	3	0.91	-0.82	1.21	-3.63	2.42	0.68 ± 0.07

Investigation of the recorded Langmuir probe data provided no conclusive evidence of the existence of the higher frequency w_2. High frequency components were identified in a number of plots. However, these were mostly attributed to harmonics of the plasma rotation fundamental frequency or effects related to the arc behaviour.

Bittencourt [55] calculated in a parametric study of VAC behaviour, that rotational speed decreased with increasing B_z. A proviso was included, stressing that this inverse dependence was only valid for constant plasma potential $\triangle\Phi$. Experimentally observed values of $\triangle\Phi$ depend on B and other plasma characteristics. Prasad [58] investigated this relationship for carbon plasmas and presented data from which the following conclusions have been made:

i) $\frac{1}{r}\frac{d\Phi}{dr}$ was proportional to B_z^2

ii) $\frac{1}{r}\frac{d(\ln(n_i))}{dr}$ was proportional to B_z.

(over the range $0.07\ T < B_z < 0.21\ T$)

To construct the model, it was assumed that the copper plasma in the ANSTO VAC behaved similarly to Prasad's carbon plasma. Equation (2.2.19) was modified and expressed in terms of B_z.

$$w_i = \Omega_i \left[-\tfrac{1}{2} \pm \tfrac{1}{2} \sqrt{1 + \frac{4}{\Omega_i B_z}\left[f_a(B_z) + \frac{kT_i}{Z_i e r} f_b(B_z) \right]} \right] \qquad (6.5.3)$$

The dependence of w_1 on B_z could then be calculated (for $\langle Z \rangle = 3$) using extrapolations from the experimental values given in Table 6.5.1. i.e.

$$\text{where } f_a(B_z) = \frac{\left[\frac{1}{r}\frac{d\Phi}{dr} \right]_V}{(0.05)^2} \times B_z^2$$

$$f_b(B_z) = \frac{\left[\frac{1}{r}\frac{d(\ln(n_i))}{dr} \right]_V}{0.05} \times B_z$$

$$\text{and} \qquad \Omega_i = \frac{Z_i e B_z}{m_i}$$

Figure 6.5.6 illustrates the dependence of w_1 on B_z calculated by equation 6.5.3 and based on measurements for V_c = 100 and 300 V. Values of rotational speed measured directly by Langmuir probes are also included for comparison.

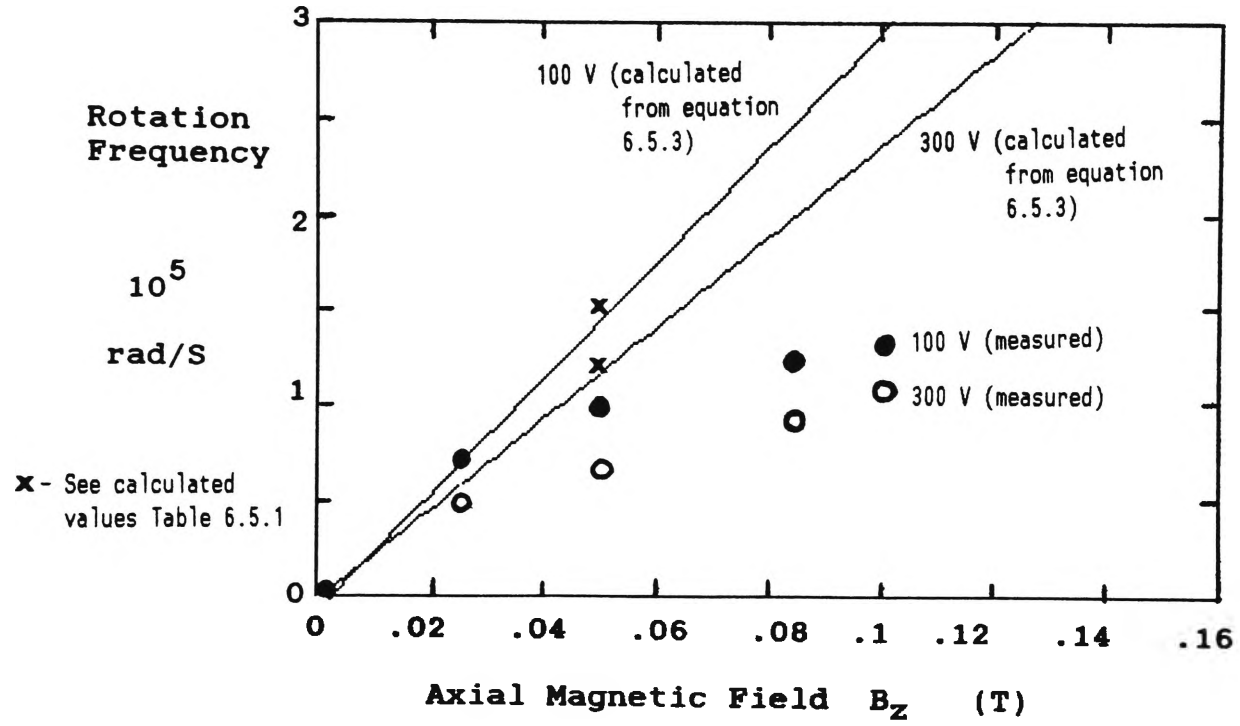

Fig 6.5.6 Comparison between the theoretical relationship between w_1 and B_z predicted by equation 6.5.3 and measured values for V_c = 100 and 300 V.

Both measured and calculated values w_1 increased with increasing B_z and were in agreement with other observations [48,53,60]. However, measured values of w_1 were below the predictions based on equation 6.5.3. A better definition based on further experimental research may help to provide a more accurate understanding of the relationship between Φ_r, B_z and w_1.

7. SEPARATION MEASUREMENTS

7.1 Rate of Erosion

Erosion measurements were made for a copper cathode connected to the 5 stage PFN. Prior to installation, a detachable copper target was weighed on an electronic balance to an accuracy of 10^{-4} g . A mean target weight was determined to be 187.7567 ± 0.0002 g.

A perforated stainless steel anode was used for this series of experiments. The hole centre to centre spacings were 4.7 ± 0.2 mm and the hole diameters were 4.1 mm. The anode steel represented a 30 % coverage of the transmission area and the anode to cathode separation distance was 60 mm.

Discharge conditions were maintained at V_c = 380 volts for 160 shots at ~23 second intervals initiated by the laser. The axial magnetic field was constant at B_z = 0.125 T. The target was removed from the VAC and re-weighed. The new mass was 187.6551 ± 0.0002 g which gave a mean mass difference of 0.1016 g or an average mass loss of 635 µg/shot.

The total electrical charge (Q_{tot}) passing through the cathode per shot was found by integrating the current pulse over the pulse duration. For the conditions described above, $Q_{tot} \approx$ 13.3 Coulombs which gave an erosion rate of approximately 48 µg/C. Hirshfield [94] measured an erosion rate of 62 µg/C for a 6 mm copper cathode with a 45° face with no applied magnetic field (see Table 3.0.1).

Ion and electron densities per shot were estimated from

the erosion data and axial probe measurements. Erosion of 635 μg yielded 5.9 X 10^{18} copper atoms. For a current pulse duration of 2.5 ms, the rate of copper atom production was 2.3 X 10^{21} atoms/s. The ion axial drift velocity was estimated in section 6.3 to be approximately 1.5 X 10^{4} m/s. A deposition radius of 40 mm was assumed, based on the experimental results reported in section 6.5. This gave a plasma column cross section of 5.0 X 10^{-3} m^2. Ion density was calculated by the following method:

$$n_i = \frac{\text{ion flux}}{\text{axial velocity}} = \frac{2.3 \text{ X } 10^{21}}{5.0 \text{ X } 10^{-3} \text{ X } 1.5 \text{ X } 10^{4}}$$

$$= 3.1 \text{ X } 10^{19} \text{ m}^{-3}$$

$$\approx 10^{19} \text{ m}^{-3}$$

For simplicity, an average ion charge state of <Z> = 3 was assumed, based on experiments by Geva [48]. Electron density was calculated with the further assumption that the plasma achieved overall charge quasineutrality [45].

$$n_e = 3 \text{ X } 3.1 \text{ X } 10^{19} = 9.3 \text{ X } 10^{19} \text{ m}^{-3}$$

$$\approx 10^{20} \text{ m}^{-3}$$

Values for n_i and n_e are similar to results reported by other VAC workers and summarised in Table 1.0.1.

The radial deposition density was measured in another experiment where samples were collected by the arrangement described in section 4.5.2. Constant V_c = 380 V and

B_z = 0.125 T were maintained for 170 shots. Plasma deposits at various radii were subsequently analysed by the PIXE technique described in section 4.6.5. The results of the analysis are shown in figure 7.1.1. A Gaussian least squares fit to the data is also included. The curve was generated with the assumption that deposition was symmetric about the VAC axis.

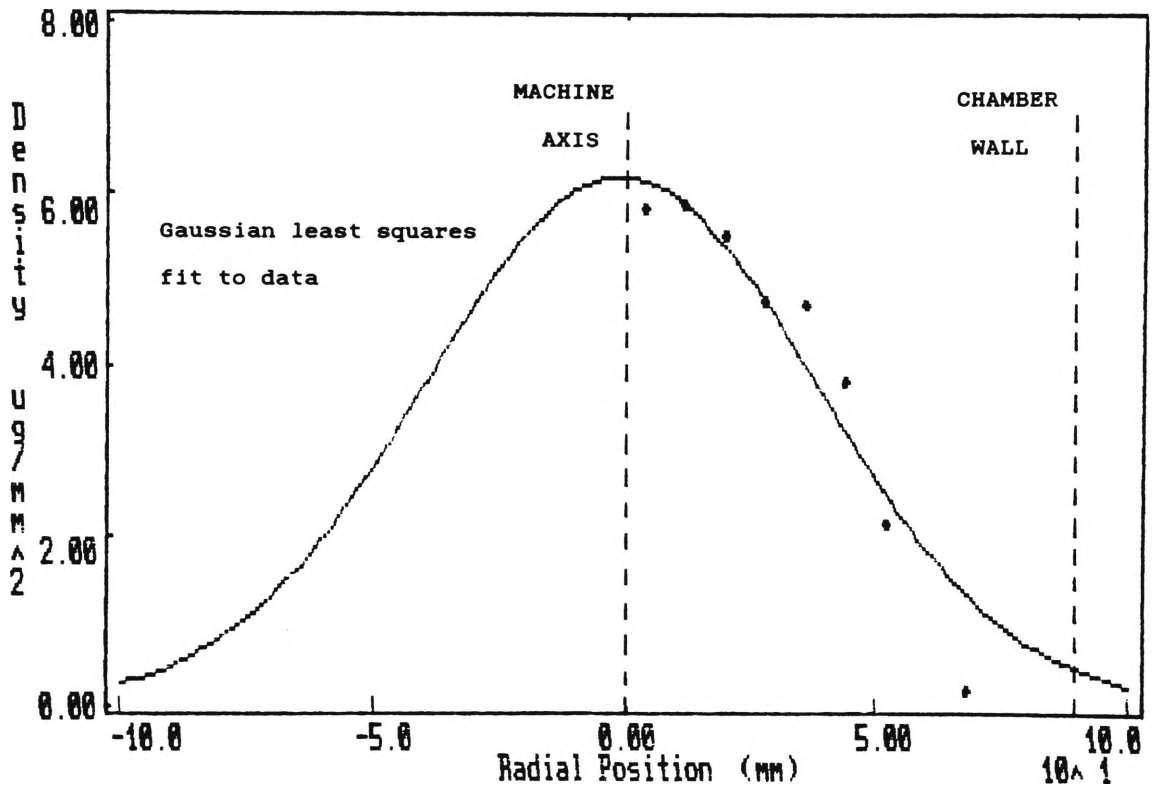

Fig. 7.1.1 Deposition density vs. radial position for a copper plasma. V_c = 380 V and B_z = 0.125 T

The collected mass was estimated from the resultant Gaussian distribution shown above. The collector was assumed to be a circular disk with a radius of 80 mm.

$$\text{Total collected mass} = 2\pi a \int_0^{80} e^{-b(r-c)^2} \, r \, dr = 0.051 \text{ g}$$

where $a = 6.22$, $b = 3.29 \times 10^{-4}$ and $c = -8.33 \times 10^{-1}$

For 170 shots, a cathode erosion of 0.108 g was calculated. The cathode-collector transmission efficiency was defined by the following:

$$\epsilon = \frac{\text{collected mass}}{\text{eroded mass}} \times 100\ \% \qquad (7.1.1)$$

$$= \frac{0.051}{0.108} \times 100\ \% \approx 47\%$$

Mass losses between the cathode and collector were attributed to the following:

i) plasma deposition on the anode may account for up to 30 % of the eroded cathode mass (0.032 g)

ii) production of neutral droplets which expand away from the cathode, are unconfined by the applied magnetic field and are deposited on the chamber walls

iii) electron-ion collisions lead to a gradual diffusion across the magnetic field lines.

Items ii) and iii) represented a total of 0.025 g or approximately 11 µg/C.

For an arc voltage of 193 V, the total electrical energy required to erode one atom of copper was 272 eV. The energy

required to deposit one copper atom on the collector was, therefore, 578 eV.

7.2 Analysis of Plasma Deposits

Separation experiments using the techniques described in section 4.7.5 were conducted for brass (66% Cu : 34% Zn) and copper cathodes. Table 7.2.1 are the results from a PIXE analysis of the collector samples.

Table 7.2.1

Results from PIXE Analysis of Copper/Zinc Deposition Samples

Radius mm	Cu Fraction µg/mm²	Zn Fraction µg/mm²	Total Density µg/mm²
0	1.518	1.329	2.847
8	1.503	1.325	2.828
16	1.611	1.375	2.986
24	1.752	1.464	3.216
32	1.305	1.070	2.375
44	0.889	0.716	1.605
56	0.508	0.430	0.938
68	0.117	0.118	0.235

One unexpected result of the analysis was the change in the deposition ratios for copper and zinc (66%:34% to 52%:48%) along the VAC centre line where no separation should be measured. This point is discussed further in section 7.3.

Figure 7.2.1 is a plot of the copper and zinc fraction distributions. Total deposition density (copper plus zinc) is plotted in figure 7.2.2. A Gaussian least squares fit to each data set has been included.

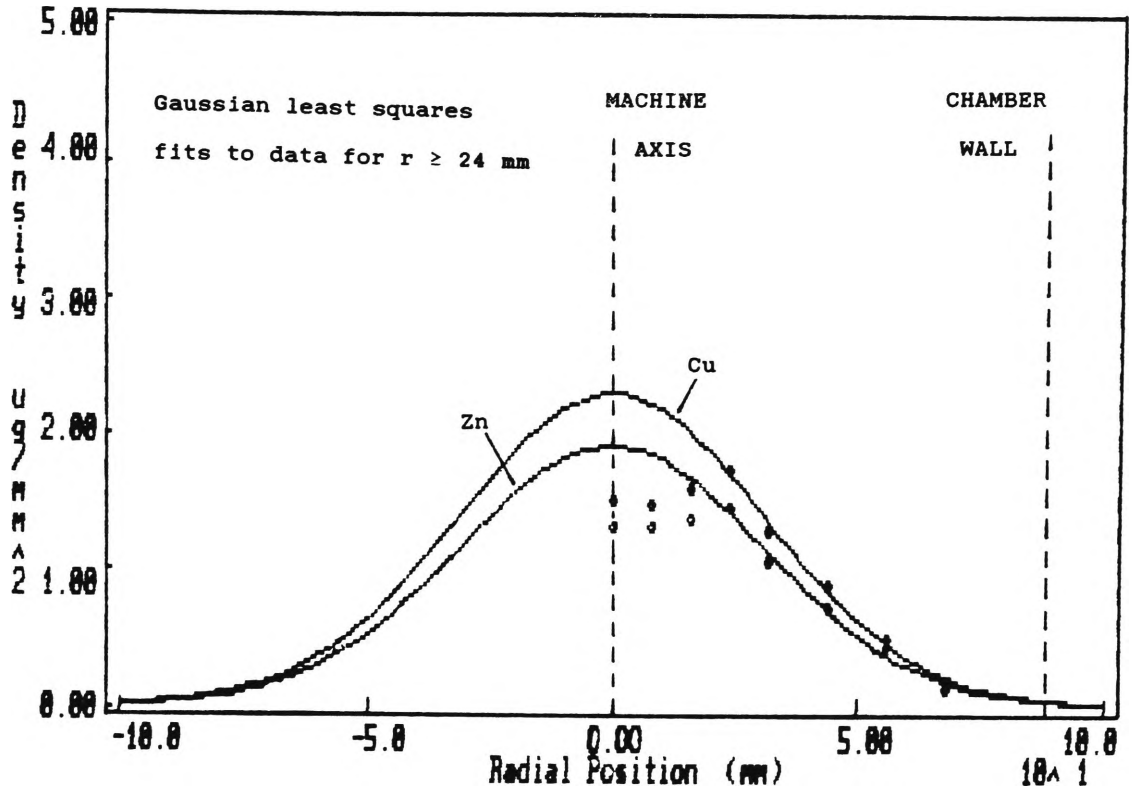

Fig. 7.2.1 Deposition densities for copper and zinc vs. radial position for a copper/zinc plasma V_C = 380 V, B_Z = 0.125T

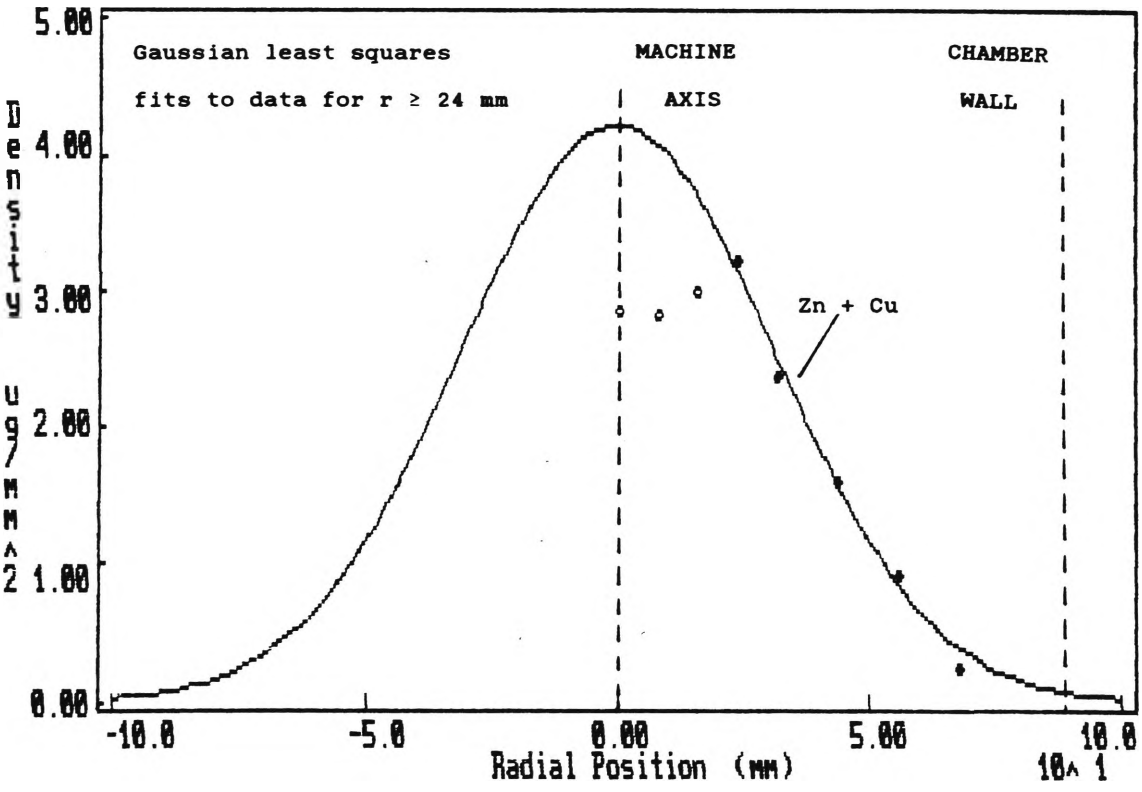

Fig. 7.2.2 Total deposition density for copper plus zinc vs. radial position for a copper/zinc plasma V_C = 380 V, B_Z = 0.125T

The following assumptions were used to generate the least squares fit.

i) data over the radius r = 0 to 24 mm was neglected

ii) the deposit was radially symmetric about the VAC axis.

For r < 24 mm, the measured deposition density curved slightly downward to the centre line. A possible explanation for this result, given that a Gaussian distribution was measured for the radial ion density (see section 6.5), was that a "crater" of r ≈ 24 mm had formed around the deposition centre. Although the deposition mechanism for the copper-zinc alloy is not yet fully understood, some possible explanations are proffered based on other vacuum deposition studies [117-118].

i) Rapid cooling of the deposited plasma after striking the collector surface may have created voids and crystalographic dislocations. Further bombardment by ions (measured velocities ≈ 10^4 m/S on the centre line) dislodged atoms already deposited.

ii) The thermal expansion differences between copper (16.6 x 10^{-6} $°K^{-1}$) and zinc (33 x 10^{-6} $°K^{-1}$) and the aluminium collector substrate (23 x 10^{-6} $°K^{-1}$) exacerbated the stresses in the deposit interface, which reduced its adhesion. The deposit was thus made more susceptible to ion etching from subsequent plasma bursts.

The calculated Gaussian curves were a close fit to the data beyond a radius of ~24 mm. Total measured deposition and

the deposition based on the full Gaussian curve were calculated.

$$\text{Total measured deposition} = \pi(24)^2 a\, e^{-b(24-c)^2} + 2\pi a \int_{24}^{80} e^{-b(r-c)^2}\, r\, dr$$

$$= .0239 \text{ g}$$

where $a = 4.23$, $b = 5.12 \times 10^{-4}$ and $c = -1.10 \times 10^{-1}$.

For the Gaussian curve, a mass of 0.0249 g was calculated. The "crater" represented less than 5 % of the total deposition.

Measured zinc separation, with respect to copper, was defined by the following expression:

$$\% \text{ Separation} = \left[\frac{\left[\frac{Zn}{Cu} \right]_r}{\left[\frac{Zn}{Cu} \right]_0} - 1 \right] \times 100\ \% \qquad (7.2.1)$$

A plot of measured separation with respect to radial position is presented in figure 7.2.3.

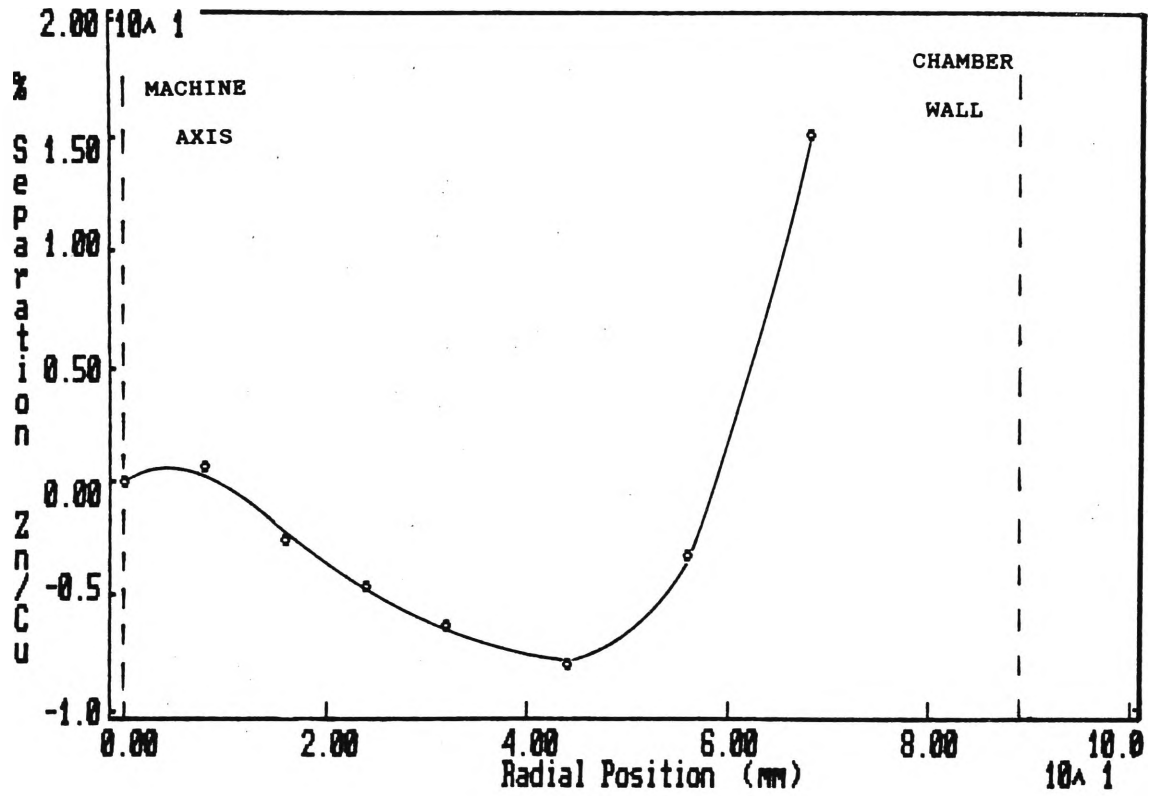

Fig. 7.2.3 Percentage separation of Zn/Cu

The measured zinc fraction, with respect to copper, decreased with radius to a minimum of - 8 % at r = 44 mm. For radii greater than 44 mm, the zinc fraction increased with radius to (the last sample point analysed) 15 % at r = 68 mm.

Copper separation was tested under the same experimental conditions already described for brass. Results from collector sample ICP-MS analysis are shown in figure 7.2.4. The measured copper isotope ^{65}Cu abundance, with respect to ^{63}Cu, increased with radius to a maximum of 1 %.

The results for both copper and copper-zinc separation are discussed in section 7.3. Comparisons are also made with theoretical predictions and equivalent results of other VAC workers.

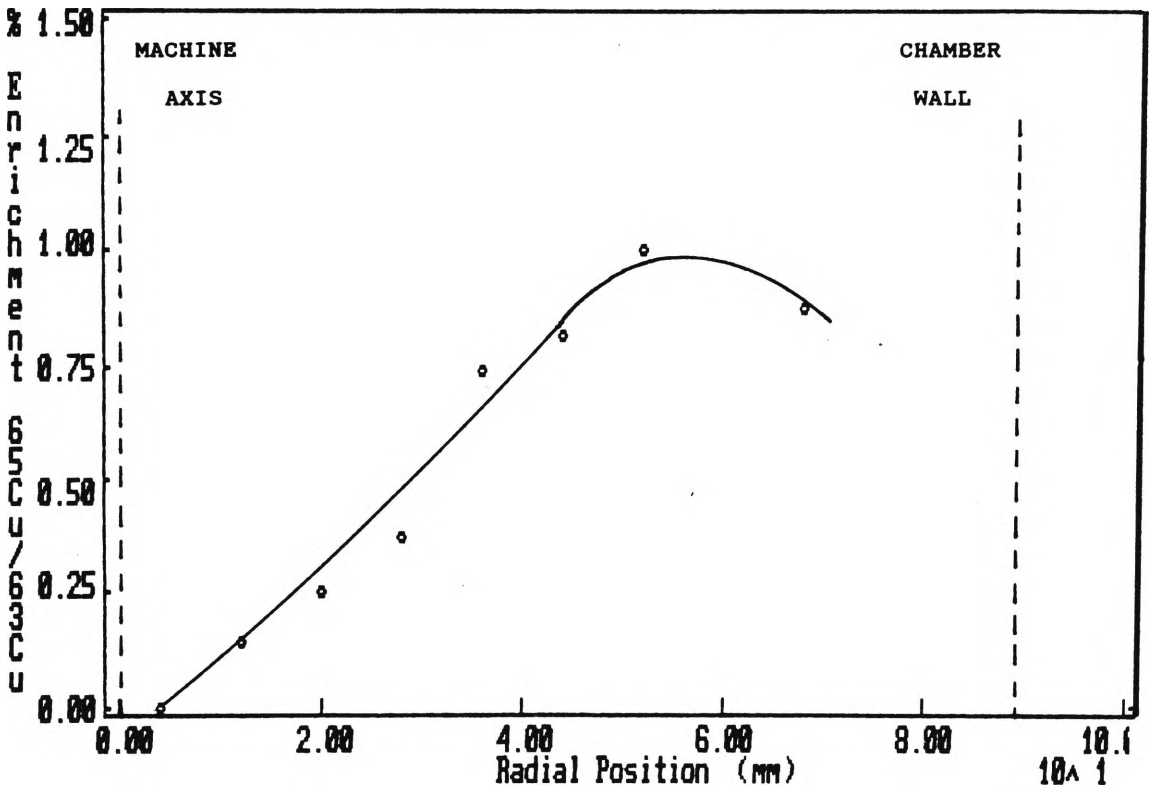

Fig. 7.2.4 Percentage separation of ^{65}Cu / ^{63}Cu

7.3 Discussion

The experimental parameters of applied magnetic field B_z and PFN initial discharge voltage V_c were chosen on the basis of the requirements of high rotational speed (hence greater separation) and high yield. While this thesis has demonstrated separation of both elements and isotopes in the ANSTO VAC, comparisons with theoretical predictions and similar research conducted elsewhere (see Table 1.2.1) reveal poor separation performance. This section is devoted to a discussion of the results of section 7.2 and reasons for the VAC performance at the described experimental conditions.

The physical properties of copper and zinc are compared in Table 7.3.1. Minor differences can be seen in each element's ionisation characteristics. Significant differences are also seen in melting and boiling points.

TABLE 7.3.1

A Comparison of Physical Properties for Copper and Zinc

Element	Melting Point °C	Boiling Point °C	Work Function eV	Atomic Weight	Successive Ionisation Enthalpies					
					I	II	III	IV	V	VI
Copper	1083	2595	4.3	63.55	0.751	1.964	3.558	5.7	8.0	10.5
Zinc	419	906	3.7	65.38	0.912	1.740	3.837	6.0	8.3	11.0

In section 7.2 the PIXE analysis of the deposits indicated that the Cu:Zn ratio had shifted toward zinc for all samples. The energies required to ionise atoms of each element were of the same order. However, it is possible that the zinc fraction, with its lower boiling point, preferentially vaporized from the cathode surface, resulting in a plasma richer in zinc.

Measured copper-zinc separation was compared to the theoretical predictions given by equation (2.5.8) for V_c = 380 V, B_z = 0.125 T and w_i = 1.25 x 10^5 rad/S (measured) and T_i = 10^4 °K (assumed). Average atomic weights of 63.55 a.m.u. and 65.38 a.m.u. were respectively assumed for copper and zinc.

Bittencourt [55] assumed a plasma with a single charge state in his parametric study. The resulting separation followed a quadratic relationship with radius. However, measurements of copper plasmas [47,74] show that they are composed of multiply charged ion species. Measurements of

plasmas which are a mixture of metals also show a range of charge states for each element (and presumably each isotope of each element) Therefore, information regarding the plasma charge state must be included in any theoretical analysis of VAC plasmas. No apparatus was available, for this thesis, to measure copper and zinc ion charge states. Therefore, fractional degrees of ionisation for a copper plasma were assumed from measurements by Geva [47]. These are summarised in Table 7.3.1. Results of studies by Davis and Miller [74] for a lower discharge current are also included which show a lower fractional ionisation degree, due to a lower arc discharge current.

Table 7.3.1

Ion Charge Distribution in Copper Plasmas

Reference	Discharge Current A	Fractional Degree of Ionisation % I	II	III	IV	V	Mean Charge State < Z >
[74]	100	30	54	15	0.4	<0.1	1.86
[47]	~700	1	29	37	33	-	3.0

For the purposes of the model, values, individually different in proportion to the copper fractions, were arbitrarily assigned to zinc. The deposit ratios of Cu:Zn were used in preference to the quoted cathode values for comparison with measured separation. The ratio of deposited copper to zinc was retained. Table 7.3.1 shows the proportion of each fraction used in the calculation.

Table 7.3.2

Percentage Fractional Degree of Ionisation Assumed for the Copper-Zinc Plasma

Element	Fractional Degree of Ionisation % II	III	IV
Copper*	15	19	17
Zinc	10	16	23

* - Based on measurements by Geva [47]

Separation for a copper-zinc plasma, which comprised II, III and IV ionisation states for both fractions, was calculated by equation (2.5.8). Equation (2.4.9) was used to model the radial distribution of each fraction over the diameter of the VAC chamber. Because a Gaussian distribution in the plasma was assumed, the conditional requirement of equation (2.4.10) was invoked.

$$\% \text{ Separation} = \left[\frac{\left[\frac{Zn^{2+} + Zn^{3+} + Zn^{4+}}{Cu^{2+} + Cu^{3+} + Cu^{4+}} \right]_r}{\left[\frac{Zn^{2+} + Zn^{3+} + Zn^{4+}}{Cu^{2+} + Cu^{3+} + Cu^{4+}} \right]_0} - 1 \right] \times 100\ \%$$

Figure 7.3.1 shows the distribution of the six plasma fractions and the resultant percentage separation. It was observed that separation followed a similar function to the values measured in section 7.2. Calculated copper and zinc plasma profiles, with the percentage separation, are shown in figure 7.3.2 . Measured separation data is included for comparison.

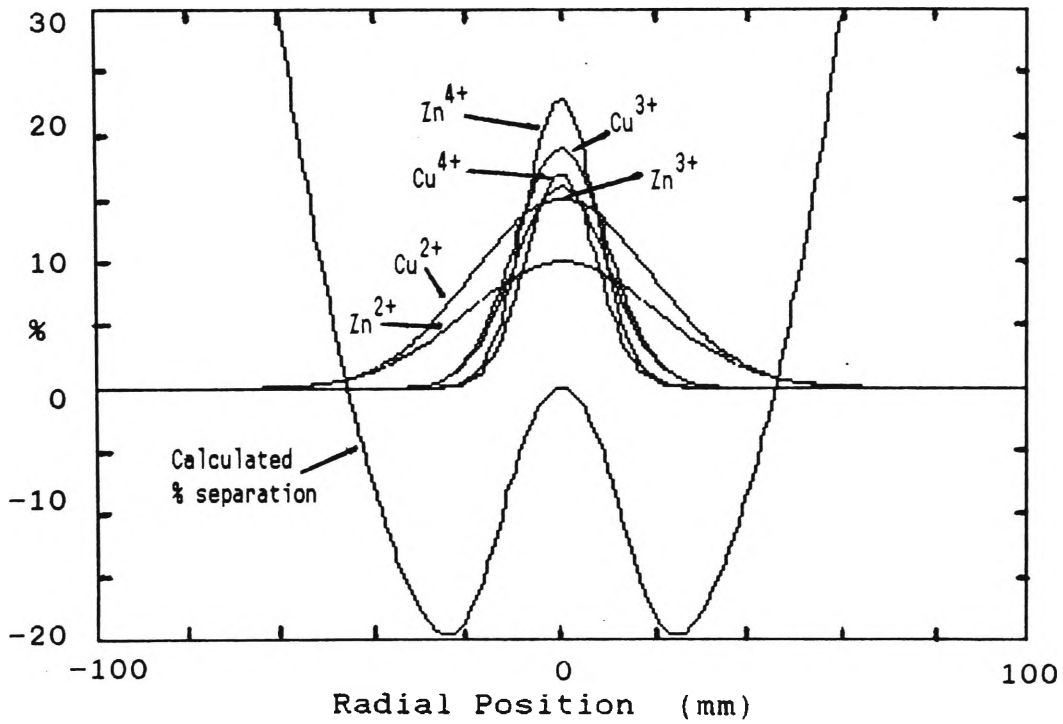

Fig. 7.3.1 Calculated fraction distributions and separation for the copper zinc plasma with B_z = 0.125 T and V_c = 380 V

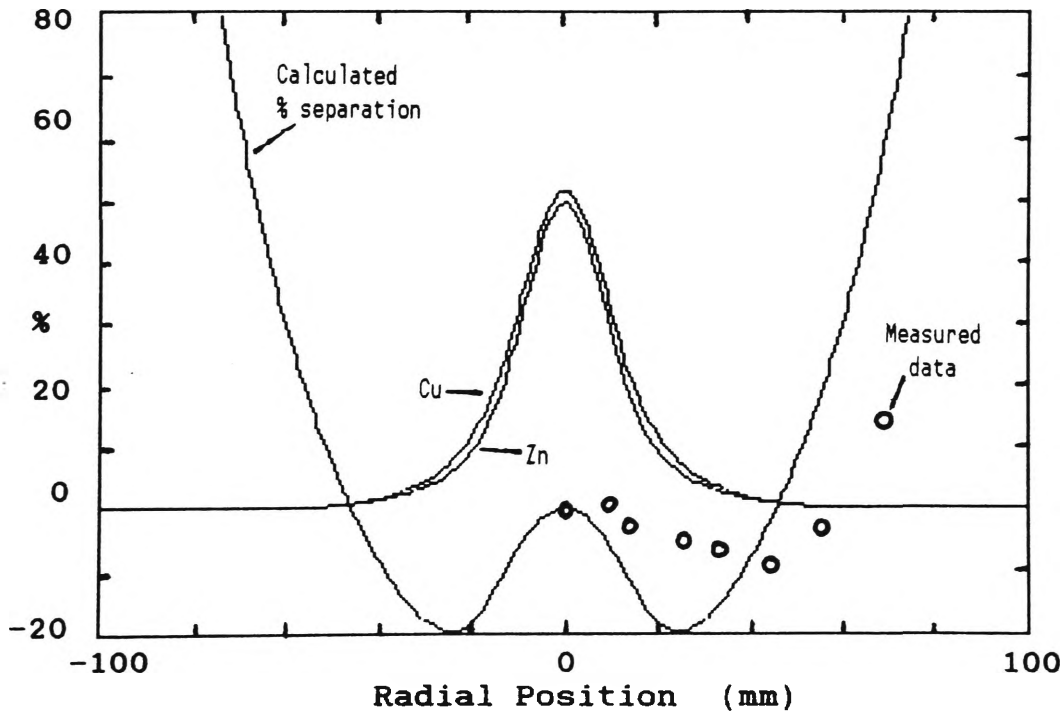

Fig. 7.3.2 Calculated copper and zinc distribution and separation from figure 7.3.1. Measured values included for comparison

The model demonstrated how it was possible to achieve negative separation. Geva [56] reported a negative separation result with aluminium-titanium plasmas. Only two mass elements were included in this treatment. A future, more accurate, computer model should include charge states for each isotope of all the elements in the plasma.

It is of interest to note that in an ANSTO VAC experiment reported by Evans et al. [119], where the high voltage discharge system was used, zinc was positively enriched with respect to copper over the entire radius of the collector. It is therefore apparent that the arc discharge current plays an important role in the level of excitation and multiplicity of charge states.

Measured copper-zinc separation of 15 % at r = 68 mm in the ANSTO VAC was achieved for the experimental conditions already described. This was less than the predicted value of 54 % calculated from the model. Geva [61] recently claimed a separation of 300 % for a copper-zinc plasma at B_z = 0.13 T. However, the measurement appears to have been made at large radii where the product yield is very small and may be of little practical use.

Although separation of copper isotopes was measured, the degree of separation was well below both the predicted values and values achieved by other VAC workers [37,43,48,61]. The theoretical model was also applied to calculate the expected separation for the experimental conditions. Table 7.3.2 shows the assigned charge states, again based on Geva's measurements [47], and apportioned between ^{63}Cu and ^{65}Cu according to the

copper natural abundance.

Table 7.3.3

Percentage Fractional Degree of Ionisation Assumed for the Copper-Zinc Plasma

Isotope	Fractional Degree of Ionisation % II	III	IV
^{63}Cu	21	25	23
^{65}Cu	9	11	11

Figure 7.3.3 shows the distribution of all six plasma fractions and the resultant percentage separation. The calculated separation followed a quadratic curve with radial position. The resultant copper isotope profiles are shown in figure 7.3.4 with the percentage separation. Measured separation data is included for comparison. The predicted separation at r = 52 mm was 59 %.

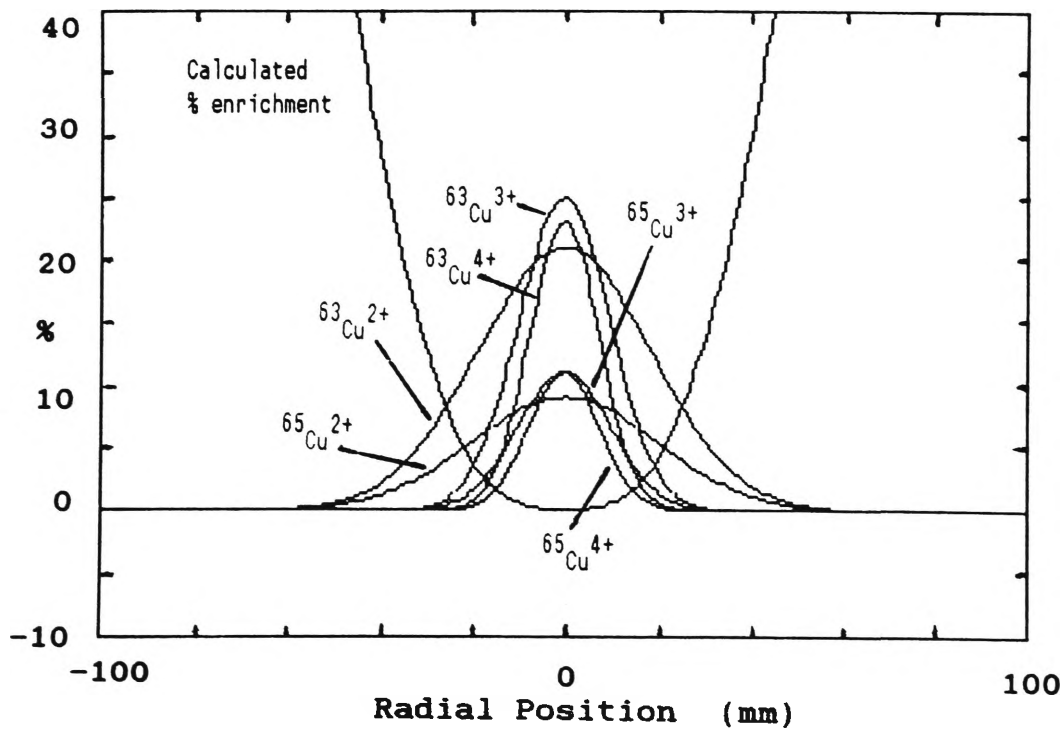

Fig. 7.3.3 Calculated fraction distributions and separation for the copper plasma with B_z = 0.125 T and V_c = 380 V

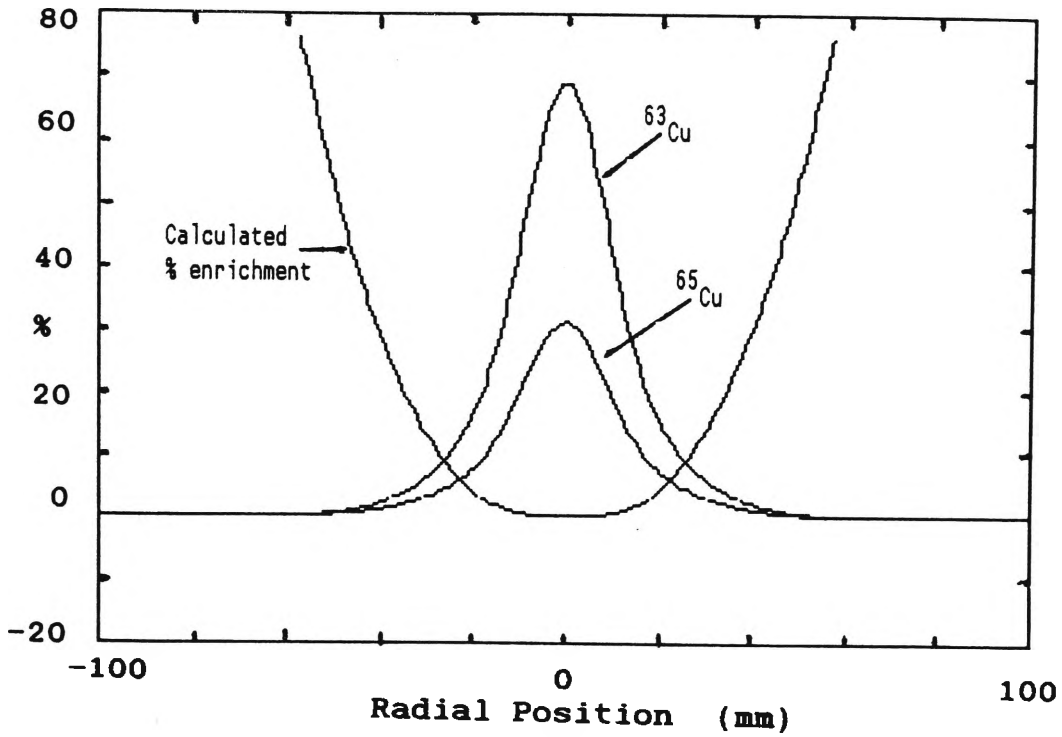

Fig. 7.3.4 Calculated copper isotope distribution and separation from figure 7.3.3.

Irregularities in the plasma column may have caused the poor VAC separation performance. Although the combination of initial voltage (V_C = 380 V) and applied axial magnetic field (B_Z = 0.125 T) parameters provide operation in the "stable" arc region of figure 5.2.4, they are close to the arc minimum voltage line. They may, therefore, be marginal in operation. Arc instability may have induced plasma irregularities due to the irregular production of electrons and ions from the cathode. Under these conditions, the plasma electric field would have also been irregular. Figure 7.3.5 shows the typical biased Langmuir probe signal for the conditions used in the copper separation experiments.

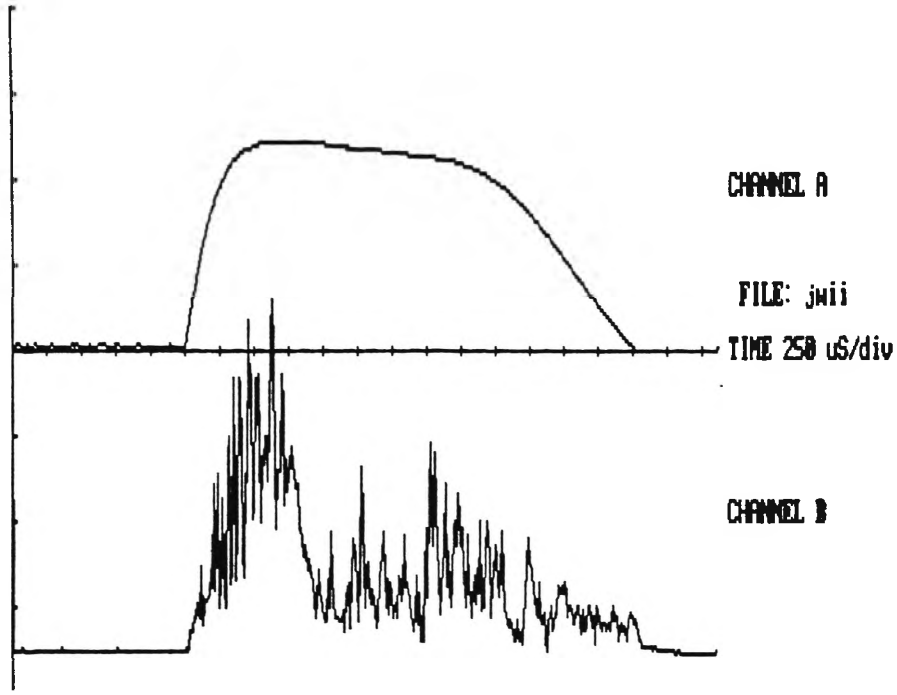

Fig. 7.3.5 Upper trace: arc discharge current 2 kA/div
Lower trace: biased Langmuir probe output
at r = 30mm

The typical signal waveform was complex and did not have a well defined rotation component. It is therefore suggested that the separation performance was degraded by the selection of a marginal combination of B_z and V_c. A dependency appears to exist between the degree of the ionisation and the magnitude of the plasma discharge current (see Table 7.3.1). Higher currents produce higher order charge states. The current levels used in the ANSTO VAC separation experiments were considerably greater than those reported by Geva [48]. It is therefore expected that some higher order ionisation states were also present.

Measurements made in the preceding sections were used to estimate the production costs of enrichment by the VAC process. Figure 7.3.6 shows the calculated yields based on the theoretical enrichment shown in figure 7.3.4.

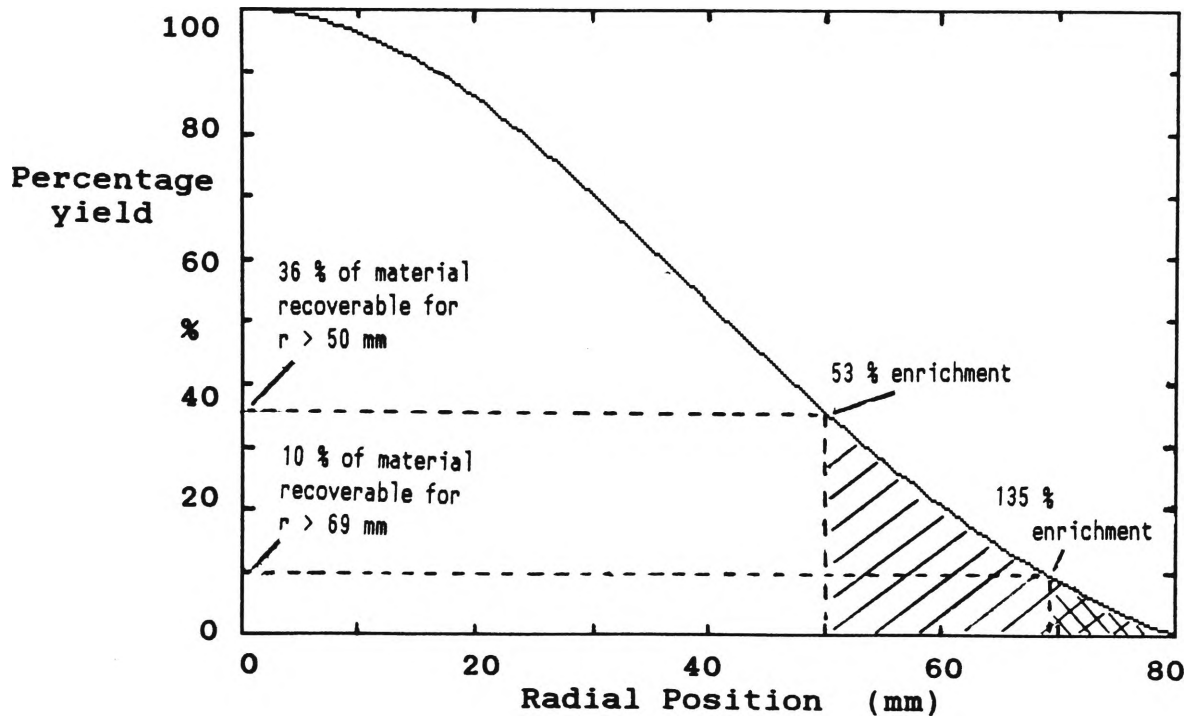

Fig. 7.3.6 Percentage yield of ^{65}Cu, based on theoretical calculations, for a minimum specified enrichment

From figure 7.3.6, 10 % of the deposit may be recovered at r > 69 mm for a minimum specified percentage enrichment level of 135 %. For a 53 % specified minimum enrichment, 36 % of the deposit is recoverable.

From section 7.1, an energy of 298 eV was required to erode a copper atom. For a 47 % cathode to collector transmission efficiency, 615 eV were required to deposit one atom of copper on the collector. A collector deposition rate of 300 µg/shot was calculated. By extrapolation, 921 kJ

would have been consumed to deposit 1 g of copper. The deposition of 10 g of copper, with 10 % recoverable as enriched material, would have required 3.3×10^4 shots. This is equivalent to an electrical energy of 9.2 MJ (2.6 kWH).

The laser was rated as 15 J/pulse. For 3.3×10^4 pulses, it delivered a total energy of 0.5 MJ. Assuming a laser efficiency of 10 %, 5 MJ (1.4 kWH) were consumed by the laser to trigger the VAC.

A continuous magnet load of 17.4 kW was measured for B_z = 0.125 T. Pulsed power, with an interval matched to the duration and frequency of the arc, would be used in a commercial facility. The duty cycle would be selected to achieve steady state field conditions for the duration of the arc and the plasma. To estimate the electrical costs for a pulsed magnet system, the duration of the magnet pulse was assumed to be twice the arc duration (5 mS). At a 1 Hz repetition rate, 0.81 kWH would be required to produce the magnetic field for 3.3×10^4 shots over 9.26 hours.

The vacuum system (roughing and diffusion pumps) operated continuously with an estimated energy consumption of 17.8 kWH. A further continuous energy consumption of 11.1 kWH was estimated for other VAC instrumentation and control equipment.

Thus, the total electrical energy consumed by the VAC to manufacture 1 g of enriched material was estimated to be 33.7 kWH. At \$0.15/kWH, the approximate cost was calculated to be \$5/g. An estimate for a commercial enrichment facility, however, would have to include maintenance and labour costs.

The following is a summary of typical operation parameters for the ANSTO VAC.

B_z variable 0 - 0.17 T

Separation and erosion measurements conducted at 0.125 T

V_c PFN: variable 0 - 400 V

Separation and erosion measurements conducted at 380 V

HV System 0 - 5 kV

Chamber Pressure: ~10^{-6} torr

Cathode: copper

brass (66% Cu : 34% Zn)

Anode: stainless steel mesh

VAC chamber length: ~1.5 m

Plasma length: ~1 m

Arc impedance: ~15 mΩ (copper cathode B_z = 0.1 T)

Axial velocity: ~10^4 m/S

Rotation frequency: ~0.5 - 1.5 x 10^5 rad/S

Erosion rate: 48 µg/C (copper cathode B_z = 0.125 T)

Ion density: ~10^{19} m^{-3}

Electron density: ~10^{20} m^{-3}

Cathode-collector transmission efficiency: 47 %

Electrical energy to erode one copper atom: 272 eV

Maximum measured separation: 15 % Zn/Cu at r = 68 mm

1 % $^{65}Cu/^{63}Cu$ at r = 52 mm

Future work, using the present VAC electrodes and PFN discharge system described in this thesis, should explore combinations of B_z for lower values of V_c. This work should be complemented with study of the plasma ion charge states.

8. CONCLUSIONS

A VAC facility has been established and successfully operated at the ANSTO research laboratories. The development of the facility has enabled Australia to join a research effort, now being pursued in a number of countries, to develop isotope and element separation by the VAC technique.

Combinations of energy storage and discharge systems were tested with various vacuum arc trigger devices. Reliable triggering was achieved with a 15 J/pulse CO_2 laser for the full range of axial magnetic fields tested. Efficient energy transfer to the arc was obtained with a PFN. The alternative high voltage, vacuum arc trigger will require further development to improve its longevity and performance at high axial magnetic fields.

The development of the VAC facility was complemented by the development of a computer controlled data acquisition system and the associated software for data storage and analysis.

In this thesis, the electrical characteristics of the ANSTO VAC were investigated and results were compared to a simple theoretical model. Experimental measurements were also compared to the published results of equivalent overseas research. The interrelationships between a number of parameters, which ultimately affect element and isotope separation performance, were identified and measured. Element separation was demonstrated for a copper-zinc plasma. Isotope enrichment was also demonstrated for a copper plasma. While

measured separation performance was low when compared to theoretical predictions and the recent published results of other VAC workers, it demonstrates that the ANSTO VAC is operational.

The following is a summary of important observations made during the experimental program:

i) electrical energy was most efficiently transferred to the arc when the discharge system source impedance was equal to the cathode terminal impedance.

ii) arc characteristics, impedance and ion production were dependent on the arc current and the applied axial magnetic field. Moreover, arc impedance decreased with increasing axial magnetic field.

iii) stable arcs were achieved for arc voltage and axial field combinations which were below the arc minimum voltage curve.

iv) the plasma column rotation direction was dependent on the orientation of the axial magnetic field vector.

v) the plasma column rotated as a solid body about the machine axis and in the same azimuthal direction as the electron cyclotron rotation.

vi) a radial electric field E_r was established within the plasma column. The radial plasma potential varied quadratically with radius about the machine axis.

vii) plasma rotation speed increased with increasing axial field B_z.

viii) plasma rotation speed decreased with increasing initial discharge voltage (arc current).

ix) ion axial drift velocity was greater than the plasma rotation velocity. Measured axial drift velocity increased with increasing discharge current.

x) the axial current path radius decreased for increasing axial magnetic field.

xi) ion distribution in the plasma column was Gaussian about the machine axis. Ion density increased for an increase in the discharge current.

xii) separation was shown to be dependent on both mass and ion charge state.

xiii) separation was also shown to have a radial dependency and follow a particular polynomial form. Copper isotope enrichment increased quadratically with radius. Copper-zinc separation followed a forth order, polynomial relationship with radius.

xiv) negative separation appeared possible when alloys with proportionally different charge species were present in the plasma.

Work covered by this thesis has detailed the background to the development of the ANSTO VAC. The experiments reported here have greatly increased our understanding of the various electrical and plasma processes. Many important parameters were characterised and incorporated in a simple numerical model.

Further research now appears necessary to increase our knowledge of the VAC operation and equilibrium conditions. The addition of a spectroscopic analyser would provide vital information regarding the identification of ionic species and the measurement of plasma temperature. Also, the inclusion of an on-line mass spectrometer and energy analyser would enable faster measurement of isotopic fractions and facilitate machine optimisation.

Cathode geometry and materials affect erosion and, possibly, also the establishment of the plasma radial electric field. Further experimentation in this area should explore a way of predicting the optimum cathode shape and size for each material to achieve stable arcs and plasmas for maximum separation and efficiency.

Rotation velocity and, thus, separation were shown to increase with plasma potential and axial magnetic field. An increase in the arc current resulted in an increase in plasma density with decrease in the rotational velocity. This latter result implies that some future optimisation will be necessary between separation and material yield. However, continued experimentation will be necessary to understand the interrelationship between these two parameters. Measurements of plasma ion distributions, charge states and radial potentials for a range of axial magnetic fields and arc currents would provide this essential information for plasma model improvement.

Overseas VAC development has taken some years to reach the performance levels currently reported in the literature.

With the initial demonstrations of element and isotope separation reported here, it is expected that rapid improvements of the ANSTO VAC will follow through a continuation of the experimental program. This thesis will serve as a useful basis for the further development of VAC technology at ANSTO.

9. ACKNOWLEDGMENTS

I wish to thank my thesis supervisor Dr. Frank Paoloni for his dedication and guidance throughout the course of this thesis. I also wish to express my appreciation to Dr. Peter Evans, the founder of the VAC project at ANSTO for his consistent encouragement and support.

The establishment of the VAC facility was made possible through the initiative of Mr. Doug Ebeling, former Chief of the ANSTO Nuclear Technology Division. ANSTO technical staff assisted in the construction of the VAC facility. Particular thanks are due to Messrs. Hans Noorman, Bert Muller and Ray Thompson. Mr. Norm Clark contributed the data acquisition program.

The PIXE analysis was by courtesy of Mr. Eric Clayton of the ANSTO Applied Physics Division. Messrs. Les Dale and Ian Warner of the CSIRO Division of Energy Chemistry kindly undertook the ICP-MS analysis.

The generous loan of the magnet coils and the high voltage capacitors by Prof. M.H. Brennan of the University of Sydney Wills Plasma Physics Laboratory is gratefully acknowledged.

I wish to thank ANSTO for granting me permission to undertake this research project for my Master's Thesis.

Finally, I wish to thank Ms. Leonie Jamieson, not only for the proof reading of my thesis, but also her love, patience and understanding during its writing.

Vienna, 1988

BIBLIOGRAPHY

[1] Dewitt, R. (1987) - *Isotope applications in the environmental field*, MLM-2487.

[2] DeWitt, R. (1979) - *Enriched isotope applications: biomedical field*, MLM-2593.

[3] Dewitt, R. (1980) - *Enriched isotope applications: agricultural field*, MLM-2715.

[4] Newman, E. (1981) - *Sources of Separated Isotopes for Nuclear Targetry*, Plenum, New York. p.229-234.

[5] Dewitt, R., Wilkes, W.R. and Wittenberg, L.J. (1977) - *Isotopically tailored materials for fission and fusion reactors*, MLM-2426.

[6] Conn, R.W., Okula, K. and Johnson, W. (1977) - *Minimizing long-term radiaoactivity in fusion reactors by isotopic tailoring*, Trans. Am. Nucl. Soc. **26**, 27.

[7] Smith, P.S., Parkins, W.E. and Forrester, A.T. (1947) - *On the separation of isotopes in quantity by electromagnetic means*, Phys. Rev. **72**, 989.

[8] Tracy, J.G., Bell, W.A., Veach, A.M., Caudill, H.H. and Milton, H.T. (1987) - *Stable isotope enrichment techniques and ORNL separation status*, Nucl. Instr. and Methods in Phys. Res. B26, 7.

[9] Hoff, R.W. (1987) - *The availability of enriched stable isotopes: present status and future prospects*, Nucl. Instr. and Methods in Phys. Res. **B26**, 1.

[10] Anon. (1987) - *Nuclear material safeguards for enrichment plants. Part 1. Uranium enrichment: general principles and processes.* Potas K/ITP-156/P1 (ISPO-284).

[11] Slepian, J. (1955) - *Failure of the ionic centrifuge prior to the ionic expander*, J. App. Phy. **26**, 1283.

[12] Slepian, J. (1957) - *The magneto-ionic expander isotope separator applied to uranium*, J. Nuc. Sci. **3**, 108.

[13] Alfven, H. (1960) - *Collision between a nonionized gas and a magnetized plasma*, Rev. Mod. Phy. **32**, 710.

[14] Lehnert, B. (1971) - *Rotating plasmas*, Nucl. Fus. **11**, 485.

[15] Bonnevier, B. (1966) - *Diffusion due to ion-ion collisions in a multicomponent plasma*, Ark. Fys. **33**, 255.

[16] Bonnevier, B. (1971) - *Experimental evidence of element and isotope separation in a rotating plasma*, Plasma Phys. **13**, 763.

[17] Nathrath, N. (1973) - *Rotational velocity and current distributions in stationary rotating arcs*, XI International Conference on Phenomena in Ionized Gases, Prague, 245.

[18] James. B.W. and Simpson, S.W. (1974) - *Isotopic separation in a rotating plasma*, Phys. Lett. **46A**, 347.

[19] Boeschoten, F. (1975) - *On the possibility to separate isotopes by means of a cylindrical plasma column, rotating around its axis*, International Conference on Uranium Isotope Separation, London, 71.

[20] Nathrath, N., Kress, H., McClure, J., Mück, G., Simon, M. and Dibbert, H. (1975) - *Isotope separation in rotating plasmas*, International Conference on Uranium Isotope Separation, London, 53.

[21] Cairns, J.B.S. (1975) - *Isotopic separation in a rotating neon plasma*, International Conference on Uranium Isotope Separation, London, 61.

[22] James, B.W., Millar, D.D. Simpson, S.W. (1975) - *The separation of neon isotopes by a plasma centrifuge*, International Conference on Uranium Isotope Separation, London, 67.

[23] James, B.W. and Simpson, S.W. (1976) - *Isotope separation in the plasma centrifuge*, Plasma Phys. **18**, 289.

[24] Himmel, G., Möbius, E. and Piel, A (1976) - *Investigation of the structure and the plasma parameters in a "critical velocity" rotating plasma*, Z. Naturforsch. **31a**, 934.

[25] Hirshfield, J.L. (1976) - *Isotope separation using plasma heating at the two-ion resonance*, Nucl. Instr. and Methods. 139, 119.

[26] Himmel, G., Möbius, E. and Piel, A. (1977) - *The motion of ions and neutrals in a "critical velocity" rotating plasma*, XIII International Conference on Phenomena in Ionized Gases, Berlin, 689.

[27] McClure, J.J. and Nathrath, N. (1977) - *The plasma centrifuge I: uranium partial pressure distributions*, XIII International Conference on Phenomena in Ionized Gases, Berlin, 693.

[28] Mück, G. and Simon, M. (1977) - *The plasma centrifuge II: measurements on rotating rare gas arcs*, XIII International Conference on Phenomena in Ionized Gases, Berlin, 695.

[29] Nathrath, N. (1977) - *The plasma centrifuge III: measurements on rotating uranium plasmas*, XIII International Conference on Phenomena in Ionized Gases, Berlin, 689.

[30] Kaneko, O., Sasaki, S. and Kawashima, N. (1978) - *Mass separation experiment with a partially ionized rotating plasma*, Plasma Phys. 20, 1167.

[31] James, B.W. and Simpson, S.W. (1978) - *The viscous dynamics of a rotating plasma*, Plasma Phys. 20, 739.

[32] Walsh, C.J., Brand, G.F. and James, B.W. (1978) - *Separation of metals in a rotating plasma*, Phys. Lett. **67A**, 33.

[33] Winjnakker, M.M.B., Granneman, E.H.A. and Kristemaker, J. (1979) - *A study of a weakly ionized rotating plasma*, Z. Naturforsch. **31a**, 672.

[34] Belorusov, A.V., Karchevskii, A.I., Muromkin, Yu.A., Potanin, E.P., Ustinov, A.L. and Babichev (1979) - *Separation of gas mixtures and xenon isotopes in a pulsed plasma centrifuge*, Sov. J. Plasma Phys. **5**, 693.

[35] Winjnakker, M.M.B. and Granneman, E.H.A. (1980) - *Limitations on mass separation by the weakly ionized plasma centrifuge*, Z. Naturforsch. **31a**, 672.

[36] Krishnan, M. and Hirshfield, J.L. (1980) - *Fast high-resolution ion energy momentum spectrometer*, Rev. Sci. Inst. **51**, 911.

[37] Krishnan, M., Geva, M. and Hirshfield, J.L., (1981) - *Plasma centrifuge*, Phys. Rev. Lett. **46**, 36.

[38] Simpson, S.W. (1981) - *A steady-state fluid model of a rotating plasma*, Phys. Fluids. **24**, 418.

[39] Korobtsev, S.V., Kosinova, T.A., Rakhimbabaev, Ya.R. and Rusanov, V.D. (1981) - *Rotation of gases in a plasma centrifuge at relatively high pressure*, Sov. Phys. Tech. Phys. **26**, 390.

[40] Hora, H. and Hoyle, I.B. (1981) - *Turbulence limits in rotating plasmas for isotope separation*, Z. Naturforsch. **37a**, 294.

[41] Simpson, S.W. (1981) - *Separative power of plasma centrifuges*, Phys. Lett. **85A**, 342.

[42] Belorusov, A.V., Gorbunova, E.F., Karchevsky, A.I., Muromkin, Y.A., Ustinov, A.L. and Kurchatov, I.V. (1981) - *Experimental research of helium and neon isotope separation in a pulsed hydrogen plasma centrifuge*, XV International Conference on Phenomena in Ionized Gases, Minsk, 885.

[43] Geva, M., Krishnan, M. and Hirshfield, J.L. (1981) - *Centrifugal mass separation in laser-initiated vacuum arcs*, Nucl. Instr. and Methods. **186**, 183.

[44] Tomimura, A. and Nicoli, C. (1982) - *Separação isotópica num plasma rotatório*, Rev. Bras. Fis. **1**, 151.

[45] Krishnan, M. (1983) - *Centrifugal isotope separation in zirconium plasmas*, Phys. Fluids. **26**, 2676.

[46] Del Bosco, E., Dallaqua, R.S. and Ludwig, G.O. (1984) - *Plasma centrifuge development at INPE*, Institute for Space Research, Plasma Physics Division. Sao Paulo. Unpublished Report.

[47] Geva, M., (1982) - PhD Thesis, Yale University, New Haven, Connecticut.

[48] Geva, M., Krishnan, M. and Hirshfield, J.L. (1984) - *Element and isotope separation in a vacuum arc centrifuge*, J. Appl. Phys. **56**, 1398.

[49] Boldyrev, V.R., Poluektov, N.P. and Kharchenko, V.N. (1985) - *Measurements of dynamic processes in a pulsed plasma centrifuge*, Sov. J. Plasma Phys. **11**, 245.

[50] Prasad, R.R. and Krishnan, M. (1986) - *Matched impedance, low-voltage vacuum-arc centrifuge*, Rev. Sci. Instr. **57**, 74.

[51] Seebacher, P., Simpson, S.W. and Messerle, H.K. (1985) - *Continuous plasma centrifuge*, 15th AINSE Plasma Physics Conference, Sydney.

[52] Bittencourt, J.A. (1986) - *Theoretical behavior of fully ionized multiple species magnetized plasmas under rotation*, Publication No. INPE-3915.

[53] Prasad, R.R., Consiglio, R. and Krishnan, M. (1986) - *Power flow and cathode erosion in a vacuum arc centrifuge*, IEEE Trans. Plasma Sci. **14**, 498.

[54] Ludwig, G.O. (1986) - *A variational principle for the plasma centrifuge*, Publication No. INPE-3989.

[55] Bittencourt, J.A. and Ludwig, G.O. (1987) - *Steady state behaviour of rotating plasmas in a vacuum arc centrifuge*, Plasma Phys. Control. Fusion. **29**, 601.

[56] Del Bosco, E., Dallaqua, R.S., Ludwig, G.O. and Bittencourt, J.A. (1987) - *Isotopic enrichment in a plasma centrifuge*, Appl. Phys. Lett. **50**, 1716.

[57] Simpson, S.W., Seebacher, P.J. and Messerle, H.K. (1987) - *Study of a continuous plasma centrifuge*, J. Phys. D: Appl. Phys. **20**, 622.

[58] Prasad, R.R. (1987) - PhD Thesis, Yale University, New Haven, Connecticut.

[59] Prasad, R.R. and Krishnan, M. (1987) - *Isotope separation in a vacuum-arc centrifuge*, J. Appl. Phys. **61**, 4464.

[60] Prasad, R.R. and Krishnan, M. (1987) - *Scaling of rotation and isotope separation in a vacuum-arc centrifuge*, Nucl. Instr. and Methods in Phys. Res. **B26**, 65.

[61] Geva, M., Cohen, C., Danziger, O., Dothan, F., Friedland, L., Levin, L.A., Maharshak, S. and Hirshfield, J.L. (1987) - *Vacuum arc plasma centrifuge for element and isotope separation*, IEEE Trans. on Plasma Sci. **15**, 583.

[62] Evans, P.J., Whichello, J.V. and Clancy, B.E. (1985) - *Development of a vacuum arc centrifuge at LHRL*, 15th AINSE Plasma Physics Conference, Sydney.

[63] Whichello, J.V., Evans, P.J., Noorman, J.T., Muller, H.H. and Paoloni, F.J. (1986) - *The development of a vacuum arc centrifuge by the Nuclear Technology Division: a progress report*, NTD/TN 20. ANSTO Internal Report.

[64] Schmeing, H., Buyers, W.J.L. and Dolling, G. (1983) - *Isotope enrichment of zirconium using a plasma centrifuge*, Final report on Contract CR31-3946, Chalk River National Laboratories, Ontario, Canada.

[65] Evans, P.J. (1984) - *Isotope separation with a vacuum arc centrifuge: a proposal*. WSCN/600. ANSTO Internal Report.

[66] AAEC Research Establishment Research Report to the Commission 11 April 1985. Field 3: Medical Applications of Radioisotopes and Radiation. ANSTO Internal Report.

[67] Lafferty, J.M. (1966) - *Triggered vacuum arcs*, Proc. IEEE. **54**, 23.

[68] Reece, M.P. (1963) - *The vacuum switch*, Proc. IEE. **110**, 793.

[69] Schrade, H.O., Auweter-Kurtz, M. and Kurtz, H.L. (1983) - *Analysis of the cathode spot of metal vapor arcs*, IEEE Trans. on Plasma Sci. **11**, 103.

[70] Fang, D.Y. (1983) - *Temperature dependence of retrograde velocity of vacuum arcs in magnetic fields*, IEEE Trans. on Plasma Sci. 11, 110.

[71] Dyuzhev, G.A., Lyubimov, G.A. and Shkol'nik, S.M. (1983) - *Conditions of the anode spot formation in a vacuum arc*, IEEE Trans. on Plasma Sci. 11, 36.

[72] Miller. H.C. (1983) - *Discharge modes at the anode of a vacuum arc*, IEEE Trans. on Plasma Sci. 11, 122.

[73] Lafferty, J.M., (Ed.), (1980) - *Vacuum Arcs*. John Wiley and Sons, New York.

[74] Davis, W.D. and Miller, H.C. (1969) - *Analysis of the electrode products emitted by dc arcs in a vacuum ambient*, J. Appl. Phys. **40**, 2212.

[75] Prock, J. (1986) - *Time-dependent description of cathode crater formation in vacuum arcs*, IEEE Trans. on Plasma Sci. **14**, 482.

[76] Smith, G.P., Dollinger, R., Malone, D.P. and Gilmore, A.S. (1980) - *Relative cathode spot and cell areas and currents in a copper cathode vacuum arc*, J. Appl. Phys. **51**, 3657.

[77] Boxman, R.L., Goldsmith, S., Izraeli, I. and Shalev, S. (1983) - *A model of the multicathode-spot vacuum arc*, IEEE Trans. on Plasma Sci. 11, 138.

[78] Kimblin, C.W. (1973) - *Erosion and ionization in the cathode spot regions of vacuum arcs*, J. Appl. Phys. **44**, 3074.

[79] Rakhovsky, V.I. (1987) - *State of the art physical models of vacuum arc cathode spots*, IEEE Trans. on Plasma Sci. **15**, 481.

[80] Jüttner, B. (1987) - *Characterization of the cathode spot*, IEEE Trans. on Plasma Sci. **15**, 474.

[81] Emtage, P.R., Gorman, J.G., Heberlein, J.V.R., Holmes, F.A., Kimblin, C.W., Slade, P.G. and Voshall, R.E. (1977) - *The interaction of vacuum arcs with transverse magnetic fields*, XIII International Conference on Phenomena in Ionized Gases, Berlin.

[82] Drouet, M.G. (1981) - *The physics of the retrograde motion of the electric arc*, Japanese J. Appl. Phys. **20**, 1027.

[83] Kimblin, C.W. and Voshall, R.E. (1973) - *Vacuum arcs subjected to axial magnetic fields*, XIII International Conference on Phenomena in Ionized Gases, Prague, 78.

[84] Kimblin, C.W. (1977) - *Anode spot ion currents and the interaction with axial magnetic fields*, XIII International Conference on Phenomena in Ionized Gases, Berlin, 675.

[85] Kaneda, T., Kaneko, E., Yanabu, S. and Ikeda, H. (1981) - *The characteristic of vacuum arcs with magnetic fields parallel to its columns*, Physica. **104C**, 124.

[86] Schellekens, H. (1983) - *The high-current vacuum arc in an axial magnetic field: an experimental investigation*, J. Appl. Phys. **54**, 144.

[87] Gorman, J.G., Kimblin, C.W., Voshall, R.E., Wien, R.E.and Slade, P.G. (1983) - *The interaction of vacuum arcs with magnetic fields and applications*, IEEE Trans. on Power Appar. and Sys. **102**, 257.

[88] Yanabu, S., Kaneko, E., Koike, H., Tsutsumi, T. and Tamagawa, T. (1983) - *The applications of axial magnetic field electrodes to vacuum circuit breakers*, IEEE Trans. on Power Appar. and Sys. **102**, 1395.

[89] Kaneko, E., Tamagawa, T., Okumura, H. and Yanabu, S. (1983) - *Basic characteristics of vacuum arcs subjected to a magnetic field parallel to their positive columns*, IEEE Trans. on Plasma Sci. **11**, 169.

[90] Yanabu, S., Okawa, M., Kaneko, E. and Tamagawa, T. (1987) - *Use of axial magnetic fields to improve high-current vacuum interrupters*, IEEE Trans. on Plasma Sci. **15**, 524.

[91] Okawa, M., Yanabu, S., Kaneko, E. and Otobe, K. (1987) - *The investigation of copper-chromium contacts in vacuum interrupters subjected to an axial magnetic field*, IEEE Trans. on Plasma Sci. **15**, 533.

[92] Plyutto, A.A., Ryzhkov, V.N. and Kapin, A.T. (1965) - *High speed plasma streams in plasma arcs*, Soviet Physics JETP **20**, 328.

[93] Kimblin, C.W. (1974) - *Cathode spot erosion and ionization phenomena in the transition from vacuum to atmospheric pressure arcs*, J. Appl. Phys. **45**, 5235.

[94] Disatnik, G., Boxman, R.L. and Goldsmith, S. (1987) - *Characteristics of macroparticle emission from a high-current-density multi-cathode spot vacuum arc*, IEEE Trans. on Plasma Sci. 15, 520.

[95] Shalev, S., Boxman, R.L. and Goldsmith, S. (1983) - *Velocities and emission rates of cathode-produced molybdenum macroparticles in a vacuum arc*, J. Appl. Phys. **58**, 2503.

[96] Rondeel, W.G.J. (1974) - *Investigation of the ions emitted from a copper-vapour arc in vacuum*, J. Phys. D: Appl. Phys. **7**, 629.

[97] Len, L.K., Burkhart, C., Cooper, G.W., Humphries, S., Savage, M. and Woodall, D.M. (1986) - *Generation and measurements of ion species from vacuum arcs*, IEEE Trans. Plasma Sci. **14**, 256.

[98] Gilmour, A.S. and Lockwood, D.J. (1972) - *Pulsed metalic-plasma generators*, Proc. IEEE. **60**, 977.

[99] Hirshfield, J.L. (1976) - *Laser initiated vacuum arc for heavy ion sources*, IEEE Trans. Nucl. Sci. **23**, 1006.

[100] Gellert, B., Schade, E. and Dullni, E. (1987) - *Measurement of particles and vapor density after high-current vacuum arcs by laser techniques*, IEEE Trans. on Plasma Sci. **15**, 545.

[101] Toya, H., Uchida, Y., Hayashi, T. and Yutaka Murai (1986) - *Spectroscopic measurement and analysis of high-current vacuum arc near copper cathode*, IEEE Trans. Plasma Sci. **14**, 471.

[102] Heberlein, J.V.R. and Porto, D.R. (1983) - *The interaction of vacuum arc ion currents with axial magnetic fields*, IEEE Trans. on Plasma Sci. **11**, 152.

[103] Brown, I.G. (1987) - *On the current intensity limit of a vacuum-arc ion source*, IEEE Trans. on Plasma Sci. **15**, 346.

[104] Farrall, G.A., Hudda, F.G. and Toney, J.G. (1983) - *The time-resolved characterization of erosion products from high current, copper vacuum arcs*, IEEE Trans. on Plasma Sci. **11**, 132.

[105] Grover, F.W., (1946) - *Inductance Calculations Working Formulas and Tables*. Dover Publications, New York.

[106] Guillemin, E.A. (1944) - *A historical account of the development of a design procedure for pulse-forming networks*, NRDC Radiation Laboratory Report 43.

[107] Guillemin, E.A. (1957) - *Synthesis of Passive Networks*. John Wiley and Sons, New York.

[108] Sprague Engineering Bulletin No. 3431E Sprague Electric Company, Lansing, NC.

[109] Requested information supplied by the manufacturer Sprague Electric Company, Lansing, NC.

[110] Davis, A.T. (Program Author) (1987) - *ECA-2 Electronic Circuit Analysis Version 2.3*. Tatum Labs Inc, Ann Arbor, MI.

[111] Cobine, J.D. (1958) - *Gaseous Conductors*. Dover Publications, New York.

[112] Huddlestone, R.H. and Leonard, S.L. (Eds.), (1965) - *Plasma Diagnostic Techniques*. Academic Press, New York.

[113] Clayton, E. (1982) - *Sample characterization by proton induced x-ray emission analysis*, Applic. of Surface Sci. 13, 136.

[114] Kunz, F.W. and Cole, G.S. (1988) - *Particle-induced x-ray energy-dispersive analysis of research materials*, International Laboratory, Jan/Feb, 18.

[115] Douglas, D.J. and Houk, R.S. (1985) - *Inductively-coupled plasma mass spectrometry (ICP-MS)*, Prog. Analyt. Atom. Spectrosc. 8, 1.

[116] Anon, *Microsoft Mouse*, Microsoft Corporation, Redmond WA.

[117] Shah, S.I. and Carcia, P.F. (1987) - *Superconductivity and resputtering effects in rf sputtered* $YBa_2Cu_3O_{7-x}$ *thin films*, Appl. Phys. Lett. 51, 2146.

[118] Merkle, B.D., Kniseley, R.N. and Schmidt, F.A. (1987) - *A new system for vacuum deposition of refractory materials using an atmospheric-pressure inductively coupled plasma*, J. Appl. Phys. 62, 1017.

[119] Evans, P.J., Paoloni. F.J., Noorman, J.T. and Whichello, J.V. (1988) - *Mass separation in a vacuum arc centrifuge*, Submitted to J. Appl. Phys..

APPENDIX 1

The VAC Laboratory and Equipment

The VAC laboratory layout showing the position of major equipment items is given in figure A1.1. Five selected view points (marked A1.2 etc.) are also included which refer to the photographs in this appendix.

The screened room was built in the laboratory and consisted of a wooden frame covered on both sides by galvanised wire mesh with a square spacing of 10 mm. The outer mesh was connected to the VAC equipment, laser and power supply metal frames. The inner mesh was connected via a heavy gauge wire strap to an earth stake outside the laboratory. Signals in and out of the screened room were connected via capacitor feed-throughs and ferrite filters. The mains supply into the screen room was isolated by a 2 kVA transformer.

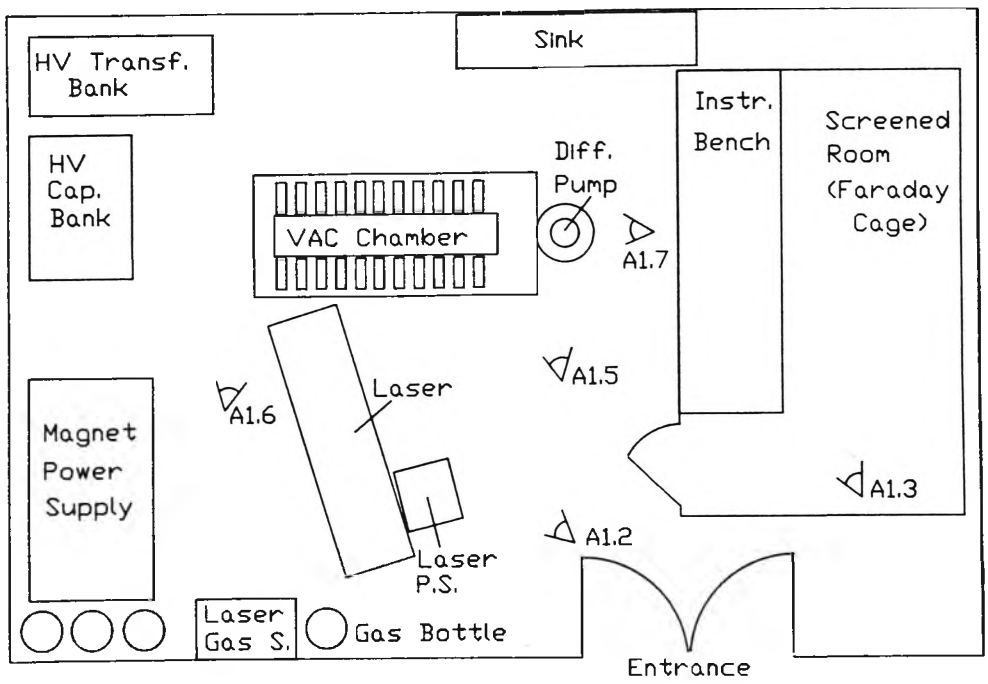

Fig A1.1 Layout of the VAC laboratory

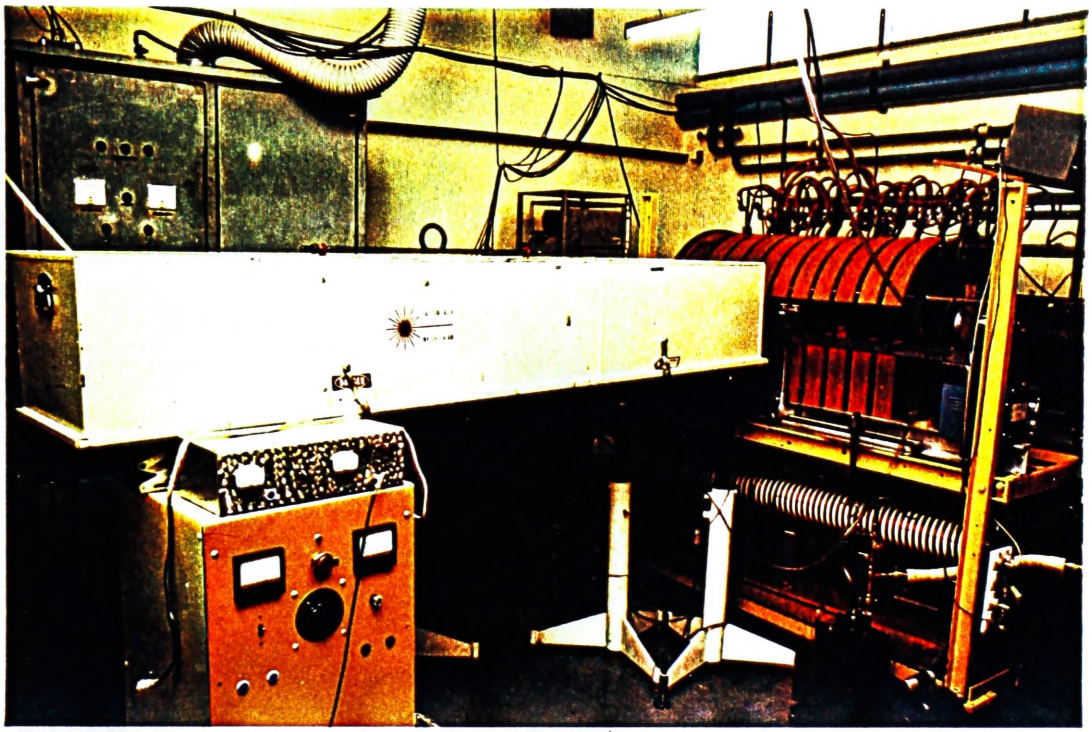

Fig. A1.2 A view of the VAC laboratory. The Lumonics 15J/pulse laser stands in the foreground. The VAC (right side) stands above the PFN. The magnet power supply is seen behind the laser.

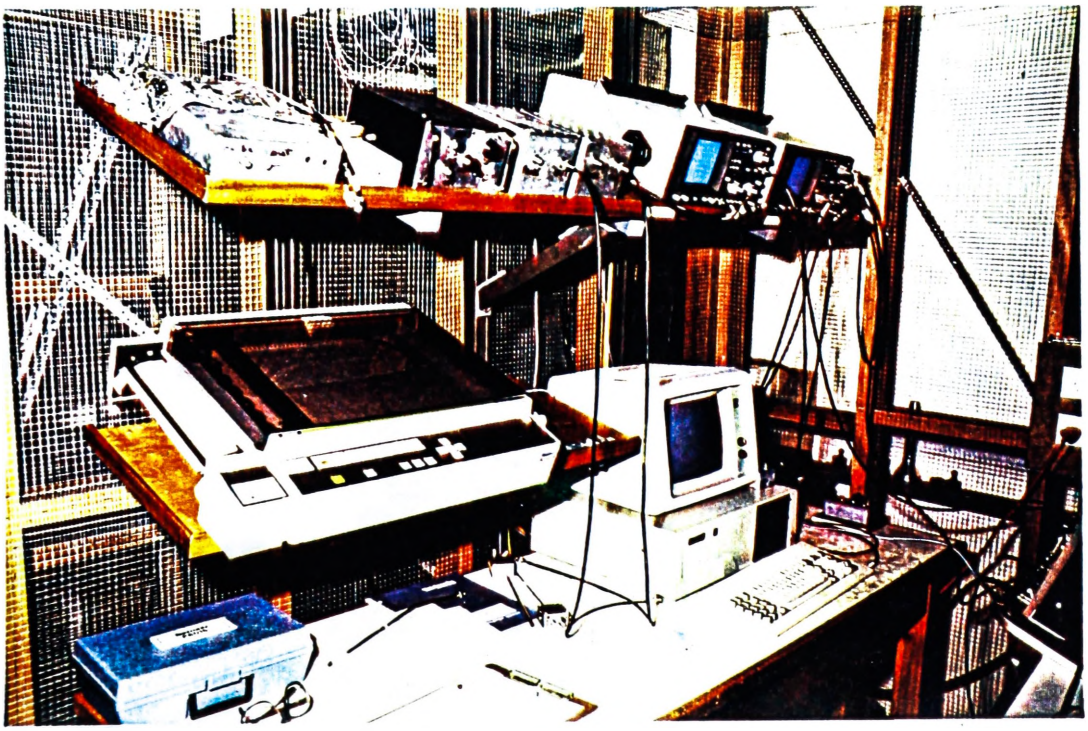

Fig. A1.3 Interior view of the screened room showing the data acquisition instruments. Inter alia are the computer (on bench) and the two Philips PM 3302 digital storage CROs.

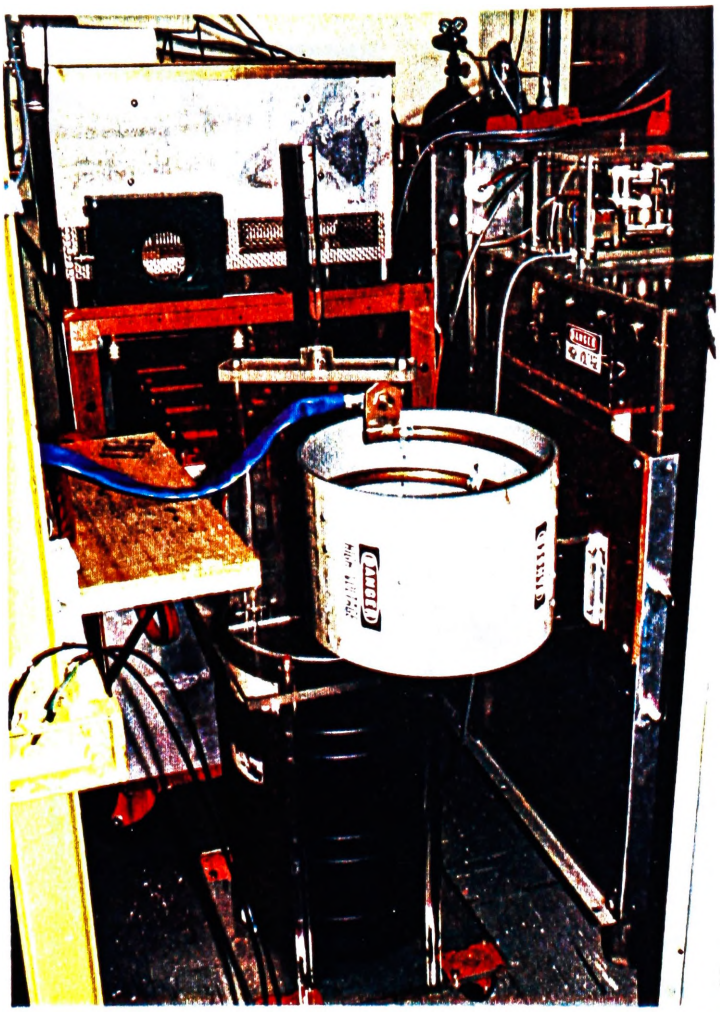

Fig. A1.4

A view of the high voltage (H.V.) discharge system connected to the VAC. The 3 μH coil and liquid resistor are seen in the centre foreground. The safety dump resistor (top of photograph) stands above the 1 mF capacitor bank.

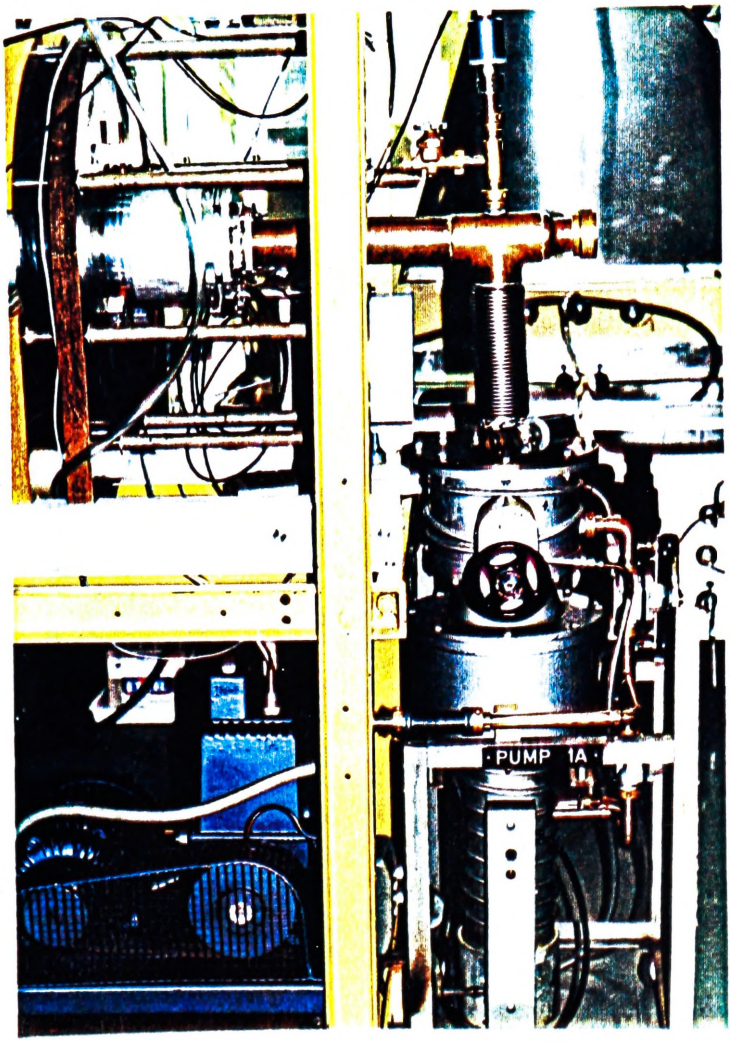

Fig. A1.5

A view of the vacuum pump system connected to the VAC. The roughing pump (lower left corner of the photograph) and the 8" oil diffusion pump are shown.

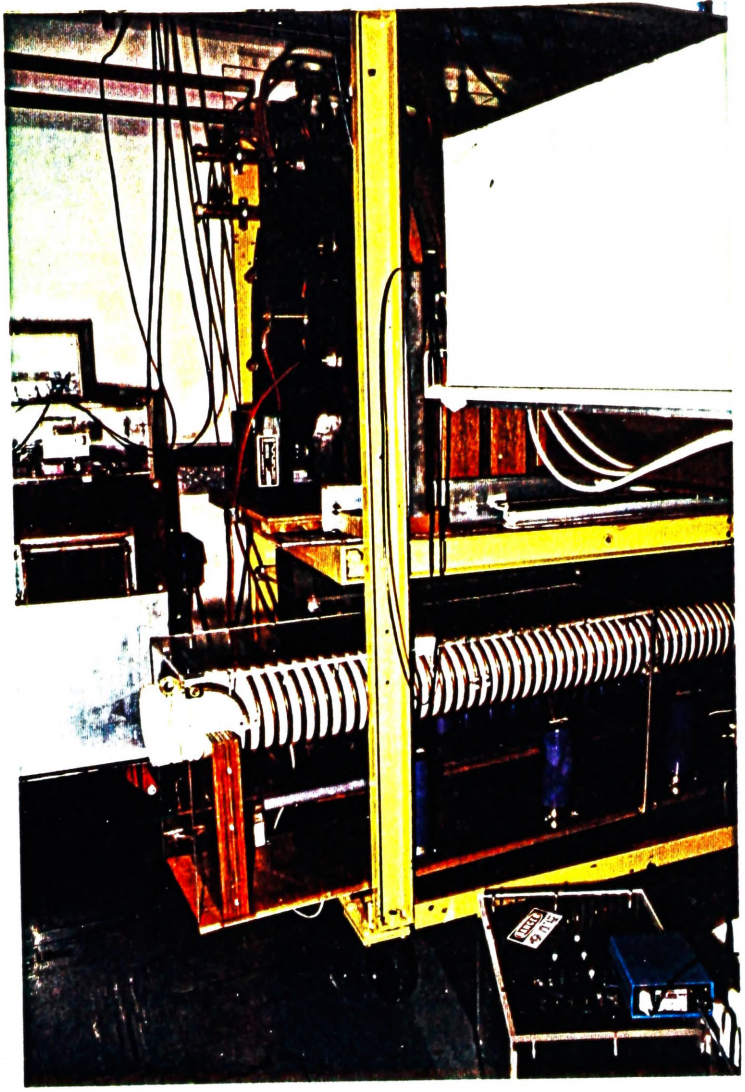

Fig. A1.6

A photograph of the cathode end of the VAC showing the connection to the PFN. The current monitor is seen in line between the PFN and the VAC.

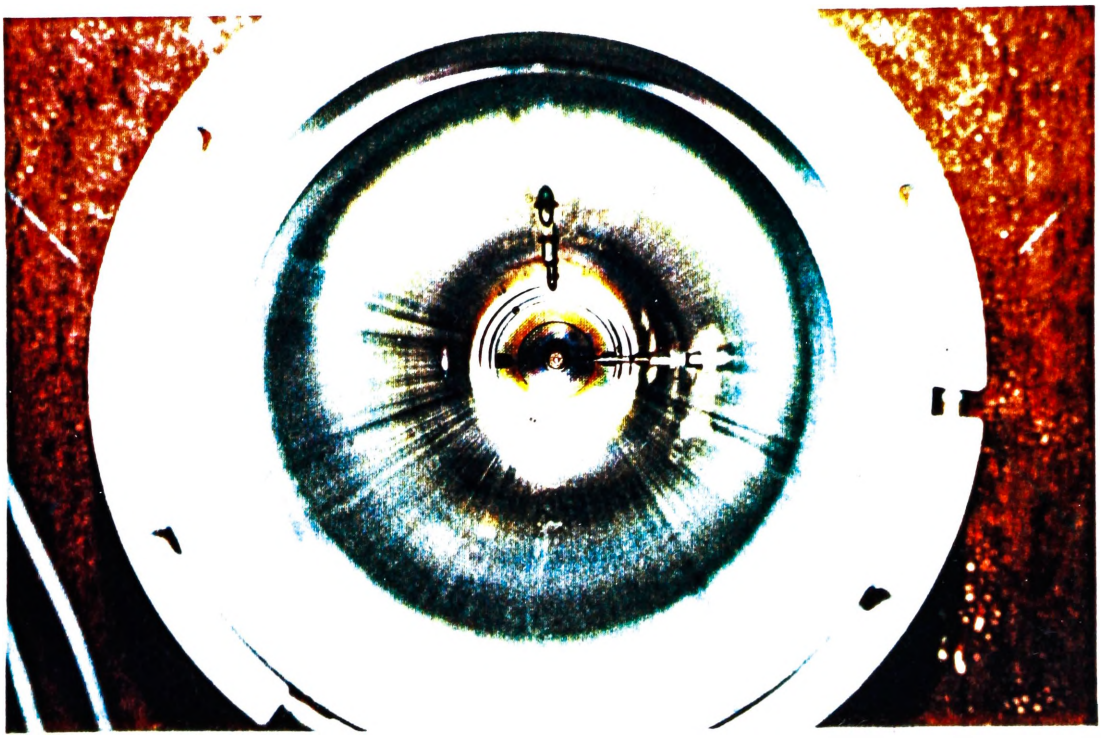

Fig. A1.7 A view inside the VAC looking toward the cathode and mesh anode (vacuum end flange removed). The probe positions are visible along the vacuum chamber.

APPENDIX 2

VAC Ancillary Equipment Electrical Circuits

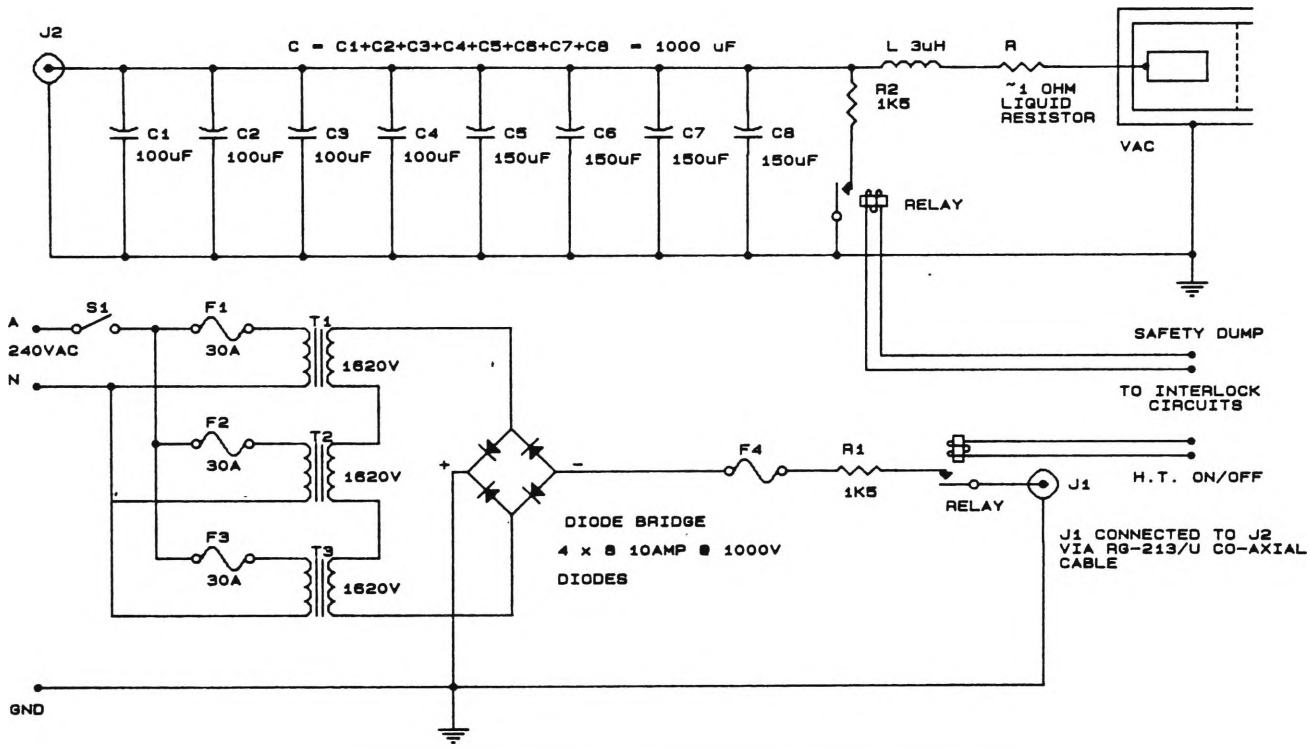

Fig. A2.1 Circuit of the high voltage (HV) energy storage and discharge system

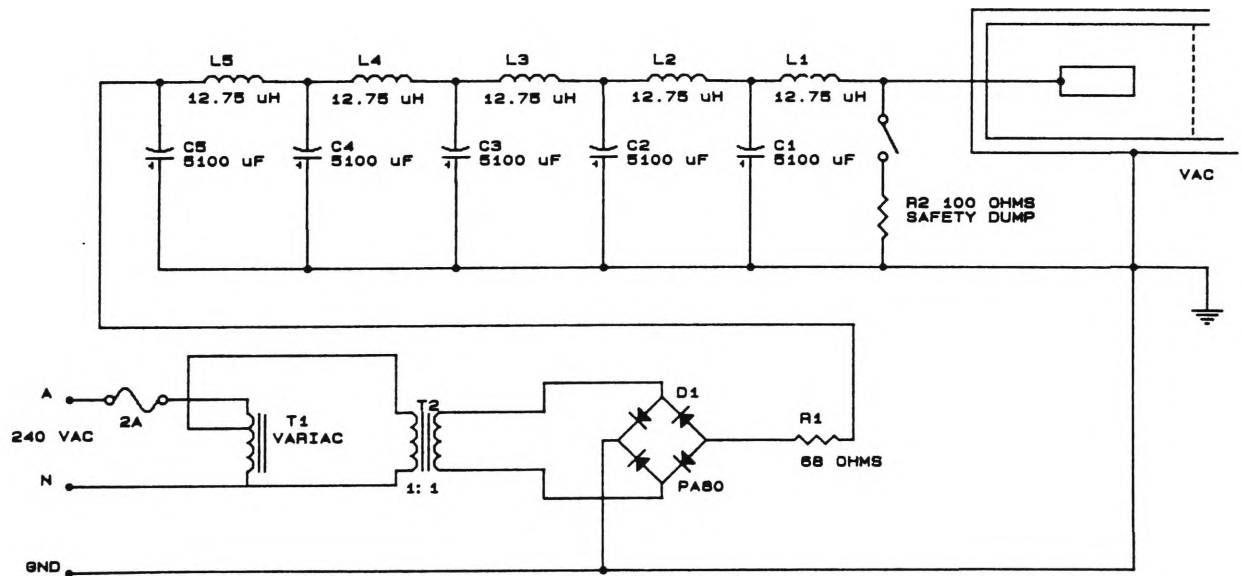

Fig. A2.2 Circuit of the pulse forming network (PFN) energy storage and discharge system

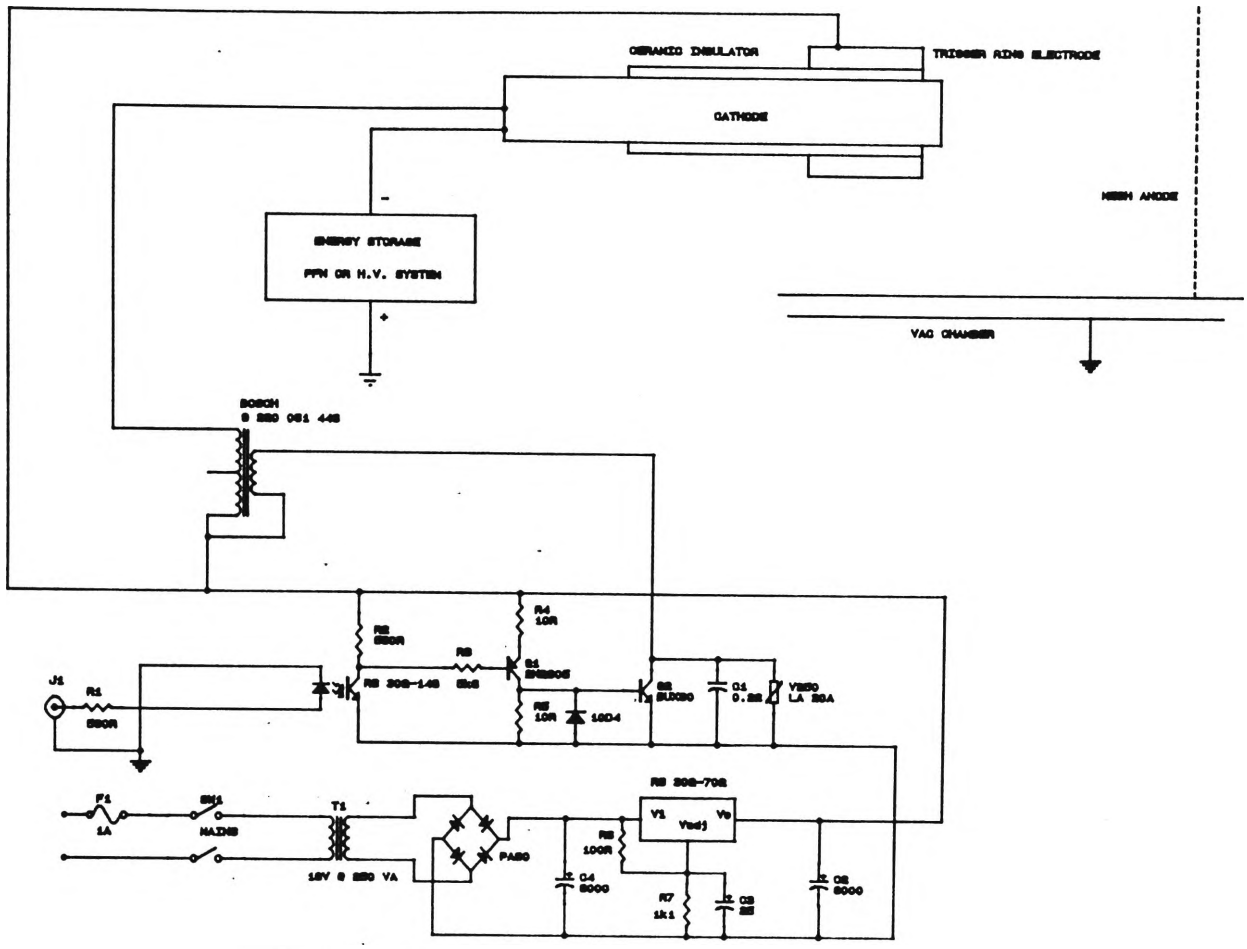

Fig. A2.3 Circuit diagram of the high voltage, vacuum arc trigger

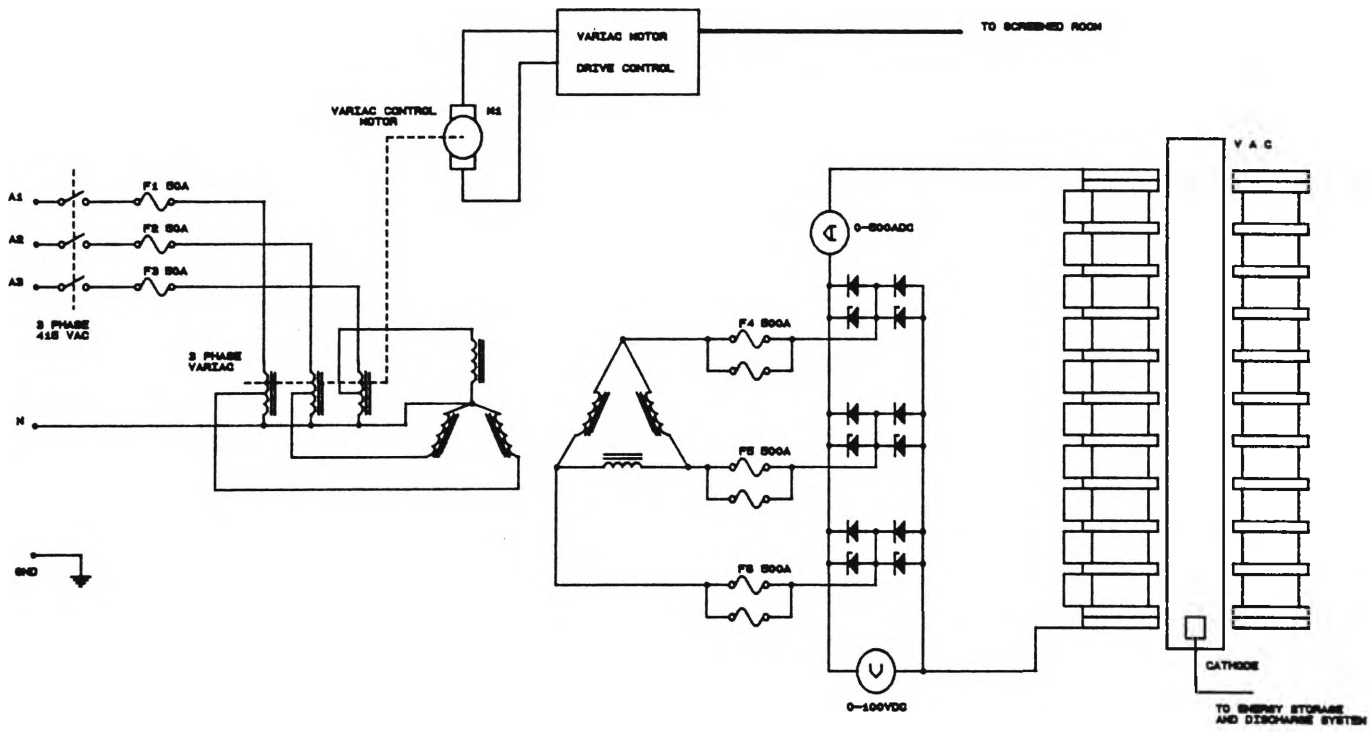

Fig. A2.4 Circuit diagram of the remote controlled, magnet power supply

APPENDIX 3

A Derivation of First Stage Design Equations for a PFN

Figure A3.1 is the equivalent circuit of a portion of an n section PFN. For exactness, the circuit includes parasitic elements for the capacitor, C_n and inductor, L_n.

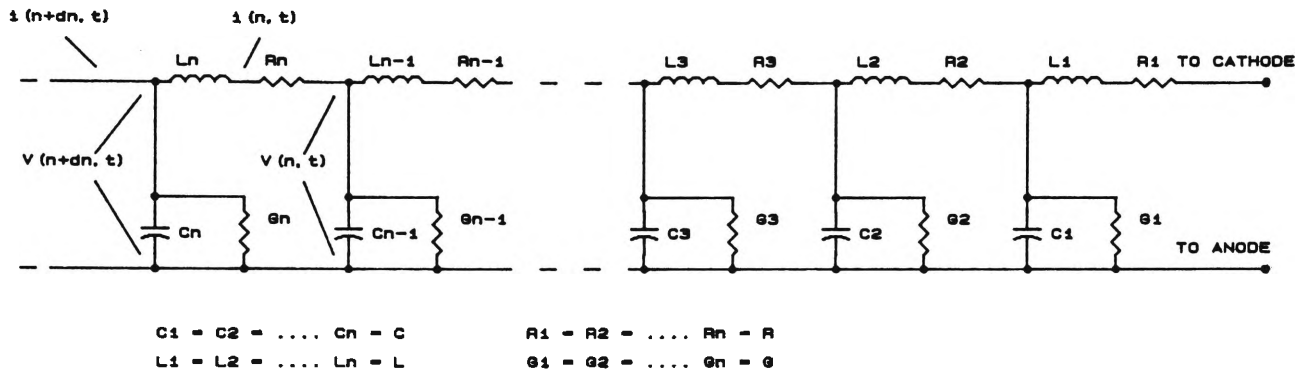

Fig. A3.1 An equivalent circuit of a PFN with n sections

As the current pulse propagates along the length of the PFN, the instantaneous voltage and current at the input and output of any one section differ and are a function of both time (t) and the relative position (n = 1,2,3,...) along the PFN.

Consider a single section (δn) of the line.

i.e. $\delta n = (n+1) - n = 1$ (A3.1)

Let the voltage at the input of the section = $v(n,t)$

Let the voltage at the output of the section = $v(n+\delta n,t)$

Define $\delta v(n,t) = v(n+\delta n,t) - v(n,t)$ (A3.2)

Likewise,

Let the current into the section = $i(n,t)$

Let the current out of the section = $i(n+\delta n,t)$

Define $\delta i(n,t) = i(n+\delta n,t) - i(n,t)$ (A3.3)

Two equations can now be written using Kirchoff's laws for the section of line:

$$\frac{\delta v(n,t)}{\delta n} = -Ri(n,t) - L\frac{\delta i(n,t)}{\delta t} \quad \text{(A3.4)}$$

$$\frac{\delta i(n,t)}{\delta n} = -Gv(n,t) - C\frac{\delta v(n,t)}{\delta t} \quad \text{(A3.5)}$$

Taking the Laplace Transform of both equations gives the following:

$$-\frac{\delta}{\delta n}\left[\!\left[V(n,s)\right]\!\right] = RI(n,s) + sLI(n,s) \quad \text{(A3.6)}$$

$$-\frac{\delta}{\delta n}\left[\!\left[I(n,s)\right]\!\right] = GV(n,s) + sCV(n,s) \quad \text{(A3.7)}$$

Differenciate (A3.6) with respect to n:

$$-\frac{\delta^2 V(n,s)}{\delta n^2} = R\frac{\delta}{\delta n}\left[\!\left[I(n,s)\right]\!\right] + sL\frac{\delta}{\delta n}\left[\!\left[I(n,s)\right]\!\right] \quad \text{(A3.8)}$$

Combine with equation (A3.7)

$$\frac{\delta^2 V(n,s)}{\delta n^2} - V(n,s)\left[(R+sL)(G+sC)\right] = 0 \qquad \text{(A3.9)}$$

$$\text{Let } \alpha = \sqrt{(R+sL)(G+sc)} \qquad \text{(A3.10)}$$

A solution exists for equation (A3.9) in the following form:

$$V(n,s) = Ae^{-\alpha n} + Be^{\alpha n} \qquad \text{(A3.11)}$$

$$\frac{\delta V(n,s)}{\delta n} = -\alpha Ae^{-\alpha n} + \alpha Be^{\alpha n} \qquad \text{(A3.12)}$$

Substitution into equation (A3.6) results in the following equation in Laplacian form:

$$I(n,s) = \sqrt{\frac{G+sC}{R+sL}}\left[Ae^{-\alpha n} - Be^{\alpha n}\right] \qquad \text{(A3.13)}$$

By definition the characteristic impedance $Z_o = \dfrac{V(n,s)}{I(n,s)}$

(A3.14)

Therefore: $Z_o = \sqrt{\dfrac{R+sL}{G+sC}}$

(A3.15)

For a losses PFN, R = G = 0 and $Z_o = \sqrt{\dfrac{L}{C}}$

(A3.16)

Solutions for A and B in equation (A3.13) can be found by the application of boundary conditions for the PFN. Suppose now one end of the PFN, with N sections, is attached to the arc load of a VAC at n = 0. For simplicity, the arc will be modeled as a fixed impedance $Z_{arc} = Z_o(s)$ in series with a voltage source $V_{arc}(s)$ and a switch which closes at t=0. The far end of the line is left as an open circuit (i.e. $Z(N,s) \approx \infty$).

The following equations now apply:

$$V(N,s) = I(N,s)\ Z(N,s) \tag{A3.17}$$

$$V_{arc}(s) = I(0,s)\ Z_{arc}(s) + V(0,s) \tag{A3.18}$$

$$I(N,s) = \frac{Ae^{-\alpha N}}{Z_o(s)} - \frac{Be^{\alpha N}}{Z_o(s)} \tag{A3.19}$$

Therefore:

$$V(N,s) = \frac{Z(N,s)}{Z_o(s)} \left[Ae^{-\alpha N} - Be^{\alpha N} \right] \tag{A3.20}$$

Solving (A3.20) for B yields the following:

$$B = A \left[\frac{Z(N,s) - Z_o(s)}{Z(N,s) + Z_o(s)} \right] e^{-2\alpha N} \tag{A3.21}$$

$$= A \left[\frac{1 - \dfrac{Z_o(s)}{Z(N,s)}}{1 + \dfrac{Z_o(s)}{Z(N,s)}} \right] e^{-2\alpha N} \tag{A3.22}$$

But $Z(N,s) \approx \infty$

Therefore:

$$B = Ae^{-2\alpha N} \qquad \text{(A3.23)}$$

From the boundary condition (A3.18), the following may be written:

$$V(0,s) = \frac{Z_{arc}(s)}{Z_o(s)}(A - B) + (A + B) = 2A \qquad \text{(A3.24)}$$

$$A = \frac{V(0,s)}{2} \qquad \text{(A3.25)}$$

Substitution of A and B into the equation (A3.19) gives the following general solution for the current:

$$I(n,s) = \frac{V(0,s)}{2Z_o(s)}\left[e^{-\alpha n} - e^{-\alpha(2N-n)} \right] \qquad \text{(A3.26)}$$

If the line is assumed lossless then $\alpha = s\sqrt{LC}$ (A3.27)

Assume that the line is initially charged to a voltage V_o. When the arc if formed the circuit can be represented as an impedance Z_{arc} in series with a step function generator. Therefore:

$$V(0,s) = \frac{V_o}{s} \qquad \text{(A3.28)}$$

$$I(n,s) = \frac{V_o}{2sZ_o(s)}\left[e^{-s\sqrt{(LC)}n} - e^{-s\sqrt{(LC)}(2N-n)} \right] \qquad \text{(A3.29)}$$

Taking the inverse Laplace Transform results in a function in the time domain:

$$i(n,t) = \frac{V_o}{2Z_o}\left[H\left[t - n\sqrt{(LC)}\right] - H\left[t - (2N-n)\sqrt{(LC)}\right]\right] \qquad (A3.30)$$

The arc load is connected to the PFN at n=0.

Therefore:

$$i(0,t) = i_{arc}(t) = \frac{V_o}{2Z_o}\left[H(t) - H(t-2N\sqrt{(LC)}) \right] \qquad (A3.31)$$

Figure A3.2 is a plot of equation (A3.31). Note that the duration of the pulse is given by the following expression:

$$T = 2N\sqrt{LC} \qquad (A3.32)$$

where N is the number of sections in the line (always an integer) and L and C are, respectively, the inductance and capacitance of each section.

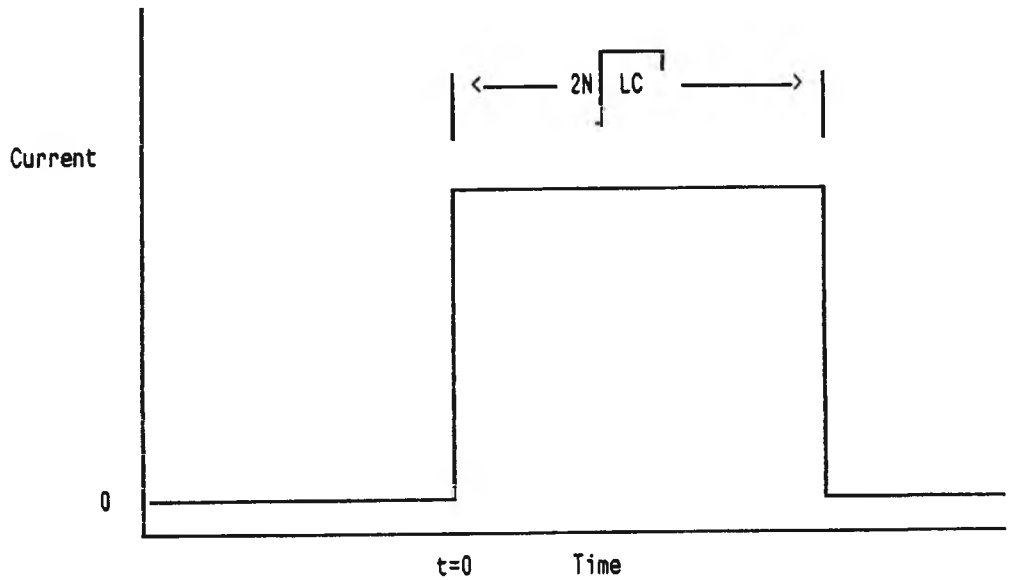

Fig. A3.2 Plot of the ideal pulse response for a PFN

APPENDIX 4

A Mathematical Model and Computer Program for the Optimization of the Solenoid Magnet Spacings

The axial magnetic field, B_z, was provided by a large solenoid magnet which comprised a number of individual pancake shaped coils. A requirement of the experimental design of the VAC rig was that sufficient access should be available between the pancake coils for instrumentation probes and optical components insertion. For ease of manufacture, wooden spacers were used to separate each pancake coil in the solenoid. The pancakes were held firmly in position by compression between two solid end plates tightened together with tie-rods.

The relative position of each pancake in the solenoid affected the overall uniformity of the axial field. Therefore, a compromise was reached between maximum space for instrumentation and maximum achievable field uniformity.

A BASIC computer program, VACMAG, was written to calculate the field at given points in the solenoid for a given current flowing in the pancakes. Figure A4.1 is a diagram of a circular current loop I in a three dimensional co-ordinate system. The radius of the loop from the z axis is R.

The field at a given point P was calculated by integration of the fields due to infinitesimally small current elements T around the loop. Because each pancake comprised a number radially distributed coils, this procedure was repeated for different values of R. For simplicity, P was chosen to be coincident with the position on the z axis of other pancakes.

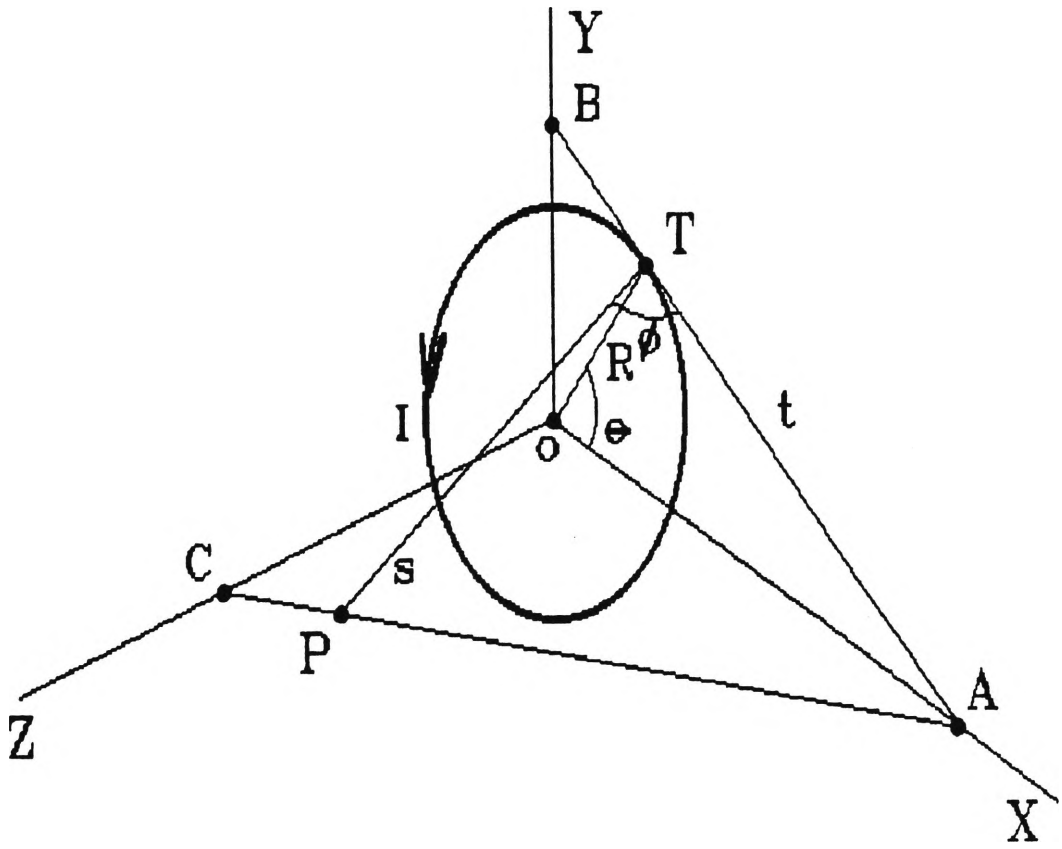

Fig. A4.1 The current loop in a three dimensional coordinate system

The computer program appears below with an output sample for the case using 11 coils, spaced at intervals of 112 mm along the z axis and conductor current of 500 Amps. Table A4.1 is the calculated value of B_z at each position P(0,0,z). The calculated value at P(0,0,0) of 0.0497 T compares well with the measured B_z for a single pancake.

TABLE A4.1

Sample Output of the Computer Program VACMAG

```
Input the number of coils to be used [JJ]=?          11
Input the coil centre to centre spacing [D]=?        0.112
Input the X co-ordinate [Xp] =?                      0
Input the line current to the magnet coils [II]=?    500
```

COORDINATES		FIELD	
X_p (m)	Z_p (m)	B_z (T)	
0.00000	0.00000	0.04970	(*)
0.00000	0.11200	0.03175	
0.00000	0.22400	0.01475	
0.00000	0.33600	0.00716	
0.00000	0.44800	0.00381	
0.00000	0.56000	0.00221	
0.00000	0.67200	0.00138	
0.00000	0.78400	0.00091	
0.00000	0.89600	0.00063	
0.00000	1.00800	0.00045	
0.00000	1.12000	0.00033	
		TOTAL Bz 0.11308	

* The measured value of B_z at (0,0,0) = 0.049 T

Table A4.2 gives the magnetic field profile for this case over the length of the solenoid. It is evident that Bz unacceptably diminishes at the solenoid ends.

For Table A4.3 the calculation was repeated but with twice the conductor current (1000 Amps) flowing in the two end pancakes. This resulted in a more uniform magnetic field. To achieve the same result without increasing the power supply line current (limited to 500 A), an additional coil was placed next to each of the end pancakes.

TABLE A4.2

Magnetic Field at X_p=0 due to a Pancake Coil at N

	COIL NUMBER										
N	1	2	3	4	5	6	7	8	9	10	11
1	0.0497	0.0317	0.0147	0.0072	0.0038	0.0022	0.0014	0.0009	0.0006	0.0005	0.0003
2	0.0317	0.0497	0.0317	0.0147	0.0072	0.0038	0.0022	0.0014	0.0009	0.0006	0.0005
3	0.0147	0.0317	0.0497	0.0317	0.0147	0.0072	0.0038	0.0022	0.0014	0.0009	0.0006
4	0.0072	0.0147	0.0317	0.0497	0.0317	0.0147	0.0072	0.0038	0.0022	0.0014	0.0009
5	0.0038	0.0072	0.0147	0.0317	0.0497	0.0317	0.0147	0.0072	0.0038	0.0022	0.0014
6	0.0022	0.0038	0.0072	0.0147	0.0317	0.0497	0.0317	0.0147	0.0072	0.0038	0.0022
7	0.0014	0.0022	0.0038	0.0072	0.0147	0.0317	0.0497	0.0317	0.0147	0.0072	0.0038
8	0.0009	0.0014	0.0022	0.0038	0.0072	0.0147	0.0317	0.0497	0.0317	0.0147	0.0072
9	0.0006	0.0009	0.0014	0.0022	0.0038	0.0072	0.0147	0.0317	0.0497	0.0317	0.0147
10	0.0005	0.0006	0.0009	0.0014	0.0022	0.0038	0.0072	0.0147	0.0317	0.0497	0.0317
11	0.0003	0.0005	0.0006	0.0009	0.0014	0.0022	0.0038	0.0072	0.0147	0.0317	0.0497
Total B_z at X_p=0	0.1131	0.1445	0.1588	0.1653	0.1682	0.1690	0.1682	0.1653	0.1588	0.1445	0.1131

TABLE A4.3

Magnetic Field at X_p=0 due to a Pancake Coil at N (Additional End Coils added)

	COIL NUMBER										
N	1	2	3	4	5	6	7	8	9	10	11
1	0.0994	0.0635	0.0295	0.0143	0.0076	0.0044	0.0028	0.0018	0.0013	0.0009	0.0007
2	0.0317	0.0497	0.0317	0.0147	0.0072	0.0038	0.0022	0.0014	0.0009	0.0006	0.0005
3	0.0147	0.0317	0.0497	0.0317	0.0147	0.0072	0.0038	0.0022	0.0014	0.0009	0.0006
4	0.0072	0.0147	0.0317	0.0497	0.0317	0.0147	0.0072	0.0038	0.0022	0.0014	0.0009
5	0.0038	0.0072	0.0147	0.0317	0.0497	0.0317	0.0147	0.0072	0.0038	0.0022	0.0014
6	0.0022	0.0038	0.0072	0.0147	0.0317	0.0497	0.0317	0.0147	0.0072	0.0038	0.0022
7	0.0014	0.0022	0.0038	0.0072	0.0147	0.0317	0.0497	0.0317	0.0147	0.0072	0.0038
8	0.0009	0.0014	0.0022	0.0038	0.0072	0.0147	0.0317	0.0497	0.0317	0.0147	0.0072
9	0.0006	0.0009	0.0014	0.0022	0.0038	0.0072	0.0147	0.0317	0.0497	0.0317	0.0147
10	0.0005	0.0006	0.0009	0.0014	0.0022	0.0038	0.0072	0.0147	0.0317	0.0497	0.0317
11	0.0007	0.0009	0.0013	0.0018	0.0028	0.0044	0.0076	0.0143	0.0295	0.0635	0.0994
Total B_z at X_p	0.1631	0.1767	0.1742	0.1734	0.1734	0.1735	0.1734	0.1734	0.1742	0.1767	0.1631

A profile of the solenoid magnetic field, along the center line ($X_p = 0$), is presented in Table A4.4. Additional points mid-way between the pancakes are included.

TABLE A4.4

MAGNETIC FIELD AT X_p DUE TO A PANCAKE COIL AT N
(Additional End Coils added)
COIL AND SPACER (SP) NUMBER

N	1	SP	2	SP	3	SP	4	SP	5	SP	6	SP	7	SP	8	SP	9	SP	10	SP	11
1	.10	.08	.06	.05	.03	.02	.01	.01	.01	.01	.00	.00	.00	.00	.00	.00	.00	.00	.00	.00	.00
2	.03	.04	.05	.04	.03	.02	.01	.01	.01	.01	.00	.00	.00	.00	.00	.00	.00	.00	.00	.00	.00
3	.01	.02	.03	.04	.05	.04	.03	.02	.01	.01	.01	.01	.00	.00	.00	.00	.00	.00	.00	.00	.00
4	.01	.01	.01	.02	.03	.04	.05	.04	.03	.02	.01	.01	.01	.01	.00	.00	.00	.00	.00	.00	.00
5	.00	.01	.01	.01	.01	.02	.03	.04	.05	.04	.03	.02	.01	.01	.01	.01	.00	.00	.00	.00	.00
6	.00	.00	.00	.01	.01	.01	.01	.02	.03	.04	.05	.04	.03	.02	.01	.01	.01	.01	.00	.00	.00
7	.00	.00	.00	.00	.00	.01	.01	.01	.01	.02	.03	.04	.05	.04	.03	.02	.01	.01	.01	.01	.00
8	.00	.00	.00	.00	.00	.00	.00	.01	.01	.01	.01	.02	.03	.04	.05	.04	.03	.02	.01	.01	.01
9	.00	.00	.00	.00	.00	.00	.00	.00	.00	.01	.01	.01	.01	.02	.03	.04	.05	.04	.03	.02	.01
10	.00	.00	.00	.00	.00	.00	.00	.00	.00	.00	.00	.01	.01	.01	.01	.02	.03	.04	.05	.04	.03
11	.00	.00	.00	.00	.00	.00	.00	.00	.00	.00	.00	.01	.01	.01	.01	.02	.03	.05	.06	.08	.10
Total B_z at X_p	.16	.17	.18	.18	.17	.17	.17	.17	.17	.17	.17	.17	.17	.17	.17	.17	.17	.18	.18	.17	.16

The results generated above were used to calculate the VAC magnetic field profile shown in Table A4.5.

TABLE A4.5
MAGNETIC FIELD PROFILE FOR THE VAC (CENTRE LINE TO WALL)
(Additional End Coils added)
AXIAL POSITION NUMBER

RADIUS (cms)	1	SP	2	SP	3	SP	4	SP	5	SP	6	SP	7	SP	8	SP	9	SP	10	SP	11
0	.16	.17	.18	.18	.17	.17	.17	.17	.17	.17	.17	.17	.17	.17	.17	.17	.17	.18	.18	.17	.16
10	.16	.17	.18	.18	.17	.17	.17	.17	.17	.17	.17	.17	.17	.17	.17	.17	.17	.18	.18	.17	.16
20	.16	.17	.18	.18	.17	.17	.17	.17	.17	.17	.17	.17	.17	.17	.17	.17	.17	.18	.18	.17	.16
30	.16	.17	.18	.18	.17	.17	.17	.17	.17	.17	.17	.17	.17	.17	.17	.17	.17	.18	.18	.17	.16
40	.17	.17	.18	.18	.17	.17	.17	.17	.17	.17	.17	.17	.17	.17	.17	.17	.17	.18	.18	.17	.17
50	.17	.17	.18	.18	.17	.17	.17	.17	.17	.17	.17	.17	.17	.17	.17	.17	.17	.18	.18	.17	.17
60	.17	.17	.18	.18	.17	.17	.17	.17	.17	.17	.17	.17	.17	.17	.17	.17	.17	.18	.18	.17	.17
70	.17	.18	.18	.18	.17	.17	.17	.17	.17	.17	.17	.17	.17	.17	.17	.17	.17	.18	.18	.18	.17
80	.18	.18	.18	.18	.18	.18	.18	.18	.18	.18	.18	.18	.18	.18	.18	.18	.18	.18	.18	.18	.18
89(*)	.18	.18	.18	.18	.18	.18	.18	.18	.18	.18	.18	.18	.18	.18	.18	.18	.18	.18	.18	.18	.18

* Chamber Wall

```
1 REM ***************************************************
2 REM * VACMAG    A program for the solution of the magnetic *
3 REM *           field at a point P(x,y,z) due to a current *
4 REM *           flowing in a circular conductor.          *
5 REM ***************************************************
10 DEFINT J-K
20 CLS
30 OPTION BASE 1
40 CLEAR
50 INPUT "Input the number of coils to be used [JJ]=";JJ
60 J=2*JJ
70 M=2*J-1
80 DIM BZ(J,M)
90 DIM TBZ(JJ)
100 INPUT "Input the coil centre to centre spacing [D]=";D
110 INPUT "Input the X co-ordinate [xp]=";XP
120 IF XP=0 THEN XP=1E-10
130 INPUT "Input the line current to the magnet coils [Il]=";IL
140 ZP=1E-10
150 TBX=0
160 TBY=0
170 TBZ=0
180 PRINT" "
190 PRINT "       xp                zp                Bz"
200 FOR K=J/2 TO J-1
210  BX=0
220  BY=0
230  BZ=0
240  TH=0
250  NN=9
260  I=IL*4
270  DTH=3.14159/NN
280  FOR QQ=0 TO 7
290       R=.1322+QQ*.0243
300       TH=DTH/2
310       FOR Q=1 TO NN
320            X=R*COS(TH)
330            Y=R*SIN(TH)
340            T=R*TAN(TH)
350            RA=COS(TH)/R
360            A=1/RA
370            RB=SIN(TH)/R
380            B=1/RB
390            C=A*ZP/(A-XP)
400            RC=1/C
410            LL=ZP*ZP+(A-XP)*(A-XP)
420            L=SQR(LL)
430            SS=ZP*ZP+Y*Y+(XP-X)*(XP-X)
440            S=SQR(SS)
450            SP=(S+T+L)/2
460            TNANG=SQR((SP-S)*(SP-T)/(SP*(SP-L)))
470            PHI=2*ATN(TNANG)
```

```
480             DB=.0000001*I*R*DTH*SIN(PHI)/SS
490             PP=1/(RA*RA+RB*RB+RC*RC)
500             P=SQR(PP)
510             DBX=DB*P*RA
520             BX=BX+DBX
530             DBY=DB*P*RB
540             BY=BY+DBY
550             DBZ=DB*P*RC
560             BZ=BZ+DBZ
570             TH=TH+DTH
580             NEXT Q
590         NEXT QQ
600  PRINT USING"     #.#####      ";XP;ZP;2*BZ
610  BZ(K,1)=2*BZ
620  TBX=TBX+BX
630  TBY=TBY+BY
640  TBZ=TBZ+BZ
650  ZP=ZP+D
660  NEXT K
670 PRINT " "
700 PRINT USING "            TOTAL Bz #.#####      ";2*TBZ
710 PRINT " "
720 FOR G=1 TO JJ
730  BZ(J/2-G,1)=BZ(J/2+G,1)
740 NEXT G
750 FOR H=2 TO JJ
760  FOR K=2 TO J-1
770  BZ(K,H)=BZ(K-1,H-1)
780  NEXT K
790 NEXT H
800 FOR H=1 TO JJ
810  BZ(J/2,H)=2*BZ(J/2,H)
820  BZ(J-1,H)=2*BZ(J-1,H)
830 NEXT H
840 FOR K=J/2 TO J-1
850  FOR H=1 TO JJ
860       PRINT USING ".#### ";BZ(K,H);
870       NEXT H
880  PRINT " "
890  NEXT K
900 PRINT " "
910 FOR H=1 TO JJ
920  FOR K= J/2 TO J-1
930       TBZ(H)=TBZ(H)+BZ(K,H)
940       NEXT K
950  NEXT H
960 FOR H=1 TO JJ
970  PRINT USING ".#### ";TBZ(H);
980 NEXT H
1000 FOR H=1 TO JJ
1005      FOR K=J/2 TO J-1
1010      BZ(K,2*JJ-(2*H-1))=BZ(K,JJ-(H-1))
1015      NEXT K
1020      NEXT H
1040 FOR K=J/2 TO J-1
```

```
1050       H=2
1060       BZ(K,H)=(BZ(K,H-1)+BZ(K,H+1))/2
1070       H=H+2
1080       IF H<2*JJ-1 THEN GOTO 1060
1090       NEXT K
1100 PRINT " "
1105 PRINT " "
1110 FOR K=J/2 TO J-1
1120       FOR H=1 TO 2*JJ-1
1130            PRINT USING ".##";BZ(K,H);
1140            NEXT H
1150       PRINT " "
1160       NEXT K
1170 PRINT " "
1180 DIM TTBZ(2*JJ)
1190 FOR H=1 TO 2*JJ-1
1200       FOR K=J/2 TO J-1
1210            TTBZ(H)=TTBZ(H)+BZ(K,H)
1220            NEXT K
1230       NEXT H
1240 FOR H=1 TO 2*JJ-1
1250       PRINT USING ".##";TTBZ(H);
1260       NEXT H
1270 PRINT " "
```

APPENDIX 5

VAC Data Acquisition, Recording, and Analysis

The data acquisition system for the VAC comprised three basic components:

i) An IBM PC/XT compatible computer.

ii) An IEEE-488 interface card.

iii) Two Philips PM3302 digitising cathode ray oscilloscopes (CROs).

Figure A5.1 shows the hardware arrangement.

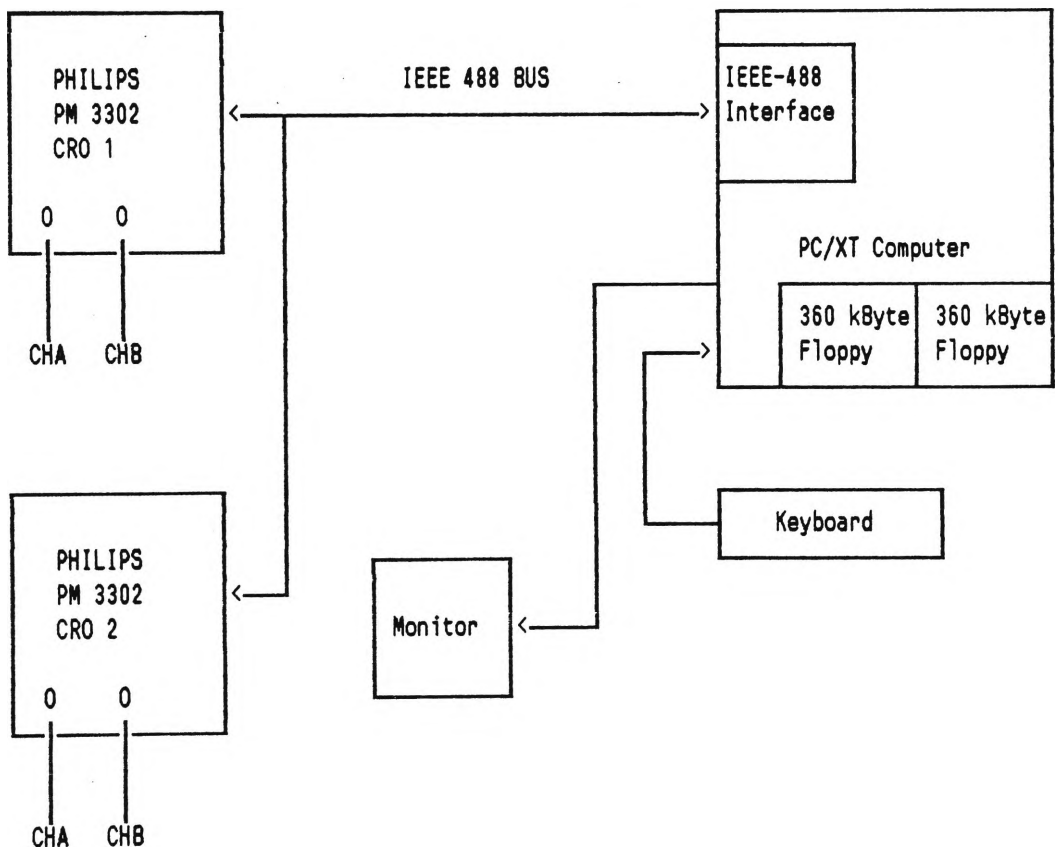

Fig. A5.1 General Arrangement of the Data Acquisition System

Analogue signals were connected to CHA and CHB inputs of both CROs. The command to store was triggered either

internally from the amplitude of the CHA analogue waveform or externally from the current waveform or the laser trigger pulse. Each channel could convert and store 1024 individual 8 bit resolution data points. The maximum time resolution was 5 µS/Div corresponding to 5 nS/data point.

A BASIC program called CROINT.BAS was used for both the instrumentation initialisation and data acquisition. Data flow from the experiment is summarised in figure A5.2.

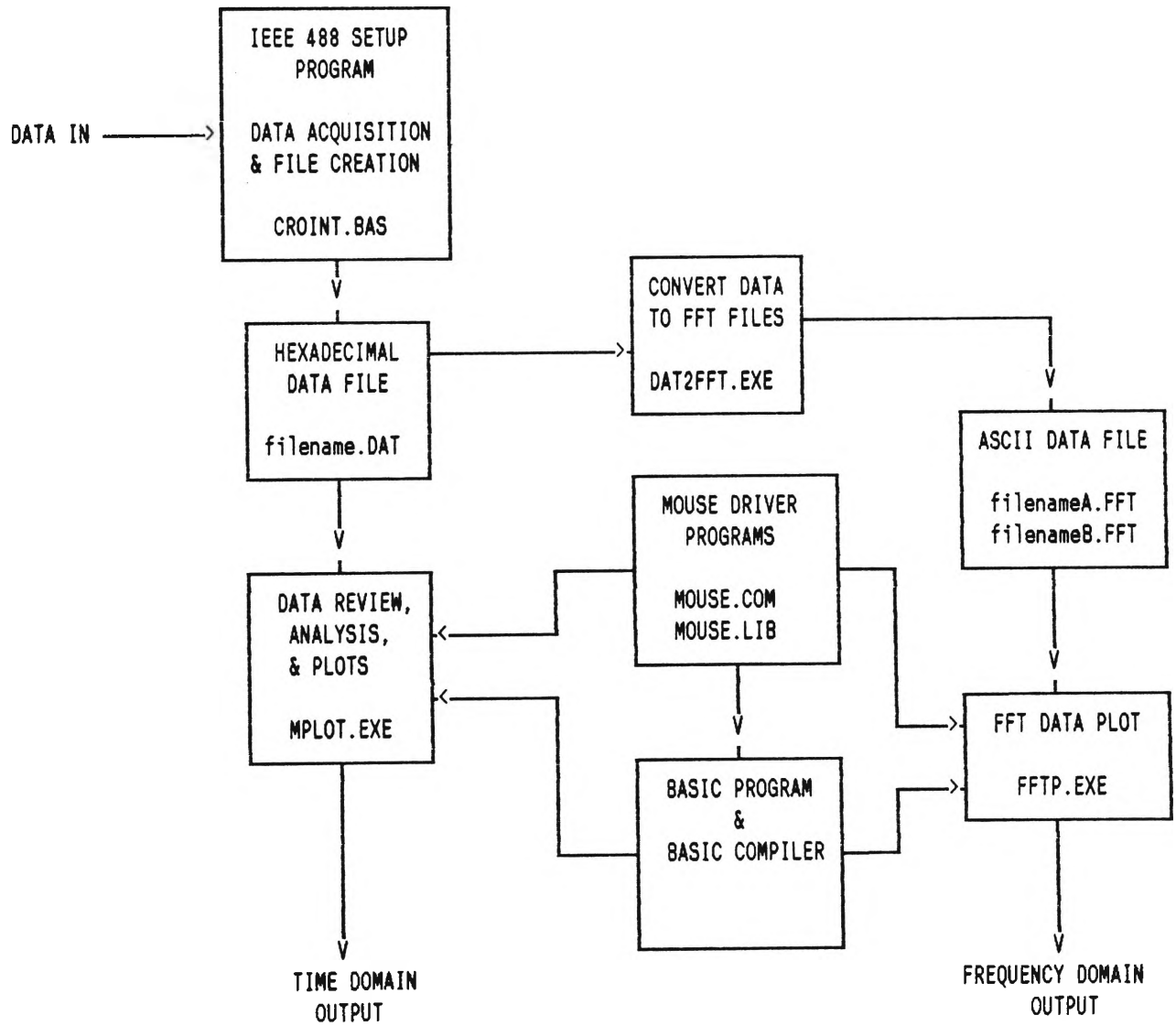

Fig. A5.2 Block diagram showing data acquisition, storage, conversion and processing programs.

Commercial software was used wherever possible to gather and process data from the VAC. However a number of additional programs were necessary for data bridging, analysis and display. These were written in either BASIC or compiled BASIC.

Following the capture of an event by the digital storage CRO, data from both CRO channels was stored by the program CROINT.BAS as a single sequential hexadecimal file. Usually a number of files were created during the course of an experimental run. Whilst it was possible to immediately plot the recorded data files on the monitor, most data processing was performed away from the laboratory. The capability to store, retrieve, copy and process the VAC data greatly facilitated the experimental program.

All data files could be viewed on the computer monitor as a time plot using the compiled BASIC program called MPLOT.EXE. This program also included an on-screen cursor that could be moved by a MOUSE connected to the computer serial port. The pointer co-ordinates were converted in the program, scaled and also displayed on the monitor. By manoeuvring the MOUSE, the instantaneous time and amplitude of an event could be directly read from the monitor. Hardcopy of data plots was made by using the "print screen" (PrtSc) command from the keyboard.

A fast fourier transform (FFT) program was used to determine the plasma rotation speed. For this purpose, the hexadecimal data file representing the stored waveform in the time domain was read by the compiled BASIC program called DAT2FFT.EXE and transformed to the frequency domain. The program then stored the frequency domain data on disk as an

ASCII file. The FFT output was plotted on the monitor by the program FFTP.EXE which also included a MOUSE routine. The amplitude and frequency of points on the screen could be directly read by using the MOUSE to move the cursor. Figure A5.3 is a typical time domain data plot from a biased Langmuir probe. Figure A5.4 is the FFT of the same data.

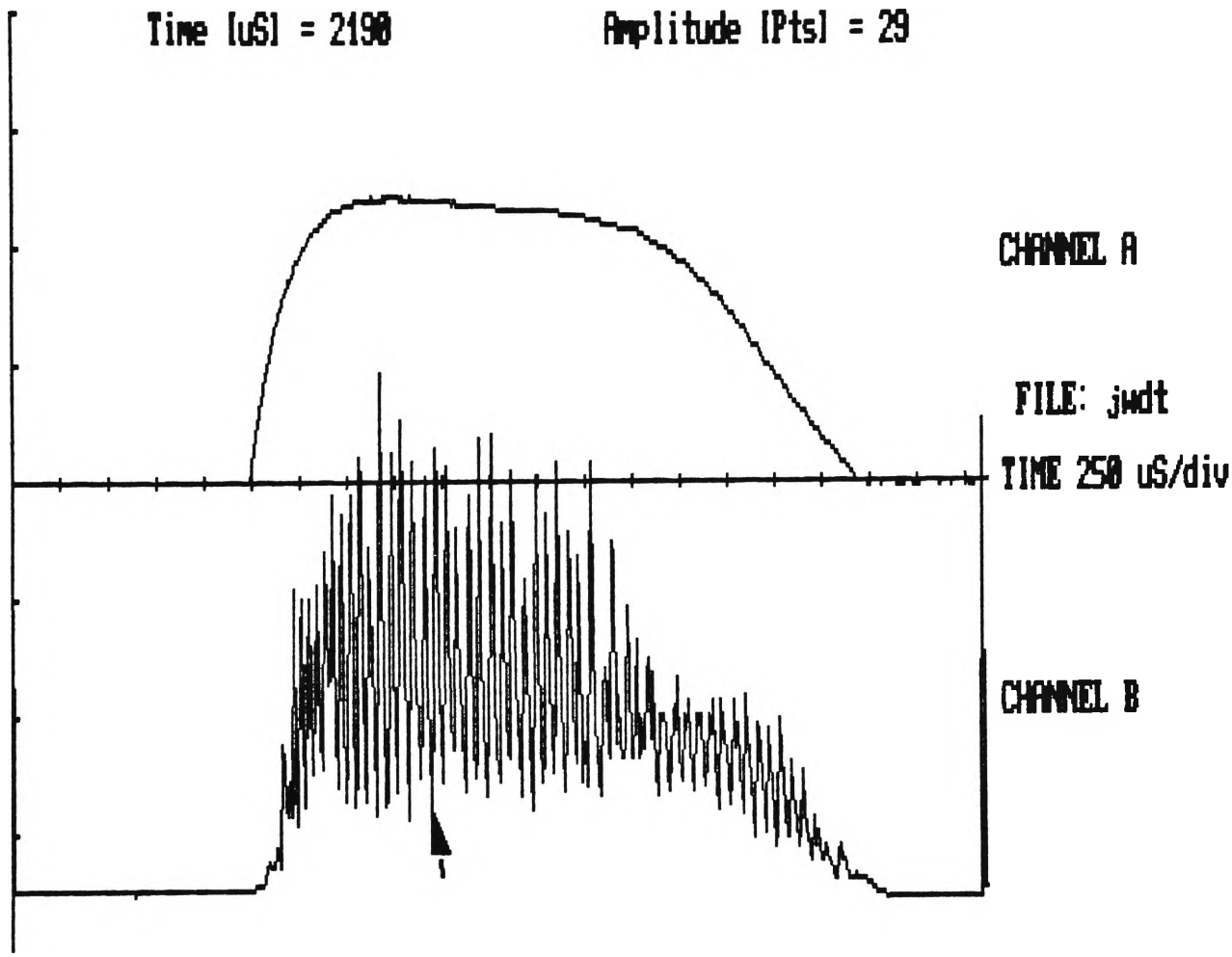

Fig A5.3 Time domain plot of a biased Langmuir probe signal showing the MOUSE cursor. Time and amplitude information (top of screen) refer to the arrow point.

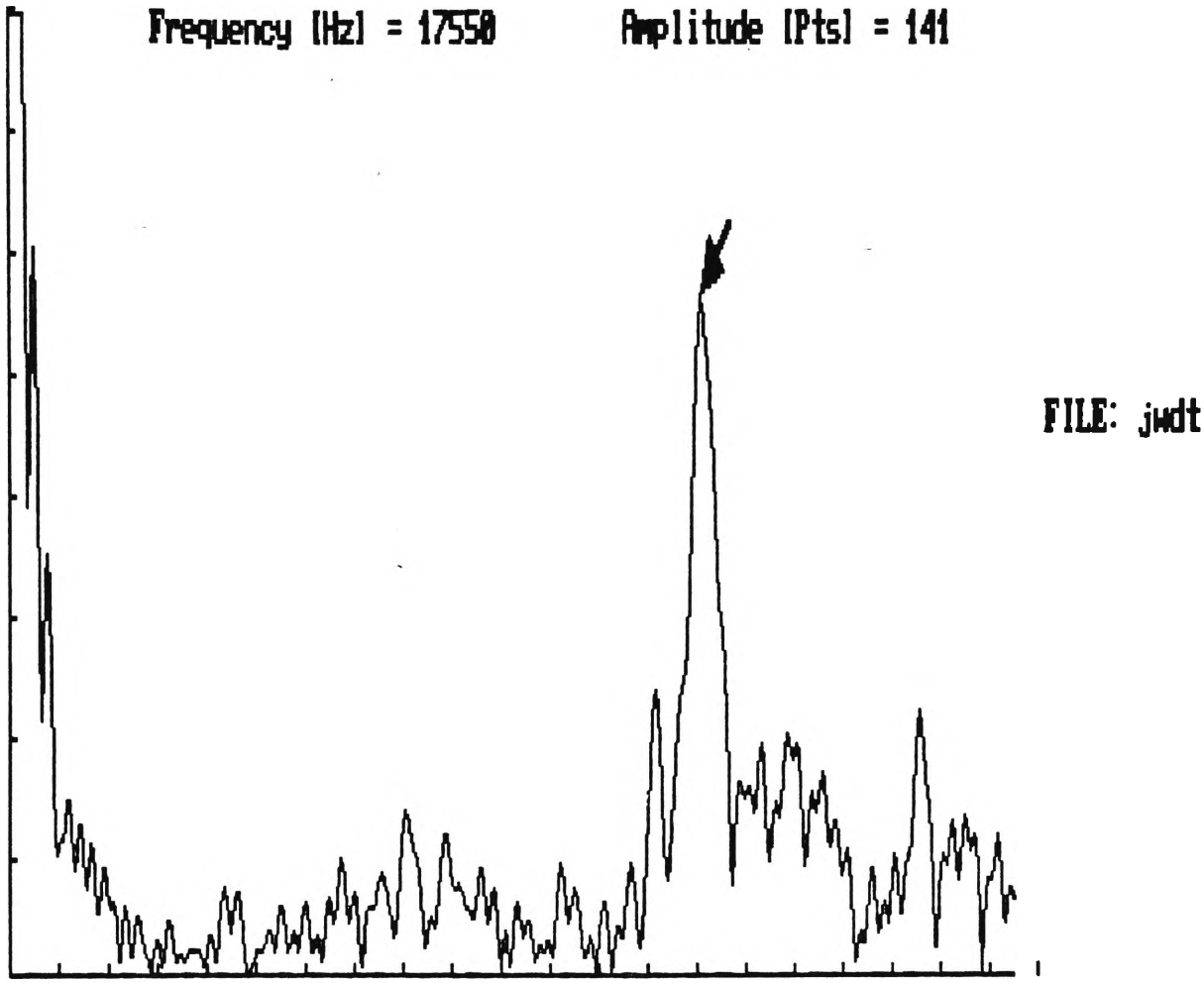

Fig. A5.4 Frequency transformed data plot of the data file shown in figure A5.3. Frequency and amplitude information (top of screen) refer to the MOUSE cursor arrow point

CROINT.BAS Computer Program Source Listing

(by N. Clarke, ANSTO)

```
1 REM ********************************************************
2 REM * CROINT   A program to transfer stored waveforms from *
3 REM *          one or two Philips PM 3302 digitising CROs. *
4 REM *          Data is transferred via an IEEE 488 bus to  *
5 REM *          the computer where it is stored on a 5 1/4" *
6 REM *          floppy disk.                                *
7 REM ********************************************************
30      CLEAR   ,30000 :DEF SEG=&HB96:     ' BASIC Declarations
40      IBINIT1% = -5791!:IBRD%=IBINIT1%+329:IBSIC%=IBINIT1%
        +220:IBFIND%=IBINIT1%+138
50      IBINIT2% = IBINIT1% + 3:IBRDF%=IBINIT1%+403:   ' Lines
        1 through 6 MUST be included in your program.
60      BLOAD "bib.m",IBINIT1%
70      REM CALL ibinit1%(IBFIND%,IBTRG%,IBCLR%,IBPCT%,IBSIC%,
        IBLOC%,IBPPC%,IBBNA%,IBONL%,IBRSC%,IBSRE%,IBRSV%,
        IBPAD%,IBSAD%,IBIST%,IBDMA%,IBEOS%,IBTMO%,IBEOT%,
        IBRDF%,IBWRTF%)
80      REM CALL ibinit2%(IBGTS%,IBCAC%,IBWAIT%,IBPOKE%,
        IBWRT%,IBWRTA%,IBCMD%,IBCMDA%,IBRD%,IBRDA%,IBSTOP%,
        IBRPP%,IBRSP%,IBDIAG%,IBXTRC%,IBRDI%,IBWRTI%,IBRDIA%,
        IBWRTIA%,IBSTA%,IBERR%,IBCNT%)
90 DIM GRAFAM[1030],GRAFBM[1030]
100 SCREEN 2:KEY OFF:CLS: LINE INPUT" (S)TORE TRACES, (P)LOT
FROM DISK, .DAT (D)IRECTORY, (G)RAPH FROM DISK, (E)ND ";ANSW$
110 CLS
120 IF ANSW$="S" OR ANSW$="s" THEN GOSUB 26000 ELSE IF ANSW$=
"E" OR ANSW$="e" THEN END
140 IF ANSW$="D" OR ANSW$="d" THEN GOSUB 2000
160 IF ANSW$="P" OR ANSW$="p" THEN GOSUB 24000
180 IF ANSW$="G" OR ANSW$="g" THEN GOSUB 3000
200 GOTO 100
1000 REM loadfile from disk
1100 LOCATE 1,1:LINE INPUT "enter filename (b: and .dat
assumed):";DATFILE$
1130 OPEN "b:"+DATFILE$+".dat" FOR INPUT AS #1
1140 RETURN
1150 FOR I=1 TO 1024
1160 A$=INPUT$(1,#1)
1164 GRAFAM(I)=ASC(A$)
1170 NEXT
1180 FOR I=1025 TO 2048
1194 GRAFBM[I-1024]=ASC(A$)
1200 NEXT:CLOSE:'CLOSE ALL OPEN FILES
1220 GOSUB 20100:RETURN
2000 REM show files on disk
2130 LOCATE 1,1:FILES "b:*.dat"
2150 PRINT "press a key to return to menu";:
2160 A$=INKEY$: IF A$="" THEN GOTO 2160:
2170 RETURN
3000 REM plot a trace
```

```
3100 GOSUB 1000:'open file
3105 CLS:A$=INPUT$(2,#1):GRAFAM[1]=ASC(MID$(A$,2,1))
3115 PSET (1,GRAFAM[1]*.78125)
3120 FOR I=2 TO 512
3130 A$=INPUT$(2,#1):GRAFAM[I]=ASC(MID$(A$,2,1))
3150 LINE -(I,GRAFAM[I]*.78125)
3160 NEXT
4000 REM plot b trace
4105 A$=INPUT$(2,#1):GRAFBM[1]=ASC(MID$(A$,2,1))
4115 PSET (1,GRAFBM[1]*.78125)
4120 FOR I=2 TO 511
4130 A$=INPUT$(2,#1):GRAFBM[I]=ASC(MID$(A$,2,1))
4150 LINE -(I,GRAFBM[I]*.78125)
4160 NEXT:CLOSE
4170 A$=INKEY$:LOCATE 1,1:PRINT"press any key to return";:
4180 A$=INKEY$:IF A$="" THEN GOTO 4180
4190 LOCATE 1,1: PRINT"                                    ";:LOCATE
     1,1:RETURN
20100 REM clear first line
20110 PRINT" ":RETURN
24000 REM plot data to plotter
24010 GOSUB 1000
24050 LOCATE 1,1:INPUT "data step size(e.g. 3 gives every
third point) ";FOOT
24060 INPUT "timebase(microseconds per div) ";TIMEBASE
24070 INPUT "PLOT SIZE A(3) or A(4) ? ";PLOTSIZE
24080 IF PLOTSIZE<4 THEN GOTO 24500
24090 LEFTX=100:RIGHTX=1636:LEFTY=152:RIGHTY=2200
24100 OPEN "com1:2400,e,7,1,bin" AS 2
24110 PRINT#2,"h":PRINT#2,"j1":PRINT#2,"m";LEFTX;","LEFTY
24120 PRINT#2,"x 0,102,20":PRINT#2,"x 1,96,16":PRINT#2,"m";
RIGHTX;",";LEFTY:PRINT#2,"x 2,102,20":PRINT#2,"m";LEFTX;",";
RIGHTY:PRINT#2,"x 3,96,16"
24130 PRINT#2,"j2"
24160 FOR I=1 TO 1024
24170 A$=INPUT$(1,#1):GRAFAM[I]=ASC(A$):
24180 NEXT
24200 PRINT#2,"m";STR$(GRAFAM[1]*6+LEFTX);","STR$(LEFTY):
PRINT#2,"d";:
24220 FOR I=1 TO 1024 STEP FOOT
24230 POINTY$=STR$(I*2+LEFTY):POINTX$=STR$((GRAFAM[I])*6+LEFT
     X)
24240 PRINT#2,POINTX$;",";POINTY$;:IF I<1024 THEN PRINT#2,",";
24250 FOR J=1 TO 200:NEXT:NEXT
24260 FOR I=1 TO 1024
24270 A$=INPUT$(1,#1):GRAFBM[I]=ASC(A$):
24280 NEXT
24290 PRINT#2," ":PRINT#2,"j3":'PUT SPACE TO GIVE <CR> ONLINE
STRING
24295 PRINT#2,"j3"
24300 PRINT#2,"m";STR$(GRAFBM[1]*6+LEFTX);","STR$(LEFTY):
     PRINT#2,"d";:
24320 FOR I=1 TO 1024 STEP FOOT
24325 IF I > 1024 THEN GOTO 24350
24330 POINTY$=STR$(I*2+LEFTY):POINTX$=STR$((GRAFBM[I])*6+
```

```
      LEFTX)
24340 PRINT#2,POINTX$;",";POINTY$;:IF I<1024 THEN PRINT#2,",";
24350 FOR J=1 TO 100:NEXT:NEXT
24355 PRINT#2," ":'PUT SPACE TO GIVE <CR> ONLINE STRING
24360 PRINT#2,"j1":PRINT#2,"s 90":PRINT#2,"q1":PRINT#2,"m";
      STR$(LEFTX+200);",";STR$(RIGHTY+40):PRINT#2,"p";DATFILE$
24370 PRINT#2,"s 30":PRINT#2,"m";STR$(LEFTX+300);",";
      STR$(RIGHTY+20):PRINT#2,"p";STR$(.5*TIMEBASE);" Usec/
      div"
24380 PRINT#2,"h":CLOSE
24390 LOCATE 1,1:GOSUB 24395
24395 PRINT"                                                    ":RETURN
24500 REM plot A3 size sheet
24510 LEFTX=100:RIGHTX=3172:LEFTY=152:RIGHTY=2200
24520 OPEN "com1:2400,e,7,1,bin" AS 2
24530 PRINT#2,"h":PRINT#2,"j1":PRINT#2,"m";LEFTX;","LEFTY
24540 PRINT#2,"x 0,128,16":PRINT#2,"x 1,154,19":PRINT#2,"m";
      RIGHTX;",";LEFTY:PRINT#2,"x 2,128,16":PRINT#2,"m";LEFTX;
      ",";RIGHTY:PRINT#2,"x 3,154,19"
24550 PRINT#2,"j2"
24560 FOR I=1 TO 1024
24570 A$=INPUT$(1,#1):GRAFAM[I]=ASC(A$):
24580 NEXT
24590 PRINT#2,"m";STR$(LEFTX);","STR$((256-GRAFAM[1])*8+
      LEFTY):PRINT#2,"d";:
24600 FOR I=1 TO 1024 STEP FOOT
24610 POINTX$=STR$(I*3+LEFTX):POINTY$=STR$((256-GRAFAM[I])*8+
      LEFTY)
24620 PRINT#2,POINTX$;",";POINTY$;:IF I<1024 THEN PRINT#2,",";
24630 FOR J=1 TO 200:NEXT:NEXT
24640 FOR I=1 TO 1024
24650 A$=INPUT$(1,#1):GRAFBM[I]=ASC(A$):
24660 NEXT
24670 PRINT#2," ":PRINT#2,"j3":'PUT SPACE TO GIVE <CR> ONLINE
      STRING
24680 PRINT#2,"j3"
24690 PRINT#2,"m";STR$(LEFTX);","STR$((256-GRAFBM[1])*8+
      LEFTY):PRINT#2,"d";:
24700 FOR I=1 TO 1024 STEP FOOT
24710 IF I > 1024 THEN GOTO 24740
24720 POINTX$=STR$(I*3+LEFTX):POINTY$=STR$((256-GRAFBM[I])*8+
      LEFTY)
24730 PRINT#2,POINTX$;",";POINTY$;:IF I<1024 THEN PRINT#2,",";
24740 FOR J=1 TO 100:NEXT:NEXT
24750 PRINT#2," ":'PUT SPACE TO GIVE <CR> ONLINE STRING
24760 PRINT#2,"j1":PRINT#2,"s 120":PRINT#2,"q0":PRINT#2,"m";
      STR$(LEFTX+200);",";STR$(RIGHTY+50):PRINT#2,"p";DATFILE$
24770 PRINT#2,"s 45":PRINT#2,"m";STR$(LEFTX+600);",";
      STR$(RIGHTY+50):PRINT#2,"p";STR$(.5*TIMEBASE);" Usec/
      div"
24780 PRINT#2,"h":CLOSE
24790 LOCATE 1,1:GOSUB 24800
24800 PRINT"                                                    ":RETURN
25000 REM initialise gpib components
25010 BDNAME$="gpib0":CROA$="pm3302a":CROB$="pm3302b"
```

```
25020 CALL IBFIND%(BDNAME$,BRD0%)
25040 CALL IBFIND%(CROA$,CROA%)
25060 CALL IBFIND%(CROB$,CROB%)
25100 REM send interface clear(IFC) to all devices
25110 CALL IBSIC%(BRD0%)
25120 RETURN
26000 REM read to file from ibrdf
26100 GOSUB 25000:LOCATE 1,1
26105 LINE INPUT "Save PM3302(A), Save PM3302(B), Return to
      Menu (R) : "; ANSW$
26110 IF ANSW$="b" OR ANSW$="B" THEN GOSUB 26300 ELSE IF
      ANSW$="r" OR ANSW$="R" THEN CLS:RETURN
26113 IF ANSW$="a" OR ANSW$="A" THEN GOSUB 26115 ELSE GOTO
      26105
26114 GOTO 26105
26115 PRINT:PRINT:PRINT"                          SAVING PM3302A
      TRACES":PRINT
26120 LINE INPUT"enter file name (b: and .dat assumed) :";
      DATFILE$
26140 THISFILE$="b:"+DATFILE$+".dat"
26150 CALL IBRDF%(CROA%,THISFILE$)
26160 PRINT "IBSTATUS= &H";HEX$(IBSTA%);"  ";:IF IBSTA%<0 THEN
      PRINT "***************ibrdf error***************"
26170 PRINT:PRINT
26200 PRINT"To Graph traces just saved, press G, any other key
      returns";:
26205 A$=INKEY$: IF A$="" THEN GOTO 26205:ELSE IF (A$ = "G" OR
      A$ = "g") THEN GOTO 26210 :ELSE CLS:RETURN
26210 GOSUB 1130
26220 GOSUB 3105
26230 RETURN
26300 PRINT:PRINT:PRINT "                          SAVING PM3302B
      TRACES":PRINT
26310 LINE INPUT"enter file name (b: and .dat assumed) :";
      DATFILE$
26320 IF DATFILE$="" THEN DATFILE$="data"
26340 THISFILE$="b:"+DATFILE$+".dat"
26350 CALL IBRDF%(CROB%,THISFILE$)
26360 PRINT "IBSTATUS= &H";HEX$(IBSTA%);"  ";:IF IBSTA%<0 THEN
      PRINT "***************ibrdf error***************"
26370 PRINT:PRINT
26380 GOTO 26200*;'to graph or return
26400 PRINT"To Graph traces just saved, press G, any other key
      returns";:
26405 A$=INKEY$: IF (A$<>"G") OR (A$<>"g") THEN RETURN
26410 GOSUB 1130
26420 GOSUB 3105
26430 RETURN
```

```
1 REM ******************************************************
2 REM * MPLOT    A program to display the data acquired by   *
3 REM *          the Philips PM 3302 digitising CRO. Data is *
4 REM *          read from a sequential hexidecimal file. A  *
5 REM *          Microsoft MOUSE driver program must be      *
6 REM *          resident and the MOUSE must be connected to *
7 REM *          the serial port.                            *
8 REM ******************************************************
10 SCREEN 2
20 CLS
30 KEY OFF
40 DIM A(1026),B(1026),C(1026)
50 PRINT "                '*.DAT'  DATA  FILES ............."
60 PRINT " "
70 PRINT " PRINTING OF FILE TABLE SUPPRESSED IN THIS VERSION"
80 PRINT " "
90 PRINT " "
100 LINE  INPUT "enter file name( '.DAT' assumed) :
";DATFILE$
110 PRINT " "
120 INPUT "AO ... offset (1-200) =";AO
130 INPUT "BO ... offset (1-200) =";BO
140 PRINT " "
150 INPUT "Horizontal Timescale  uS/Div";T
160 PRINT " "
170 IF DATFILE$="" THEN DATFILE$="data"
180 OPEN DATFILE$+".dat" FOR INPUT AS #1
200 CLS
210 GOSUB 840
220 GOSUB 1020
270 LOCATE 7,66
280 PRINT "CHANNEL A"
290 LOCATE 19,66
300 PRINT "CHANNEL B"
310 LOCATE 11,66
320 PRINT " FILE: ";DATFILE$
330 LOCATE 13,66
340 PRINT "TIME";T/2;"uS/div"
350 J=1
360 FOR I=1 TO 1024
370   A$=INPUT$(1,#1)  'take 1 byte from device #1
380   A(I)=ASC(A$)
390 A(I)=INT(A(I)*200/256)
400 A(I)=A(I)+AO
410   GOSUB 680
420 NEXT I
430 LINE -(512,100),0
440 PSET (0,100)
450 FOR I=1025 TO LOF(1)
460   K=I-1024
470   A$=INPUT$(1,#1)
480   B(K)=ASC(A$)
```

```
490 B(K)=INT(B(K)*200/256)
500 B(K)=B(K)+BO
510   GOSUB 770
520 NEXT I
590 LOCATE 24,1
610 CLOSE #1
620 GOSUB 1060
630 GOTO 640
640 GOTO 630
650 END
660 '----------------------------CHANNEL  A here.....
670 '
680 IF J=2 THEN GOTO 690 ELSE 730
690 LINE -(I/2,A(I)),1
710 J=1
720 RETURN
730 J=J+1
740 RETURN
750 '----------------------------CHANNEL  B here.....
760 '
770 IF J=2 THEN GOTO 780 ELSE 820
780 LINE -(K/2,B(K)),1
790 'PSET(K/2,B(K))
800 J=1
810 RETURN
820 J=J+1
830 RETURN
840 '----------------------------DRAW SCALES.............
850 X=0
860 PSET (0,100)
870 FOR I=99 TO 101
880     PSET (X,I)
890 NEXT I
900 IF X>500 THEN GOTO 930
910 X=X+25
920 GOTO 870
930 Y=0
940 PSET (0,0)
950 FOR I=0 TO 3
960     PSET (I,Y)
970 NEXT I
980 IF Y>200 THEN GOTO 1010
990 Y=Y+25
1000 GOTO 950
1010 RETURN
1020 LINE(0,0)-(0,200)
1030 LINE(0,100)-(512,100)
1040 PSET (0,100)
1050 RETURN
1060 '
1070 '  I N I T I A L I Z E
1080 '
1090 DEFINT A-S
1100 DIM CURSOR(15,1)
1110 KEY OFF
```

```
1120 PLAY"MF"
1130 SCREEN 2
1140 '
1150 '  Determine mouse driver location, if not found, quit.
1160 '
1170 DEF SEG=0
1180 MSEG=256*PEEK(51*4+3)+PEEK(51*4+2)   ' Get mouse segment
1190 MOUSE=256*PEEK(51*4+1)+PEEK(51*4)    ' Get mouse offset
1200 IF MSEG OR (MOUSE-2) THEN 1250
1210 PRINT"Mouse driver not found"        ' Not found, so print
1215                                      ' error.
1220 PRINT
1230 PRINT"Press any key to return to system"
1240 I$=INKEY$ : IF I$="" THEN 1240 ELSE SYSTEM
1250 DEF SEG=MSEG : MOUSE=MOUSE+2         ' Set mouse segment
1260 IF PEEK(MOUSE-2) = 207 THEN 1210     ' 207 is iret
1270                                      ' Mouse Driver is
1275                                      ' there, continue.
1280 M1 = 0 : CALL MOUSE(M1,M2,M3,M4)     ' Initialize the
1285                                      ' mouse.
1290 '
1300 '  Set mouse sensitivity
1310 '
1320 M1 = 15 : M3=8 : M4=16
1330 CALL MOUSE(M1,M2,M3,M4)
1340 '
1350 '  Define the "logical and" cursor mask
1360 '
1370 CURSOR( 0,0)=&HFFFF          ' Binary 1111111111111111
1380 CURSOR( 1,0)=&HFFFF          ' Binary 1111111111111111
1390 CURSOR( 2,0)=&HFFFF          ' Binary 1111111111111111
1400 CURSOR( 3,0)=&HFFFF          ' Binary 1111111111111111
1410 CURSOR( 4,0)=&HFFFF          ' Binary 1111111111111111
1420 CURSOR( 5,0)=&HFFFF          ' Binary 1111111111111111
1430 CURSOR( 6,0)=&HFFFF          ' Binary 1111111111111111
1440 CURSOR( 7,0)=&HFFFF          ' Binary 1111111111111111
1450 CURSOR( 8,0)=&HFFFF          ' Binary 1111111111111111
1460 CURSOR( 9,0)=&HFFFF          ' Binary 1111111111111111
1470 CURSOR(10,0)=&HFFFF          ' Binary 1111111111111111
1480 CURSOR(11,0)=&HFFFF          ' Binary 1111111111111111
1490 CURSOR(12,0)=&HFFFF          ' Binary 1111111111111111
1500 CURSOR(13,0)=&HFFFF          ' Binary 1111111111111111
1510 CURSOR(14,0)=&HFFFF          ' Binary 1111111111111111
1520 CURSOR(15,0)=&HFFFF          ' Binary 1111111111111111
1530 '
1540 '  Define the "exclusive or" cursor mask
1550 '
1560 CURSOR( 0,1)=&H200           ' Binary 0000001000000000
1570 CURSOR( 1,1)=&H300           ' Binary 0000001100000000
1580 CURSOR( 2,1)=&H380           ' Binary 0000001110000000
1590 CURSOR( 3,1)=&H3C0           ' Binary 0000001111000000
1600 CURSOR( 4,1)=&H3E0           ' Binary 0000001111100000
1610 CURSOR( 5,1)=&H3F0           ' Binary 0000001111110000
1620 CURSOR( 6,1)=&H3F8           ' Binary 0000001111111000
1630 CURSOR( 7,1)=&H3FC           ' Binary 0000001111111100
```

```
1640 CURSOR( 8,1)=&H3FE          ' Binary 0000001111111110
1650 CURSOR( 9,1)=&H3FF          ' Binary 0000001111111111
1660 CURSOR(11,1)=&H30           ' Binary 0000000000110000
1670 CURSOR(12,1)=&H30           ' Binary 0000000000110000
1680 CURSOR(13,1)=&H18           ' Binary 0000000000011000
1690 CURSOR(14,1)=&H18           ' Binary 0000000000011000
1700 CURSOR(15,1)=&H0            ' Binary 0000000000000000
1710 '
1720 '  Set the mouse cursor shape
1730 '
1740 M1 = 9 : M2 = 6 : M3 = 0
1750 CALL MOUSE(M1,M2,M3,CURSOR(0,0))
1760 '
1770 '  Draw the quit box
1780 '
1790 'LINE(QX,QY)-(319,199),3,B
1800 'LOCATE 24,36 : PRINT"Quit";
1810 '
1820 '  Set mouse cursor location, then turn on cursor
1830 '
1840 M1 = 4 : M3 = 320 : M4 = 160 : CALL MOUSE(M1,M2,M3,M4)
1850 M1 = 1 : CALL MOUSE(M1,M2,M3,M4)
1860 '
1870 '  M A I N    L O O P
1880 '
1890 M1=3 : CALL MOUSE(M1,BT,MX,MY)      ' Get mouse location
1895                                      ' and button status.
1900 X=MX*T/50
1910 Y=199-MY
1920 LOCATE 1,10
1930 PRINT "Time [uS] =";X: LOCATE 1,40: PRINT "Amplitude
[Pts] =";Y
1932 K$=INKEY$
1934 IF K$="r" THEN GOTO 10
1936 IF K$="q" THEN GOTO 9000
1940 GOTO 1890                           ' Keep looping...
1950 '
1960 '  R E T U R N   T O   M A I N   L O O P
2000 '
2030 RETURN
9000 END
```

DAT2FFT Computer Program Source Listing

```
1 REM ******************************************************
2 REM * DAT2FFT  A program which creates a fast fourier      *
3 REM *          transform from a stored CRO trace. Data from*
4 REM *          one trace (1024 bytes) is read from the     *
5 REM *          hexidecimal sequential file. The program    *
6 REM *          uses sin and cos lookup tables. The complex *
7 REM *          time function is defined from -T/2 to +T/2  *
8 REM *          in N steps. The complex frequency function  *
9 REM *          will be from 0 to +F/2 in steps of 1/T. Data*
10 REM *         from -F/2 to 0 is discarded.                *
11 REM ******************************************************
10 CLS
60 REM THE FREQUENCY POINT (1+N/2) IS ZERO FREQUENCY
70 REM N=2**NL     SN=-1 IS FOWARD, SN=+1 IS REVERSE TRANSFORM
80 DIM XR(4096),XI(4096),C(2048),S(2048)
90 N=4096: NL=12: SN=-1: REM FOWARD TRANSFORM
100 PRINT"*********************************DOING LOOKUP TABLES"
110 PI=3.141593
120 FOR K=1 TO N/2
130     C(K)=COS(PI/K):S(K)=SIN(PI/K)
140 NEXT K
150 PRINT"*******************************DEFINING TEST FUNCTION"
160 LINE INPUT "enter file name( '.DAT assumed) :  ";DATFILE$
170 IF DATFILE$="" THEN DATFILE$="data"
180 OPEN DATFILE$+".dat"FOR INPUT AS #1
190 FOR I=1 TO 1024
200     A$=INPUT$(1,#1)  'take 1 byte from device #1
210     XR(I)=ASC(A$)
220     XI(I)=0
230 NEXT I
235 CLOSE #1
240 FOR I=1025 TO N
250     XR(I)=XR(1024):XI(I)=0
260 NEXT I
270 PRINT"*********************************************DOING FFT"
280 GOSUB 520
290 PRINT "*********************************CALCULATION OF XR(I)"
300 FOR I=N/2+1 TO N
310     XR(I)=SQR(XR(I)*XR(I)+XI(I)*XI(I))
320 NEXT I
325 PRINT "************************************STORE FFT DATA"
330 LINE INPUT "Enter file name( '.FFT assumed) : ";DATFILE$
340 OPEN DATFILE$+".FFT" FOR OUTPUT AS #1
350 FOR I=N/2+1 TO N
360     V=XR(I)
365     IF V>99999.99 THEN V=99999.99
370     PRINT #1, USING "#####.##";V
372 NEXT I
374 CLOSE #1
440 PRINT "************TYPE 's' TO RESTART WITH NEW DATA FILE"
441 PRINT "*****************************TYPE 'q' TO END PROGRAM"
442 K$=INKEY$
```

```
460 IF K$="s" THEN GOTO 480
465 IF K$="q" THEN GOTO 500
470 GOTO 442
480 CLOSE #1
490 GOTO 150
500 PRINT "************************************ END OF PROGRAM"
510 END
530 REM COMPUTES FFT OF SEQUENCE OF N INTEGER COMPLEX POINTS
535 REM (XR,XI)
540 REM NL=LOG2(N)
550 REM TIME FUNCTION FROM -T/2 TO +T/2
560 REM FREQUENCY FROM -F/2 TO <+F/2 WHERE F=N/T
570 REM SN=-1 FORWARD,  SN=+1 INVERSE
580 REM PROGRAM USES INTEGERISED SIN & COS LOOKUP TABLES
590 REM PASS FROM MAIN PROGRAM  XR(N),XI(N),S(N/2),C(N/2),NL,
600 REM SN
610 N2=N/2
620 REM REARRANGE INPUT FOR -T/2 TO +T/2
630 GOSUB 1040
640 REM REORDER SEQUENCE
650 J=1
660 FOR L=1 TO N-1
670     IF L>=J THEN GOTO 710
680     TR=XR(J): TI=XI(J)
690     XR(J)=XR(L): XI(J)=XI(L)
700     XR(L)=TR: XI(L)=TI
710     K=N2
720     IF K>=J GOTO 760
730     J=J-K
740     K=K/2
750     GOTO 720
760     J=J+K
770 NEXT L
780 REM CALC FFT
790 ME=1
800 FOR M=1 TO NL
810     K=ME
820     ME=2*ME
830     UR=1: UI=0
840     WR=C(K): WI=SN*S(K)
850 FOR J=1 TO K
860     FOR L=J TO N STEP ME
870         LK=L+K
880         TR=XR(LK)*UR-XI(LK)*UI
890         TI=XI(LK)*UR+XR(LK)*UI
900         XR(LK)=XR(L)-TR
910         XI(LK)=XI(L)-TI
920         XR(L)=XR(L)+TR: XI(L)=XI(L)+TI
930     NEXT L
940     VR=UR: VI=UI
950     UR=VR*WR-VI*WI: UI=VI*WR+VR*WI
960 NEXT J,M
970 REM REARRANGE OUTPUT
980 GOSUB 1040
990 IF SN=-1 THEN RETURN
```

```
1000 FOR I=1 TO N
1010     XR(I)=XR(I)/N: XI(I)=XI(I)/N
1020 NEXT I
1030 RETURN
1040 REM REARRANGE DATA SEQUENCE
1050 FOR KJ=1 TO N2
1060     JK=KJ+N2
1070     TR=XR(JK): TI=XI(JK)
1080     XR(JK)=XR(KJ): XI(JK)=XI(KJ)
1090     XR(KJ)=TR: XI(KJ)=TI
1100 NEXT KJ
1110 RETURN
```

```
1 REM ******************************************************
2 REM * FFTP      A program to display the fast fourier       *
3 REM *           transform as a data plot. Data is read from *
4 REM *           a ".FFT" data file. A Microsoft MOUSE driver*
5 REM *           program must be resident and the MOUSE must *
6 REM *           be connected to the computer serial port.   *
7 REM *           Hardcopy may be obtained if GRAPHICS.COM has*
8 REM *           been loaded and the "Print Screen"  button  *
9 REM *           is pressed.                                 *
10 REM ******************************************************
11 GOSUB 640
12 SCREEN 2
20  CLS
30 KEY OFF
40 DIM A(1026)
50 PRINT "                    '*.FFT'  DATA  FILES ............."
60 PRINT " "
70 FILES"*.fft
80 PRINT " "
90 PRINT " "
100 LINE  INPUT "Enter file name( '.fft' assumed) :
";DATFILE$
110 PRINT " "
115 INPUT "Enter horizontal timescale setting of the PM3302
[uS/Div] = ";T
117 PRINT " "
118 INPUT "Enter horizontal magnification = ";XMAG
119 INPUT "Enter vertical magnification   = ";YMAG
120 IF DATFILE$="" THEN DATFILE$="au"
130 OPEN DATFILE$+" .FFT" FOR INPUT AS #1
140 CLS
150 GOSUB 420
160 GOSUB 600
170 LOCATE 11,66
180 PRINT " FILE: ";DATFILE$
190 N=LOF(1)
200 I=1
210 FOR J= 1 TO N
220     IF EOF(1) THEN GOTO 280
230     INPUT #1,V
240     A(I)=INT(V)/100*YMAG
250     GOSUB 350
260     I=I+1
270 NEXT J
280 CLOSE #1
310 GOSUB 1390
320 GOTO 330
330 GOTO 320
340 END
350 '----------------------------CHANNEL  A here.........
360 '
370 IF A(I)>199 THEN A(I)=199
```

```
380 F=I*XMAG
390 LINE -(F,200-A(I)),1
400 IF F>512 THEN CLOSE #1: GOTO 310
410 RETURN
420 '----------------------------DRAW SCALES.............
430 X=0
440 PSET (0,199)
450 FOR I=197 TO 199
460 PSET (X,I)
470 NEXT I
480 IF X>500 THEN GOTO 510
490 X=X+25
500 GOTO 450
510 Y=0
520 PSET (0,0)
530 FOR I=0 TO 3
540 PSET (I,Y)
550 NEXT I
560 IF Y>200 THEN GOTO 590
570 Y=Y+25
580 GOTO 530
590 RETURN
600 LINE(0,0)-(0,199)
610 LINE(0,199)-(512,199)
620 PSET (0,0)
630 RETURN
640 '
650 '  I N I T I A L I Z E
660 '
670 DEFINT B-S
680 DIM CURSOR(15,1)
690 KEY OFF
700 PLAY"MF"
710 SCREEN 2
720 '
730 '  Determine mouse driver location, if not found, quit.
740 '
750 DEF SEG=0
760 MSEG=256*PEEK(51*4+3)+PEEK(51*4+2)   ' Get mouse segment
770 MOUSE=256*PEEK(51*4+1)+PEEK(51*4)    ' Get mouse offset
780 IF MSEG OR (MOUSE-2) THEN 830
790 PRINT"Mouse driver not found"        ' Not found, so print
795                                      ' error.
800 PRINT
810 PRINT"Press any key to return to system"
820 I$=INKEY$ : IF I$="" THEN 820 ELSE SYSTEM
830 DEF SEG=MSEG : MOUSE=MOUSE+2         ' Set mouse segment
840 IF PEEK(MOUSE-2) = 207 THEN 790      ' 207 is iret
850                                      ' Mouse Driver is
855                                      ' there, continue.
860 M1 = 0 : CALL MOUSE(M1,M2,M3,M4)     ' Initialize the mouse
870 '
880 '  Set mouse sensitivity
890 '
900 M1 = 15 : M3=8 : M4=16
```

```
910 CALL MOUSE(M1,M2,M3,M4)
920 '
930 '  Define the "logical and" cursor mask
940 '
950 CURSOR( 0,0)=&HFFFF          ' Binary 1111111111111111
960 CURSOR( 1,0)=&HFFFF          ' Binary 1111111111111111
970 CURSOR( 2,0)=&HFFFF          ' Binary 1111111111111111
980 CURSOR( 3,0)=&HFFFF          ' Binary 1111111111111111
990 CURSOR( 4,0)=&HFFFF          ' Binary 1111111111111111
1000 CURSOR( 5,0)=&HFFFF         ' Binary 1111111111111111
1010 CURSOR( 6,0)=&HFFFF         ' Binary 1111111111111111
1020 CURSOR( 7,0)=&HFFFF         ' Binary 1111111111111111
1030 CURSOR( 8,0)=&HFFFF         ' Binary 1111111111111111
1040 CURSOR( 9,0)=&HFFFF         ' Binary 1111111111111111
1050 CURSOR(10,0)=&HFFFF         ' Binary 1111111111111111
1060 CURSOR(11,0)=&HFFFF         ' Binary 1111111111111111
1070 CURSOR(12,0)=&HFFFF         ' Binary 1111111111111111
1080 CURSOR(13,0)=&HFFFF         ' Binary 1111111111111111
1090 CURSOR(14,0)=&HFFFF         ' Binary 1111111111111111
1100 CURSOR(15,0)=&HFFFF         ' Binary 1111111111111111
1110 '
1120 '  Define the "exclusive or" cursor mask
1130 '
1140 CURSOR( 0,1)=&H3            ' Binary 0000000000000011
1150 CURSOR( 1,1)=&H7            ' Binary 0000000000000111
1160 CURSOR( 2,1)=&HE            ' Binary 0000000000001110
1170 CURSOR( 3,1)=&H41C          ' Binary 0000010000011100
1180 CURSOR( 4,1)=&HE38          ' Binary 0000111000111000
1190 CURSOR( 5,1)=&HF70          ' Binary 0000111101110000
1200 CURSOR( 6,1)=&HFE0          ' Binary 0000111111100000
1210 CURSOR( 7,1)=&H1FC0         ' Binary 0001111111000000
1220 CURSOR( 8,1)=&H1FE0         ' Binary 0001111111100000
1230 CURSOR( 9,1)=&H1FF0         ' Binary 0001111111110000
1235 CURSOR(10,1)=&H3FF8         ' Binary 0011111111111000
1240 CURSOR(11,1)=&H3FE0         ' Binary 0011111111100000
1250 CURSOR(12,1)=&H3F80         ' Binary 0011111110000000
1260 CURSOR(13,1)=&H7C00         ' Binary 0111110000000000
1270 CURSOR(14,1)=&H6000         ' Binary 0110000000000000
1280 CURSOR(15,1)=&H8000         ' Binary 1000000000000000
1290 '
1300 '  Set the mouse cursor shape
1310 '
1320 M1 = 9 : M2 = 0 : M3 = 15
1330 CALL MOUSE(M1,M2,M3,CURSOR(0,0))
1340 RETURN
1390 '
1400 '  Set mouse cursor location, then turn on cursor
1410 '
1420 M1 = 4 : M3 = 320 : M4 = 160 : CALL MOUSE(M1,M2,M3,M4)
1430 M1 = 1 : CALL MOUSE(M1,M2,M3,M4)
1440 '
1450 '  M A I N    L O O P
1460 '
1470 M1=3 : CALL MOUSE(M1,BT,MX,MY)      ' Get mouse location
1475                                      ' and button status
```

```
1480 X=MX/4/.000001/T/10/XMAG
1490 Y=199-MY
1500 LOCATE 1,10
1510 PRINT "Frequency [Hz] =";X: LOCATE 1,40: PRINT "Amplitude
[Pts] =";Y
1520 K$=INKEY$
1530 IF K$="r" THEN GOTO 1660
1540 IF K$="q" THEN GOTO 1620
1550 GOTO 1470                          ' Keep looping...
1555 RETURN
1560 '
1570 '  R E T U R N   T O   M A I N   L O O P
1580 '
1620 M1=2 : CALL MOUSE(M1,M2,M3,M4)     ' Turn off mouse cursor
1650 END
1660 M1=2 : CALL MOUSE(M1,M2,M3,M4)     ' Turn off mouse cursor
1680 GOTO 12
```